

**ON SOME CHALLENGING AVENUES IN
HYDROGEN STORAGE**

A THESIS

submitted by

LINGAM HIMA KUMAR

for the award of the degree

of

DOCTOR OF PHILOSOPHY



**DEPARTMENT OF CHEMISTRY
INDIAN INSTITUTE OF TECHNOLOGY, MADRAS
CHENNAI - 600 036, INDIA**

APRIL -2008

*Dedicated
To
My Parents*

CERTIFICATE

This is to certify that the thesis entitled “**ON SOME CHALLENGING AVENUES IN HYDROGEN STORAGE**” submitted by **L. Hima Kumar** to the Indian Institute of Technology, Madras for the award of degree of **Doctor of Philosophy** is a bonafide record of research work carried out by him under my supervision. The contents of this thesis, in full or in parts, have not been submitted to any other Institute or University for the award of any degree or diploma.

Research Guides

Prof. B. Viswanathan

Department of Chemistry

IIT Madras Chennai-36

Prof. S. Srinivasa Murthy

Department of Mechanical Engineering

IIT Madras Chennai-36

Date:

Place:

ACKNOWLEDGEMENTS

It is my great pleasure to express my gratitude to my guide **Prof. B. Viswanathan**, for his guidance, inspiration and constant encouragement throughout my research work. I am grateful to him for introducing me to the various aspects of materials chemistry. The many discussions during group meetings I had with him were a major source of learning and improving my knowledge and skills. Mere words are not sufficient to express my heartfelt thanks for his enthusiastic support in all efforts during my research period. I would like to express my gratitude to his sincerity, dignity and dedication towards work. He has been a constant inspiration for me and I still believe that I have a lot to learn from him. I feel privileged to have been associated with him.

I am indebted to thank my co-guide **Prof. S. Srinivasa Murthy** for his help, constant encouragement and support to carry out my research work.

I wish to express my sincere thanks to the Doctoral committee members, **Prof. R. P. Viswanath, Prof. T. K. Varadarajan, Prof. K. Vidyasagar, Prof. S. Ramaprabhu** and **Prof. A. Subrahmanyam** for their fruitful discussions and suggestions during doctoral committee meetings.

I am grateful to **Prof. B. Viswanathan, Late Prof. S. Vanchesan, Prof. M. N. S. Rao, Late Prof. G. Sundararajan** (former Heads of the Department) and **Prof. R. Dhamodharan** (Head of the Department) for their kind help and for providing the necessary infrastructures to carry out the research work. I wish to acknowledge MNES-New Delhi, IIT-Madras and Columbian Chemical Company-U.S.A for graduate fellowship. I am thankful to DST, for creating National Centre for Catalysis Research, where most of my work is carried out.

I wish to thank **IIT Madras** for providing opportunity and all facilities to carry out my research.

I thank all the non-teaching staff members of the chemistry department for their timely help. I am thankful to **Mr. Narayanan** for TGA and DSC, **Mr. Ram Kumar** for CHN analysis and **Mr. Mohan** for NMR. I would like to extend my thanks to present and former heads and staff of CGBS, SAIF and Department of Metallurgy IIT Madras for providing various facilities. I am thankful to **Mr. M. Sankaran, Mr.**

Janarthanan, Mr. P. Amulraj and **Ms. Srividya** for their untiring and continues help.

I thank my seniors **Dr. Raghuv eer, Dr. R. Ganesan, Dr. V. Chidamabaram, Dr. Aulice Scibioh, Dr. Ch. Subrahmanyam, Dr. S. Shanmugam, Dr. M. Sankaran, Dr. T. Meiyalagan** and **Dr. Sathish** for their constant encouragement and suggestions. I must also thank them for imparting valuable laboratory skills and experimental techniques when I was new to the laboratory.

I wish to thank my lab mates **Mrs. Chandravathanam. Mr. Venkateswara Rao, Mr. Indraneel, Ms. Helen, Mr. Kishore, Mr. Navaladian, Mr. Mahesh, Mrs. Janet, Mrs. Rajeswari** and **Mr. Kuppan, Dr. Mahalaxmi, Dr. Murugan, Dr. Joyce, Dr. Sabia, Mr. Sangaranarayanan, Mr. Ganesh, Mr. Ramana Murthy, Mr. Vamsi Krishna, Mr. Sudhagar, Mr. Poliraju, Mr. Jude** and **Ms. Bhanu** for their co-operation, fruitful discussions during group meetings and generous help throughout my research period.

I am thankful to **Late Prof. G. Sundararajan, Dr. Vijaya Krishna** and **Mr. Karthikeyan** for their help with glove box. I also thank **Prof. S. Ramaprabhu** and **Dr. Leela Mohan Reddy** for their help with ball mill.

I am extremely thankful to **Mr. E. Anil Kumar** and **Mr. D. Ebenezer** for their help during the experiments at R&AC lab. I extend my thanks to my all other colleagues **Dr. B.G. Mishra, Mr. R. Prakash Babu, Mr. Sumanth Kumar Meher** Department of Chemistry and **Dr. R. Vijay, Dr. P. Muthu Kumar, Mr. G. Mohan** and **Mr. M. Ajay** R&AC lab IIT Madras for their help and encouragement.

My heart felt thanks to my dear friends **Dr. Raju, Mr. Ramana, Mr. Anji Reddy** and **Mr. P. S. Ramanjaneyulu** for their motivation, constant encouragement and support through my research period. I thank all my beloved friends **Dr. Kishore, Dr. Prabhakara Rao, Dr. Ram Prasad, Mr. Ramakanth, Mr. Biswas, Mr. Jashuva, Mr. Prasanna, Mr. Hari, Mr. Asirinaidu** and **Mr. Charan** for encouragement and timely help in all my needs during research programme. I must also thank their companionship for making my stay here pleasant and fulfilling.

I want to express my heartfelt gratitude to my parents **Sri L. Rama Krihna** and **Smt. L. Mangatayaru** and my grand mother **D. Satyavathi** whose limitless love and affection has made my world beautiful place. I thank them for all the sacrifices they have made to help me achieve my goals. I thank my brothers **L. Gouri Shankar** and **L. Durga Prasad** for their wishes and my uncles **L. Haribabu, L. Murali Mohan Rao** and **L. Malli Karjuna Rao** for cheering me up when I needed it. I also want to thank **N. Sarada** for her care and affection towards me.

L. Hima Kumar

ABSTRACT

KEYWORDS: Hydrogen storage, Complex metal hydrides, Alanates, Borohydrides, Magnesium, Carbon nanomaterials

Hydrogen storage is a key enabling technology for the introduction of hydrogen economy and the use of hydrogen as energy carrier. The benchmark requires 6.5 weight percent hydrogen. Intermetallic compounds (AB , AB_2 , and AB_5) can store hydrogen at ambient conditions with fast absorption/desorption kinetics (Ex. $LaNi_5$, $FeTi$). But hydrogen storage capacity is limited to about 3 wt%. Light metal hydrides like magnesium and its alloys, alanates and borohydride show a high potential for reversible hydrogen storage because of their high hydrogen storage capacity (> 5 wt. %). However, kinetics of hydriding and dehydriding of Mg and its alloys is slow. The potential benefits of using alanates/borohydrides as hydrogen storage systems were overshadowed by the fact that the synthesis of alanates is a difficult process and the kinetics of the reaction used for storing hydrogen is slow. Moreover, high temperatures are needed to desorb stored hydrogen. Various attempts have been made in the past to facilitate (or even enhance the kinetic parameters or decrease the activation parameters) desorption process by addition of suitable materials. However, the role of these additives has to be carefully understood, since they do not only function as catalysts but have also to facilitate the transport of the species to the surface before desorption.

In the present study, nanosized Mg_2Ni alloy particles have been synthesized by polyol reduction method followed by annealing. The hydriding/dehydriding kinetics as well as electrochemical characteristics of this material were investigated. The effect of carbon materials (commercial carbons, carbon nanofibers, nitrogen containing carbon

nanotubes) as additives to the LiAlH_4 has been examined. Carbon nanofibers (CNFs) were prepared by catalyzed decomposition of gaseous ethylene on NiCu/H-ZSM-5. Nitrogen containing carbon nanotubes (NCNT) were synthesized by using PVP as carbon source and alumina membrane as template. These materials were characterized by XRD, SEM, TEM and FT-IR techniques. Dehydrogenation characteristics of LiAlH_4 admixed with Vulcan XC72R, CDX975, Mesoporous carbon and CNFs were studied and compared with that of pure lithium aluminum hydride. Carbon nanofibers have shown prominent effect on the dehydrogenation properties of LiAlH_4 . On the basis of the dehydrogenation characteristics a possible mechanism for the improved dehydriding of LiAlH_4 upon adding carbon materials has been considered. Effect of NCNT on the hydrogenation/ dehydrogenation properties of NaAlH_4 and LiAlH_4 was studied. Thermal decomposition properties of alanate-NCNT composites were examined by DSC analysis and in-situ DRIFT-IR studies. NaAlH_4 -NCNT composite was capable of taking reversibly 4 wt. % of hydrogen.

Effect of hetero atom (B and N) containing carbon material on hydrogen sorption properties was studied. Nitrogen containing carbon increases hydrogen absorption and desorption kinetics compared to boron containing and also results in the decrease of dehydriding temperature of MgH_2 by 20 K. Cobalt based catalysts (Co, Co-Ni, Co-Cr, Co-Mo) were employed to study the hydrogen evolution reaction from alkali stabilized sodium borohydride. Among examined catalysts Co-Mo system is found to be highly active for the hydrolysis of sodium borohydride. The rate of hydrogen evolution was measured as a function of the concentration of NaOH, as well as the reaction temperature. The activation energies for hydrogen evolution reaction were calculated.

TABLE OF CONTENTS

	Page No.
ACKNOWLEDGEMENTS	i
ABSTRACT	iv
TABLE OF CONTENTS	vi
LIST OF TABLES	xi
LIST OF FIGURES	xii
LIST OF SCHEMES	xvi
ABBREVIATIONS	xvii
NOTATIONS	xviii
 CHAPTER 1 INTRODUCTION	
1.1 Hydrogen economy	1
1.1.1 Why hydrogen?	2
1.2. Hydrogen production	4
1.2.1 From fossil fuels	4
1.2.2 Gasification of coal	5
1.2.3 Water electrolysis	5
1.2.4 Thermal decomposition of water.....	6
1.2.4 Biological or biochemical methods	6
1.3 Hydrogen storage	7
1.3.1 Gaseous hydrogen storage	9
1.3.2 Liquid hydrogen	9
1.3.4 Solid state storage	10
1.3.5 Carbon materials	11

Table of contents (contd.)

1.3.6	Other high surface area materials	12
1.4.	Metal hydrides	13
1.4.1	The metal-hydrogen reaction	15
1.4.2	Thermodynamics	17
1.4.3	Reaction mechanism and kinetics	19
1.4.4	Types of metal hydrides	21
1.4.4.1	Binary hydrides	21
1.4.4.2	Intermetallic hydrides	22
1.4.4.3	Magnesium and Magnesium-Based Compounds	25
1.5	Complex metal hydrides	27
1.5.1	Alanates	27
1.5.1.1	Synthesis and characterization of alanates	29
1.5.1.2	Dehydrogenation and rehydrogenation reactions	31
1.5.1.3	Thermodynamics	32
1.5.1.4	Kinetics of catalyzed Alanates	34
1.5.2	Borohydrides	41
1.5.2.1	Dehydrogenation and rehydrogenation reactions	41
1.6	Motivation and scope	43

CHAPTER 2 EXPERIMENTAL METHODS

2.1	Chemicals and materials used	45
2.2	Experimental procedures	45
2.2.1	Purification of hydrogen	45
2.2.2	Electrochemical studies	46
2.3	Characterization techniques	46

Table of contents (contd.)

2.3.1	Powder X-ray Diffraction (XRD)	46
2.3.2	Elemental analysis	46
2.3.3	Scanning Electron Microscopic studies (SEM).....	47
2.3.4	Transmission Electron Microscopic studies (TEM)	47
2.3.5	Thermogravimetric Analysis (TGA)	47
2.4	Hydrogen evolution kinetics measurements	48
2.5	High pressure apparatus	50
2.5.1	Kinetic measurements	50
3.1.1	Static PCI measurements	54

CHAPTER 3 SORPTION PROPERTIES OF Mg₂Ni PREPARED BY POLYOL REDUCTION METHOD

3.1	Introduction	55
3.2	Synthesis of Mg ₂ Ni alloy	58
3.3	Results and discussion	59
3.3.1	Kinetics	61
3.3.2	Pressure-Compositions Isotherms	64
3.3.3	Electrochemical characteristics	66

CHAPTER 4 DEHYDRIDING BEHAVIOR OF CARBON ADMIXED LiAlH₄

4.1	Introduction	71
4.2	Experimental	75
4.2.1	Synthesis of carbon nanofibers (CNFs)	75
4.2.2	Preparation of carbon admixed LiAlH ₄	76
4.3	Results and discussion	76

Table of contents (contd.)

4.3.1	Characterization of carbon nanofibers	76
4.3.2	Effect of carbon additives	78
4.3.2.1	Dehydrogenation measurements for carbon admixed LiAlH_4	79
4.3.3	Effect of Carbon Nanofibers	83
4.3.3.1	Dehydrogenation kinetics of CNFs admixed LiAlH_4 composite	85
4.4	Role of carbon in the dehydrogenation kinetics of LiAlH_4	92

CHAPTER 5 HYDROGEN STORAGE PROPERTIES OF ALANATES ADMIXED NITROGEN CONTAINING CARBON NANOTUBES

5.1	Introduction	98
5.2	Experimental	100
5.2.1	Synthesis of Nitrogen containing carbon nanotubes (NCNT)	100
5.2.2	Preparation of NaAlH_4 -NCNT (SAH-NCNT) and LiAlH_4 -NCNT (LAH- NCNT) composites	100
5.3	Results and discussion	101
5.3.1	DSC Studies	104
5.3.2	Constant temperature dehydrogenation studies	106
5.3.3	Kissinger analysis	110
5.3.4	IR studies	114
5.3.5	Rehydrogenation studies	119
5.3.6	Reaction mechanism	120

CHAPTER 6 HYDROGEN STORAGE PROPERTIES OF Mg-N OR B CONTAINING CARBON COMPOSITES

6.1	Introduction	122
6.2	Experimental	125

Table of contents (contd.)

6.2.1	Synthesis of boron containing carbon	125
6.2.2	Synthesis of Nitrogen containing carbon	126
6.2.3	Preparation of Magnesium- N or B containing carbon composites	127
6.2.4	Activation	127
6.3	Results and discussion	127
6.3.1	Hydrogen Storage properties	133
6.3.2	DSC studies	137

CHAPTER 7 CATALYTIC EFFECTS IN GENERATION OF HYDROGEN FROM NaBH₄

6.1	Introduction	140
6.2.	Preparation of cobalt based catalysts	125
6.3	Results and discussion	146
6.3.1	Calibration of catalytic activity.....	150
6.2.3	Effect of NaOH concentration on hydrogen generation rate	152
6.2.3	Effect of temperature on hydrogen generation rate.....	154

CHAPTER 8 SUMMARY AND CONCLUSIONS159

REFERENCES164

LIST OF PUBLICATIONS182

LIST OF TABLES

Table	Title	Page
1.1.	Comparison of fuel properties of hydrogen and other fuel systems	3
1.2.	Summary of reported hydrogen storage capacities in carbon nanostructures	12
1.3.	Hydrogen storage capacities of different alanates	28
3.1.	Enthalpies and entropies of Mg ₂ Ni alloy	65
4.1.	Surface area and dehydrogenation rate for various carbons	81
4.2.	Rate constants and Avrami exponents of LiAlH ₄ +CNFs composite	90
5.1.	Activation energies for SAH-NCNT	110
5.2.	Peak temperatures for SAH and SAH-NCNT composites at different heating rates	111
5.3.	Apparent activation energies for two decomposition processes of SAH and SAH-NCNT composites	112
5.4.	Peak temperatures for LAH and LAH-NCNT composites at different heating rates	113
5.5.	Apparent activation energies for two decomposition processes of LAH and LAH-NCNT composites	114
5.6.	Infrared frequencies of SAH and SAH-NCT composites at room temperature	116
5.7.	IR frequencies of NAH-NCNT composite (in cm ⁻¹) at different temperatures	118
6.1.	Adsorption capacities of Mg-C composites for 15 min, at 573 K and 2 MPa	134
6.2.	Desorption capacities of Mg-C composites for 15 min, at 573 K and 0.1 MPa	137
6.3.	Decomposition temperatures of MgH ₂ and Mg-C composites	139
7.1.	Hydrogen generation rates for various catalysts; solution mixtures: 1.5 wt. % NaBH ₄ + 10 wt. % NaOH	151
7.2.	Hydrogen generation rates for the Co-Ni, Co-Sn, Co-Cr and Co-Mo catalysts at different temperatures from solution mixture of 20 ml of 1.5 wt. % NaBH ₄ + 10 wt. % NaOH	156
7.3.	Activation energies and borohydride hydrolysis rates for cobalt based catalysts	157

LIST OF FIGURES

Figure	Title	Page
1.1	Global energy systems transition, 1850 – 2150	2
1.2	Comparison of hydrogen storage densities of different hydrogen storage methods	8
1.3	Schematics of potential energy curves of hydrogen approaching metal surface. The hydrogen molecule is attracted by weak van der Waal forces lead to physisorbed state, then the molecule dissociates and chemisorbs followed by diffusing into bulk metal	16
1.4	Schematic pressure composition isotherm	18
1.5	Pressure composition isotherms at different temperatures and corresponding van't Hoff plot	19
1.6	Comparison of van't Hoff plots of NaAlH ₄ and Na ₃ AlH ₆ systems with those of various intermetallic and elemental hydrides	33
2.1	Experimental set-up for the measuring the hydrogen evolution	49
2.2	Experimental set-up for measuring the sorption kinetics	51
3.1	XRD pattern of Mg ₂ Ni prepared by polyol reduction followed by annealing at 573 K for 3 h	60
3.2	TEM image of Mg ₂ Ni prepared by polyol reduction followed by annealing at 573 K for 3 h	61
3.3	Kinetic curves of hydriding of nano-Mg ₂ Ni at an initial pressure of 2.5 MPa and 473, 523 and 573 K	62
3.4	Hydrogen desorption curves of nano-Mg ₂ Ni at a pressure of 10 kPa bar and 473, 523 and 573 K.	63
3.5	Pressure-composition isotherms of nano-Mg ₂ Ni at 548, 573 and 603 K.	64
3.6	van't Hoff plot, Ln (P _{eq}) vs 1/T	65
3.7	Galvanostatic discharge curves of nano-Mg ₂ Ni at current densities of 20, 50 and 100 mA/g	67
3.8	Cycle test data of the nano-Mg ₂ Ni	69
3.9	Electrochemical pressure composition isotherm at a discharge current density of 20 mA/g for the nano-Mg ₂ Ni alloy	70

List of Figures (Contd.)

Figure	Title	Page
4.1	(a) SEM image (b) TEM image of purified carbon nanofibers	77
4.2	X-ray diffraction pattern of the CNFs	78
4.3	X-ray diffraction patterns of as-received LiAlH ₄ , Black pearls 2000 admixed LiAlH ₄ and CDX admixed LiAlH ₄	79
4.4	Dehydrogenation profiles for the (■) pure LiAlH ₄ (●) 5 wt% Vulcan XC 72R admixed LiAlH ₄ (◆) 5 wt% mesoporous carbon admixed LiAlH ₄ (▲) 5 wt% CDX 975 admixed LiAlH ₄ (▼) Black pearls 2000 admixed LiAlH ₄	81
4.5	Dehydrogenation kinetics of LiAlH ₄ admixed with 5 wt% of Black Pearls 2000 admixed LiAlH ₄ at (■) 408 K (◆) 413 K (▲) 418 K	82
4.6	Dehydrogenation kinetics of LiAlH ₄ admixed with different (5, 7 and 9) wt% of Black Pearls 2000	83
4.7	SEM images of LiAlH ₄ admixed with CNFs at (a) lower and (b) higher magnification	84
4.8	Dehydrogenation kinetics of LiAlH ₄ admixed with CNFs and LiAlH ₄ admixed with Vulcan carbon and LiAlH ₄	85
4.9	X-ray diffraction pattern of the LiAlH ₄ + CNFs composite after dehydrogenation at 408 K	86
4.10	Dehydrogenation curves at (A) 398 K (b) 408 K (c) 418 K for a LiAlH ₄ sample admixed with CNFs	87
4.11	Fit of the John–Mehl Avrami model to experimental dehydrogenation data	89
4.12	Plot of $\ln[-\ln(1-\alpha)]$ vs. $\ln(t)$ at (▲) 398 (■) 408 (◆) 418 K and (●) 428 K	89
4.13	$\ln k$ vs. $1/T$ for LiAlH ₄ +CNFs composite	90
4.14	Comparison of dehydrogenation curves for (A) LiAlH ₄ doped with CNF + 3 mol % VCl ₃ and (B) LiAlH ₄ admixed with CNF at 398 K	91
5.1	SEM images of Nitrogen containing carbon nanotubes	101
5.2	XRD pattern of nitrogen containing carbon nanotubes	102
5.3	IR spectrum of nitrogen containing carbon nanotubes	102
5.4	XRD pattern of SAH and SAH-NCNT composites	103
5.5	XRD pattern of LAH and LAH-NCNT composites	104

List of figures (contd.)

Figure	Title	Page
5.6	DSC curves of SAH and SAH-NCNT composites	105
5.7	DSC curves of LAH and LAH-NCNT composites	106
5.8	Dehydrogenation behavior of LAH-NCNT composite at 423 K	107
5.9	XRD pattern for LAH-NCNT composite after dehydrogenation at 423 K	107
5.10	Isothermal dehydrogenation kinetics of SAH-NCNT composite at 473, 483 and 493 K	108
5.11	XRD pattern for the dehydrogenated SAH-NCNT composite at 493 K	109
5.12	Arrhenius plot of the SAH-NCNT composite for first and second step decomposition reaction.	109
5.13	Kissinger plot for dehydrogenation of SAH and SAH-NCNT composites	112
5.14	Kissinger plot for dehydrogenation of LAH and LAH-NCNT composites	114
5.15	Infrared spectra of (a) SAH and (b) SAH-NCNT composites at room temperature	115
5.16	DRIFT-IR spectra of SAH-NCNT composites between the temperatures 300 K and 563 K	117
5.17	Rehydrogenation profile for the SAH-NCNT composite at 473 K and 10 MPa	120
6.1	(a) XRD pattern and (b) SEM image of boron containing carbon	128
6.2	XRD patterns for the boron and nitrogen containing carbon (a) before and (b) after treating with HCl	129
6.3	SEM image and EDX spectra of as synthesized carbon fibers	130
6.4	SEM Image of Carbon fibers after HCl treatment	131
6.5	SEM images of Mg-C (a) Mg- NC (b) Mg-G and (c) Mg- BC composites	132
6.6	XRD pattern for the Mg-C (G, NC and BC) composites	133
6.7	Absorption curves for Mg-C composites at 573 K and 2 MPa pressure	134

List of figures (contd.)

Figure	Title	Page
6.8	XRD pattern for the hydrided Mg-C composites	135
6.9	Desorption curves for Mg-C composites at 573 K and 0.1 MPa	136
6.10	DSC curves for the hydrided Mg-C composites and MgH ₂ at the scan rate of 5 °C /min.	138
7.1	XRD pattern for Co catalyst after annealing in H ₂ atm at 623 K	146
7.2	SEM image of Co catalyst after annealing in H ₂ atm at 623 K	147
7.3	X-ray diffraction pattern of (a) Co-Ni (b) CoSn	148
7.4	X-ray diffraction pattern of (a) Co-Mo (b) Co-Cr	148
7.5	SEM images of (a) Co-Sn (b) Co-Cr (c) Co-Ni (d) Co.Mo catalysts	149
7.6	Catalytic performance of cobalt based catalysts (■) Co-commercial (▲) Co-Ni commercial (▽) Co (●) Co-Ni (□) CoSn (★) Co-Cr (o) Co-Mo and (20 ml of 1.5 wt% NaBH ₄ + 4 wt% NaOH)	150
7.7	Effect of NaOH concentration on the hydrogen generation rate measured using 20 ml of <i>x</i> wt. % NaOH + 1.5 wt. % NaBH ₄ solutions (<i>x</i> = 4, 8, 12, 16, 20, 24) at room temperature using 0.1 g of Co-Ni catalyst.	152
7.8	Hydrogen storage capacity of the NaBH ₄ + NaOH solution system as a function of the NaOH concentration	153
7.9	Effect of solution temperature on the hydrogen generation rate, measured from 1.5 wt. % NaBH ₄ + 10 wt. % NaOH solutions using 0.1 g of CoSn catalyst.	155
7.10	Arrhenius plots of the Co-Sn, Co-Cr Co-Mo catalysts for hydrogen generation	157

LIST OF SCHEMES

Scheme	Title	Page
5.1	Schematic representation of hydrogen spill over from activation centre in carbon nanotubes to metal	121

ABBREVIATIONS

MPa	-	mega Pascal
SEM	-	Scanning electron microscope
SWNT	-	Single walled nanotubes
MWNT	-	Multi walled nanotubes
NMR	-	Nuclear magnetic resonance
XRD	-	X-ray diffraction
THF	-	Tetrahydrofuran
GNFs	-	Graphitic nanofibers
CNFs	-	Carbon nanofibers
EDX	-	Energy Dispersive X-ray Analysis
FT-IR	-	Fourier transform infrared spectroscopy
LAH	-	Lithium aluminum hydride
SAH	-	Sodium aluminum hydride
DOE	-	Department of energy
JMA	-	Jhonson-Mehl-Avrami
TEM	-	Transmission electron microscope
HT	-	High temperature
MT	-	Medium temperature
LT	-	Low temperature
AR	-	Analytical reagent
PVP	-	Poly(N-vinyl pyrrolidine)
MH	-	Metal hydride
HF	-	Hydro fluoric acid
TG	-	Thermo gravimetry
FCC	-	Face centered cubic
BCC	-	Body centered cubic
PCI	-	Pressure composition isotherm

NOTATIONS

\sim	-	approximately
%	-	percentage
η	-	Avrami exponent
α	-	fraction of material reacted (decomposed)
β	-	heating rate
ν	-	rate of reaction
ΔH	-	Enthalpy change of formation
ΔS	-	Entropy change of formation
μm	-	micrometer
A	-	pre-exponential factor
atm	-	atmosphere
at.%	-	Atomic percentage
cm	-	centimeter
cm^{-1}	-	centimeter inverse
cm^3	-	cubic centimeter
$\text{cm}^2 \text{ s}^{-1}$	-	centimeter square per second
$^{\circ}\text{C}$	-	degree celcius
E	-	electrode potential
E_a	-	Activation energy
g	-	gram
G	-	graphite
H/M	-	hydrogen to metal ratio
h	-	hour
I	-	discharge current
K	-	Kelvin
k	-	rate constant
kg	-	kilogram
kgTNT m^{-3}	-	kilogram trinitrotoluene per meter cube
km	-	kilometer
kWh kg^{-1}	-	kilowatt hour per kilogram
$\text{J}/(\text{mol K})$	-	Joules per mole per Kelvin
mA	-	milliampere
mA/g	-	miliampere per gram
mAh/g	-	milliampere hour per gram
mg	-	milligram
ml	-	Milliliter

$m^2 g^{-1}$	-	meter square per gram
ml/min	-	milliliter per minute
m_d^t	-	mass of hydrogen desorbed at time t
m_{alloy}	-	mass of the alloy
m_t	-	mass of the hydrogen absorbed by the material at time t
m_a^t	-	the total mass of the hydrogen in void volume of measurement facility at time t
$m_{V_1}^t$	-	mass of hydrogen at any time t in volume V_1
$m_{V_2}^t$	-	hydrogen mass at any time t in volume V_2
m_s	-	mass of hydrogen in volume V_1 at the start
min	-	minutes
$m s^{-1}$	-	meter per second inverse
mW	-	milliwatt
$N m^{-2}$	-	Newton per meter square
nm	-	nanometer
P_e	-	Equilibrium pressure
p	-	Pressure
$Q_{discharge}$	-	discharge capacity
R	-	gas constant
r	-	atomic radius
rpm	-	rotations per minute
t	-	time
T_m	-	peak temperature
$t_{1/2}$	-	half life for the decomposition of sodium borohydride solution
V	-	volume
Vol. %	-	volume percent
V'	-	volume of pipes
V_1	-	volume of pipes and reference cell
V_2	-	void volume of reactor
V_{CC}	-	reference volume
wt.	-	weight
WC	-	tungsten carbide
z	-	compressibility factor

CHAPTER 1

INTRODUCTION

1.1 HYDROGEN ECONOMY

Energy is one of the basic needs of human beings and is extremely crucial for continued development of human life. It is essential to provide adequate and affordable energy for eradicating poverty, improving human welfare, and raising living standards. The global energy demand is increasing with increasing human population and modernization. The world at present relies on fossil fuels (such as oil, gas and coal) to meet its energy requirements. The growth in global energy demand is projected to rise sharply over the coming years. Presently available energy systems may not be able to make up the future energy requirements. Depletion of fossil fuel reserves may prompt the developed countries to employ nuclear power. The use of fossil fuel and nuclear energy, production and consumption, causes environmental degradation that threatens human health and affects ecological balance. Therefore, if the rapidly increasing global energy needs are to be met without damaging the environment, it is necessary to exploit energy systems that should not jeopardize the life of current and future generations.

Increase in energy quality is one of the most significant transitions in global energy systems (Fig. 1.1). Each successive transition from one source to another has entailed a shift to fuels that had lower carbon content and higher hydrogen content (decarbonization). It is also evident that at each transition accompanied by greater energy density. At present, the use of natural gas (with highest hydrogen content) is growing fast among the fossil fuels. The next logical fuel in this progression is hydrogen.

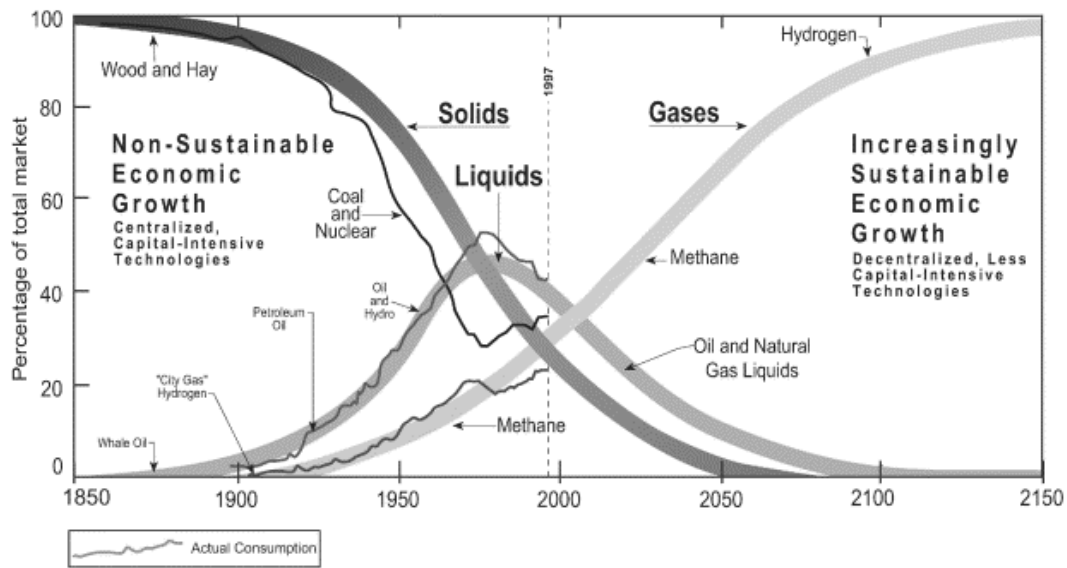


Fig. 1.1 Global energy systems transition, 1850 – 2150 (Dunn, 2002)

Renewable energy sources that use indigenous resources have the potential to provide energy services with almost zero emissions. Renewable energy sources such as solar energy, wind power, biomass and geothermal energy are abundant, inexhaustible and widely available. The so-called hydrogen economy is a long-term project that can be defined as an effort to change the current energy system to one which attempts to combine the cleanliness of hydrogen as an energy carrier with the efficiency of fuel cells; devices that transform energy into electricity and heat (Marbán and Valdés-Solís, 2007). As an energy carrier, hydrogen must be obtained from renewable energy sources, which survive for long term and avoid or minimize CO₂ emissions.

1.1.1 Why hydrogen?

Hydrogen is not a natural fuel, but a synthetic energy carrier. It only carries energy generated by other processes. Hydrogen is the cleanest, sustainable and renewable energy carrier. Hydrogen is the simplest, lightest and most abundant element in the universe, making up 90% of all matter. It is made up of just one electron and one proton and is, therefore, the first element in the periodic table. In its normal gaseous

state, hydrogen is odourless, tasteless, colourless and non-toxic. Hydrogen burns readily with oxygen, releasing considerable amounts of energy as heat and producing only water as exhaust.

Table 1.1 Comparison of fuel properties of hydrogen and other fuels systems

Property	Unit	Hydrogen H ₂	Methane CH ₄	Gasoline -(CH ₂) _n -
Lower heating value	kWh kg ⁻¹	33.33	13.9	12.4
Self ignition temperature	K	858	813	498-774
Flame temperature	K	2318	2148	2473
Ignition limits in air	Vol. %	4 - 75	5.3 - 15	1.0-7.6
Min. ignition energy	mW	0.02	0.29	0.24
Flame propagation in air	m s ⁻¹	0.02	0.4	0.4
Explosion energy	kg TNT m ⁻³	2.02	7.03	44.22
Diffusion coefficient in air	cm ² s ⁻¹	0.61	0.16	0.05
Toxicity		No	No	High

Hydrogen is highly flammable with a high flammability range, burning when it makes up 4% to 74% of air by volume. It has high energy content by weight nearly three times that of gasoline. In contrast, hydrogen has a low energy density by volume at a standard temperature and atmospheric pressure. One gram of hydrogen gas at room

temperature occupies about 11.2 liters of space. Storing the hydrogen gas under pressure or at temperatures below 23 K, at which point it turns into a liquid, raises its volumetric density. In many ways, hydrogen seems to be an attractive replacement for existing fossil fuel system by the properties as given in Table 1.1.

Hydrogen does not exist in a natural state on earth and must be manufactured using a hydrogen-rich compound such as water as the raw material. Once it is extracted, it becomes a useful feedstock, or input, to a variety of industrial activities and sufficient to energize virtually all aspects of society, namely homes, electric utilities, business, industry and transportation.

1.2 HYDROGEN PRODUCTION

Hydrogen can be produced from a variety of feed stocks. These include fossil resources, such as natural gas and coal, as well as renewable resources, such as biomass and water with input from renewable energy sources (*e.g.* sunlight, wind, wave or hydro-power). A variety of process technologies can be used, including chemical, biological, electrolytic, photolytic and thermo-chemical. Each technology is in a different stage of development, and each offers unique opportunities, benefits and challenges. Local availability of feedstock, the maturity of the technology, market applications and demand, policy issues, and the cost will influence the selection and timing of the various options for hydrogen production.

1.2.1 From fissile fuels

There are many industrial methods currently available for the production of hydrogen; almost all the hydrogen produced in the world today involves the steam reforming of fossil fuels using a nickel catalyst. At present, this is a proven, commercial technology and is the cheapest way of making hydrogen on a large scale. In most of the cases, natural gas (methane) is the raw material. *Partial oxidation* of methane is also used to

produce hydrogen (Narayanan and Viswanathan, 1998). The process involves, reacting methane with oxygen to produce hydrogen and carbon monoxide, which is then reacted with water to produce more hydrogen and carbon dioxide (Water gas Shift reaction).

1.2.2 Gasification of coal

Hydrogen can be produced from coal through a variety of gasification processes. Gasification of coal is the traditional technique for making hydrogen, and is still used in some parts of the world. Hydrogen production from coal is commercially mature, but it is more complex than the production of hydrogen from natural gas. The cost of the resulting hydrogen is also higher. But since coal is abundant in many parts of the world and will probably be used as an energy source, it is worthwhile to explore the development of clean technologies for its use (Narayanan and Viswanathan, 1998).

1.2.3 Water electrolysis

Hydrogen production using water electrolysis is minimal today, because it requires large amounts of electricity, which is expensive. This technique is normally used only to produce highly purified hydrogen, required in some industrial processes, or other products, such as chlor-alkali, with hydrogen as a by-product (Narayanan and Viswanathan, 1998). But electrolysis could be used to produce small quantities of hydrogen close to the point of use; for example, at refueling stations. To be economic, the electricity would need to be cheap. The environmental benefits of electrolysis-based hydrogen energy depend on the production process of hydrogen. If it were generated from nuclear or renewable energy sources, such as wind, solar and biomass, electrolysis would produce carbon-free hydrogen. But large reductions in the cost of renewable-based electricity and nuclear power are needed to enable hydrogen

produced by electrolysis to compete with conventional sources of energy on a large scale.

1.2.4 Thermal decomposition of water

Direct decomposition of water into hydrogen and oxygen occurs only at temperatures above 4000 K. To reduce the temperature levels used in the process, other techniques for high temperature splitting of water have been suggested. But, splitting of water by thermo-chemical methods requires temperature ranges around 1500 K. The thermochemical cycles include the following: sulfuric acid–iodine cycle, hybrid sulfuric acid cycle, hybrid sulfuric acid–hydrogen bromide cycle, calcium bromide–iron oxide cycle (UT-3), and iron - chlorine cycle (Narayanan and Viswanathan, 1998). Only, limited heat sources are available like nuclear reactor, which can provide the required range of temperatures. The main problem with this method is related to materials required for extremely high temperatures, recombination of the reaction products at high temperatures, toxicity of some of the chemicals involved and separation of hydrogen.

1.2.5 Biological or biochemical methods

The *biological* or *biochemical methods* for the production of hydrogen by splitting water have also been under investigation. Micro organisms are capable of producing H₂ via either fermentation or photosynthesis.

Photo-biological production of hydrogen is based on two steps:

- Photosynthesis and
- Hydrogen production catalyzed by hydrogenases like algae and cyanobacteria.

In biomass conversion processes, a hydrogen-containing gas is normally produced in a manner similar to the gasification of coal. However, no commercial plants exist to produce hydrogen from biomass. Currently, the pathways followed are steam gasification (direct or indirect), entrained flow gasification, and more advanced

concepts such as gasification in supercritical water, application of thermo-chemical cycles, or the conversion of intermediates (*e.g.* ethanol, bio-oil or torrefied wood). None of the concepts have reached a demonstration phase for hydrogen production.

Although the technology for production of hydrogen from renewable sources is well understood, it is currently not used for producing hydrogen in large quantities. Hydrogen produced from renewable energy sources is currently very expensive. Production of significant quantities of hydrogen using such methods would take considerable time and investment to develop, to allow capital costs to be reduced to a satisfactory level. However, in the long term, hydrogen offers a potential way of gaining energy independence from fossil fuels.

1.3 HYDROGEN STORAGE

The obstacle to realize the hydrogen economy is neither the production nor utilizing hydrogen but rather effective and safe means of storing hydrogen. However hydrogen is produced, its widespread use will require large-scale infrastructure to transport, distribute, store and dispense it as a fuel for vehicles or for stationary usage. A range of storage technologies that address this problem like compressed gas, liquified hydrogen, metal hydride, and carbon based systems. These are under development for stationary and onboard vehicle uses. Which choice is best, depends on several factors: the application, the energy density needed, the amount to be stored and the storage time, the forms of energy available, maintenance requirements, and capital and operating costs. Hydrogen storage basically implies the reduction of the enormous volume of the hydrogen gas. In order to increase the hydrogen density in a storage system, work must either be applied to compress hydrogen, or the temperature has to be decreased below the critical temperature.

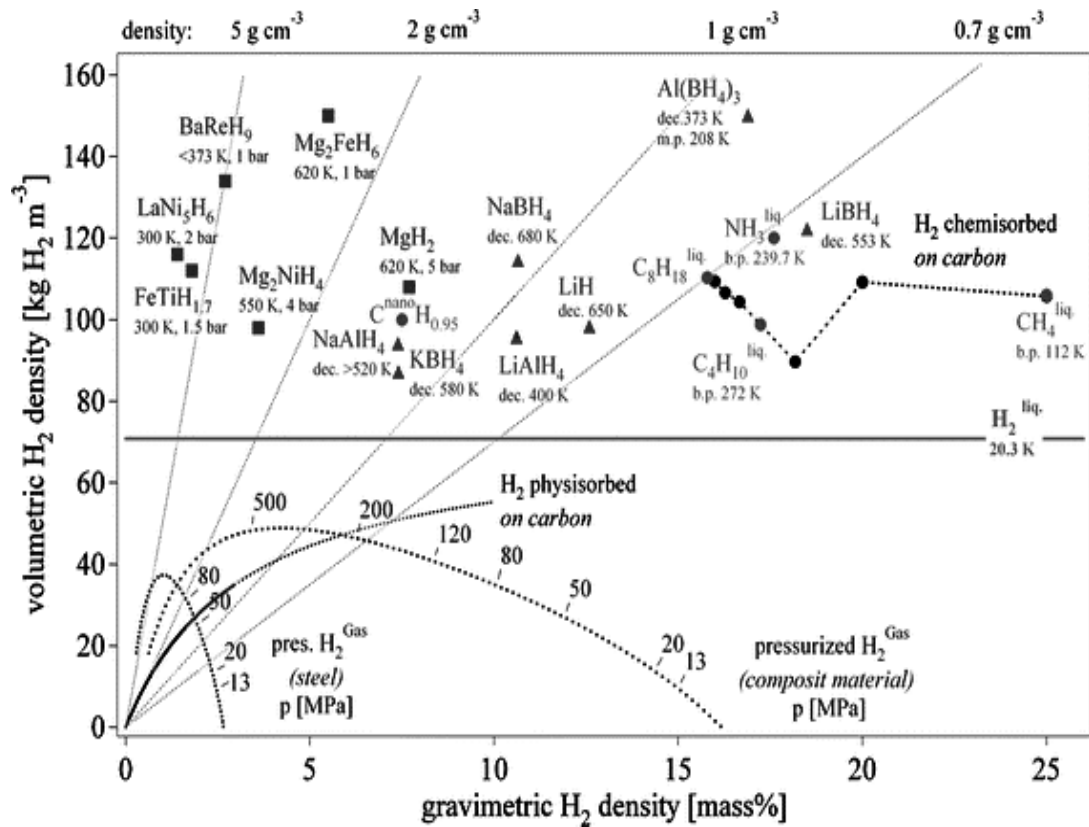


Fig. 1.2 Comparison of hydrogen storage densities of different hydrogen storage methods (Zuttel, 2003)

For stationary systems, the weight and volume of the system used for hydrogen storage is not a key factor. However, for mobile applications, such as fuel cell electric vehicles or hydrogen-fuelled (internal combustion) cars, hydrogen storage system has to be compact, lightweight, safe and affordable. The US Department of Energy (DOE), Hydrogen Plan has set a standard for this discussion by providing a commercially significant benchmark for the amount of reversible hydrogen absorption. The benchmark requires system-weight efficiency (the ratio of stored hydrogen weight to system weight) of 6.5 wt. % hydrogen and a volumetric density of $62 \text{ kg H}_2/\text{m}^3$, since a vehicle powered by a fuel cell would require more than 3.1 kg of hydrogen for a 500 km range. Fig. 1.2 shows that various storage options that meet the long-term needs.

To reach the high volumetric and gravimetric density suitable for mobile applications, basically six reversible storage methods are known today. They are;

1. High- pressure gas cylinders,
2. Liquid in cryogenic tanks,
3. Physisorbed on a solid surface e.g. carbon-nanotubes
4. Metal hydrides of the metals or intermetallic compounds.
5. Complex hydrides of light elements such as alanates and borohydrides,
6. Storage via chemical reaction.

1.3.1 Gaseous hydrogen storage

The most common method to store hydrogen is as compressed gas, either above or below ground or on board vehicles. With a compressed gas system, the hydrogen is typically compressed and stored in gas cylinders or spherical containers. For storing hydrogen on board vehicles, compressed hydrogen is the simplest and presently the cheapest method, requiring a compressor and a pressure vessel only. Its main obstacle is its low storage density. Higher storage pressures raise the cost, as well as raise safety issues.

1.3.2 Liquid hydrogen

As an alternative to compression, hydrogen can be liquefied for storage in stationary or onboard vehicle systems. Liquefaction takes place through a number of steps in which the hydrogen is compressed and cooled to form a dense liquid. The liquid hydrogen must then be stored at low temperatures. A major drawback with liquefied hydrogen storage is the high cost of liquefaction process and the significant liquid “*boil off*”. Liquefying hydrogen gas also consumes a huge amount of electricity.

1.3.3 Solid state storage

Storing the hydrogen in solid state is safe and the most advantageous. Hydrogen can be stored in solid state by combining the hydrogen with solid state material through physisorption or chemisorption or by chemical reaction. Many metals have the property of combining chemically with hydrogen to form a class of compounds called metal hydrides. Metal hydrides have high volumetric hydrogen density (number of hydrogen atoms per unit volume) compared to liquid hydrogen and gasoline. For moderate thermal stability, the enthalpy of formation of the hydride should be less than 50 kJ/mole H₂ (van Mal, 1976). Based on the hydrogen desorption temperatures hydrogen storage in metal hydrides can be grouped into:

- a) Low temperature hydrides which release at ambient conditions but with hydrogen capacity restricted to < 1.5 wt. % H₂ (e.g. FeTiH_{1.8} and LaNi₅H₆) and
- b) High temperature hydrides which require heating to above 573 K for hydrogen desorption but with hydrogen capacities > 7 wt. % (e.g. LiH, MgH₂).

Another sub-class of solid state hydrogen storage materials is complex metal hydrides (alanates and borohydrides). In contrast to conventional metal hydrides the complex metal hydrides prepared through chemical reaction release large quantities of hydrogen (> 5wt %) at temperatures approximately 373 K. The main issue with the complex hydrides is the reversibility, which has remained unresolved till today. Other issues associated with these systems are synthesis and safety.

Amides of lithium and magnesium are another group of solid state materials capable of storing 6.5 wt% hydrogen but need temperatures above 573 K (Ichikawa *et al.*, 2004, 2005). Complex metal hydrides like borohydrides with high storage capacity

are highly stable hydrides. They need to be heated to high temperatures in order to release hydrogen e.g. NaBH_4 and LiBH_4 . These hydrides have been considered for irreversible on-board hydrogen storage by releasing hydrogen through hydrolysis viz. chemical reaction with water (Schlesinger *et al.*, 1953; Aiello *et al.*, 1999). This method is sometimes referred to as chemical hydride hydrogen storage. The oxide or hydroxide product can be subjected to off-board regeneration. Another option of hydrogen storage is by physisorption (adsorption) of hydrogen on high surface area materials such as carbon nanotubes, carbon nanofibers and activated carbon.

1.3.4 Carbon materials

A variety of carbon nanostructures like activated carbon, carbon nanofibers, multi-walled and single-walled nanotubes, carbon nanohorns are known in literature. Hydrogen can be stored into the nanotubes by chemisorption or physisorption. The methods of trapping hydrogen are not known very accurately. Even though molecular hydrogen physisorption has been demonstrated, it is useful only at cryogenic temperatures and extremely high surface area carbons are required. Pure atomic hydrogen chemisorption in carbon materials has also been demonstrated, but the covalent-bound hydrogen is liberated only at high temperatures (> 673 K). Adsorption up to a few wt. % of H_2 at room temperature is occasionally reported, but has not been reproducible. So far, the surface and bulk properties needed to achieve practical room temperature storage are not clearly understood. Moreover, the hydrogen storage capacity of carbon materials is limited to about 2 wt. % H_2 and reports of higher capacities are often explained by erroneous results (Schlapbach and Zuttel, 2001; Zuttel, 2003). The summary of various reported hydrogen storage capacity of carbon materials are given in Table 1.2.

Table 1.2 Summary of reported hydrogen storage capacities in carbon nanostructures

Adsorbent	Hydrogen storage (wt. %)	Conditions	References
		Temperature (K) / Pressure (MPa)	
SWNT(low purity)	5-10	273/0.04	Dillon <i>et al.</i> , 1997
SWNT(high purity)	3.5-4.5	298/0.04	
SWNT(high purity)	8	80/8	Ye <i>et al.</i> , 1999
SWNT(50% purity)	4	300/12	Liu <i>et al.</i> , 1999
SWNT	2	80/10	Wang and Johnson, 1999
SWNT	11	80/10	Wu <i>et al.</i> , 2000
SWNTs	~0.1	300-520/0.1	Hirscher <i>et al.</i> , 2002
SWNT	6.5	300/16	Yin <i>et al.</i> , 2000
MWNT	2.4	298/10	Cao <i>et al.</i> , 1999
Li doped MWNT	20	200-400/0.1	Chen <i>et al.</i> , 1999
K doped MWNT	14	300/0.1	
Li doped MWNT	2.5	200-400/0.1	Yang, 2000
K doped MWNT	1.8	<313/0.1	
MWNT	5	300/10	Zhu <i>et al.</i> , 2001
K doped MWNT	1.8	300/0.1	Pinkerton <i>et al.</i> , 2000
GNFs (tubular)	11.26	298/11.35	Chambers <i>et al.</i> , 1998
GNFs (herring bone)	67.55	298/11.35	
CNFs	~10	300/10.1	Fan <i>et al.</i> , 1999
CNFs	~5	300/10.1	Cheng <i>et al.</i> , 2000
Nano-structured graphite	7.4	~300/1.0	Orimo <i>et al.</i> , 1999
SWNT-Fe	-	300/0.08	Hirscher <i>et al.</i> , 2001
SWNT-Ti-6Al-4V	1.47	300/0.08	

1.3.5 Other high surface area materials

The most predominant examples of other high surface area materials are zeolites, metal-organic frameworks (MOFs) and clathrate hydrates. Zeolites are complex aluminosilicates with engineered pore sizes and high surface areas. They are known as “molecular sieves”. The capturing of non-H₂ gases in zeolites is well known. Metal-organic frameworks (MOFs) are typically ZnO structures bridged with benzene

rings. These materials have an extremely high surface area, and are highly versatile and allow for many structural modifications. Clathrate hydrates are crystalline water (ice) cage structures, often containing “guest” molecules such as CH₄ and CO₂. The cage size and structure can often be controlled by organic molecules such as THF. These materials are characterized by high surface areas that can physisorb molecular H₂. They have been shown to store a few wt. % H₂ at cryogenic temperatures. Recently metal-organic frameworks (MOFs) (Rosi *et al.*, 2003) have received attention as hydrogen storage candidates with preliminary results reporting 3 and 4.5 wt. % H₂ at 270 and 78 K respectively. However, the possibility of engineering these materials to reversibly store high levels of H₂ near room temperature is still questionable.

Apparently, no solid state hydrogen storage solution combines a high gravimetric hydrogen storage density with favorable thermodynamics. Thus, despite a tremendous research effort, potentially commercial candidate which can reversibly store significant amount > 2 wt. % H₂ below 373 K has not yet been realized (Guther and Otto, 1998; Sandrock and Thomas, 2007).

1.4 METAL HYDRIDES

The essential requirements that should be satisfied by metal hydrides proposed for hydrogen storage application at a commercial level are (Sastry *et al.*, 1998):

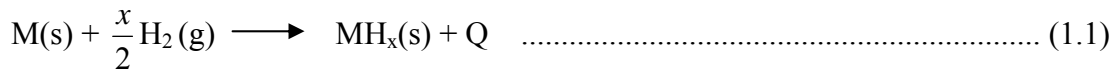
- High hydrogen storage capacity.
- Facile reversibility of hydride formation and decomposition reactions. The hydride should be decomposable at moderate temperatures that can be provided from locally available heat sources, like solar, automobile exhaust and waste heat resources.

- Absorption-desorption kinetics should be compatible with the charge-discharge requirements of the system.
- The equilibrium dissociation pressure of the hydride at peak desorption rates should be compatible with the safety requirements of the hydride containment system. The hydrides themselves should have high safety factor.
- The hydride should have a sufficient chemical and dimensional stability to permit its being unchanged over a large number of charge–discharge cycles.
- Minimal hysteresis in adsorption–desorption isotherms.
- The hydride should be reasonably resistant to deactivation by low concentrations such as O₂, H₂O, CO₂ and CO.
- The total cost of hydride should be affordable for the specified application. Long term availability of raw materials must be ensured. The cost of the hydride system (which includes its containment) per unit of reversibly stored hydrogen should be as low as possible.
- The cost of storage vessel and ancillary equipment and the fabrication/installation costs should be moderate.
- Operating and maintenance costs and purchased energy requirements per storage cycle should be low.

A careful combination of technical and economic considerations will determine the suitability of a hydride product for a given hydrogen storage or hydrogen containment application.

1.4.1 The metal-hydrogen reaction

The reaction between hydrogen and a metal can be expressed by the following reaction



where M is metal, a solid solution or an intermetallic compound, MH_x metal hydride and x is ratio of hydrogen to metal denoted as H/M. Q is released heat during reaction.

The hydrogen absorption reaction is generally exothermic. The mechanism of hydride formation which involves many processes has a high degree of complexity and can be described adequate in terms of a simplified one-dimensional potential energy curve.

The Lennard-Jones picture: The reaction between gas phase hydrogen and a metal surface is schematically illustrated as the one-dimensional Lennard-Jones potential of atomic H and molecular H_2 (Fig. 1.3). Far from the surface the hydrogen atoms are separated by the hydrogen dissociation energy 436 kJ/mol. The first interaction of a H_2 molecule moving towards the surface is weak van der Waals forces in the range of 0-10 kJ/mol corresponding to molecular physisorption. If the molecule is moved closer to the surface the potential energy will increase due to repulsion. When hydrogen molecule crosses this activation barrier, dissociation will occur and H atoms will be bonded to the metal surface. If intersection is at a potential energy larger than zero relative to gas phase H_2 , dissociation is said to be non-activated and the height determines the activation barrier.

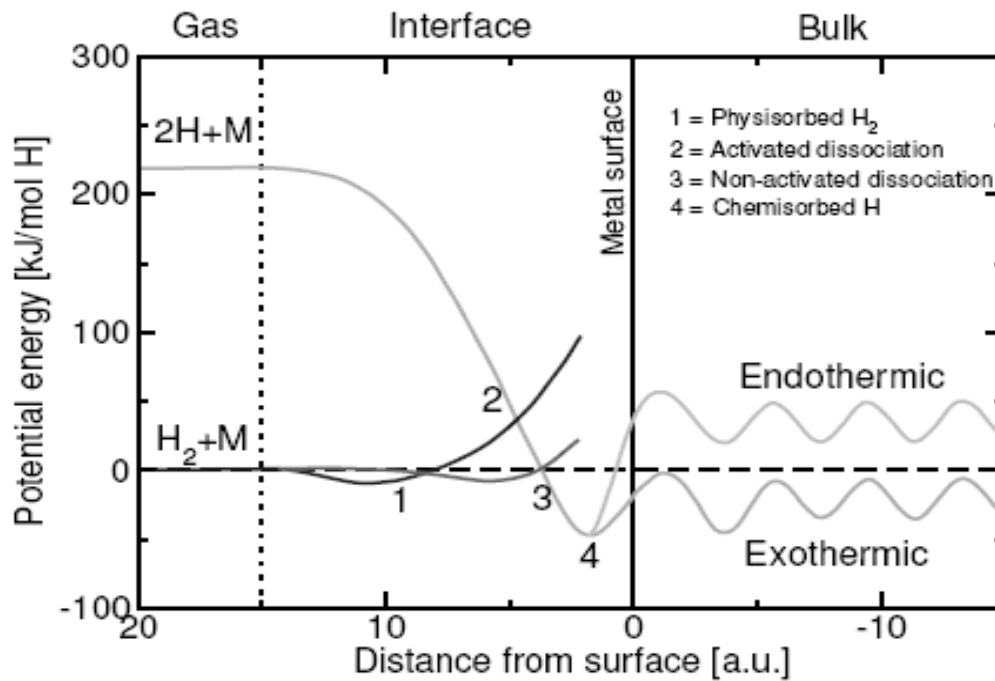


Fig. 1.3 Schematics of potential energy curves of hydrogen approaching metal surface. The hydrogen molecule is attracted by weak Van der Waal forces lead to physisorbed state, then the molecule dissociates and chemisorbs followed by diffusing into bulk metal (Schlapbach, 1988)

If intersection is located at approximately zero potential energy, dissociation is said to be activated. In the former case only the fraction of H_2 molecules with energy larger than the activation barrier will be able to dissociate. After dissociation, the hydrogen atoms find a potential energy minimum which corresponds to the H atoms being bonded to the metal surface (chemisorption). If the H-M bond is stronger than the H-H bond, chemisorption is said to be exothermic and if the H-H bond is the stronger, chemisorption is said to be endothermic. Beyond the point of chemisorption, the hydrogen atoms can penetrate the first metal atomic layer into the subsurface through an activated process from which it can diffuse into the bulk (as a solid solution) of the metal. If the potential energy of bulk H-atoms is below zero relative to gas phase H_2 , hydrogen solid solution is said to exothermic, if the potential energy of bulk H-atoms is above zero, hydrogen solid solution is said to be endothermic.

1.4.2 Thermodynamics

The Pressure Composition Isotherm: The behavior of metal-hydride systems can be best represented by pressure-composition isotherm (PCI or PCT). A generic PCI is depicted in Fig. 1.4. At isothermal conditions initially the adsorbed amount of hydrogen will increase slightly with increasing hydrogen pressure. This corresponds to the formation of a solid solution of hydrogen and this is denoted the α -phase. When the maximum solubility of hydrogen in the α -phase is reached the hydride phase (β -phase) begins to form (Muller *et al.*, 1968). Increasing the hydrogen pressure further will now result in a substantial increase in the absorbed amount of hydrogen. This is in accordance with Gibbs phase rule.

The pressure at which this transformation takes place is referred to as the *plateau pressure*, the most important segment of PCI and in this region the α -phase and β phase co-exist. When the stoichiometric hydride has formed completely the additional absorption of hydrogen will now require a large pressure increase. This corresponds to the solid solution of hydrogen in the β -phase. The plateau pressure in other words, dissociation pressure of metal hydride gives valuable information on reversible storage capacity; the width of the plateau and the position of the plateau at a given temperature give an idea on the stability of the hydride. Stable hydrides require higher temperatures than less stable hydrides to reach a certain plateau pressure. P-C isotherms of metal hydride systems generally exhibit sloping, rather than flat, horizontal plateaus, indicating that different parts of the substrate material absorb hydrogen at different equilibrium pressures, because of surface heterogeneities, impurities and stresses (Sastry *et al.*, 1998).

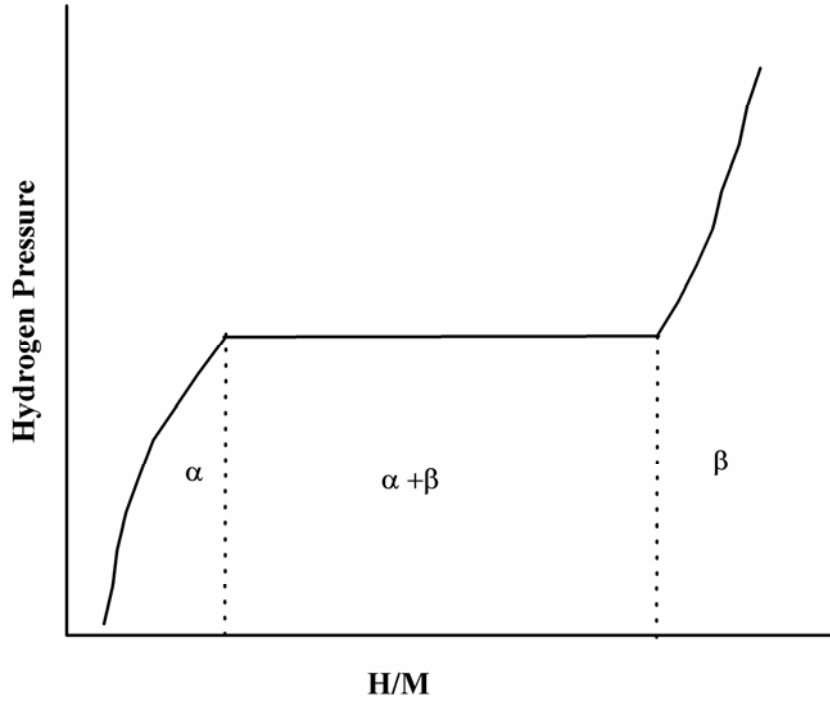


Fig. 1.4 Schematic pressure composition isotherm

Thermodynamic parameters, standard enthalpy of formation ΔH_f° , the standard free energy ΔG_f° and standard entropy of formation ΔS_f° of metal hydrides can be calculated from PC isotherms, using the following equations (Sastry *et al.*, 1998):

$$\Delta G_f^\circ = -RT \ln K_p = \frac{x}{2} RT \ln P_{H_2} \dots\dots\dots (1.2)$$

$$\Delta G_f^\circ = \Delta H_f^\circ - T \Delta S_f^\circ \dots\dots\dots (1.3)$$

$$\ln P_{H_2} = \frac{2}{x} \frac{\Delta H_f^\circ}{RT} - \frac{2}{x} \frac{\Delta S_f^\circ}{R} \dots\dots\dots (1.4)$$

Eq. 1.4 is known as the Van't Hoff equation. ΔH_f° can be evaluated from the slope of the straight line plot of $\ln P_{H_2}$ vs $1/T$ as shown in Fig. 1.5. Hence, from a number of measurements of plateau pressures at different temperatures the Van't Hoff equation can be applied to determine enthalpy and entropy of formation of metal hydride.

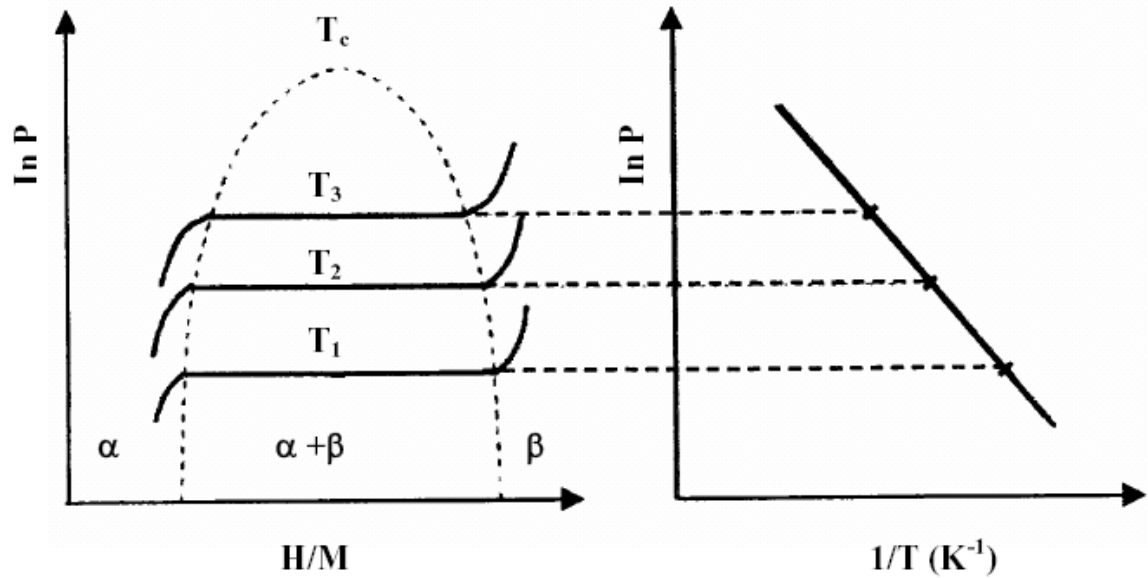


Fig. 1.5 Pressure composition isotherms at different temperatures and corresponding van't Hoff plot (Schlapbach, 1988)

As the entropy change corresponds mostly to the change from molecular hydrogen to dissolved hydrogen. The entropy for all metal hydrogen systems under consideration is approximately the standard entropy of hydrogen, $\sim 130 \text{ J/ (mol K)}$. The criterion regarding thermodynamics for a hydrogen storage material is desorption of hydrogen above 0.1 MPa and temperatures $< 373 \text{ K}$. In order to meet the criterion for a metal hydride, enthalpy of formation should be 40 kJ/mol (Zuttel, 2003)

1.4.3 Reaction mechanism and kinetics

The reaction kinetics of hydrogen absorption and desorption in metal-hydrogen systems is an important consideration in selecting materials for practical storage applications. Kinetics is hard to follow quantitatively because many reactions that involve hydrides have rate constants of the order of a few seconds. Usual methods cannot follow such rapid changes. A temperature change of a few Kelvin is sufficient to alter the kinetics significantly. The formation of the metal hydride composed of the following five essential processes.

- (1) Physisorption of hydrogen molecules;
- (2) Dissociation of hydrogen molecules and chemisorption;
- (3) Surface penetration of hydrogen atoms;
- (4) Diffusion of hydrogen atoms through the hydride layer, either by an interstitial or a vacancy mechanism;
- (5) Hydride formation at the metal/hydride interface

For dehydrogenation, the process is the reverse i.e. the hydride phase decomposes and hydrogen atoms diffuse to the sub-surface and subsequently to the surface, where the hydrogen atoms recombine and desorb as H₂. A reaction mechanism can be proposed on the basis of the above reversible reactions. When experimental kinetic data is fitted with a rate equation, both hydride nucleation and growth or diffusion processes assumed to be rate limiting steps. When reviewing the shape of reported hydrogenation/dehydrogenation curves, i.e. hydrogen absorption/desorption as a function of time, they can be divided into two major classes; (A) one with a monotonically decreasing sorption rate and (B) one with a sigmoidal shape. Former processes are usually rationalized in terms of either a surface process such as dissociation or bulk diffusion is rate limiting the overall kinetics. Second one is usually rationalized in terms of a nucleation and growth mechanism limiting the overall kinetics. Nucleation and growth kinetics is usually explained by a Johnson-Mehl-Avrami (JMA) rate equation (Avrami, 1939; Jackson, 2004).

The JMA equation has the following form

$$\alpha = 1 - \exp(-kt)^n \quad \dots\dots\dots (1.5)$$

where α fraction reacted at time t and k rate constant. The exponent, n , referred as the Avrami exponent is an integer or non integer, the value of which is governed by the

geometries associated with the rate-controlling process. The temperature dependency of the rate constant k is usually described by an Arrhenius relation.

$$k = A \exp\left(-\frac{E_a}{RT}\right) \dots\dots\dots (1.6)$$

where A is a pre-exponential factor, E_a is the apparent activation energy and R is the gas constant.

The most interesting property of the JMA equation is that it explains not only curves with a sigmoidal shape, but also curves of type A i.e. situations where diffusion may be rate limiting, when n is having values of 1 or less. Probably hence JMA model is often successfully invoked in dealing the kinetics of hydrogenation/dehydrogenation of metal hydrides. Even though the JMA equation may provide a good fit, any conclusions about nucleation and growth being rate limiting in such a process should be considered with care.

1.4.4 Types of metal hydrides

1.4.4.1 Binary hydrides

Hydrogen directly interacts with many metal atoms individually to form binary hydrides MH_x . The formation of binary hydrides requires a high metal-hydrogen chemical affinity, which means a strong metal hydrogen bond must be formed. It takes place for the stable metal hydrides, such as hydrides of alkali and alkaline earth metals, rare earth elements, actinides and Ti group elements. For these hydrides the reaction between metal and hydrogen gas is reversible at only high temperatures i.e. slow kinetics. The PCT properties are not very convenient relative to the 0.1–1 MPa, 0–373 K range of utility chosen for practical applications. Palladium has been used for hydrogen storage for more than 100 years, but it is very expensive and doesn't

hold much hydrogen and also requires heating well above 373 K to liberate the stored hydrogen.

1.4.4.2 Intermetallic hydrides

Apart from binary hydrides, the class of hydrides of intermetallic compounds (IMC) having a common formula $A_xB_yH_z$ exists. The IMC are the compounds of two or more metals, at least one of which has strong affinity to hydrogen i.e. hydride forming metal A. The other component is non hydride forming metal B. Based on the ratio of A to B, IMCs are classified as several families in which many of them of practical importance, namely AB_5 (CaCu₅ structure type), AB_2 (Laves phase), AB (CaCl – related structure type) and A_2B (AlB_2 related structure type). In AB_5 type rare earth elements or Ca are the A- component; in AB_2 and AB, A is the element of Ti group elements and in A_2B , A is mainly magnesium. Of all the class of compounds, B component is mainly formed by transition metals (Fe, Co, Ni, V, Mn, Cr, etc). Among the metal hydrides IMCs have biggest practical importance including hydrogen storage applications.

AB₅ Compounds

In the AB_5 , system, the majority of studies have been on $LaNi_5$; this material has a hexagonal or orthorhombic structure with a CaCu₅ type lattice. Hydrides are formed with plateau pressures of a few atmospheres at temperatures up to 373 K. The enthalpy change, ΔH is in the order of 30.1 kJ/mol H₂. Attractive properties include low hysteresis and good tolerance to gaseous impurities, and ease of activation in the initial cycle. $LaNi_5$ shows good kinetics, with nickel serving as a catalyst for the hydriding reactions. The major problems associated with these materials are alloy costs and degradation during cycling. Alloy costs can be lowered by substituting Ce, Nd, Gd, Y, Er, Th and Zr for La and Al, Co, Fe, Cr and Cu for Ni. The $LaNi_5$ -H₂

system has been extensively investigated. The Al substitutions result in a wide range of decomposition pressures for the hydride. In the range 0-20%Al, the plateau pressures of the LaNi₅-LaNi₄Al hydride system are reduced by a factor of ~300. The hydrogen capacity of AB₅ hydrides is unfortunately low. A maximum capacity of 1.9 wt. % can be achieved with LaCo₅ and Ca_{0.7}Mm_{0.3}Ni₅ with a nominal amount of about 1 wt. % (Sandrock, 1999). The reversible capacity of 1.28 wt. % can be achieved with LaNi₅, with the nominal amount being about 0.7 – 1 wt. % (Sandrock and Thomas, 2007).

AB Compounds

The AB alloys store hydrogen at a low cost and exhibit plateau pressures of a few atmospheres at temperatures up to 373 K. Most of the work done on AB compounds has been restricted to FeTi which has a CsCl type crystal structure. Reilly and Wiswall Jr. (1974) reported that iron and titanium form two known stable intermetallic compounds, FeTi and FeTi₂. Two hydrides; a monohydride with a tetragonal structure and a dihydride with a cubic structure are formed. It is necessary to initially activate FeTi, before it reacts at a practical rate with hydrogen. Reaction kinetics is considerably slower than in the AB₅ case and can be affected by contaminants such as O₂, H₂O and CO. Other disadvantages of the FeTi-H system are pronounced hysteresis and the weight of the alloys. These problems can be eliminated to some extent by the substitution of various alloying elements such as Mn and Al for Fe. Manganese substitution reduces hysteresis and provides some resistance to poisoning while aluminum lowers the overall weight of the alloy.

AB₂ Compounds

The research on AB₂ type Laves phase hydrogen storage alloys started early in the 1960's. In ZrB₂ (B=V, Cr, Mn, Fe, Co, Mo and Al) compounds for B=V, Cr and Mn

the alloys could absorb and desorb large quantities of hydrogen ($H/M \sim 5$) (Shaltiel, 1978). In AB_2 Laves phase alloys, as the atomic radius of element A is much bigger than that of B (optimum ratio $r_A/r_B = 1.225$), the atoms are arranged in very compact layered lattice structure with 17 tetrahedral interstitial cavities, which are potential sites for storing hydrogen atoms. Due to electrostatic repulsion forces, any two adjacent tetrahedral cavities can not store hydrogen atoms simultaneously. The maximum absorbable number of hydrogen atoms is around 6 for both AB_2 and AB_5 alloys. AB_2 compounds have much higher hydrogen wt. % capacity than AB_5 compounds.

The AB_2 compounds have a high storage capacity, show good resistance to impurities and exhibit low hysteresis. The best sorption characteristics have been observed for ZrV_2 , $ZrCr_2$ and $ZrMn_2$ with 6 hydrogen atoms per formula unit. Hydrided AB_2 compounds tend to be quite stable, with ΔH values greater than 50 kJ/mol in magnitude. The methods available to lower the stability with adequate absorption capacity include:

(1) Substitute some of the Mn, Cr, V with Fe or Co (2) Substitute Ti or Ho for Zr, (3) Substitute A and B elements simultaneously; (4) Use excess B to form a non-stoichiometric alloy. In these ways, the stabilities can be reduced to acceptable levels. Partial substitution of Ti for Zr can also be employed in order to reduce the cost of the hydriding alloy.

Other Intermetallic Compounds

In addition to AB_5 , AB and AB_2 compounds, there are several other families of intermetallics having a capability of hydrogen adsorption, none of which has attained commercial interest. These include, for example, A_2B , AB_3 , A_2B_7 , A_3B , etc. PCT properties of these materials are not favorable even though some of them have good

hydrogen capacities. Those with PCT properties in the area of practical applications have usually either poor hydrogen capacities or too narrow plateaus.

How to achieve required storage capacity?

The most logical approach to develop a high storage material would be to decrease the weight of metals by considering the light metals like Li, Be, B, Na, Mg and Al and their alloys. These metals form a large class of compounds called complex metal hydrides.

1.4.4.3 Magnesium and Magnesium-Based Compounds

Magnesium and Mg-based alloys as hydrogen storage materials meet two important storage criteria: they can store large amounts of hydrogen (7.6wt% and 3.8 wt% respectively), more than twice as much as either rare-earth hydrogen-storage alloys (e.g., LaNi₅ absorbs 1.4wt% hydrogen) or titanium hydrogen-storage alloys (e.g., FeTi absorbs 1.9 wt% hydrogen), and they are inexpensive. Magnesium-based alloys are considered to be most promising materials for hydrogen storage because of their high hydrogen-storage capacity, light weight, abundance of the constituents in the earth's crust, and low-cost compared with alternative systems. On the debit side, however, the reactions of Mg-and Mg alloys with hydrogen require appreciably higher temperatures (473-573 K) and pressures (up to 1 MPa) due to sluggish hydriding/dehydriding kinetics at room temperature. Owing to the relative stability of MgH₂, modifications are made to decrease the dissociation temperature of the hydride and increase the absorption/desorption kinetics. These can be achieved by changing the microstructure of the hydride by mechanical milling and/or addition of proper catalysts. The ball-milling, (creating fresh surfaces during processing) is widely applied to metal hydrides to achieve good surface properties. The increased surface contact with catalyst during ball-milling leads to fast kinetics of hydrogen

transformations. Nanocrystalline Mg can be produced by ball milling that gives remarkable improvement of kinetics and surface activity for hydrogenation (Zaluski et al., 1997; Zaluska *et al.*, 2001; Imamura *et al.*, 2005). Imamura *et al.* (1996) have studied Mg-based composites which are prepared by mechanical milling of magnesium powder and graphite in the presence of various additives (tetrahydrofuran, benzene or cyclohexane). Presence of tetrahydrofuran in the milling process strongly affected the hydriding and dehydriding kinetics of the resulting composites.

Additions of transition metals have been reasonably successful in increasing desorption rates of hydrogen in magnesium. Reilly and Wiswall (1967, 1968) reported successful hydriding and dehydriding experiments with Mg_2Cu and Mg_2Ni . Oesterricher *et al.* (1980) have suggested that the partial substitution of Mg in Mg_2Ni by an element of a more exothermic heat of hydride formation, such as Ca, Sc or Y may result in a rise of equilibrium pressure for the substituted Mg_2Ni . This would bring Mg_2Ni into the range of reversible room temperature hydrogen sorption. The absorption and desorption rates for these alloys are close to those obtained with Mg_2Ni . The ΔH value for the Mg_2Ni alloy is -64.4 kJ/mol H_2 . Mg_2NiH_4 attracts wide interest for being a promising hydrogen store material due to its relatively high capacity, low cost, light weight and low-toxicity and for its unusual structural and bonding properties (Zaluski *et al.*, 1995; Orimo and Fuji, 2001). High hydrogen capacity of four hydrogen atoms per Mg_2Ni , combined with the small specific weight of the alloy is the most important advantage of Mg_2Ni over other magnesium hydrides. Dehydriding temperature of Mg_2NiH_4 is 523-573 K at desorption pressure of 0.2–0.3 MPa (Zaluska *et al.*, 1999; Abdellaoui *et al.*, 1998, 2006; Zhu *et al.*, 2006).

1.5 COMPLEX METAL HYDRIDES

One more class of metal hydrides is coordination compounds where hydrogen presents as ligand, called as complex metal hydride. These hydrides can be synthesized only by preparative chemistry and cannot be made as reversible medium for hydrogen storage. However, in the systems based on sodium alanate the reversible hydrogenation - dehydrogenation is possible in the presence of catalyst (Bogdanovic and Schwickardi, 1997). The general formula of complex metal hydrides is $A_xM_yH_z$, where A is an alkali metal or alkaline earth metal or transition metal and M is a non-transition or transition metal. These materials have high hydrogen gravimetric densities (Table 1.3) and some of them are commercially available. Hence, a priori, they would seem to be viable candidates for application as practical, on-board hydrogen storage materials.

1.5.1 Alanates

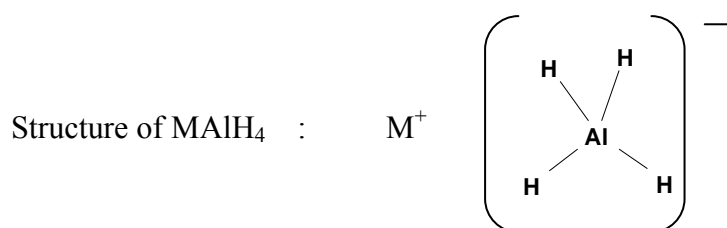
If M is aluminum in $A_xM_yH_z$, then they are called as Alanates $[A^{n+}(AlH_4)_n]$. Alanates distinctly differ from intermetallics in their structure and properties. These are mixed ionic-covalent hydrides. Al-H bond has covalent character and the bonding between cation and $[AlH_4]^-$ is ionic in nature. Many metal hydrides form through hydrogen occupation of interstitial sites in the host metal lattice. The alanates, however, are formed through complex chemical reactions with the formation of at least one intermediate phase, M_3AlH_6 .

Two types of alanates are known one which contains $[AlH_4]^-$ anions and the other $[Al_3H_6]^{3-}$ anions with appropriate cations. In $[AlH_4]^-$ type, H atoms are tetrahedrally coordinated around the Al atom and have a distinct electron rich character. Ex: $LiAlH_4$, $NaAlH_4$, $Mg(AlH_4)_2$, etc. In AlH_6^{3-} type alanates, H atoms are octahedrally coordinated around the Al atom and have a distinct electron rich character (Bulchev *et*

al., 1970). Ex: Na_3AlH_6 , Li_3AlH_6 , etc. In this type of hydrides either sodium or lithium can be replaced by one another, to form mixed alanates like $\text{Na}_2\text{LiAlH}_6$, $\text{Li}_2\text{NaAlH}_6$. Transition metal also form aluminum based complex metal hydrides ex: $\text{Ti}(\text{AlH}_4)_2$ and $\text{Zr}(\text{AlH}_4)_2$.

Table 1.3 Hydrogen storage capacities of different alanates

Material	Hydrogen storage capacity (wt %)
LiAlH_4	10.5
NaAlH_4	7.5
KAlH_4	5.7
$\text{Mg}(\text{AlH}_4)_2$	9.3
$\text{Ca}(\text{AlH}_4)_2$	7.7
$\text{LiMg}(\text{AlH}_4)_3$	9.6
LiBH_4	18
NaBH_4	10.4
KBH_4	7.42
$\text{Mg}(\text{BH}_4)_2$	14.8
$\text{Ca}(\text{BH}_4)_2$	11.4
$\text{Al}(\text{BH}_4)_3$	17



1.5.1.1 Synthesis and characterization of alanates

One of the attractive features of alanates is that lithium and sodium alanates are readily available commercially. LiAlH_4 is the first alanate material synthesized by Finholt *et al.*, (1947), from the LiH and Aluminum halides in diethyl ether. NaAlH_4 is formerly industrially produced via the direct synthesis from the elements. Zakharkin and Gavrilenko (1961) prepared NaAlH_4 from NaH and AlCl_3 in benzene, using $\text{Al}(\text{C}_2\text{H}_5)_3$ as a catalyst. Clasen (1961) and Ashby *et al.*, (1963) described, the ‘*direct synthesis*’ of NaAlH_4 using trialkylaluminium as a catalyst, starting from activated aluminum, Na or NaH and hydrogen under pressure.

THF / 413 K/15 MPa



Dymova *et al.* (1974) succeeded in synthesizing the NaAlH_4 directly from the elements in absence of solvents by carrying out the process in the melt.

$p > 17.5 \text{ MPa} / T < 553 \text{ K}$



Other alanates can be synthesized from these two alkali metal alanates. Magnesium alanate can be readily prepared with sodium alanate and magnesium hydride via a metathesis reaction (Claudy *et al.*, 1979). The mixed metal alanate, $\text{Na}_2\text{LiAlH}_6$, is prepared through ball milling of sodium hydride, lithium hydride, and sodium alanate (Claudy *et al.*, 1982; Huot *et al.*, 1999). Potassium alanate can be prepared by the direct synthesis of potassium hydride and aluminum under high temperature and pressure.

Alanates can be characterized by variety of techniques. Diffraction techniques like x-ray diffraction and neutron diffraction, Thermal decomposition techniques like

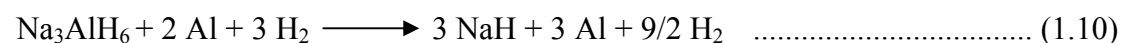
Thermo gravimetry, Differential thermal analysis, and Differential Scanning Calorimetry (DSC) and Spectroscopic techniques like IR, Raman and solid state NMR are useful techniques for the characterization of alanates. Dilts and Ashby (1972) demonstrated that thermal decomposition of sodium alanate, lithium alanate and potassium alanate are similar with characteristic three-step loss of hydrogen and an endothermic peak for phase change.

Wiberg (1953) and Clasen (1961) reported X-Ray diffraction studies for the characterization of alanates. Raman spectra of vibration modes in $[\text{AlH}_4]^-$ crystalline systems have been studied. Shirk and Shriver (1973) studied Infrared and Raman spectra of NaAlH_4 in both solid phase and in ether solutions. The lower limit to the frequency range of their Raman study is approximately 450 cm^{-1} , and a tentative assignment for the vibrational spectra in solution is offered, but difficulties are found in the solid phase due to band broadening. The lower frequency region is well studied by Temme and Waddington (1973), by inelastic neutron scattering and FT-IR. These measurements cover a frequency range from approximately 50 to 1000 cm^{-1} , and assignments for the vibrational and torsional modes in that region of the spectrum are made. Ashby *et al.* (1970) is reported XRD and IR data for the Magnesium alanate. Recently Balema *et al.* (2001) and Weinch *et al.* (2004) reported the characterization of alanates by solid state Al^{27} NMR. Since Sodium and lithium alanates attracted as storage media for hydrogen, a more detailed studies on the structure of NaAlD_4 (Hauback *et al.*, 2003) LiAlD_4 (Hauback *et al.*, 2002) and Li_3AlD_6 (Brinks and Hauback, 2003) are reported recently by using powder neutron diffraction, synchrotron X-ray diffraction and Raman spectroscopy techniques.

1.5.1.2. Dehydrogenation and rehydrogenation reactions

Thermal decomposition of sodium alanates:

Alkali metal alanates undergo dehydrogenation in the 473-573 K temperature range (Li, 474 K; Na, 538 K; K, 563 K) to give aluminum metal and the corresponding alkali metal hydrides. Ashby and Kobetz (1966) established that the dehydriding of NaAlH₄ initially proceeds through the reaction 1.9. Upon controlled heating, at 483 K, it forms Na₃AlH₆ and evolve 3.7 wt% and gave rise to aluminum metal. A second dehydriding reaction is observed at 523 K



The occurrence of these two reactions during dehydriding process has been verified in subsequent studies of the thermal behavior of NaAlH₄ by variety of techniques including thermo gravimetric analysis (Dilts and Ashby 1972; Kuznetsov *et al.*, 1974), differential thermal analysis (Dymova and Bakum, 1969) and differential scanning calorimetry (Caludy *et al.*, 1980). The thermal dehydrogenation of LiAlH₄ is studied by Block and Gray (1965) through differential scanning calorimetry. This study confirmed the multistep dehydrogenation pathway. They found that LiAlH₄ undergoes a phase transition at 433-450 K before undergoing an initial dehydrogenation reaction to give Li₃AlH₆, at 460-491 K. This first dehydrogenation process is exothermic, a non spontaneous process under all conditions. A second dehydrogenation reaction is observed to occur at 501-555 K which is found to be endothermic. Finally, the dehydrogenation of LiH is observed in the 633-701 K temperature range.

Rehydrogenation

The hydrogenation process is accomplished independently by Clasen (1961) and Ashby *et al.* (1963) in the presence of triethyl aluminum catalyst. Dymova *et al.* (1993) have reported the constant-temperature, equilibrium studies of NaAlH₄, but the conditions required (the formation of NaAlH₄ from the elements required temperatures of 473-673 K and hydrogen pressures of 10-15 MPa.) are impractical in their severity. Bagdonavic and Schwickardi (1997) showed that, the addition of Ti catalyst makes the reversibility of reaction profoundly easier.

1.5.1.3 Thermodynamics

From thermodynamic point of view, the mostly studied systems in alanates are sodium alanate and lithium alanate. Dissociation of MAIH₄ with M = Li, Na or K follows the same two-step endothermic processes. The first step involves the decomposed products of M₃AlH₆, Al and H₂. The second step involves MH, Al and H₂. From a thermodynamic point of view, since majority of the entropy change for hydrogen releasing reactions comes from the generation of the gaseous hydrogen (about 130 J/(mol K)), the entropy contribution to the free energy change would only vary within a narrow range. As a result, applicability of a given substrate for reasonable operation depends mainly on the enthalpy change of the reaction. An enthalpy change of 25–50 kJ/mol would provide the favorable thermodynamic conditions for being rechargeable at below 10 MPa of hydrogen gas. For sodium alanate, enthalpy changes for both the first (37 kJ/mol) and the second steps (28 kJ/mol) fall in this favorable range.

Thermodynamics of alanate decomposition reaction are comparable with many other metallic, ionic and covalent hydrides. Bogdanovic and Schwickardi (1997) reported the pressure-composition isotherms for the Ti catalyzed sodium alanate system, which

is having typical low-hysteresis, two-plateau absorption and desorption isotherms. Temperature dependencies of the plateau pressures P are related to the van't Hoff equation (Eq. 1.4). The enthalpy changes (ΔH) for the NaAlH_4 and Na_3AlH_6 calculated from van't Hoff plot are about 37 kJ/mol and 47 kJ/mol respectively. The conclusions drawn from the studies are,

- The gaseous synthesis of NaAlH_4 is thermodynamically possible only at higher pressures (>13 MPa) at 453 K.
- At room temperature Na_3AlH_6 is very stable and in practice cannot decompose. This hydride has equilibrium pressure of 0.1 MPa at about 343 K.
- At lower temperatures NaAlH_4 cannot be decomposed fully because Na_3AlH_6 remains stable at lower temperatures.
- Under gaseous hydrogen, formation of NaAlH_4 has to be stepwise process, involving formation of Na_3AlH_6 as intermediate phase. Direct synthesis of NaAlH_4 without formation of Na_3AlH_6 may occur at only very high pressures and high temperatures (>573 K).

The temperature at which the (hydrogen) dissociation pressure of a metal hydride reaches 0.1 MPa H_2 , can be utilized to classify reversible metal hydrides as *low temperature* (LT; 0.1 MPa H_2 below 323 K), *medium temperature* (MT; 0.1 MPa H_2 between 323 and 573 K) and *high temperature* metal hydrides (HT; 0.1 MPa H_2 at above 573 K). Bogdanovic *et al.* (2000) have shown that Ti-doped Na_3AlH_6 reaches 0.1 MPa of hydrogen pressure at 373 K, and thus it comes under the category of medium temperature hydrides, also the temperature required for an equilibrium pressure of 0.1 MPa from catalyzed NaAlH_4 is 306 K. Fig. 1.6 shows the comparison of thermodynamic properties of sodium alanates with some known metal hydrides. Hence Ti-doped NaAlH_4 behaves as LT hydride. The decomposition of Lithium

alanate and potassium alanates is similar to the sodium alanate (Dymova and Bakum, 1969; Zaluski *et al.*, 1999).

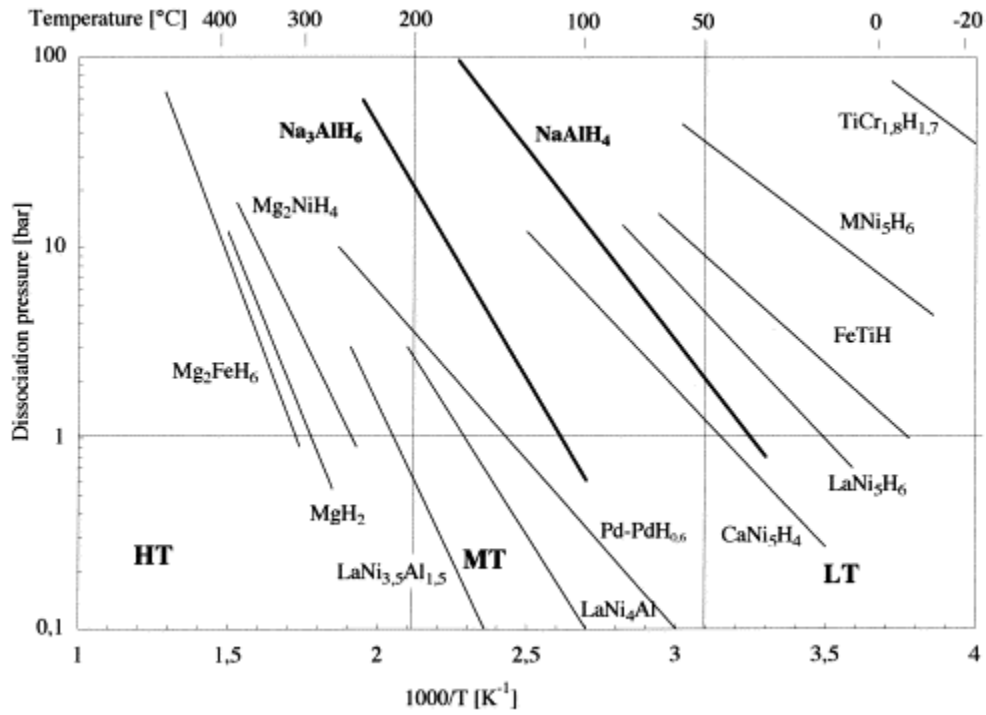


Fig. 1.6 Comparison of van't Hoff plots of NaAlH_4 and Na_3AlH_6 systems with those of various intermetallic and elemental hydrides (Bogdanovic *et al.*, 2000)

1.5.1.4 Kinetics of catalyzed Alanates

For technical applications, the kinetics of hydrogen uptake and release is an important issue. The hydrogenation and dehydrogenation rates of alanates are very slow (Dymova and Bakum, 1969). Since discovery of Bogdanovic and Schwickardi (1997), there have been considerable efforts to develop new catalysts, advanced methods of doping and material processing, as well as better fundamental understanding and practical understanding of the hydriding mechanisms (Jensen *et al.*, 1999; Jensen and Gross, 2001; Zaluska *et al.*, 2000; Sandrock *et al.*, 2002a, 2002b; Gross *et al.*, 2003; Anton, 2003). The rate of absorption and desorption are strongly dependent on the catalyst, particle size and heating temperatures (Sun *et al.*, 2004). The hydrogenation rate (v) can be approximately written as

$$v = \kappa \left[\frac{P - P_e}{C} \right]^a \dots\dots\dots (1.11)$$

$$k = A \exp(-E/RT) \dots\dots\dots (1.12)$$

where k is the rate constant, P and P_e are respectively the applied pressure and the equilibrium plateau pressure, C the hydrogen concentration in the material, a the order of reaction, A the pre-exponential factor, E the activation energy, R the ideal gas constant and T the absolute temperature. The hydrogenation rate is controlled by the two terms k and $[(P-P_e)/C]^a$. The term k , reflecting the dynamic property of the reaction, is temperature dependent. The term, $[(P-P_e)/C]^a$, is the driving force of the reaction, and is related to the pressure factor. However, the contribution to the rate from these two terms may cancel out each other. For instance, raising the temperature would increase k , which in turn increases v , but the concurrent rise of P_e causes an adverse effect on the rate, v . Therefore an increase or decrease of v depends on the term which plays a dominant role.

Effect of catalyst:

The Improvement in the kinetics will depend on type of catalyst, method of doping and catalyst precursor. Bagdonavic and Schwickardi (1997) disclosed that doping of NaAlH₄ with 2-mol% Ti compounds significantly enhanced the kinetics of hydriding and dehydriding process. Doping of NaAlH₄ with Ti catalyst is done by solution-chemistry techniques, where by non-aqueous liquid solutions or suspensions of sodium alanate and 2-mol% of either TiCl₃ or Titanium (IV) n-butoxide catalyst precursors, which decomposed to precipitate solid Ti-doped NaAlH₄ (Bogdanovic *et al.*, 2000). The temperature required for rapid dehydriding is found to be lowered to ~423 K. The conditions required for dehydriding also reduced 5 h at 443 K and 15

MPa. Furthermore, they observed that $\text{Ti}(\text{OBU}^n)_4$ shows better results than TiCl_3 . However hydrogen storage capacity of Ti-doped alanate is decreased from 4.2 wt% to 3.1 wt% after 31 cycles. During the doping process, the liberated amount of hydrogen is measured and it is found to be 1.5 and 2.0 mol of $\text{H}_2/\text{mol Ti}(+3)$ and $\text{Ti}(+4)$ respectively hence they assumed that the catalyst is in zero valent state. The nature of catalyst and its mode of operation are not discussed.

Jensen *et al.* (1999) introduced a novel method (dry doping) for the preparation of titanium containing materials by adding prescribed amounts of $\text{Ti}(\text{OBU}^n)_4$ to freshly re-crystallized NaAlH_4 under an atmosphere of argon, then homogenizing mixtures using a mortar and pestle for 15-min. Amount of catalyst is varied and the dehydriding behavior of wet and dry doping methods are compared. Important observations are enhancement of the dehydrogenation kinetics of NaAlH_4 upon introduction of titanium to the material is highly sensitive to the doping method. Variation in the amount of $\text{Ti}(\text{OBU}^n)_4$ used in the preparation has little effect on the dehydrogenation temperature. However, increasing the titanium content of the material decreases hydrogen storage capacity. Ti doped by dry method is more catalytically active than Ti doped by wet chemical method. The reason attributed for this is the action of wet doping method is restricted to the surface of the hydride while the dry doping method introduces active titanium sites in the bulk.

Zidan *et al.* (1999) performed the hydriding and dehydriding operations for sodium alanate doped with Ti and Zr by using dry doping method and $\text{Zr}(\text{OPr})_4$ and $\text{Ti}(\text{OBU}^n)_4$ as precursors. In case of Zirconium, in contrast to the titanium-doped material, the catalytic effect is pronounced for the dehydriding of Na_3AlH_6 to NaH and Al rather than the dehydriding of NaAlH_4 to Na_3AlH_6 and Al . The zirconium-doped material shows improved cyclable hydrogen capacity of ≈ 4.5 wt% with good cycling stability.

However, the kinetics of the first dehydriding reaction in this material is inferior to that of material, with titanium doping. Hence materials containing both Zr and Ti may show better results.

Ball milling is known to change various properties of materials as a result of the formation of special microstructures, metastable phases or modified surfaces. Hydrogenation properties are sensitive to these modifications and in some cases substantial changes of the hydriding behavior can be obtained after ball milling. For example, formation of nanocrystalline or amorphous structures produced by ball milling results in dramatic changes in hydrogen sorption properties (Srinivasan *et al.*, 2004), especially by elimination of the need for activation and improvement of hydriding/dehydriding kinetics.

Zaluski *et al.* (1999) described the hydrogenation properties of complex metal hydrides fabricated by mechano-chemical synthesis (ball milling). Li_3AlH_6 prepared by ball milling, found to be thermodynamically stable and cannot be hydrogenated at pressures below 5 MPa. Na_3AlH_6 synthesized by mechano-chemical reaction exhibited a reversible hydrogenation performance with effective kinetics, and desorption rate is of the same order as catalyzed materials. Na_3AlH_6 prepared in a conventional way, i.e. from NaAlH_4 and NaH under pressure of 14 MPa of hydrogen (stirred intensively in heptane at 435 K for 72 h) required 20 h to desorb 2.5 wt% of hydrogen at 473 K. Na_3AlH_6 prepared by mechano-chemical synthesis can desorb the same amount of hydrogen at 473 K within only 2.5 h and without a catalyst, giving a reaction rate about 10 times faster than for conventionally fabricated, non-catalyzed hydrides. In the case of alanates fabricated by mechano-chemical synthesis, the materials can be successfully hydrogenated, even without catalysis. In the case of catalyzed alanates, Bogdanovic and Schwickardi (1997) needed at least 16 h at 473 K

under 6 MPa of hydrogen to absorb 2.5 wt% of hydrogen in Na_3AlH_6 . But hydrogen absorption of the same amount of hydrogen occurs within 30 min at 503 K, but in a non-catalyzed alanate.

Alloying with other elements or compounds in general changes the hydrogen sorption properties of hydrides. For the alanates, the most effective method of such alloying is by using mechanical grinding (ball milling) of the hydride in the presence of additives. Zaluska *et al.* (2000) reported the effect of ball milling on the kinetics of decomposition of sodium alanate, which are further enhanced by the addition of carbon in the milling process. The rates of decomposition for sodium alanate at 433 K with and with out carbon (10 wt. %) are measured and compared with that of Ti-catalyzed alanates. Sodium alanates activated by ball milling with carbon can be rehydrogenated without the use of catalysts, under more practical conditions (hydrogen pressure of about 7.5–9 MPa and temperature <403 K) with in 3-5 h. In this case also the role of additive (carbon) is not explained. Bagdonavic *et al.* (2000) reported that the kinetics of hydrogen desorption and absorption of solid doped NaAlH_4 depends upon the kind and amount of the metal compound used as a dopant, morphology and size of NaAlH_4 particles used and the doping procedure. Various metal compounds are used as dopants and the degree of rehydrogenation is measured for the doped alanates. Kinetic enhancement of the reversible dehydriding of NaAlH_4 which is similar to that produced by Ti compounds has been found to occur upon doping with Zr, V and some rare earth compounds. It has been also observed that combined catalysts like Ti-Fe and Ti-Ni result in good adsorption kinetics compared to the either of dopants alone.

Sandorck *et al.* (2002a, 2002b) reported the cyclic capacity and engineering rates of a scale up bed containing 100g Sodium alanate doped with Ti/Zr alkoxides (2-mol%

each). The kinetics of NaAlH₄ and Na₃AlH₆ decomposition reactions over a wide range of temperatures (298–423 K for NaAlH₄ and 323-453 K for Na₃AlH₆) are determined using a sample of NaAlH₄ doped with 2-mol% of TiCl₃ and plotted in Arrhenius form. The sample is prepared by milling NaAlH₄ for 3h with solid catalyst precursor. The rates for the decomposition of both NaAlH₄ and Na₃AlH₆ expressed as Arrhenius equations as follows. The rate of reaction for both hydriding and dehydriding are second order for Ti⁴⁺ or Zr⁴⁺ catalysts.

$$\text{Rate (for NaAlH}_4) = 7.19 \times 10^{10} \exp(-9559/T) \dots\dots\dots (1.13)$$

$$\text{Rate (for Na}_3\text{AlH}_6) = 5.33 \times 10^{11} \exp(-11652/T) \dots\dots\dots (1.14)$$

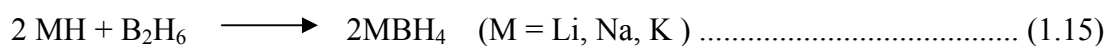
It has been reported that Ball milling of sodium alanate with liquid alkoxide catalyst precursors would contaminate H₂ with hydrocarbons by the decomposition of organic groups. Hence, if ball milling is used for doping process then the inorganic solid precursors are the better choice. The initial absorption kinetics are so high that reaction self-heating is significant, easily exceeding the 455 K melting temperature of NaAlH₄. Partial melting of the alanate bed did not appear to hinder the subsequent absorption/desorption kinetics. On the contrary, it results in a moderately sintered porous structure that effectively fixes the particulates, thus simplifying large bed design. The absorption/desorption volume changes of alanate beds are lower than conventional metallic hydrides. This also simplifies large bed design and may allow higher hydride fillings. The activation energies calculated to be 79.5 and 97 kJ/mol H₂ for NaAlH₄ and Na₃AlH₆ respectively. It has also been reported that the first small addition of Ti- catalyst significantly lowers the thermal activation energies (E_a) for both decomposition steps and with higher concentrations of TiCl₃ beyond 0.9 mol% further enhances the kinetics, but only via increasing the pre-exponential factor. As Ti-halide doping level increases, the total reversible capacity decreases. The addition

of more TiCl_3 had no further effect on the activation energy. Gross *et al.* (2003) demonstrated the indirect Ti doping, in which TiCl_2 is pre reacted with LiH by mechanical milling followed by milling with NaH (6 mol%) and Al. This enables Ti to enter into the host lattice; also it shows an activation process that is more profound than in direct Ti-halide doped materials. However, enhanced kinetics is showed only after a prolonged activation period. Also identical kinetics is observed for TiH_2 . Hydrogen desorption kinetics of sodium alanate with various catalysts has been studied by Anton (2003). The dependence of ionic size of catalysts and hydrogen discharge rate was explored. Very low rates are observed for the dopants with radii significantly larger or smaller than 0.76 \AA . The cations having a radius in the range of $0.73\text{-}0.80 \text{ \AA}$ should hold the highest potential for enhanced hydrogen discharge rate. This range is near to the mid point radius 0.74 \AA (Na^+ being 0.97 \AA and that of Al^{3+} being 0.51 \AA). But Ti^{+4} and Ti^{+2} having different ionic radii from 0.74 \AA will show faster desorption kinetics than Ti^{+3} . Kiyobayashi *et al.* (2003) observed that both NaAlH_4 and Na_3AlH_6 undergo dehydrogenation at nearly equal rates directly following mechanical doping with titanium. This finding is an interesting result and quite different from the other results, as the Na_3AlH_6 arising from the initial dehydrogenation of Ti-doped NaAlH_4 undergoes dehydrogenation at slower rates. They concluded that Ti doping does not innately enhance the dehydrogenation of NaAlH_4 to a greater extent than Na_3AlH_6 . Instead it seems plausible that the dehydrogenation of doped NaAlH_4 yields Na_3AlH_6 in which the Ti dopant is not properly distributed for the maximum enhancement of the dehydrogenation of the hexahydride. Ti-doped NaAlH_4 and Na_3AlH_6 undergo dehydrogenation at the same rates clearly indicating that the dehydrogenation kinetics are insensitive to variation in the Al-H bonding interactions and are probably influenced by processes such as nucleation and growth or the diffusion of atoms and molecules. Sun *et al.* (2003,

2004) demonstrated that rehydrogenation may be possible at moderate conditions by optimizing the doping materials, temperature, and hydrogen pressure, the reverse of reactions (1.9) and/or (1.10) occur at temperatures of 298-393 K and pressures of 2-12 MPa for the dehydrogenated NaAlH₄ both in the undoped and in the Ti-doped forms. Ti-doped LiAlH₄, NaAlH₄, and Mg(AlH₄)₂ all undergo dehydrogenation at appreciable rates at temperatures at or below 373 K, suggesting their possible application as hydrogen carriers for on-board applications. Although there are instances of transition-metal-doped alanates that have hydrogen cycling capacities, thermodynamic properties, or kinetic performances that are suitable for onboard vehicular hydrogen storage no material meets all the three criteria.

1.5.2 Borohydrides

Borohydride are another class of complex metal hydrides with general formula [Aⁿ⁺(BH₄)_n]. The alkali metal and alkaline-earth metal borohydride belong to a class of materials with gravimetric hydrogen densities that are among the highest known today. The bonding and chemical behavior of borohydride are similar to that of alanates. LiBH₄ and NaBH₄ are commercially available. Schlesinger and Brown (1940) synthesized the first pure alkali metal borohydride (LiBH₄) by the reaction of ethyl lithium with diborane (B₂H₆).in etheral solvents.



They can be synthesized directly from the metal, boron, and hydrogen at 823-973 K and 3-15 MPa H₂ pressure.

1.5.2.1 Dehydrogenation and rehydrogenation reactions

Hydrogen storage by borohydride can be divided into two types

A) Pyrolysis (decomposition of the substance upon heating to generate hydrogen),

B) Hydrolysis (reaction of the substance with water to liberate hydrogen).

Thermal decomposition:

The dehydrogenation reaction of borohydride is given as



Thermal analysis of alkali metal tetrahydroborides is investigated by Stasinevich and Egorenko (1968). Hydrogen desorbs from LiBH₄ at temperatures greater than 743 K. With 18 wt. % hydrogen content, LiBH₄ is studied by Zuttel *et al.* (2003); three step decomposition and 13:5 wt% hydrogen production are reported. But reversibility is reported to be difficult even at high pressures and temperatures; 923 K and 15 MPa H₂ pressure, so work on these compounds as a fuel source is not progressed. Recently, Millennium Cell has developed a process that takes advantage of the inherent energy density of boron-hydrogen compounds. The contained hydrogen is stored safely at ambient conditions in form of a non-flammable liquid fuel – an aqueous solution of sodium borohydride, NaBH₄. The process supplies pure hydrogen for energy applications without the need for compression or liquefaction. The system releases the hydrogen stored in sodium borohydride solutions by passing the liquid through a chamber containing a special catalyst. Hydrogen is only produced when the liquid fuel is in direct contact with the catalyst, thereby minimizing the amount of gaseous hydrogen present in the system at any given time. The fuel solution itself is non-flammable, non-explosive, and easy to transport. The only other reaction product, sodium metaborate, is water-soluble and environmentally benign, can be recycled off board.

1.6 MOTIVATION AND SCOPE

Magnesium based hydrogen storage systems and complex metal hydrides based on alanates and borohydrides are potential candidates for hydrogen storage because of their high storage capacity (> 6 wt %). But these systems do not release hydrogen near ambient conditions (Stioui *et al.*, 1986; Bogdanovic and Schwickardi, 1997). Various attempts have been made to facilitate (or even enhance the kinetic parameters or decrease the activation parameters) desorption process by addition of suitable materials that are conventionally termed as “catalysts” (Bagdonovic *et al.*, 2000; Zaluska *et al.*, 2000; Gross *et al.*, 2002). However, the role of these additions has to be carefully understood, since they not only function as catalysts but also have to facilitate the transport of the species to the surface before desorption. A catalyst only functions in the surface transformations but the diffusion of hydrogen from the solid bulk has to be achieved by some affinity parameters and the kinetics of this transport process is related to the ad-lineation that can take place between the species and the added component. Mg_2Ni alloy is an interesting material for metal hydride battery applications because of its high energy density (Rongeat *et al.*, 2006). Attempts have been made to improve sorption kinetics and discharge capacity of Mg-Ni alloy by preparing in nano/amorphous form through mechanical milling (Liu *et al.*, 1997) which is an energy expensive process. The effect of graphite on hydriding properties of Mg (Imamura *et al.*, 2002) and the effect of graphite as co-dopant on dehydrogenation properties of Ti catalyzed sodium alanates (Dehouche *et al.*, 2005; Wang *et al.*, 2005) have been reported. Carbon can act as a catalyst to improve kinetics by facilitating transport of hydrogen atoms from bulk to surface or vice versa. Moreover there is no clear understanding on the effect of carbon on the hydrogenation and dehydrogenation properties of alanates.

In the light of the above observations, the present study aims to show how the addition of carbon materials and hetero atom substituted carbon materials affect the hydrogen storage properties of Magnesium and alanates. Since borohydride decomposes at high temperatures (>573 K), other possibility i.e. generating hydrogen by hydrolysis of borohydride has been studied by using cobalt based catalysts. The thesis focuses on the following aspects:

- Synthesis of Mg_2Ni alloy by polyol reduction method and the study of its sorption kinetics and the electrochemical characteristics
- The study of the desorption kinetics of carbon admixed alanates
- The role of carbon additives has also been addressed.
- Synthesis of nitrogen containing carbon nanotubes (NCNT) and test the reversibility of NCNT admixed alanates
- Synthesis of boron and nitrogen containing carbon materials and to study their effect on the sorption properties of Mg
- The study of the catalytic effect of cobalt based catalysts on the hydrogen generation from alkali stabilized sodium borohydride.

CHAPTER 2

EXPERIMENTAL METHODS

2.1 CHEMICALS AND MATERIALS USED

The chemicals used and the sources from which they were obtained are as follows:

The magnesium powder (99.9%) and graphite powder were purchased from CERAC, USA. The Whatman Anodisc Membrane Filters (Alumina) with pore diameter, thickness and percentage porosity of 200 nm, 60 μm and 65 % respectively were purchased from Whatman Inc. U.S.A. H-zeolite-Y was obtained from Sud-Chmie Pvt Ltd., India.

All other chemicals and solvents used in the investigation were of analytical (AR) grade and were obtained from (Sisco Research Laboratory, India or E.-Merck, India). These chemicals were used as such without further purification.

2.2 EXPERIMENTAL PROCEDURES

2.2.1 Purification of hydrogen

Hydrogen gas obtained from M/s. Indian Oxygen Ltd. was purified through a heated trap containing reduced copper powder kept at 623 K followed by traps containing potassium hydroxide pellets, fused calcium chloride and silica gel. Then it was followed by passing through liquid nitrogen trap, evacuated and cooled at liquid nitrogen temperature of activated carbon trap. Hydrogen of high purity is thus obtained for reduction of catalysts and sorption measurements.

2.2.2 Electrochemical studies

The measurement of the electrochemical properties, such as charge-discharge characteristics, capacity, and open circuit potential were carried out at room temperature using an open tri-electrode measurement system. The test electrodes were fabricated by pressing mixture of 0.3 g alloy powder and Cu powder in a weight ratio of 1:2, into a pellet of 1.3 cm in diameter. Pellet was pasted on glass electrode with Araldite. Subsequently, as current conductor, a copper wire was attached to the pellet by silver paint. Electrochemical measurements were performed using an automatic battery-testing instrument controlled by a computer. Pt and Hg/HgO were used as the counter electrode and the reference electrode, respectively. In charge–discharge cycle tests, each negative electrode was charged for 12 h at 50 mA g^{-1} . After 10 min rest the discharge process is conducted with current densities of 20, 50 and 100 mA/g until the potential reached -0.6 V versus Hg/HgO in a 6M KOH aqueous solution. The temperature was kept at 300 K. The potential of the negative electrode is recorded as a function of time for discharge processes.

2.3 CHARACTERIZATION TECHNIQUES

2.3.1 Powder X-ray Diffraction (XRD)

X-ray diffraction patterns of the various samples were recorded using SHIMADZU XD-D1 diffractometer using Ni-filtered Cu K_{α} radiation ($\lambda = 1.5418 \text{ \AA}$) in the range of 5 - 90 degrees at a scan rate of 2 degrees per minute using Bragg-Brantán configuration.

2.3.2 Elemental analysis

The C, H and N analysis was done using the Heraeus CHN analyzer.

2.3.3 Scanning Electron Microscopic studies (SEM)

Scanning electron micrographs were taken using JEOL, JSM5610LV microscope (acceleration voltage 15 kV). The sample powders were deposited on a carbon tape (Adhesive tape, normally used in SEM measurements for conduction purpose) and mounted on the sample holder and imaged.

2.3.4 Transmission Electron Microscopic studies (TEM)

Transmission electron micrographs were recorded with a JEOL-JEM 100SX microscope, working at a 100 kV accelerating voltage. Samples for TEM were prepared by dispersing the powdered sample in acetone by sonication and then dropped on a copper grid (400 mesh) coated with carbon film.

2.3.5 Thermogravimetric Analysis (TGA)

Thermogravimetric analyses of materials were performed using Perkin Elmer TGA (Delta series, TGA7) instrument with different heating rates under nitrogen atmosphere.

2.3.6 Differential Scanning Calorimetry (DSC)

The DSC analysis was carried out under dynamic non-isothermal conditions with a flow of extra-pure nitrogen in a Perkin-Elmer DSC-7 differential scanning calorimeter (Accuracy ± 0.1 K; Precision ± 0.01 K). Activation energies of thermal decomposition of materials were calculated using the Kissinger method.

2.3.7 Infrared (IR) Absorption studies

FT-IR absorption spectra of the samples were recorded using a Bruker FT-IR (Bruker Tensor 27) spectrometer in argon atmosphere at room temperature in the range 4000-400 cm^{-1} .

In-situ DRIFT-IR

The thermal decomposition of NaAlH_4 -NCNT composite was studied by diffuse reflectance infrared Fourier transform (DRIFT) spectroscopy under inert atmosphere in the temperature range of room temperature to 473 K. A FTIR spectrophotometer (Bruker Tensor 27) in conjunction with a Praying Mantis diffuse reflectance FT-IR spectroscopy accessory (Harrick Scientific, DRP) was used to collect infrared spectra.

A high-temperature chamber (HVC; Harrick HVC-DRP-1) made of 316 stainless steel was used as the reaction chamber in this study. It was equipped with a sample cup to hold the powder and a dome to cover the sample. The HVC dome contained three KBr windows transparent to IR. The HVC was equipped with two gas ports, two coolant ports, and one vacuum port. A K-type thermocouple and an electric heater were connected on the sample cup. The reaction chamber was located inside the compartment of the FT-IR instrument. A temperature controller directly connected to the thermocouple and heater of the HVC provided accurate temperature control (± 1 K). A mesh was put in the sample cup, which could be filled with sample powder using an overflow tray, to prevent the sample powder from being blown out. Reaction chamber was taken in to glove box and sample was loaded in order to avoid exposing sample to atmosphere. Argon was introduced from one gas port, flowed through the reactor, and exited from another gas port. After flushing two three times gas ports were closed. The HVC was designed for operation up to 873 K, but operation at

temperatures above 373 K required water-cooling via the coolant ports connected to a water chiller.

2.4. Hydrogen evolution kinetics measurements

The experimental set-up used to measure the volume of hydrogen evolved was shown in Fig. 2.1. It consists of a reaction vessel, a 20.0 ml syringe and a water trap to measure the volume of hydrogen generated. The reaction vessel consisted of 100 ml conical flask sealed with rubber septum. A calibrated burette of 1000 ml capacity was filled with water, is connected to the water bulb by a flexible tube. The top outlet of the reaction vessel was connected to the gas burette. Temperature of the water bath was maintained constant within a variation of ± 0.1 K using a thermostatic circulator.

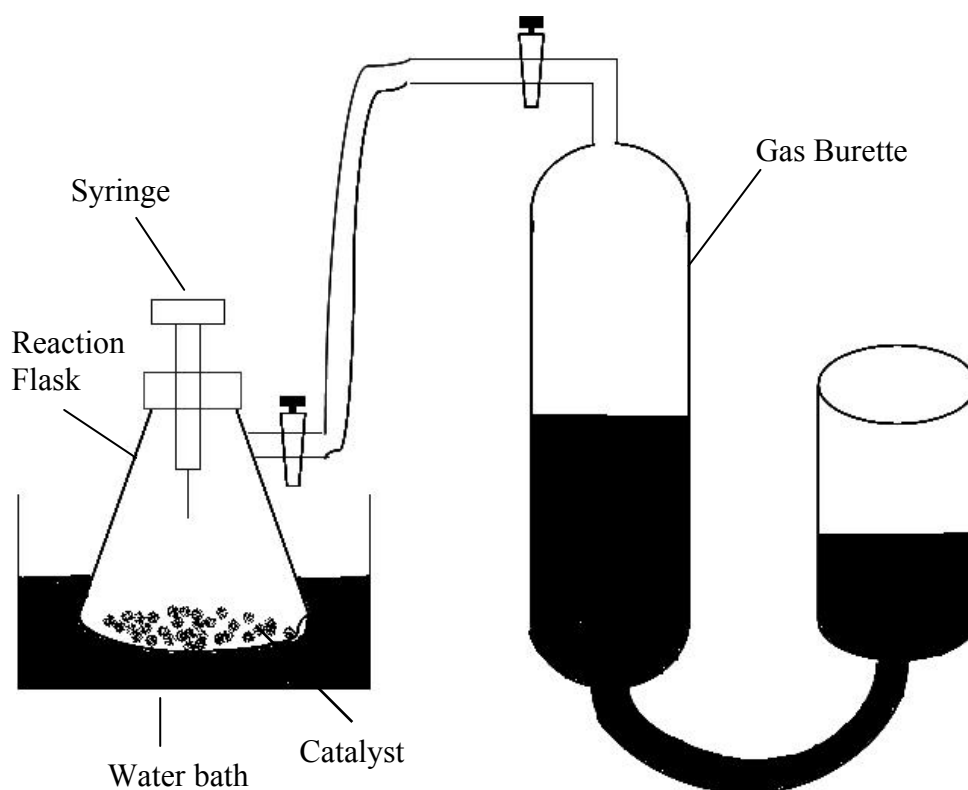


Fig. 2.1 Experimental set up for the measuring the hydrogen evolution

The reaction flask was preheated by submerging it for 5 min in the water bath maintained at the desired reaction temperature. The desired amount of solid catalyst in powder form was preloaded into the reaction flask. The syringe was inserted through the septum and was used to introduce measured amount of alkaline NaBH₄ solution into flask. The volume of hydrogen generated from the solution was measured by the displacement of water in the burette.

2.5 High pressure apparatus

2.5.1 Kinetic measurements

Description of set up:

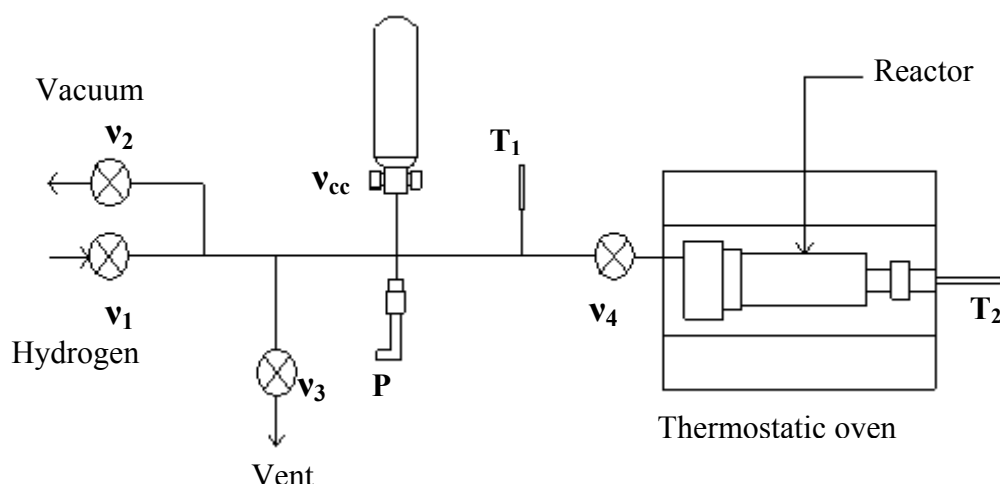
Volumetric high pressure hydrogen sorption measurements have been carried out using custom built volumetric apparatus (Fig. 2.2). The apparatus consists of:

- (1) A cylindrical sample holder of known volume, 30 cm³, and a 0.1 μm filtering gasket for avoiding sample drag from reactor to tubes,
- (2) A furnace (max. temperature 673 K),
- (3) A hydrogen reservoir of known volume,
- (4) Piezoresistive -type pressure transducer of range 0–10 MPa (accuracy 0.1% of full scale) to monitor system pressure,
- (5) A rotary vacuum pump,
- (6) A pirani gauge with gauge head to measure vacuum pressure,
- (7) “K” type thermocouples (sensitivity 0.1 K) to measure the temperature.

Using this system pressure up to 12 MPa can be achieved. All components are made of stainless steel (SS-316). High-pressure bellow valves are used in the gas line for controlling the gas flow. The sintered SS-316 filter of 2 micron is used just after the supply cylinder to ensure the purity in hydrogen supply during the absorption

measurements. All possible sources of leakage were carefully inspected. Care has been taken to avoid the errors due to factors such as temperature instability, leaks and additional pressure and temperature effects caused by expanding the hydrogen from the reservoir to reactor.

The amount of hydrogen uptake/release for the material was calculated from the pressure changes in a known volume using the ideal gas law. The sample temperature and applied pressure were monitored and recorded by an Agilent data logger. The set up is divided into volumes V_1 and V_2 . V_1 is sum of the volumes of V' and V_{CC} , where V' is volume between the valves v_1, v_2, v_3, v_4 and v_{CC} . V_2 is reactor void volume up to valve v_4 (Fig. 2.2).



where v- Bellow Valve, P – Pressure Transducer, T – Thermo Couple,
C.C – Calibrated Cylinder

Fig. 2.2 Experimental setup for measuring the sorption kinetics

Pipe volume V' and void volume of the sample holder in the presence of material was determined using high pure argon at different pressures from a known reference

volume V_{CC} (33.8 ± 0.05 ml). The method used for volume determination was based on isothermal expansion of an ideal gas from known volume at room temperature and low pressure (< 0.3 MPa). The volume V' is found to be 19.2 ± 0.05 ml. The reactor volume varies with respect to material and its quantity. Hence the reactor volume V_2 is measured each time it is connected.

Volumes of pipes (V') and reactor (V_2) are measured as follows:

Volumes V_{CC} and V' evacuated initially then flushed with high pure argon with three four times. Valve v_4 is closed and V_{CC} is filled with argon gas pressure at p_1 (0.3 MPa). After reaching steady state argon was allowed to occupy additional volume V' . Then the pressure p_2 is recorded after reaching steady state. The volume V' is measured by the following equation.

$$V' = V_{CC} \frac{(p_1 - p_2)}{p_1} \dots\dots\dots (2.1)$$

The procedure was repeated four times and the mean value of V' is calculated. The volume of reactor is calculated by same procedure by taking $V_{CC} + V'$ as new reference.

Absorption kinetics

At the beginning of the absorption experiment both volumes of kinetic set-up V_1 and V_2 were evacuated down to 10^{-3} mbar by opening all valves except v_1 . During evacuation reactor temperature was maintained at 473 K. After evacuation valve v_2 and v_4 were closed. Hydrogen was introduced into volume V_1 by opening valve v_1 to a predetermined pressure (p_s). The system is allowed to reach steady state. Since the free volume in V_2 is very less and the pressure is below 10^{-3} mbar, mass of the

hydrogen in this volume is neglected. The mass of hydrogen in volume V_1 at the start of absorption measurement (m_s) is calculated as follows:

$$\text{Mass of the hydrogen in volume } V_1 = m_s = \frac{p_s V_1}{Z_1 R_{H_2} T_1} \dots\dots\dots (2.2)$$

Then valve v_4 was opened and hydrogen was allowed to flow into the reactor. The pressure and respective temperatures were recorded with definite time intervals. The hydrogen mass at any time t in volumes in V_1 ($m_{V_1}^t$) and V_2 ($m_{V_2}^t$) can be calculated using equations

$$m_{V_1}^t = \frac{p_t V_1}{Z_1 R_{H_2} T_1} \dots\dots\dots (2.3)$$

$$m_{V_2}^t = \frac{p_t V_2}{Z_2 R_{H_2} T_2} \dots\dots\dots (2.4)$$

At any time t , the total mass of the hydrogen in void volume of measurement facility (m_a^t) is sum of the masses of hydrogen in volumes V_1 and V_2 .

$$m_a^t = m_{V_1}^t + m_{V_2}^t \dots\dots\dots (2.5)$$

At time t , the mass of the hydrogen absorbed by the material (m_t) is the difference between hydrogen mass in void volume at the start and mass of hydrogen at time t .

$$m_t = m_s - m_a^t \dots\dots\dots (2.6)$$

At time t , wt% of hydrogen absorbed by the material was calculated by

$$\text{wt. \% of hydrogen} = \frac{m_t}{m_{\text{alloy}}} \times 100 \dots\dots\dots (2.7)$$

where m_{alloy} is mass of the material. While steady state value of quantity absorbed by the material is the absorption capacity of material, quantity absorbed with time gives the absorption kinetics.

Desorption kinetics

The hydrogen desorption kinetics and storage capacity were determined by the following steps. The reactor volume V_2 and volume V_1 were evacuated down to about 10^{-3} mbar. Then the whole system was flushed three times using hydrogen gas to remove any other trace gases. Now the valve v_4 is closed and V_1 was evacuated fully. Then the valves v_1 , v_2 and v_3 were closed. The mass of the hydrogen in the volume V_2 is calculated as per Eq. 2.2. When the vacuum in the volume V_1 reached 10^{-3} mbar, valve v_4 is opened and allowing the hydrogen gas desorbed by the material to occupy volume V_1 . The mass of hydrogen at anytime t in the volume V_1 and volume V_2 were calculated by using equations 2.3 and 2.4. The mass of the hydrogen at any time t is the sum of these masses. The mass of the hydrogen desorbed by the material at any time t , m'_d is the difference between masses of hydrogen in the volumes V_1 and V_2 at time t and mass of hydrogen at start of the desorption. The weight percentage of hydrogen desorbed by the material at any time t is calculated as per Eq. 2.6. The quantity of hydrogen desorbed by material at steady state gives the desorption capacity and with time is desorption kinetics.

2.5.2 Static PCI Measurements

A cylindrical reactor of 15 mm inner diameter and 2 mm thickness is used for the static PCI measurements. The details of the set-up used for measuring the static PCI characteristics of metal hydride alloys is described elsewhere (Anil Kumar *et al.*, 2007).

CHAPTER 3

SORPTION PROPERTIES OF Mg₂Ni PREPARED BY POLYOL REDUCTION METHOD

3.1 INTRODUCTION

Magnesium, its alloys and composites constitute an unique and promising materials for hydrogen storage application since these exhibit high hydrogen storage capacity, light weight and low cost. Mg-based intermetallics form hydrides that are unstable than MgH₂. However, the reactions of Mg-and Mg alloys with hydrogen require appreciably higher temperatures (473-573 K) and pressures (up to 1 MPa) due to sluggish hydriding/dehydriding kinetics at room temperature. Additions of rare earth and transition metals such as nickel help in increasing desorption rates of hydrogen from magnesium. Owing to the relative stability of MgH₂, modifications of MgMH_x, (M = transition metal) are made to decrease the dissociation temperature of the hydride. Cu and Ni have been added to Mg either as alloying additions or as catalysts.

Reilly and Wiswall (1967, 1968) reported successful hydriding and dehydriding experiments with Mg₂Ni and Mg₂Cu. In Mg-Ni system, two intermetallic compounds are formed: Mg₂Ni and MgNi₂. Among these MgNi₂ does not react with hydrogen at pressures up to 2.76 MPa and temperatures up to 623 K; However, Mg₂Ni reacts readily with hydrogen at 2.07 MPa and 598 K. On the basis of the stoichiometry of the system and X-ray diffraction studies, the reaction in the plateau region is believed to be as follows:



Hydrogen storage alloys have been widely studied for battery electrode application. Metal hydrides are used as the negative electrode of a rechargeable battery, essentially replacing the cadmium electrode in the widely used Ni-Cd battery. Since Cd is relatively toxic material, it needs to be replaced due to environmental considerations. Moreover metal hydrides have a less detrimental effect on the environment, a high energy density, a higher charge/discharge rate, low temperature capacity and an absence of memory effect (Kohler *et al.*, 2002). Of all the magnesium-based alloys, Mg₂Ni is one of the promising material due to its relatively high hydrogen storage capacity (3.8 wt. %). However, the reaction of magnesium alloys with hydrogen requires quite high temperatures (573 K) and pressures due to hydriding /dehydriding difficulties. And moreover the polycrystalline Mg₂Ni shows a very low electrochemical discharge capacity (less than 10 mAh/g) (Cui *et al.*, 1996).

For preparation of the Mg based alloys, several methods such as conventional melting (Reilly and Wiswall, 1968), mechanical alloying (MA) (Song 1995; Liang *et al.*, 1998), replacement–diffusion method (Yuan *et al.*, 1997) combustion synthesis (Akiyama *et al.*, 1998), melting spinning (Spasov and Koster, 1999) and rotation-cylinder method (Hong and Kim, 2002) have been developed. Because of the large difference in the vapor pressure and the melting point between Mg and Ni, it is difficult to prepare pure Mg₂Ni compound by conventional melting method. A re-melting process with an addition of magnesium is usually needed to obtain stoichiometric Mg₂Ni compound.

The common technique for producing Mg–Ni-based alloys is mechanical alloying. Several studies have employed the mechanical alloying for producing amorphous or nanocrystalline Mg–Ni alloys in order to enhance reaction kinetics and desorption

temperatures. By employing a mechanical alloying easy activation can be achieved and also hydrogen storage capacity can be improved (Singh *et al.*, 1995; Sun *et al.*, 1995; Chen *et al.*, 1996; Iwakura *et al.*, 1996; Kohno *et al.*, 1996; Liu *et al.*, 1996; Aymard *et al.*, 1997; Abdellaoui *et al.*, 1998; Goo *et al.*, 1999; Suryanarayana 2001; Abe *et al.*, 2002; Vijay *et al.*, 2005). Improved hydriding kinetics is attributed to the appearance of a nanocrystalline or amorphous state of the material rich in dislocations and special defects and clean and highly reactive surfaces, which lead to an increase of the hydrogen absorption rate.

The nanoparticles usually possess unusual electronic and chemical properties, and these make them different from the bulk materials due to their extremely small particle size and large specific surface area. It is reported that amorphous Mg₂Ni alloy and metallic Ni or Pd composite prepared by mechanical treatment of the Mg₂Ni alloy with Ni or Pd powder, improved greatly the charge/discharge characteristics (Kohno *et al.*, 1999; Janot *et al.*, 2004). For the mechanical alloying method, the raw materials are milled by balls made up of iron. It requires long milling time to obtain homogeneous particles and thus sample will be oxidized even in a protective atmosphere. Moreover this process results in the introduction of impurities during milling. In addition, this method consumes energy and results in higher cost to synthesis these alloys.

Hence, it is necessary to look for other alternative method to synthesize nanocrystalline alloys. The most common low-temperature strategies for synthesizing intermetallics are solution based methods which employ either aqueous or non-aqueous solvents. Over the past two decades, the polyol process has been largely studied and well adapted for the preparation of metal powders such as Co, Ni, Cu, Ag, Au, Pt, and Pd (Fievet *et al.*, 1989; Sanguesa *et al.*, 1992; Sanguesa *et al.*, 1993;

Silvert *et al.*, 1995) and also to the synthesis of binary alloys such as Ag–Pd, Co–Ni, Pt–Fe and Mg–Ni (Toshima and Wang, 1994; Viau *et al.*, 1996; Wang *et al.*, 2000; Chen and Jehng, 2004). The advantage of this method is that, it gives the flexibility to synthesize uniform size nanoparticles in desired composition range by adjusting the preparation conditions such as reducing agent, concentration of protecting reagent, temperature and reaction time. Among the various physical and chemical methods commonly used for the preparation of metallic powders (e.g., atomization, electrolysis, reduction by hydrogen or hydride), the polyol process presents large advantages. It consists of the reduction of metallic compounds such as oxides, hydroxides, and salts in a liquid alcohol medium, at moderate temperatures. The organic liquid (e.g., ethylene glycol, glycerol, diethylene glycol) acts as a reducing agent and dissolving medium. This method enables an accurate control over the size distribution and shape of the particles from the micrometric to the colloidal scale. The polyol medium composition, the reaction temperature, the nature of the precursors, the use of additives (surfactants, foreign nuclei), the pH of the medium, and the reaction time are some of the parameters that can be separately or simultaneously adjusted, depending on the system and on the desired characteristics of the final product.

In the present study, nanosized Mg₂Ni alloy have been synthesized by polyol reduction method followed by annealing. The hydrogen storage properties, hydriding/dehydriding kinetics and electrochemical characteristics of this material are investigated.

3.2. SYNTHESIS OF Mg₂Ni ALLOY

The nano sized Mg–Ni alloy was prepared by chemical reduction using polyol process according to slightly modified procedure reported by Chen and Jehng (2004). In a

typical procedure, 0.027 moles magnesium acetate and 0.013 moles nickel acetate were dissolved in 150 ml of ethylene glycol with 2:1 mole ratio. Then 10 g of the poly (N-vinylpyrrolidone) (PVP) dissolved in 150 ml of ethylene glycol was added and stirred for 30 min. The resulting mixture was refluxed at 458–463 K. When the temperature had reached the set temperature of 453 K, refluxing is continued for an additional 10 min. PdCl₂ with 0.001 mole ratio (Pd/metal) dissolved in 10 ml ethylene glycol was further added and refluxing was continued for an hour at the set temperature. Pd acts as a nucleating agent for the growth of nanoparticles of Mg and Ni metals. Then the product was washed with absolute ethanol to remove the PVP and centrifuged at 6000 rpm for several times. The as synthesized Mg–Ni alloy was dried at 343 K in vacuum followed by annealing at 573 K in hydrogen atmosphere for 3 h.

3.3 RESULTS AND DISCUSSION

Polyol reduction method produces metal/alloy nanoparticles at low temperatures and hence this method is an efficient alternative method to high energy ball milling. During the polyol reduction process the dehydration of ethylene glycol takes place to form acetaldehyde. This acetaldehyde reduces the metal precursor to form metal nanoparticles and transforms into diacetyl as shown below (Fievet *et al.*, 1989).



Chen and Jehng (2004) prepared Mg-Ni alloys with various Mg/Ni ratios by polyol (ethylene glycol) reduction method in the presence of PVP. Higher temperatures beyond the boiling point of the ethylene glycol make the reduction complete and a suitable concentration of PVP can effectively avoid the aggregation of the particles.

Heterogeneous nucleation is achieved by the addition of a small amount of PdCl_2 to the medium, which is readily reduced to give Pd nanoparticles. These Pd nanoparticles act as nuclei for the further growth of the magnesium-nickel particles. However, the as synthesized material does not transform fully into Mg_2Ni alloy. Therefore it is necessary to anneal the as synthesized material to facilitate the formation of Mg_2Ni alloy.

The X-ray powder diffraction pattern of the Mg_2Ni alloy prepared by polyol reduction followed by annealing at 573 K in hydrogen atmosphere for 3 h is shown in Fig. 3.1. The main reflections are indexable in the hexagonal unit cell of the Mg_2Ni compound (space group P6222).

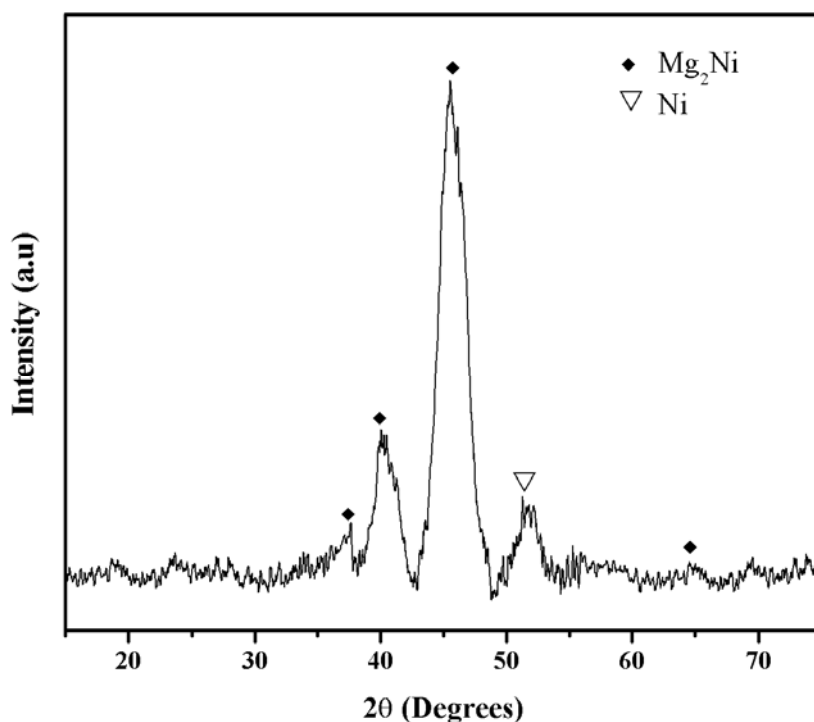


Fig. 3.1 XRD pattern of Mg_2Ni prepared by polyol reduction followed by annealing at 573 K for 3 h

The presence of unreacted Ni is detected by a small reflection at $2\theta = 52.1^\circ$. The broad peaks indicate that the alloy formed by this method is either nanocrystalline or

amorphous which is also confirmed by electron microscopy. Fig. 3.2 presents the TEM image of Mg₂Ni alloy after annealing. TEM image shows the agglomeration of particles and the average particle size of the nanocrystalline Mg₂Ni alloy is in the range of 50 ±20 nm.

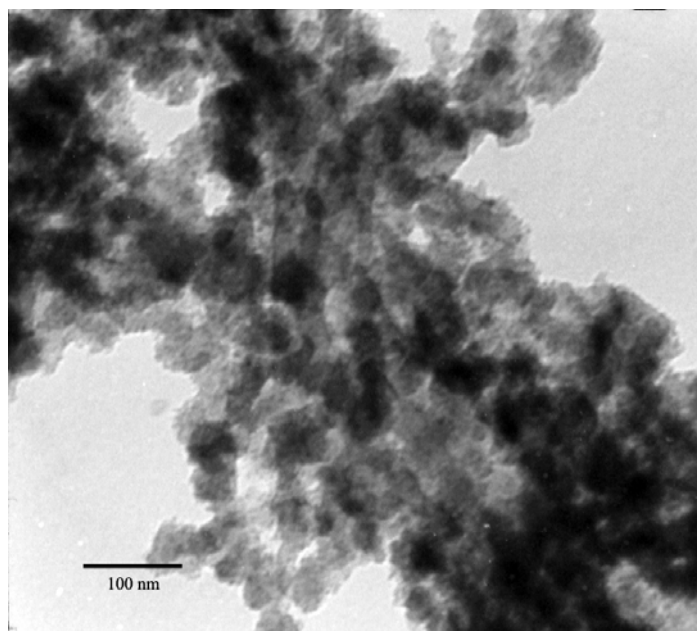


Fig. 3.2 TEM image of Mg₂Ni prepared by polyol reduction followed by annealing at 573 K for 3 h.

3.3.1 Kinetics

Usually hydrogen absorption kinetics of Mg₂Ni is very poor. Lot of efforts have been made to improve the kinetics, like surface modification, ball milling to induce lattice strain and milling with transition metal/metal oxide catalysts. The kinetic curves of hydrogen absorption at different temperatures and an initial pressure of 2.5 MPa for the Mg₂Ni, prepared by polyol reduction method followed by annealing, are shown in Fig. 3.3. In the case of the polycrystalline Mg₂Ni phase, for hydrogen absorption/desorption it requires high temperatures (higher than 573 K).

Conventional melted Mg_2Ni can only absorb hydrogen after more than 10 hydrogen absorption and desorption cycles as the activation process (Song *et al.*, 1984). However, at a temperature as low as 473 K, nanocrystalline Mg_2Ni prepared in this study is able to absorb and desorb hydrogen. One can see that the Mg_2Ni compound absorbs hydrogen quickly and reaches maximum within 1 min at 573 K. The hydrogen absorption curves shown in Fig. 3.3 are obtained after first hydrogenation and dehydrogenation cycle at 573 K. It is worth mentioning that the hydrogen absorption takes place even from the first cycle.

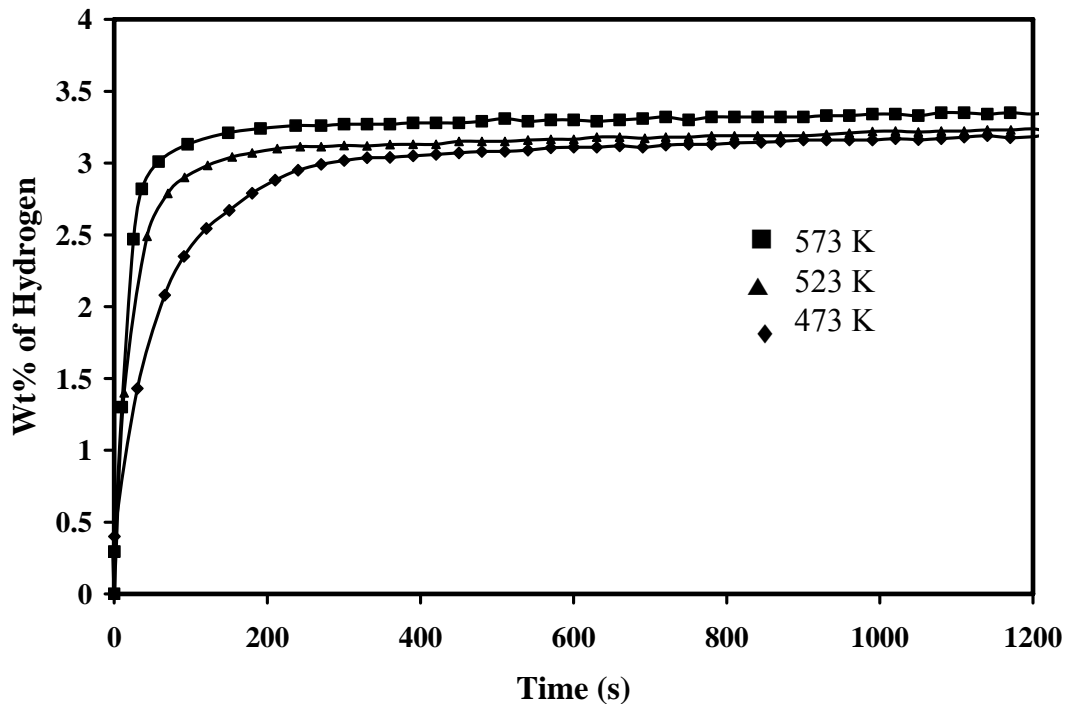


Fig. 3.3 Kinetic curves of hydriding of nano- Mg_2Ni at an initial pressure of 2.5 MPa and 473, 523 and 573 K

The hydrogen absorption rate is high due to the smaller size of the Mg_2Ni particles. Since large number of interfaces and grain boundaries are available, the diffusion of hydrogen atoms is easier in the alloy nanoparticles than in the bulk alloys. Moreover the presence of palladium (Zaluski *et al.*, 1995) added during the synthesis of alloy

and nickel nanoparticles (shown by the XRD) will facilitate the hydrogen absorption (Iwakura *et al.*, 1996). After 5 min the maximum hydrogen storage capacity of the obtained Mg₂Ni compound is about 3.0, 3.12 and 3.23 wt. % at 473, 523 and 573 K respectively.

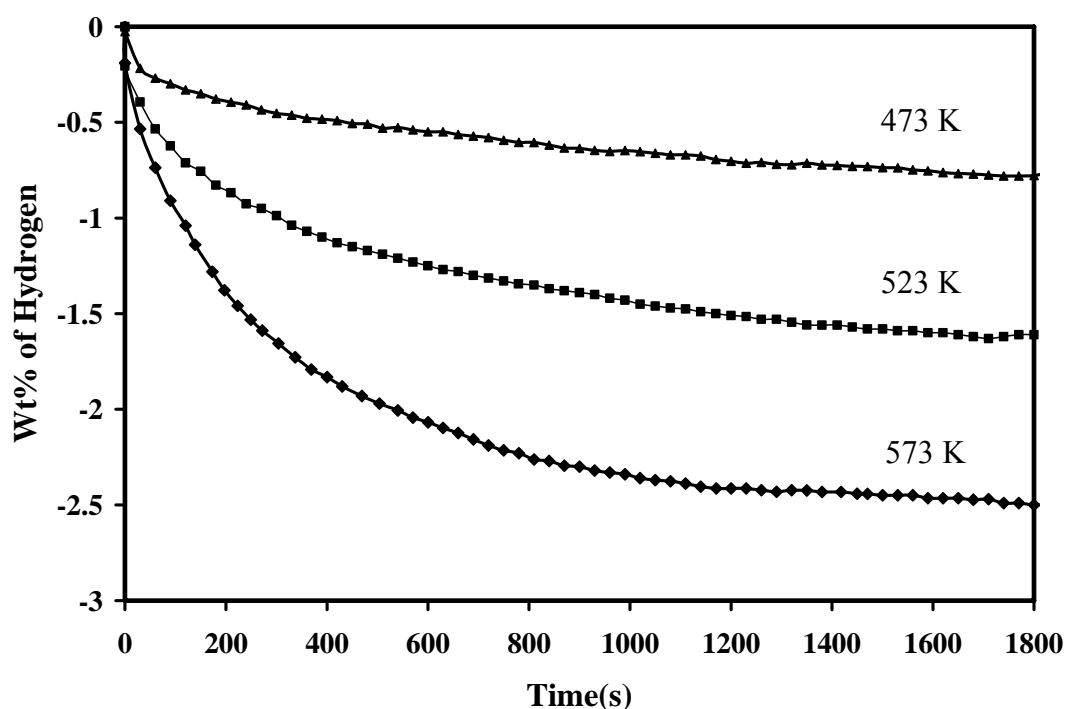


Fig. 3.4 Hydrogen desorption curves of nano-Mg₂Ni at a pressure of 10 kPa and 473, 523 and 573 K

The dehydriding kinetic curves for the Mg₂Ni alloy nanoparticles at different temperatures and a pressure of 10 kPa are presented in Fig. 3.4. The dehydriding kinetics is measured after the Mg₂Ni is fully hydrogenated at 573 K. As shown in Fig. 3.4 the material desorbs hydrogen even at 473 K. The rate of desorption is low at lower temperatures and increases with increasing temperature. Desorption rate is lower at temperatures below 523 K. Maximum amount of hydrogen desorbed is found to be 0.75, 1.61 and 2.5 wt. % at 473, 523 and 573 K respectively in 30 min.

3.3.2 Pressure-Compositions Isotherms

Fig. 3.5 shows the pressure composition isotherms of Mg_2Ni at 548, 573 and 603 K. Single sloping plateau is observed for absorption / desorption process indicating the presence of nanocrystalline / amorphous nature of the alloy. The absorption plateau for Mg_2Ni begins at 0.7 MPa and at a temperature of 603 K. The plateau with slope indicates that the absorption of hydrogen is by diffusion controlled mechanism as in the case of amorphous or nanocrystalline materials (Orimo and Fuji, 2001). The slope of plateau decreases with increasing temperature. The decrease in slope with increase in temperature may be due to increase in the crystallinity which reduces the lattice strain and amorphous nature of the alloy. The hydrogen absorption capacities are 2.8, 3.03 and 3.20 wt. % at 548, 573 and 603 K respectively.

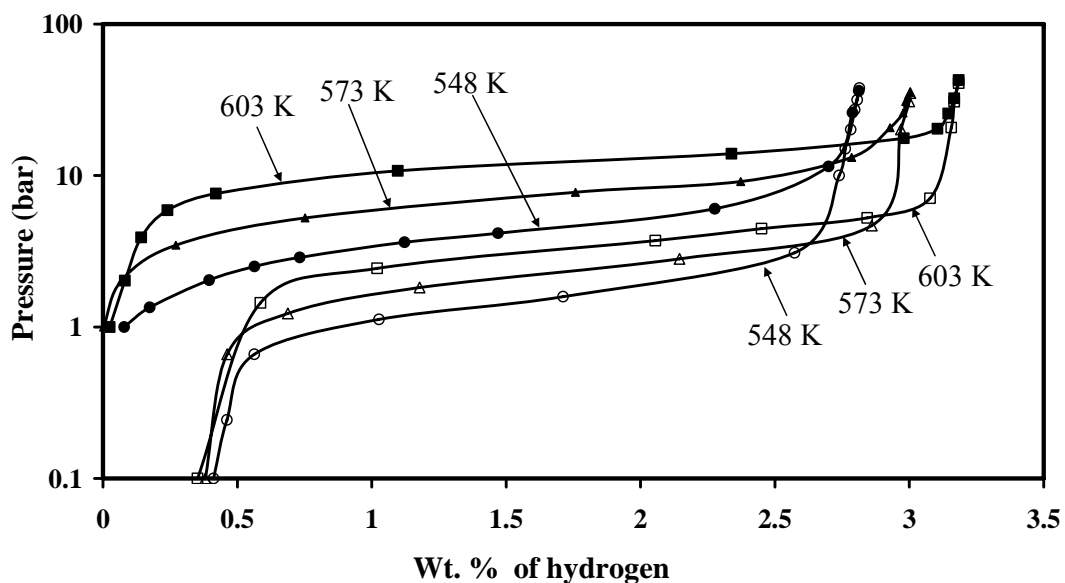


Fig. 3.5 Pressure-composition isotherms of nano- Mg_2Ni at 548, 573 and 603 K

The enthalpy (ΔH) and entropy (ΔS) change of hydride formation have been derived by utilizing van't Hoff, plot of $\ln P_{eq}$ vs $1/T$. van't Hoff plots for plateau region for

both absorption and desorption are shown in Fig. 3.6. The pressure data are obtained from the midpoint of plateau region from Fig. 3.5. The parameters, entropy and enthalpy change, are obtained using the least square technique from the slope and Y intercept of van't Hoff plots as shown in Fig. 6. The enthalpies and entropies of the Mg₂Ni prepared by polyol reduction and annealing at 573 K are given in Table 3.1.

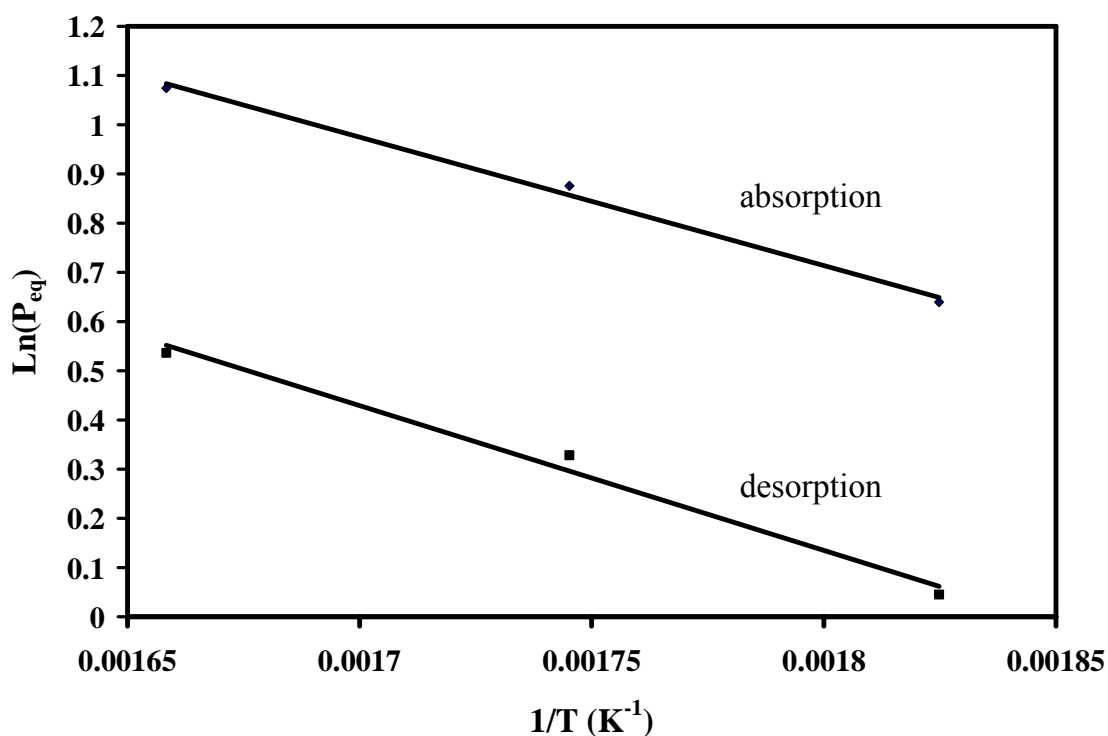


Fig. 3.6 van't Hoff plots for nano Mg₂Ni alloy absorption and desorption

Table 3.1 Enthalpies and Entropies of Mg₂Ni alloy

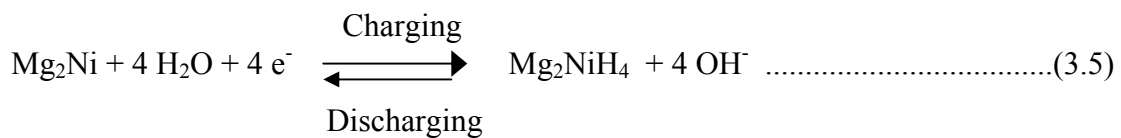
	Enthalpy change (kJ/mol)	Entropy change (J/(mol K))
Absorption	-50.03	-103.60
Desorption	56.35	105.36

3.3.3 Electrochemical characteristics

Electrochemical galvanostatic charge/discharge is a convenient method than a gas absorption technique for determining the hydrogen absorption capacity and thermodynamic parameters of a metal hydride at low temperatures. The discharge capacities of Mg₂Ni electrodes are calculated from the discharge current and the time required for reaching a potential of -0.6 V with respect to Hg/HgO, by using the following equation:

$$Q_{\text{discharge}} = I \times t \dots\dots\dots (3.4)$$

Where Q is discharge capacity (mA/g), I, discharge current (mA/g) and t is discharge time (h). The electrode is charged/discharged galvanostatically in 6 M KOH aqueous solution at room temperature. The electrochemical hydriding/dehydriding reaction taking place at Mg₂Ni hydrogen storage alloy electrode in an alkaline solution during charging/ discharging can be expressed as follows:



Hence each Mg₂NiH₄ molecule formed corresponds to the storage of 4 electrons. The typical discharge curves at the 1st cycle measured at discharge current densities of 20, 50, 100 mA/g are shown in Fig. 3.7. The discharge capacity decreases with increasing discharge current because of an increase in the over voltage. The maximum discharge capacity obtained is 408 mAh/g at a discharge current density of 20 mA/g in the first cycle. This is much more than that of polycrystalline Mg₂Ni reported previously (Cui *et al.*, 1995).

The increase in the discharge capacity is due to the formation of nanocrystalline / amorphous alloy by the polyol reduction which improves hydrogenation ability of Mg_2Ni electrode at low temperatures because the hydrogen diffusion in nanocrystalline or amorphous alloy is facile than the polycrystalline alloy.

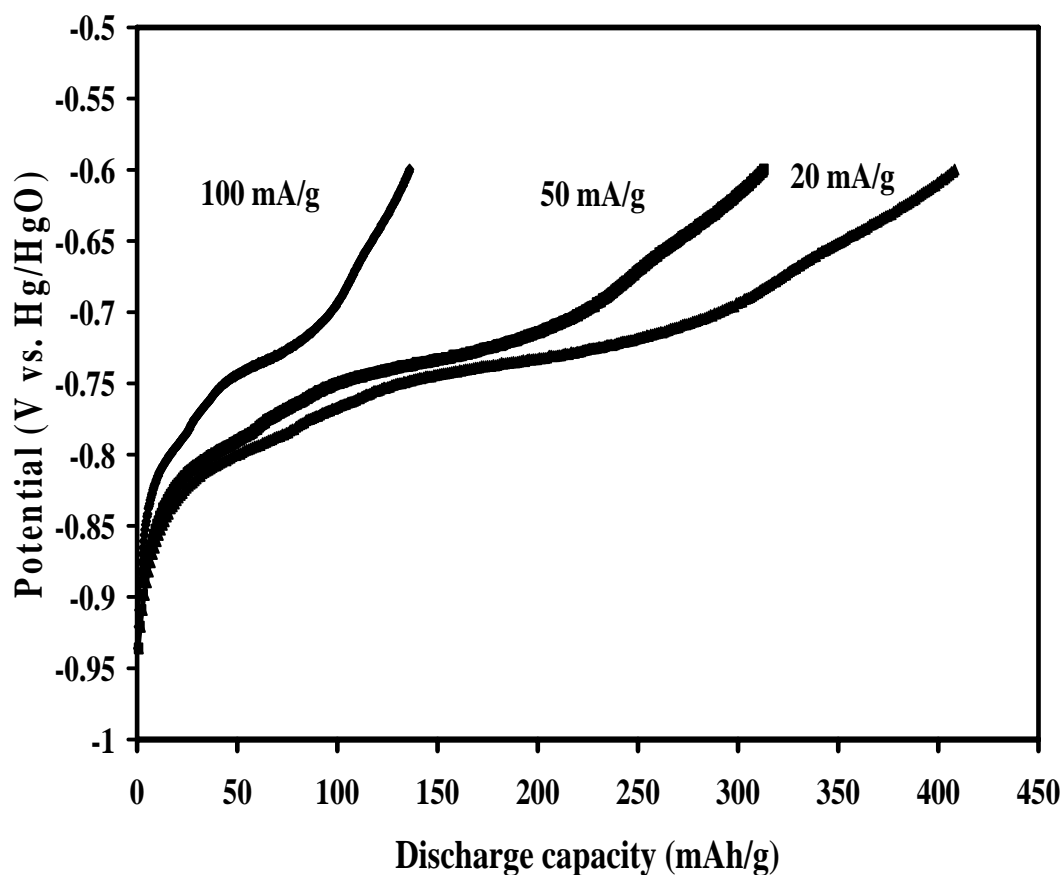


Fig. 3.7 Galvanostatic discharge curves of nano- Mg_2Ni at current densities of 20, 50 and 100 mA/g

Assuming that 4 hydrogen atoms are absorbed by one formula of Mg_2Ni alloy, the theoretical capacity is calculated to be 1000 mAh/g. For nanosized Mg_2Ni , maximum obtained discharge capacity is 408 mAh/g, which is only about 41% of the theoretical capacity. The surface of the Mg_2Ni alloy is usually contaminated by oxide and/or hydroxide when it is exposed to the KOH solution. This surface layer may inhibit the reduction of H^+ ions on the electrode surface. Hence oxide or hydroxide layer on the

surface of electrode reduces the growth of hydride phase in charging and migration of hydrogen to solution/electrode interface during discharging. Moreover the hydride formed at the surface will provide a barrier for hydrogen diffusion and hydriding of alloy will be slowed down. Since the diffusion of hydrogen into Mg_2Ni lattice is slow at lower temperatures the Mg_2Ni cannot be hydrided completely hence lower discharge capacity is obtained against the theoretical discharge capacity of 1000 mAh/g.

Fig. 3.8 shows discharge capacities at room temperature as a function of cycle number for the Mg_2Ni nanocrystalline alloy prepared by polyol reduction method. The initial discharge capacity is 408 mAh/g at a discharge current density of 20 mA/g. A large change occurs in discharge capacity for first 5 cycles and capacity decay is low in subsequent cycles. The cycling capacity of polycrystalline Mg_2Ni is low due to the magnesium in Mg_2Ni is easily oxidized in alkaline solution and $Mg(OH)_2$ passive film is formed (Liu *et al.*, 1997; Abe *et al.*, 2002).

In order to improve the cyclic stability, several modifications like elemental substitution, coating with palladium, nickel and carbon which will protect the alloy surface have been reported in literature (Rongeat *et al.*, 2006). It is observed that Ni coating is more effective in protection of the surface of the alloy. It can be seen (from Fig. 3.8) that the decrease in discharge capacity is low. The degradation is about 32% of maximum discharge capacity. This may be because of the coverage of small amount of palladium and nickel nanoparticles on the surface of Mg_2Ni , which improves the kinetics of hydrogen diffusion and also act as a protecting layer for the alloy.

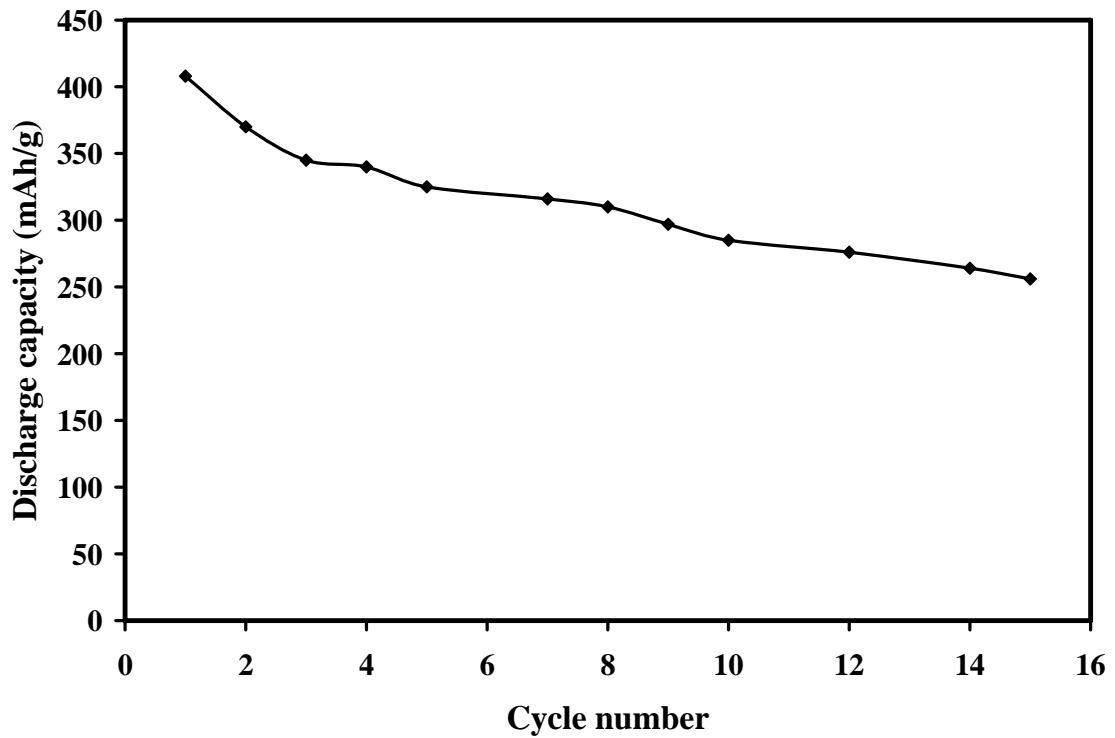


Fig. 3.8 Cycle test data of the nano-Mg₂Ni

The charge and discharge curves in galvanostatic mode are the electrochemical equivalents of the pressure-composition isotherms of the gas/solid-phase reaction. The electrode potential (E) measured in an electrochemical cell is related to the equilibrium pressure measured in the gas phase reaction. The E value of the metal hydride (MH) electrode in alkaline solution, measured with respect to the Hg/HgO reference electrode, is converted to the hydrogen equilibrium pressure, based on the Nernst equation. Taking the values of the standard potentials, the fugacity coefficient of hydrogen and the activity of water, for the MH electrode in 6 M KOH at 293 K, the relationship between E and P_{H₂} is as follows:

$$E \text{ (V vs. Hg/HgO)} = -0.932 - 0.0296 \log P_{\text{H}_2} \dots\dots\dots (3.6)$$

where E is the potential of MH alloy electrode in Volts and the P_{H₂} is the equilibrium hydrogen pressure in atmospheres (Iwakura *et al.*, 1989). From this equation the measured potential can be converted to pressure, obtaining the dependence of the

equilibrium pressure versus the amount of desorbed hydrogen, the so called electrochemical pressure-composition isotherms.

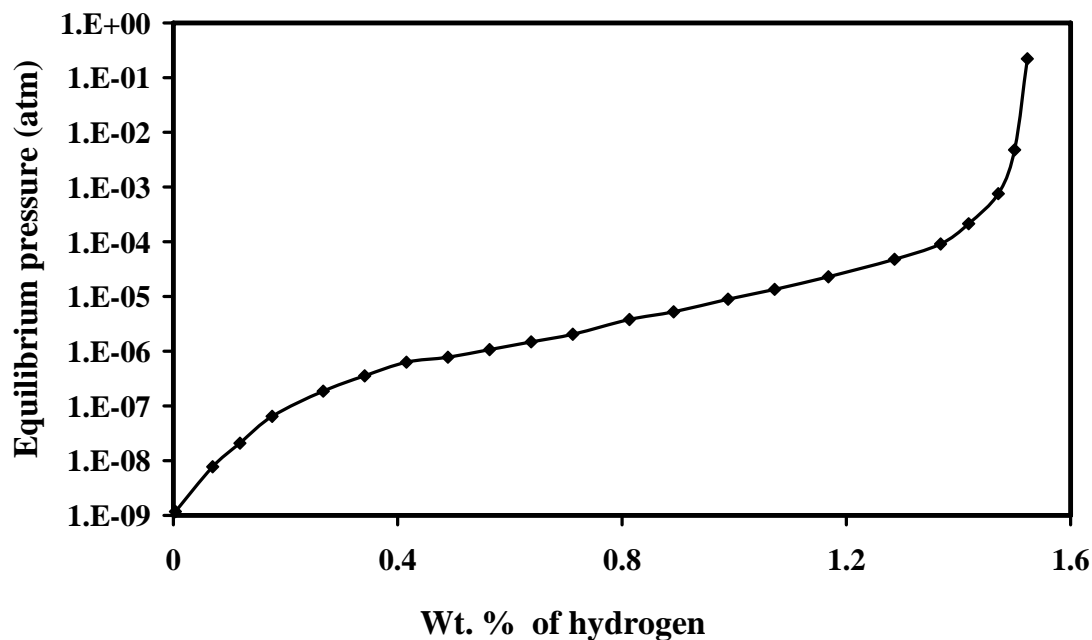


Fig. 3.9 Electrochemical pressure-composition isotherm at a discharge current density of 20 mA/g for the nano-Mg₂Ni alloy

The electrochemical pressure-composition isotherm for desorption of hydrogen is obtained from the equilibrium potential values of the electrodes, measured during intermittent discharge cycles at constant current density of 20 mA/g. Fig. 3.9 shows the pressure-concentration isotherm that is, theoretically derived from the equilibrium potential during the electrochemical measurement. The trend of the isotherm is the same as that obtained from volumetric measurements. Plateau of the electrochemical isotherm is not flat because of nanocrystalline/amorphous nature of the material. The maximum absorbed hydrogen amount is about 1.5 wt. %.

CHAPTER 4

DEHYDRIDING BEHAVIOR OF CARBON ADMIXED LiAlH_4

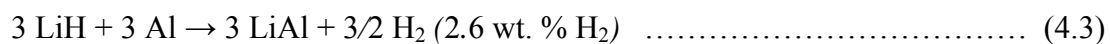
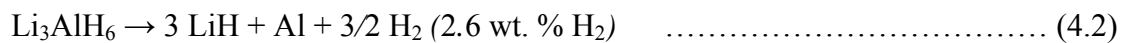
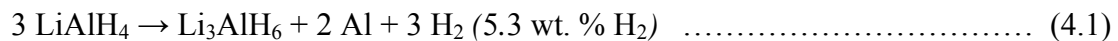
4.1 INTRODUCTION

Aluminum-based complex metal hydrides such as sodium and lithium aluminum hydrides (NaAlH_4 and LiAlH_4) attract considerable attention as potential high-capacity hydrogen storage media because their hydrogen content reaches 7.4 and 10.5 wt. % by weight, respectively.

Bogdanovic and Schwickardi (1997) reported the adsorption and desorption pressure-concentration isotherms for catalyzed NaAlH_4 at temperatures of 453 K and 483 K. The isotherms exhibit no hysteresis with a nearly horizontal plateau pressure region. Furthermore, the catalyzed system reversibly absorbed and desorbed hydrogen up to 4.2 wt % and the mechanism of the two-step desorption reaction was delineated. Following this, there have been efforts aimed at the utilization of NaAlH_4 and related hydrides with high gravimetric hydrogen storage capacity as practical hydrogen storage materials. Advancements have been made in accelerating the kinetics of solid state NaAlH_4 dehydrogenation and rehydrogenation through modification by dopant compositions and processing conditions (Bogdanovic and Schwickardi, 1997; Bagdonavic *et al.*, 2000; Gross *et al.*, 2002; Sun *et al.*, 2002; Miesner *et al.*, 2002; Sandrock *et al.*, 2002; Bagdonavic *et al.*, 2003; MajZoub *et al.*, 2003). Unfortunately, only 5.5 wt% of the hydrogen in NaAlH_4 can be released under reasonable conditions. The hydrogen content of LiAlH_4 is higher than that of NaAlH_4 and, therefore, may have sufficient reversible hydrogen content to be applied practically.

To date, the main focus has been on NaAlH₄, although it does not fully meet the DOE targets for gravimetric hydrogen storage and thermodynamics. LiAlH₄, on the other hand, has a higher gravimetric hydrogen storage capacity. Thermodynamics allows hydrogen desorption at 0.1 MPa pressure and at a temperature of 373 K. But LiAlH₄ has not yet been investigated as thoroughly as NaAlH₄. In the present study, the focus is on LiAlH₄ with carbon additives.

Lithium alanate, LiAlH₄, was first synthesized in 1947 (Finholt *et al.*, 1947) and is used as a reducing agent. Its total hydrogen storage capacity is approximately 10.6 wt. % desorbed in a three-step decomposition reaction, as given in the reaction scheme (Dilts and Ashby, 1972; Dymova *et al.*, 1994; Wiench *et al.*, 2004; Grochala and Edwards, 2004; Balema *et al.*, 2000a):



Reactions 4.1, 4.2 and 4.3 occur with a theoretical hydrogen release of 5.3 wt. %, 2.6 wt. %, and 2.6 wt %, respectively. However, due to the thermodynamic stability of LiH, i.e. high decomposition temperature, only 7.9 wt. % hydrogen is considered accessible for practical applications.

In dehydrogenation, reaction 4.1 occurs around 423-493 K (Dymova *et al.*, 1994; Balema *et al.*, 2000a) and is initiated by the melting of LiAlH₄ (endothermic), which is subsequently transformed into solid Li₃AlH₆ and Al during release of hydrogen. Second reaction (4.2) takes place around 463-533 K (Dymova *et al.*, 1994; Blanchard

et al., 2004). Reaction 4.3 (endothermic) proceeds at elevated temperatures around 623-673 K (Blanchard *et al.*, 2004; Resan *et al.*, 2005) and is probably followed by the formation of a Li-Al alloy (Wiberg and Amberger, 1971; Blanchard *et al.*, 2004; Kang *et al.*, 2004).

Reaction 4.1 is an exothermic process with an ΔH of -3 to -10 kJ/(mol H₂) and reaction 4.2 is endothermic with ΔH of 27 to 40 kJ/(mol H₂) (Dymova *et al.*, 1994; Smith and Bass Jr., 1963; Lovvik *et al.*, 2004; Chen *et al.*, 2001; Chung and Morika, 2004). Reaction 4.3 is an endothermic process with ΔH of 140 kJ/(mol H₂).

Experiments have demonstrated that reaction 4.1 may proceed spontaneously at room temperature directly from solid LiAlH₄ during prolonged storage (Dymova *et al.*, 1994). ²⁷Al NMR has also demonstrated direct decomposition of solid LiAlH₄ into Li₃AlH₆ at 423 K (Wiench *et al.*, 2004). LiAlH₄ is usually not considered as a candidate for on-board reversible hydrogen storage because the formation of LiAlH₄ from LiH + Al is difficult under moderate reaction conditions, due to its high plateau pressure. But it can be rehydrogenated off-board. On the other hand, Li₃AlH₆, which can be synthesized from LiH and LiAlH₄ by mechano-chemical treatment (Chen *et al.*, 2001; Balema *et al.*, 2000b; Zaluski *et al.*, 1999) with a theoretical hydrogen capacity of 5.6 wt. % H₂ shows reversibility at only 40 bar hydrogen (Chen *et al.*, 2001).

Doping with VCl₃ (Blanchard *et al.*, 2004) and TiCl₃.1/3 AlCl₃ (Chen *et al.*, 2001) results in a lowering of the decomposition temperature of both the reactions 4.1 and 4.2. Doping with TiCl₃.1/3 AlCl₃ has also been shown to facilitate isothermal dehydrogenation at temperatures in the range of 373-548 K at a time scale of 50 min

to a few hours (Chen *et al.*, 2001). Ball milling of pure LiAlH_4 decreases the decomposition temperature of reactions 4.1 and 4.2 (Resan *et al.*, 2005). Pure LiAlH_4 does not decompose during ball milling at ambient temperatures (Balema *et al.*, 2000a), whereas LiAlH_4 doped with catalytic additives e.g. TiCl_3 , TiCl_4 , VCl_3 and FeCl_3 rapidly decomposes during milling (Blanchard *et al.*, 2004; Balema *et al.*, 2000b; Balema *et al.*, 2001).

Improvements in the hydrogen desorption/absorption kinetics of metal hydrides upon milling with carbon has been reported (Zaluska *et al.*, 2002; Imamura *et al.*, 2002; Pukazhselvan *et al.*, 2005; Wang *et al.*, 2005; Dehouche1 *et al.*, 2005), suggesting that carbon plays a catalytic role. The catalytic effect of carbon on the dehydrogenation properties of alanates has been evaluated to a limited extent and there is no clear understanding in the role of catalyst in improving decomposition kinetics of alanates. This serves as main motivation for studying dehydrogenation kinetics of LiAlH_4 -C composites.

The purpose of this study is to improve the understanding on how additives, in particular, carbon, affect the dehydrogenation kinetics of alanates. The kinetics of dehydrogenation of LiAlH_4 -Carbon composites is investigated by carrying out isothermal experiments below the melting point of LiAlH_4 . The effect of carbon content on dehydrogenation kinetics was investigated. Further, the catalytic effect of carbon nanofibers on dehydrogenation kinetics was investigated. In order to extract parameters for dehydrogenation reaction, Johnsen-Mehl-Avrami (JMA) model is used, and kinetic parameters are obtained by fitting the experimental data.

4.2 EXPERIMENTAL

Lithium aluminum hydride, LiAlH_4 (purity 95% minimum, typically 97%), in powder form was purchased from Sigma-Aldrich. Four different types of carbons, Vulcan XC72R ($250 \text{ m}^2 \text{ g}^{-1}$), Black Pearls 2000 ($1500 \text{ m}^2 \text{ g}^{-1}$), CDX 975 ($240 \text{ m}^2 \text{ g}^{-1}$) and Mesoporous carbon ($1400 \text{ m}^2 \text{ g}^{-1}$) were used as received. Carbon nanofibers were synthesized by using Ni-Cu catalyst.

4.2.1 Synthesis of carbon nanofibers (CNFs)

The zeolite supported catalyst Ni-Cu (70:30 at. %), was prepared by the incipient wetness impregnation method (Chidambaram and Viswanathan, 2007). The metal content was 10 wt. % with respect to the support. In a typical process, aqueous solutions of nickel nitrate (99%, Merck) and copper nitrate (99%, Merck) were added to an aqueous suspension of H-ZSM-5 (Ranbaxy). pH of about 8.5-9.0 was maintained by using ammonium bicarbonate (98%, Merck). The mixture was stirred for 24 h at room temperature followed by heating to evaporate the water till dryness and cooled to room temperature. The catalyst was placed in a quartz boat located in the middle of the quartz reactor. The catalyst was then calcined under air atmosphere at 773 K for 12 h and reduced in hydrogen atmosphere at 623 K for 3 h.

Around 100 mg of catalyst was placed on a quartz boat and given a reduction treatment in hydrogen atmosphere at 873 K for 30 min. After reduction, $\text{C}_2\text{H}_4/\text{H}_2$ (4:1) gas mixture was introduced into the reactor at a flow rate of 100 ml/min for 1.5 h. After completion of the deposition, reactor was allowed to cool to room temperature in the presence of argon flow. To remove all the metallic inclusions, the synthesized CNFs were treated with 20% HNO_3 (Ranbaxy) for 24 h and 48% HF (Merck) for 24 h to remove zeolite matrix, then washed with water and dried at 373 K for 8 h. This was

followed by air oxidation at 773 K for 4 h to remove the amorphous carbon (Colomer *et al.*, 1999).

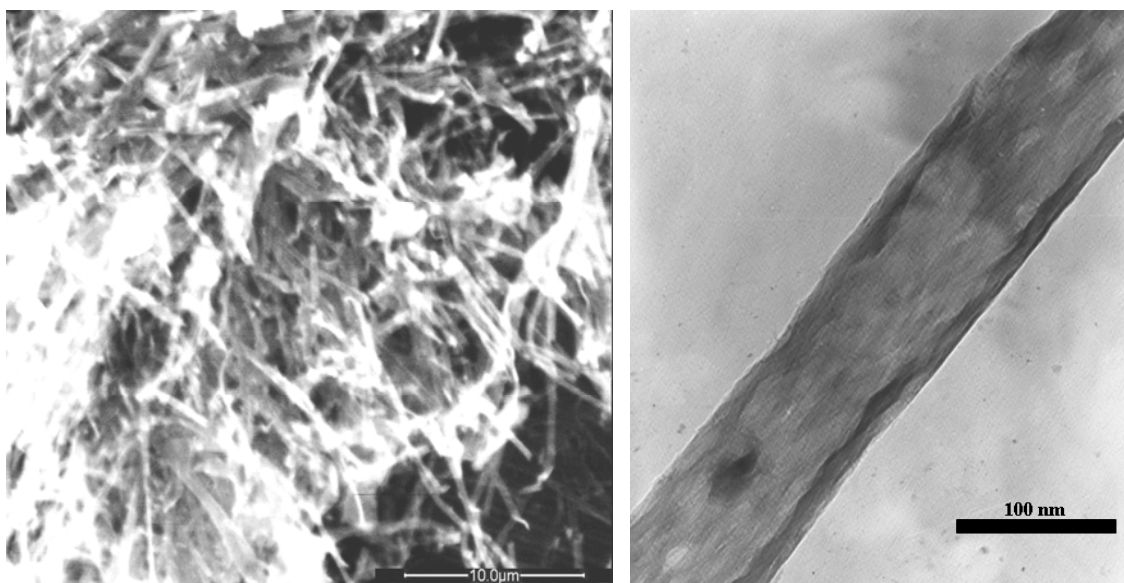
4.2.2 Preparation of carbon admixed LiAlH₄

All material handlings (including weighing and loading) were performed in a glove box with a carefully controlled atmosphere, with low oxygen and water vapour content. Typically 2 g of LiAlH₄ was admixed with 5 wt% of carbon by mechanical milling under argon atmosphere for 45 min. The milling experiments were performed in a Fritsch P5 planetary ball mill at a speed of 300 rpm using WC vial and WC steel balls. Ball-to-powder weight ratio is 15:1. After ball milling, the samples were transferred to the reactor in the glove box.

4.3 RESULTS AND DISCUSSION

4.3.1 Characterization of carbon nanofibers

For the synthesis of carbon nanofibers, Ni-Cu (7:3) alloy supported on H-ZSM-5 has been used as catalyst. Ni metal and Ni-Fe alloys have been recognized to be active for CNFs growth through the steps of carbonate precipitation, thermal decomposition into oxides, reduction to metal or alloys, conditioning with carbon source and hydrogen (Colomer *et al.*, 1999; Mestl *et al.*, 2001; Serp *et al.*, 2003; Best and Russell, 1954; Sinfelt *et al.*, 1972; Rodriguez, 1993). Further, finer catalyst particles are believed to improve the catalyst performance in CNFs synthesis (Park *et al.*, 1997, Perk and Baker 1998). Metals or their alloys have often been used in supported form on Al₂O₃, SiO₂, TiO₂ and zeolite, in which the physical and chemical interactions between metal precursors and support are expected to markedly decrease the particle size of catalyst. In general, a good homogeneity of catalytic components is assured in bimetallic catalysts prepared by co-precipitation method.



(a)

(b)

Fig. 4.1(a) SEM image (b) TEM image of purified carbon nanofibers

Several morphologies of carbon nanofibers have been reported in the literature, e.g. straight, bidirectional, twisted, helical and branched. In our preparation, we observed straight, rod type fibers as shown in SEM image (Fig. 4.1a). TEM image of CNFs produced over Ni–Cu (7:3) on the H-ZSM-5 at 873 K for 1.5 h from an ethylene/hydrogen mixture (4:1) are shown in Fig. 4.1b. As shown in figure, the diameter of the carbon nanofiber is around 90 nm and the length is above 10 μm . Thick fibers were observed with the diameter distribution in the range of 100–200 nm. The yield of CNFs obtained was 30 % with purity of 98%.

A typical XRD pattern of the synthesized carbon nanofibers is shown in Fig. 4.2. The high and low intense peaks at 2θ values of 26.0 and 43.5 respectively can be indexed to (002) and (110) diffraction planes of hexagonal graphite (JCPDS card files, no. 41-1487). The (002) diffraction peak is broad in shape suggesting that the prepared carbon nanofibers possess low graphitization and crystallization. Also, the broadening

of the graphite peaks indicates the existence of some disordered structures. No metal impurities were observed in the XRD pattern.

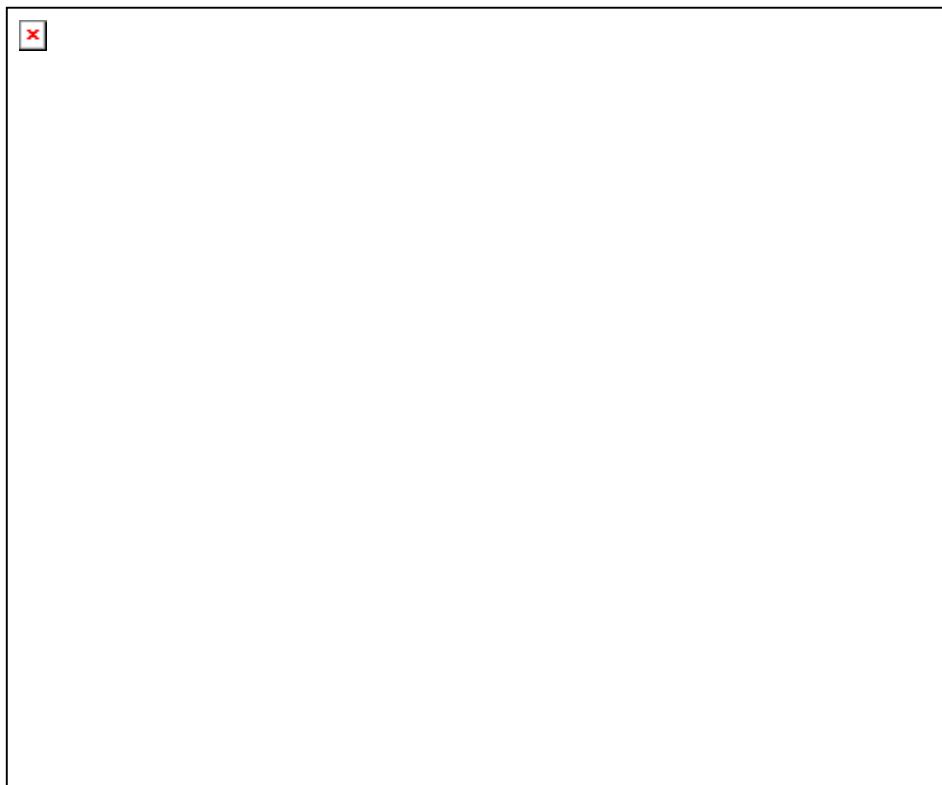


Fig. 4.2 X-ray diffraction pattern of the CNFs

4.3.2 Effect of carbon additives

Four different types of carbons were used as additives; 2 g of LiAlH_4 was admixed with 5 wt. % of carbon by milling for 45 min in argon atmosphere. For comparison, pure LiAlH_4 without any additive was milled for 45 min and the decomposition kinetics was followed at 403 K. The composites were characterized by powder X-ray diffraction. The samples for X-ray diffraction (XRD) studies samples were prepared in the glove box. To avoid exposure to air, the samples were covered with parafilm.

XRD patterns obtained from the carbon (Black pearls 2000 and CDX) admixed samples and that of pure LiAlH_4 are shown in Fig. 4.3. Broad peaks around 15° and

2θ values of 21.7° and 23.8° correspond to the parafilm. In the diffraction pattern of the as-received LiAlH_4 , peaks at 2θ values at 19.9° , 23° , 26.9° , 27.4° , 29.8° , 30.4° , 36.5° , 38.3° , 42.0° and 44.2° are attributed to the (100), (110), (012), (112), (121), (120), (031), (202), (210) and (221) planes of a monoclinic unit cell (P21/c) with unit cell parameters $a = 4.84$, $b = 7.82$, $c = 7.917$. The diffraction pattern of the LiAlH_4 after admixing with carbon (Black pearls 2000 and CDX) for 45 min closely resembles that of pure LiAlH_4 as seen from Fig. 4.3 with decrease in intensity of some planes.

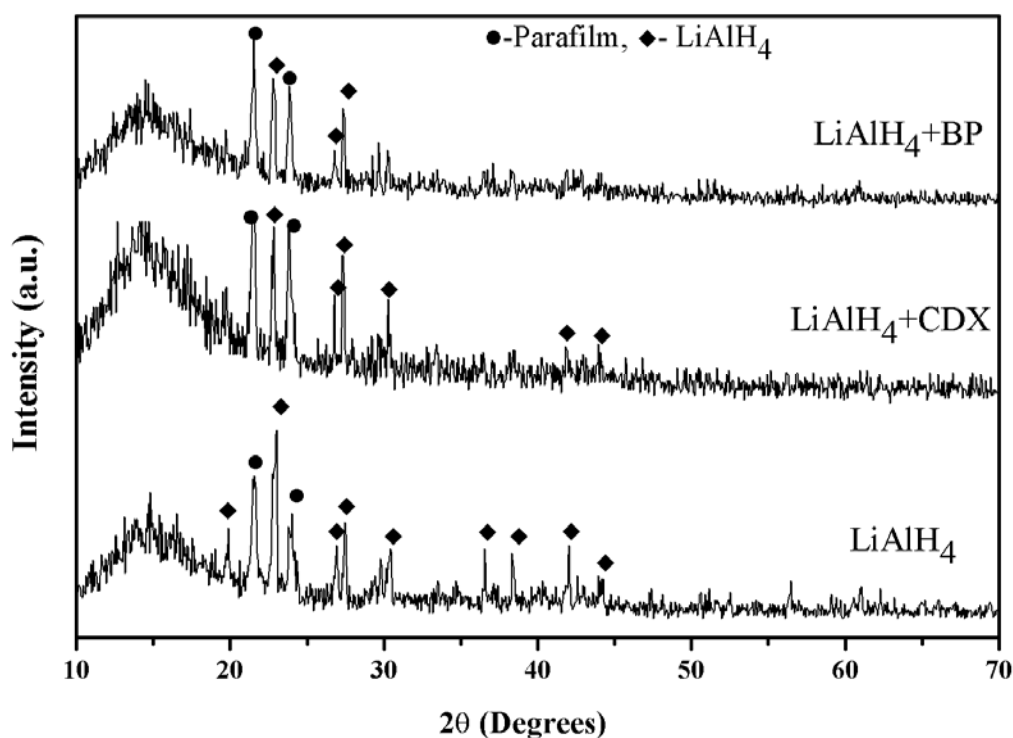


Fig. 4.3 X-ray diffraction patterns of as- received LiAlH_4 , Black pearls 2000 admixed LiAlH_4 and CDX admixed LiAlH_4

4.3.2.1 Dehydrogenation measurements for carbon admixed LiAlH_4

Zaluska *et al.* (2002) reported the improvement in the absorption and desorption kinetics by the addition of carbon. The effect of carbon on the dehydrogenation

kinetics is visualized by isothermal dehydrogenation curves for all LiAlH₄-C (Vulcan XC72R, Black Pearls 2000, CDX 975 and Mesoporous carbon) composite samples as shown in Fig. 4.4. Same isothermal dehydrogenation temperature was applied to all composites. For comparison the dehydrogenation kinetics of pure LiAlH₄ milled for 45 min, decomposed at the same temperature (403 K) was included as a reference. From the graph, it was observed that dehydrogenation kinetics improved considerably by addition of various carbon materials. The enhancement is nearly 4-5 times for the Black Pearls 2000, CDX 975, mesoporous carbon and ~2 times for the Vulcan XC-72R in comparison to pure LiAlH₄ (at 45 min). The dehydrogenation profile of the Vulcan XC-72R admixed LiAlH₄ resembles the as-received LiAlH₄ curve. On the other hand, the Black Pearls 2000, CDX 900, mesoporous carbon containing composites give higher rates significantly altering the curve profile. It suggests that the reaction does not follow the same mechanism in all the cases. It follows different paths in the case of Black Pearls 2000, CDX 975 and mesoporous carbon admixed LiAlH₄.

Among the four carbons, Black Pearls and CDX 975 show high desorption kinetics. The rate is higher for the mesoporous carbon in the initial stages and drops down slowly. The surface area and dehydrogenation rates for the corresponding four carbons used are given in Table 4.1. The rate is not directly proportional to surface area of the carbon. The order of dehydriding reaction rate is Black Pearls ~ CDX > mesoporous carbon > Vulcan XC72R. Hence the change in the rate cannot be solely attributed to the surface area of the carbon.

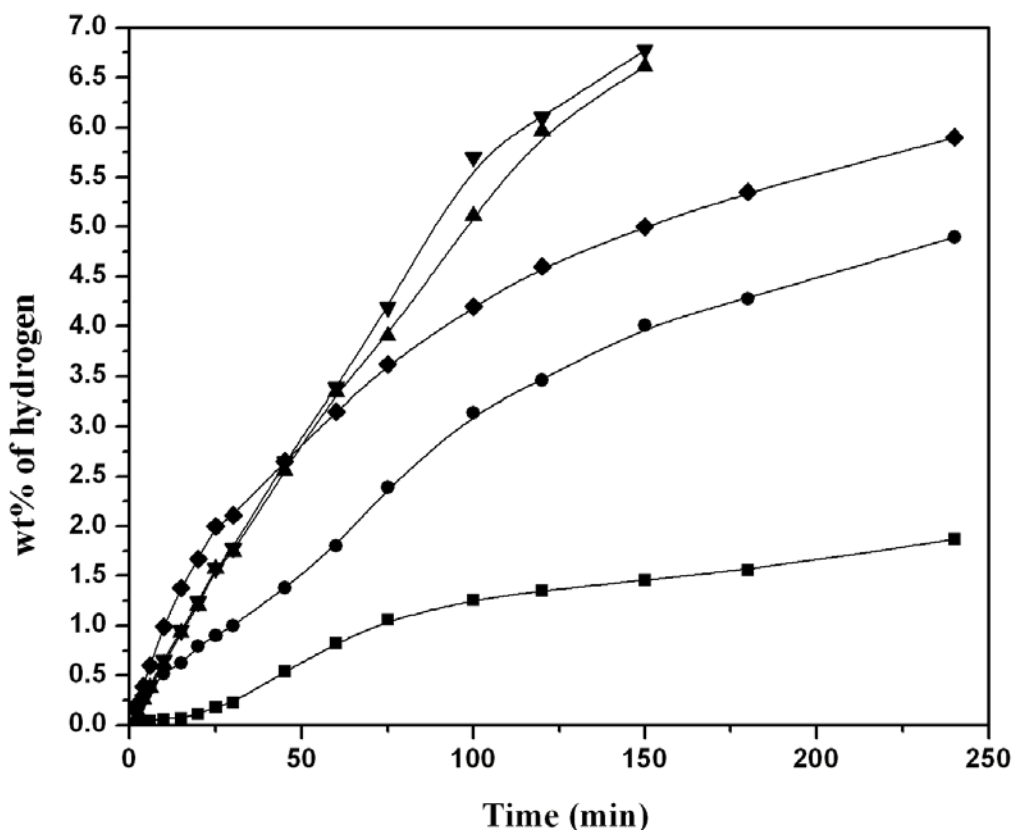


Fig. 4.4 Dehydrogenation profiles for the (■) pure LiAlH₄ (●) 5 wt. % Vulcan XC 72R admixed LiAlH₄ (◆) 5 wt. % mesoporous carbon admixed LiAlH₄ (▲) 5 wt. % CDX 975 admixed LiAlH₄ (▼) 5 wt. % Black pearls 2000 admixed LiAlH₄

Table 4.1 Surface area and dehydrogenation rate for various carbons

Carbon additive	Specific surface area (m ² g ⁻¹)	Dehydrogenation rate (wt. % min ⁻¹)
Black Pearls 2000	1500	0.053
Mesoporous carbon	1400	0.036
Vulcan XC72R	250	0.03
CDX 975	240	0.051

The effect of temperature on the dehydrogenation kinetics of Black pearls 2000 admixed LiAlH₄ is shown in Fig. 4.5. Activation energy for the decomposition reaction is calculated from Arrhenius equation. For Black pearls 2000 admixed

LiAlH₄ system, the activation energy is found to be 56 kJ/mol. Blanchard *et al.* (2005) reported apparent activation energy of 100 kJ/mol for reaction 4.1. Chen *et al.* (2001) investigated the dehydrogenation kinetics of TiCl₃.1/3AlCl₃ doped LiAlH₄. They found the apparent activation energy for the first step decomposition to be 43 kJ/mol.

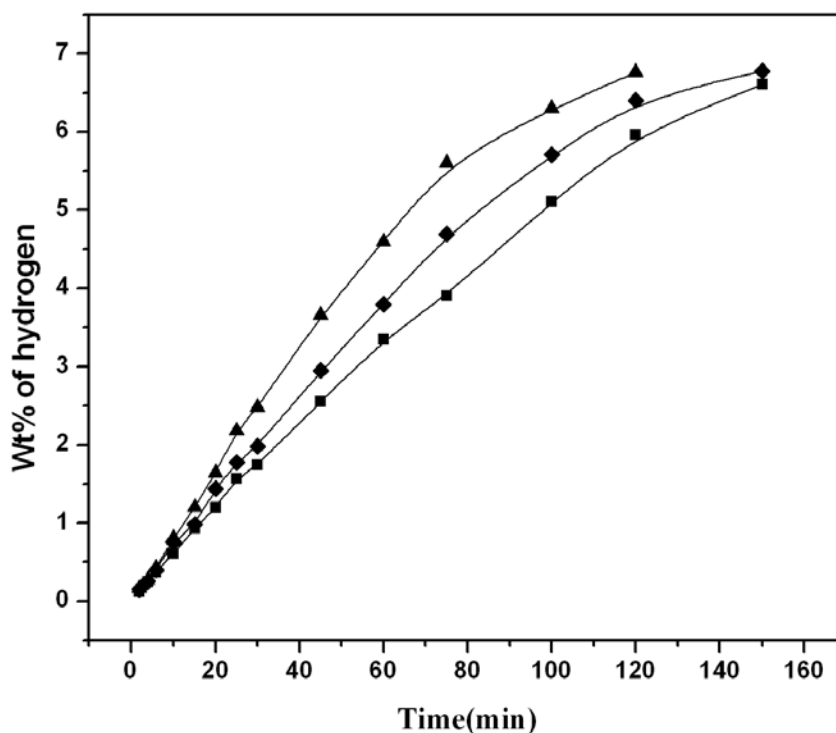


Fig. 4.5 Dehydrogenation kinetics of LiAlH₄ admixed with 5 wt. % of Black Pearls 2000 admixed LiAlH₄ at (■) 408 K (◆) 413 K (▲) 418 K

In order to find out the optimum level of mixing, dehydrogenation kinetics of LiAlH₄ with different amounts of carbon (3, 5, 7 and 9 wt. %) was studied. With an increase in the carbon content, the rate increases as shown in Fig. 4.4. 7 to 9 wt. % of carbon is sufficient to produce the enhancement in the dehydrogenation kinetics of LiAlH₄; further increase in carbon amount may lead to decrease in the total hydrogen capacity by adding weight to material.

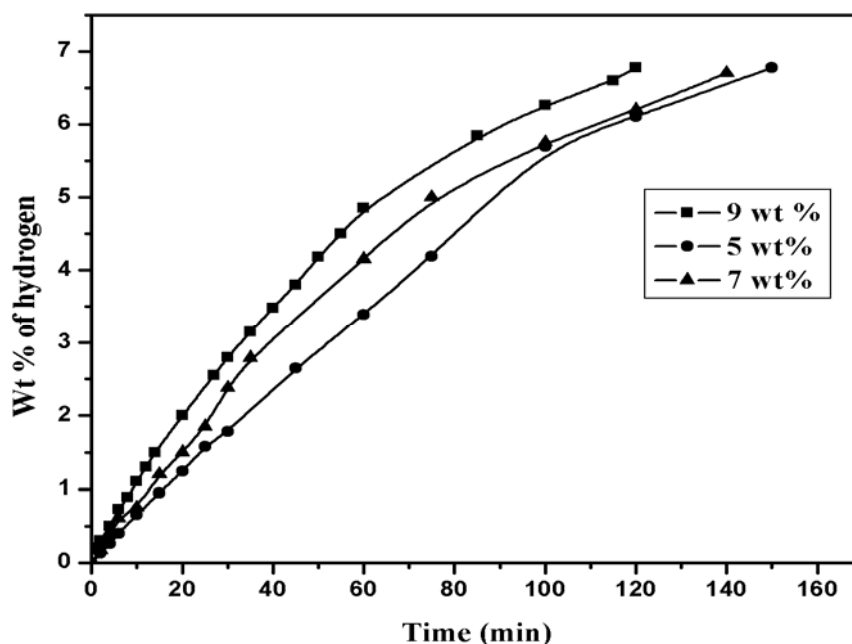


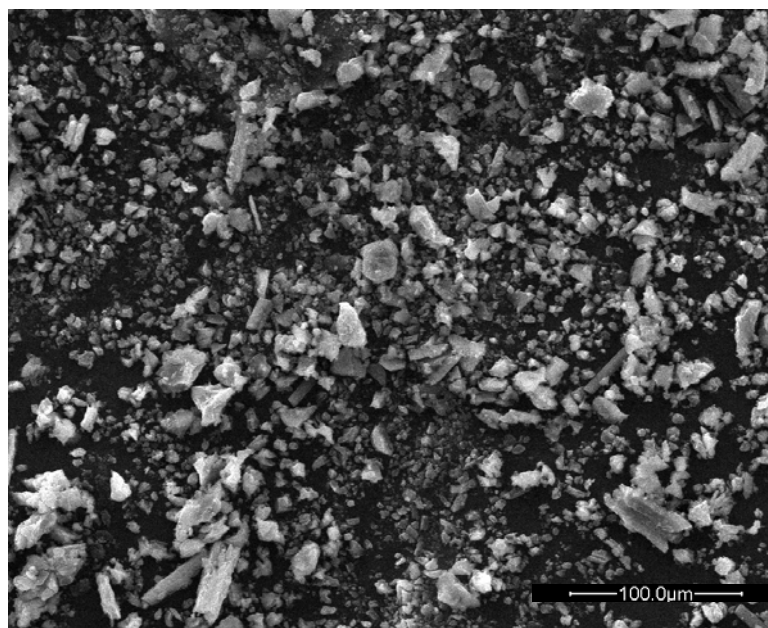
Fig. 4.6 Dehydrogenation kinetics of LiAlH_4 admixed with different (5, 7 and 9) wt. % of Black Pearls 2000

4.3.3 Effect of Carbon Nanofibers

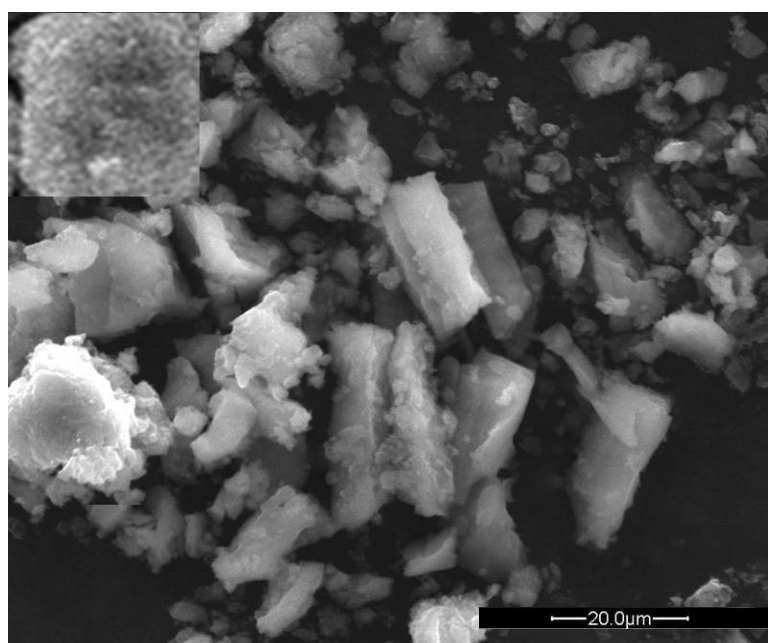
The fabrication and properties of carbon nanofibers are interesting because of their chemical similarity to carbon nanotubes (CNT) and their unique structure and potential for particular applications. CNFs have been used as catalysts in oxidative dehydrogenation of ethyl benzene to styrene (Mestl *et al.*, 2001). Carbon nanofibers are easier to manipulate than nanotubes and more susceptible to the air oxidation (Serp *et al.*, 2003). Compared to carbon nanotubes carbon nanofibers will have more active sites for catalytic use because of their greater disordered structure. Moreover the layered structure of the fibers facilitates fast hydrogen transfer.

Fig. 4.7a and Fig. 4.7b depict the scanning electron micrograph of the LiAlH_4 after ball milling with carbon nanofibers for 15 min. Particles with different shape and sizes ranging from about 1 to 30 μm were observed. This wide range in particle size is due to agglomeration of smaller particles during collisions between the balls which are normal (processes) in mechanical milling. Dispersion of alanate particles on the

surface of the carbon fibers is not clearly seen in SEM image (Fig. 4.7a). Since CNFs have been taken in catalytic amount, most of the fibers will be surrounded by alanate particles and cannot be seen clearly. Spotty surfaces of alanate have been noticed from the micrographs (Fig. 4.7b).



(a)



(b)

Fig. 4.7 SEM images of LiAlH_4 admixed with CNFs at (a) lower and (b) higher magnification

4.3.3.1. Dehydrogenation kinetics of CNFs admixed LiAlH_4 composite

The isothermal dehydrogenation kinetic traces of composite materials based on lithium aluminum hydride admixed with carbon nanofibers and Vulcan XC72R are shown Fig. 4.8. These curves were plotted by calculating the total hydrogen released (at 408 K under atmospheric pressure) in terms of weight percentage with respect to the dehydrogenation time under dynamic conditions. For comparison, the dehydrogenation kinetics of pure LiAlH_4 milled for 45 min, decomposed at the same temperature, 408 K is included.

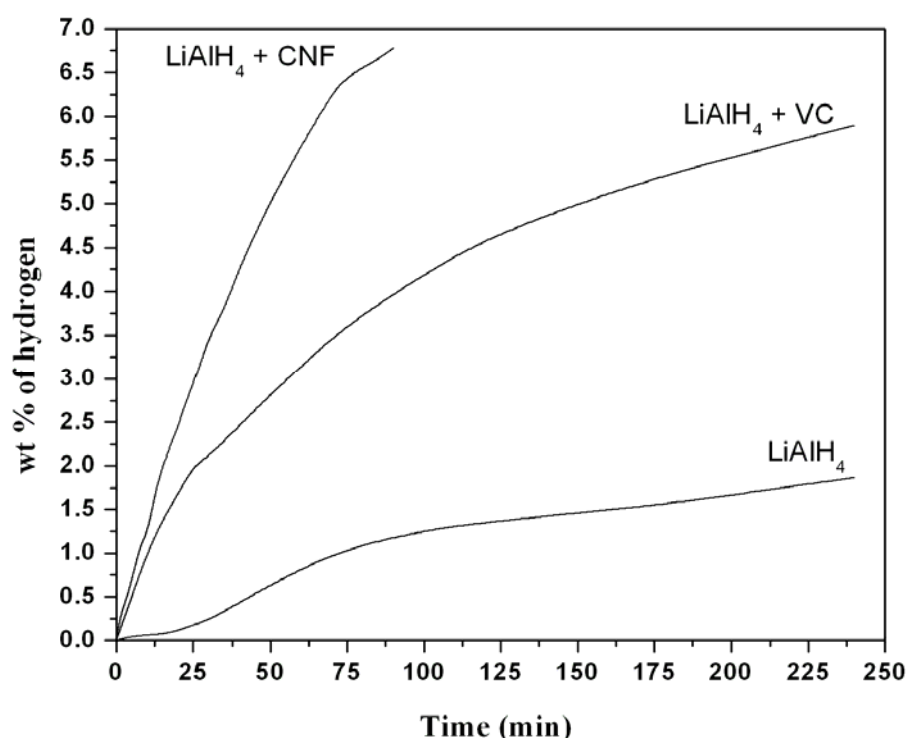


Fig. 4.8 Dehydrogenation kinetics of LiAlH_4 admixed with CNFs and LiAlH_4 admixed with Vulcan carbon and LiAlH_4

The dehydrogenation kinetics improved considerably by the addition of Vulcan XC72R carbon and remarkably with carbon nanofibers. Zaluska *et al.* (2002) observed similar result in the dehydrogenation kinetics of NaAlH_4 with carbon as an activator. As seen in Fig. 4.9, the decomposition is not stepwise, rather apparently, it

occurs simultaneous. In XRD pattern, after complete dehydrogenation, only peaks corresponding to the Al were observed. Diffraction peaks for the LiH were not seen (Fig. 4.9). This may be because of amorphous nature of LiH. The maximum released hydrogen from $\text{LiAlH}_4 + \text{CNFs}$ is found to be 6.8 wt. % of the composite, which is slightly lower than the theoretical limit even after correcting the observed hydrogen release with the purity of the sample. The decrease in maximum capacity may be due to partial decomposition of LiAlH_4 during mechanical milling with carbon nanofibers.

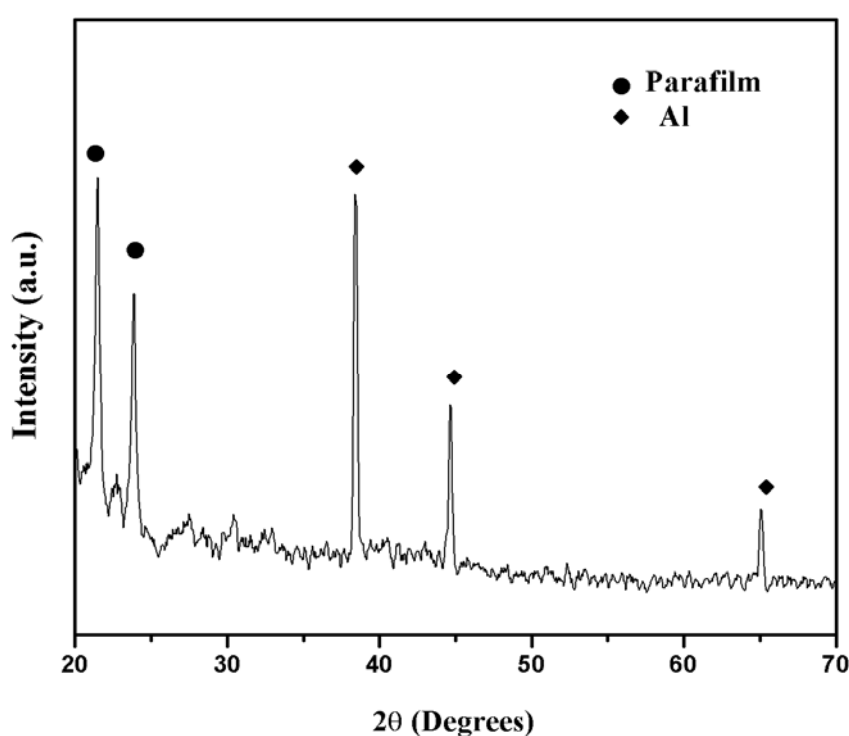


Fig. 4.9 X-ray diffraction pattern of the $\text{LiAlH}_4 + \text{CNFs}$ composite after dehydrogenation at 408 K

The effect of temperature on the dehydrogenation kinetics of carbon admixed LiAlH_4 is shown in Fig. 4.10. As the temperature increases, the rate also increases which is the case for many solid thermal decomposition reactions. Isothermal kinetic studies including Arrhenius analysis yield useful information on the basic effects of carbon catalysts.

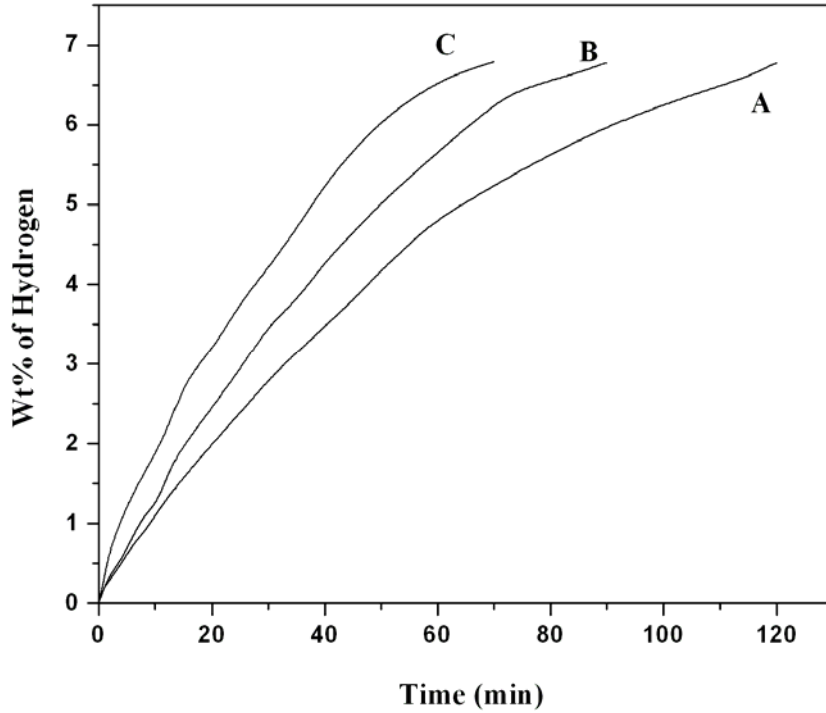


Fig. 4.10 Dehydrogenation curves at (A) 398 K (B) 408 K (C) 418 K for a LiAlH_4 sample admixed with CNFs

The study of the kinetics of solid-solid and solid-gas reaction is more complex than the study of homogeneous reactions. In the reactions of solids, various different processes overlap each other in the course of the reaction, making the isolation of different steps difficult regardless of the experimental technique used to follow the course of the reaction. As a consequence, the activation energy is to be seen as an overall one, and dependent on the extent of reaction. The kinetic model for nucleation and crystal growth in solids was formulated by Avrami (Avrami, 1939; 1940; 1941). The JMA model has been widely used to analyze solid-state kinetics, also of metal hydrides. It is derived from the nucleation and growth theory considering the number of nuclei or the nucleation rate as constant. The equation is as follows:

$$[-\ln(1-\alpha)]^{1/\eta} = kt \quad \text{or} \quad \alpha = \exp(-(kt)^\eta) \quad \dots\dots\dots (4.4)$$

where α is the extent of the reaction, which can be identified with a normalized hydrogen wt. % (range: from 0 to 1), t is the time, and k is rate constant and η is Avrami exponent (at constant temperature). Equation 4.4 can be written as

$$\ln(-\ln(1-\alpha)) = \eta \ln k + \eta \ln t \quad \dots\dots\dots (4.5)$$

According to equation 4.5, graph of $\ln[-\ln(1-\alpha)]$ vs. $\ln(t)$, so-called *double logarithmic plot* for isothermal experimental data results in a straight line. The Avrami exponent η is calculated from the slope of the regression line; and k , the rate coefficient, is calculated from the intercept. The value of η depends on the mechanism and dimensionality of nucleation and growth. For interface-controlled growth, η is an integer, and for diffusion-controlled growth, η takes either integer or half-integer values. The η value is assumed and the rate equation which best fits the observed data can be found for the appropriate value of η . When applying this model to LiAlH₄+CNFs composite, a good agreement between the fit and the experimental data is observed (Fig. 4.11). For LiAlH₄+CNFs composite, the Avrami exponent was determined as 1.15 by fitting the experimental data at 408 K indicating an interface controlled process with one dimensional growth. Fig. 4.12 shows the $\ln[-\ln(1-\alpha)]$ vs. $\ln(t)$ plot for LiAlH₄+CNFs composite decomposed at temperatures of 398, 408, 418 and 428 K. The k values are determined using the best-fitted lines. The values are given in Table 4.2.

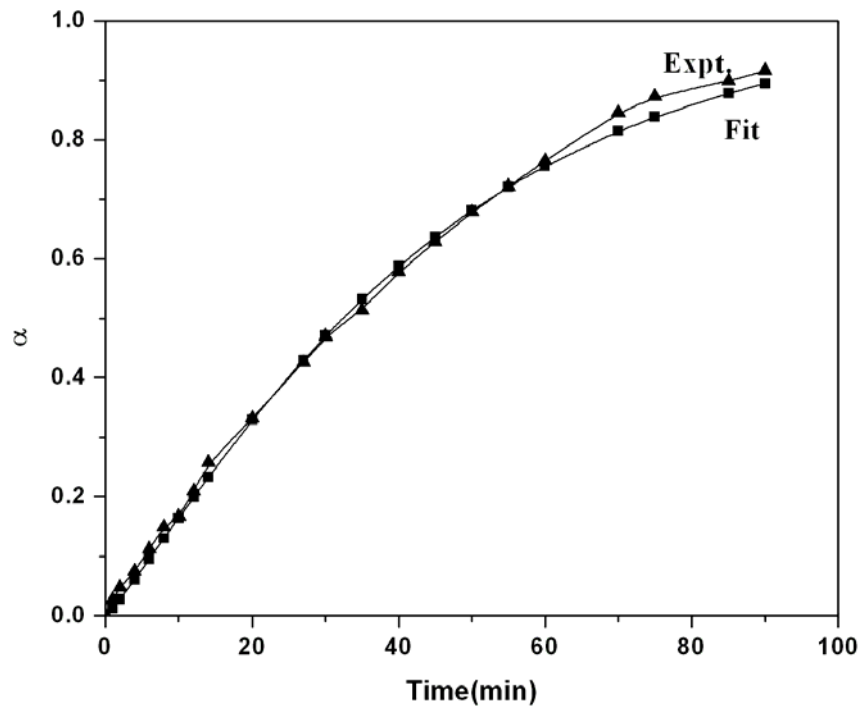


Fig. 4.11 Fit of the John-Mehl-Avrami model to experimental dehydrogenation data

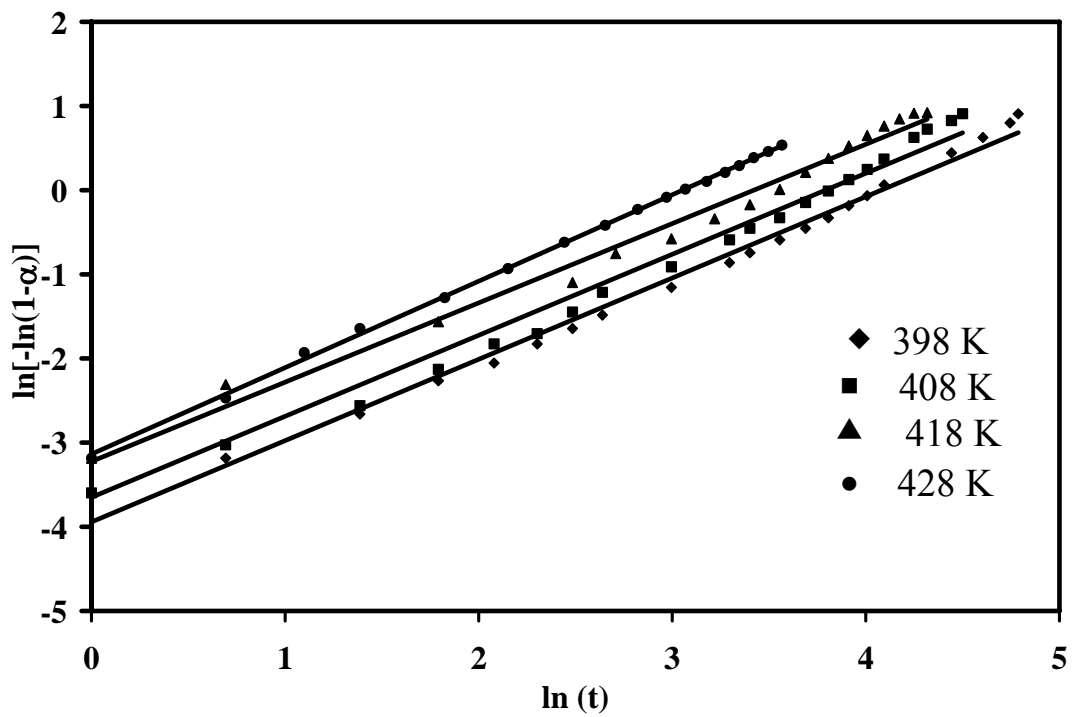


Fig. 4.12 Plot of $\ln[-\ln(1-\alpha)]$ vs. $\ln(t)$ at (\blacktriangle) 398 (\blacksquare) 408 (\blacklozenge) 418 and (\bullet) 428 K

The rate of decomposition depends on temperature, and can be described by the familiar Arrhenius-type equation. The plot of $\ln(k)$ against $1/T$ (Fig. 4.13) was made and the value of activation energy was calculated from the slope of the line. The activation energy E_a , obtained is 45 ± 0.2 kJ/mol. This value is of same order of the activation energy of 42.6 kJ/mol reported for LiAlH_4 with 2 mol% $\text{TiCl}_3 \cdot (1/3)(\text{AlCl}_3)$ (Chen *et al.*, 2001).

Table 4.2 Rate constants and Avrami exponents of LiAlH_4 +CNFs composite

Temperature (K)	Rate constant (s^{-1})	Avrami exponent
398	0.016913	0.99
408	0.022573	1.15
418	0.032644	0.94
428	0.043378	1.08

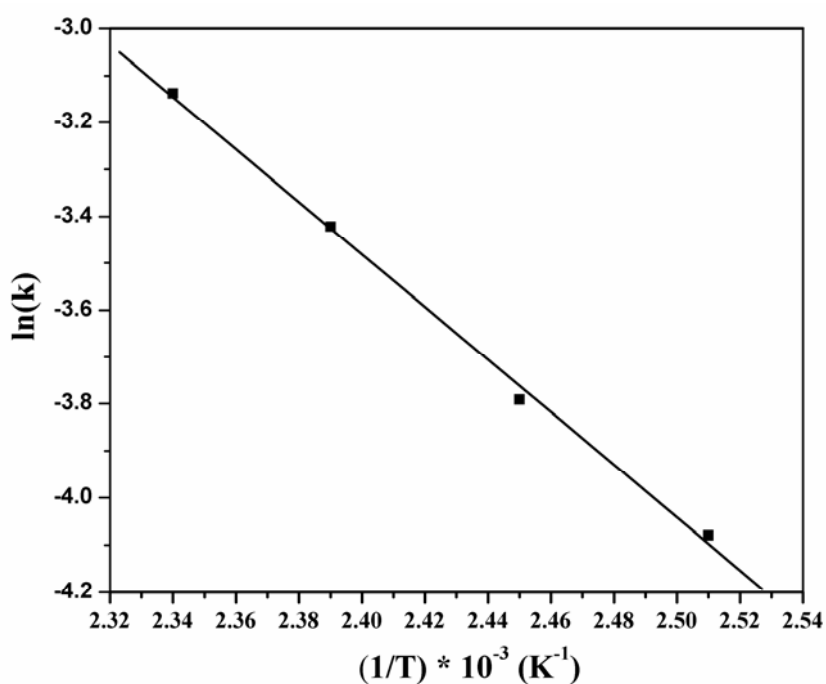


Fig. 4.13 $\ln k$ vs. $1/T$ for LiAlH_4 +CNFs composite

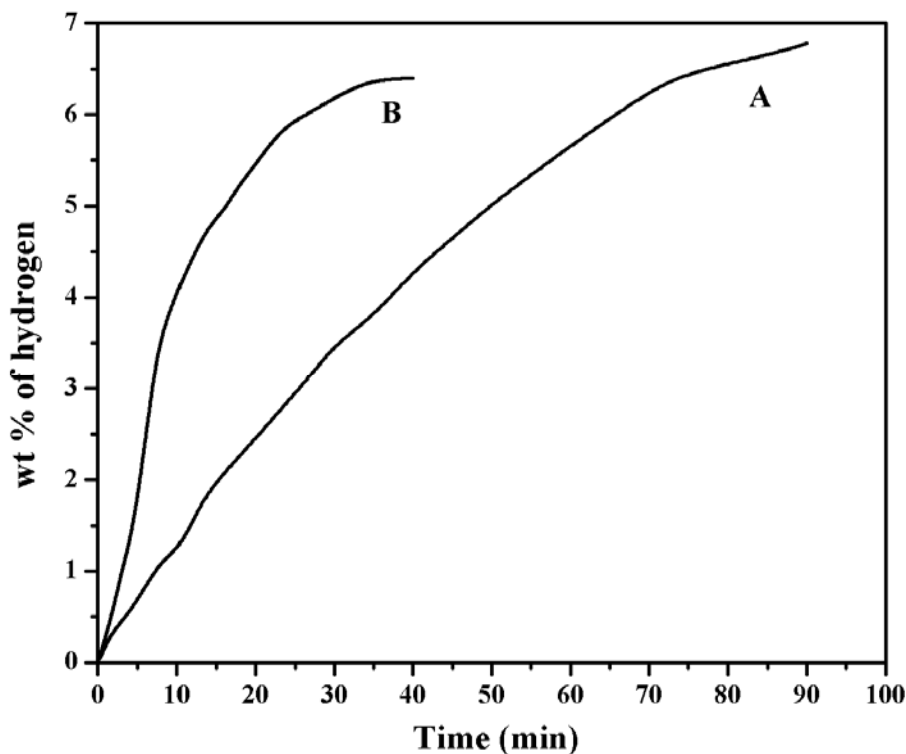


Fig. 4.14 Comparison of dehydrogenation curves for (A) LiAlH₄ doped with CNFs + 3 mol % VCl₃ and (B) LiAlH₄ admixed with CNFs at 398 K

Even though LiAlH₄+CNFs composite releases hydrogen at a fast rate compared to pure Lithium alanate, it is still not fast enough for the practical applications which require high hydrogenation and dehydrogenation rate. Transition metals proved to be better catalysts for the thermal decomposition of alanates, especially, vanadium for LiAlH₄. VCl₃ is a good catalyst for the dehydrogenation of LiAlH₄. In order to improve the kinetics further, CNFs admixed LiAlH₄ was co-doped with VCl₃. As expected, LiAlH₄ with CNFs and 3 mol% VCl₃ shows better desorption kinetics than LiAlH₄ with CNFs (Fig. 4.14). This is because of cumulative catalytic effect of CNFs and vanadium chloride on the kinetics of dehydrogenation.

To check the recyclability, after complete dehydrogenation the samples were subjected to rehydrogenation studies. In order to get the maximum amount of hydrogen rehydrogenated, the reactor was evacuated at 373 K and 1×10^{-3} mbar for

3 h and then pressurized with 2 MPa of hydrogen pressure at the temperature of 383 K for 6 h. The pressure fluctuation was monitored and the hydrogen storage capacity was calculated from the reduction in the pressure. The rehydrogenation of LiAlH_4 , doped individually with VCl_3 or CNFs was observed only to a smaller extent (0.9 wt. % for CNFs and 1.2 wt. % of hydrogen for VCl_3) where as LiAlH_4 doped with both VCl_3 and CNFs showed rehydrogenating capacity up to 3.9 wt. % under similar conditions.

4.3.4 ROLE OF CARBON IN THE DEHYDROGENATION KINETICS OF LiAlH_4

The nature of the active catalyst species in transition metal doped alanates has been a subject of interest. There is speculation and controversy in this aspect. It was initially suggested that the remarkable enhancement of the hydrogen cycling kinetics in Ti-doped NaAlH_4 was due to surface-localized catalytic species consisting of titanium metal or a Ti–Al alloy (Bagdonavic *et al.*, 2000; Gross *et al.*, 2002). Alternatively, Sun *et al.* (2002) reported the possibility of substitution of titanium into the hydride lattice. Evidence for both the presence of a Ti–Al alloy in the doped hydride (Bagdonavic *et al.*, 2003) and substitution of Ti into the bulk hydride lattice (Sun *et al.*, 2002; Sandrock *et al.*, 2002) was also reported. However, neither a catalytically active Ti–Al alloy nor evidence for well-characterized sites of lattice substitution has yet been obtained.

The results presented suggest that the grain/particle size and specific surface area of carbon are not the only key factors that are responsible for the improved hydrogen storage properties of carbon admixed alanates. Pukazhselvan *et al.* (2005) investigated the effect of carbon nanotubes on the cycling behavior of NaAlH_4 . But the reason for the enhancement in the kinetics was not clearly understood.

It is appropriate at this stage to summarize the observations and the postulates reported in literature on the effect of addition of carbon on the kinetics of hydrogenation and dehydrogenation of alanates.

The anxiety to modulate the adsorption and desorption process in alanate materials has led to a spate of studies involving additives especially carbon materials. These studies have thrown out a number of seemingly contradicting observations and postulates. These can be summarized as follows:

- Imamura *et al.* (2002) observed that the active composites as hydrogen absorber are formed only when ground with benzene or THF or cyclohexane. The role of these organic additives as envisaged by them is to facilitate the fracture along the graphite layers thus enhancing the particle size reduction in magnesium. It is to be remarked that the essentiality of the organic substrates has not been unambiguously re-established in subsequent studies.
- Zaluska *et al.* (2002) reported that NaAlH_4 or Na_3AlH_6 milled with carbon exhibited enhancement of kinetics of adsorption and desorption in terms of hydrogenation/dehydrogenation at lower pressures and temperatures (353 K) and faster kinetics. However, Shang and Guo (2004) observed that addition of graphite shows little influence on the desorption properties of MgH_2 . However, according to them, addition of graphite favored rapid rehydrogenation, which is attributed to the interaction between the crystalline graphite with hydrogen dissociation close to the MgH_2 or Mg surface. They also postulated that the presence of graphite could inhibit the formation of oxide layer on the metallic particles.

- Wang *et al.*(2005) reported that co-doping of NaAlH₄ with Ti-graphite improved the kinetics of both the first and second reactions of the decomposition of alanates by decreasing the temperature of reaction as much as 15 °C compared to the system without the addition of graphite. The kinetics of the dehydrogenation reaction also increased by 3-6 times depending on the temperature of the reaction. The role of graphite has been postulated to be both a mixing agent manifested through lubrication (graphene layer slippage and breakage) as well as a micro-grinding agent.
- Dehouche *et al.* (2005) have examined the effect of addition of SWNT with Ti/Zr doped NaAlH₄ and observed fast adsorption/desorption kinetics. They postulated that the creation of new hydrogen transition sites might be the factor responsible for the observed increase of the kinetics of absorption/desorption process.
- Pukazhselvan *et al.* (2005) showed that CNT admixed NaAlH₄ exhibited good rehydrogenation characteristics and also stated that 8 mol% CNT is the optimum material composition. The observed effects have been attributed to increased solid-gas surface area resulting from the presence of CNT.
- Darok *et al.* (2006) showed that the Mg thin films generated in presence of carbon contain lesser surface oxygen as compared to the thin film obtained from pure metal based targets. The presence of carbon (in other words lower oxygen content) facilitates the ex-situ hydrogenation of Mg based thin films. This observation agrees with the earlier observation of Shang and Guo (2004).
- Huang *et al.* (2007) reported that there is no significant difference in the hydrogen storage capacity; the composite containing graphite displayed

remarkable decrease in the desorption temperature. This observation is in agreement with those of Wang *et al.* (2005)

- Recently Balde *et al.* (2006) have stated that nano sized NaAlH₄ displayed improved hydrogen absorption and desorption characteristics compared to the bulk alanates.

Against this background and based on the results obtained, the hydrogenation and dehydrogenation behaviour of LiAlH₄ has been evaluated as follows:

During the mechanical milling, the carbon materials may get incorporated into the hydride matrix resulting in an increase in the phase boundary. Also, the nature of carbon fragments generated various SP hybridized valence forces. These hybridized orbitals can interact with hydrogen. In this sense, these additives can be considered to provide a transition site for the hydrogen. Moreover, the additives can have greater affinity for hydrogen compared to aluminum, thus destabilizing the Al-H bond. However, with transition metal additives, the tendency to form metal hydrides with hydrogen is probable, and hence the kinetics and storage capacity can be affected. While doping NaAlH₄ with Ti, possibility of formation of TiH₂ has been reported (Sandrock *et al.*, 2002; Majzoub and Gross, 2003). Thus, the loss of catalytic activity of Ti species upon cycling (Miesner *et al.*, 2002) can be due to the formation of Titanium hydride. Theoretical studies (Sankaran and Viswanathan 2006) suggest that under the experimental conditions employed, carbon cannot dissociate hydrogen while can bind with dissociated hydrogen and this facilitates the hydrogen sorption and desorption. Since carbon is anisotropic with only weak van der Waals forces accounting the bonding interaction between the individual graphene layers, the layers tend to slide past one over the other quite easily during the milling process. Therefore lithium aluminum hydride can be well dispersed within the layers of carbon. Hence,

the oxidation of hydride surface and the agglomeration of Al during the dehydrogenation process can be prevented. This is another advantage of using carbon as catalyst. Similarly, during the rehydrogenation process, hydrogen molecule was adsorbed on the carbon surface and dissociated into active hydrogen atoms, which would react with the LiH and Al to form alanates. Wang *et al.* (2005) studied the effect of graphite as a co-dopant. Recently, Dehouche *et al.* (2005) reported the effect of single walled nanotubes on cycling behavior of NaAlH₄. In both the cases, it is observed that hydriding and dehydriding kinetics improved significantly by the addition of carbon in addition to Ti and Zr. The increase in the catalytic activity of transition metals upon co-doping with carbon is due to the formation of bridged species for the transport of active species between the alanate and the additive particles. The exact nature of this carbon layer, which facilitates the transfer of hydrogen from the activating site to the storage site, is not yet known. This is similar to hydrogen spill-over promoted by water molecules. This speculation is further confirmed by the rehydrogenation studies of CNFs admixed LiAlH₄.

During the rehydrogenation process, hydrogen molecule was adsorbed on the catalyst surface and dissociated into active hydrogen atoms, which will be transferred through carbon nanofibers to react with the LiH and Al to form alanates. The model proposed needs further experimental support. Furthermore, the reduction of particle and crystallite size of LiAlH₄ during mechanical milling could have an influence on the dehydrogenation process. Particle size reduction leads to short diffusion paths for the hydrogen, and reduction of crystallite size enhances dehydrogenation kinetics due to the high density of grain boundaries which can act as nucleation centers for new phases.

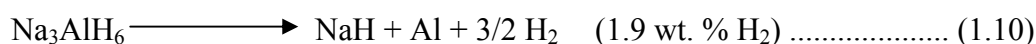
From SEM images of CNFs admixed LiAlH_4 (Fig. 4.7b) one can see that alanate particles are well dispersed on the surface of the carbon fibers. It is also noticed that agglomeration of some particles occurs due to the high energy ball milling. Mixing of alanates with carbon will increase the grain boundaries which ultimately help to improve the dehydrogenation kinetics. Therefore, they could improve the decomposition process of LiAlH_4 using high energy ball milling.

CHAPTER 5

HYDROGEN STORAGE PROPERTIES OF ALANATES ADMIXED NITROGEN CONTAINING CARBON NANOTUBES

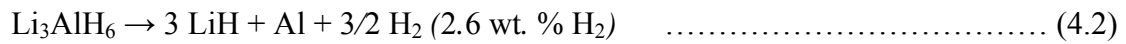
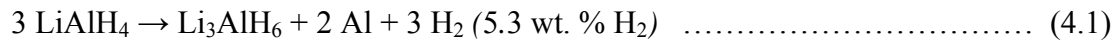
5.1 INTRODUCTION

Alkali metal aluminohydrides, like NaAlH₄ and LiAlH₄, have been considered as promising solid-state hydrogen storage materials because they are able to release reversibly 7.9 and 5.6 wt. % of hydrogen, respectively. However, pure alanates normally show poor kinetics, with dehydrogenation, taking place at temperatures well above 473 K, and reversibility only being achieved under high temperature and pressure conditions. Bogdanovic *et al.* (1997, 2000) showed that by the addition of small amount of Ti, NaAlH₄ can reach a reversible storage capacity of more than 5 wt. % in mild thermodynamic conditions. The dehydriding/hydriding reactions take place in two steps as follows:



Theoretically, the first reaction releases 3.7 wt. % of hydrogen, while the second reaction gives 1.9 wt%. Various attempts have been made in the past to facilitate (or even enhance the kinetic parameters or decrease the activation parameters) desorption process by addition of suitable materials that are conventionally termed as “catalysts”. The kinetics of the above reversible reactions of NaAlH₄ can be improved markedly by addition of suitable materials, such as Ti-based compounds. Other transition metals have also proven to be effective catalysts for the hydrogenation and dehydrogenation kinetics of NaAlH₄ (Anton, 2003). Most of the transition metal catalysts improve both the hydrogenation and dehydrogenation kinetics by decreasing the activation energy

of the respective reactions (Zidan *et al.*, 1999; Bogdanovic *et al.*, 2000; Wang *et al.*, 2005a, 2005b; Dehouche *et al.*, 2005). LiAlH₄ decomposes at 433 – 453 K to give 5.3 wt. % of hydrogen and 473-493 K to give 2.6 wt. % of hydrogen as shown below.



Effects of transition metals like Ti, V, Fe and ball milling on hydrogen desorption from LiAlH₄ have been reported (Blanchard *et al.*, 2004; Easton *et al.*, 2005; Andreasen *et al.*, 2005; Balema *et al.*, 2001; Chen *et al.*, 2001). However, the role of these additions has to be carefully understood, since they do not only function as catalysts but also have to facilitate the transport of the species to the surface before desorption. A catalyst only functions in the surface transformations but the diffusion of hydrogen from the solid bulk has to be achieved by some affinity parameters and the kinetics of this transport process is related to the ad-lineation that can take place between the species and the added component. In this regard, the effect of carbon materials as additions to the hydrogen storage materials has been examined (Chapter 4). The results obtained show that the ad-lineation and transport of hydrogen from the bulk to the surface and its subsequent desorption to the gas phase can be facilitated by the addition of carbon based materials because of the grain boundary effects. However the desired properties have not reached yet. Even though the addition of carbon materials enhances the dehydrogenation kinetics of alanates the rehydrogenation is difficult in these systems (Chapter 4). In order to facilitate the rehydrogenation of dehydrogenated alanates, nitrogen containing carbon nanotubes have been used as catalysts in which nitrogen atoms can act as active centers to facilitate the hydrogen dissociation.

5.2 EXPERIMENTAL

The Whatman Anodisc Membrane Filters (Alumina) with pore diameter, thickness and percentage porosity of 200 nm, 60 μm and 65% respectively were purchased from Whatman Inc. U.S.A.

5.2.1 Synthesis of Nitrogen containing carbon nanotubes (NCNT)

Nitrogen containing carbon nanotubes were prepared by using poly(N-vinyl pyrrolidone) as a carbon precursor and alumina membrane as a template (Maiyalagan and Viswanathan, 2005). In the typical procedure, 5 g of polyvinylpyrrolidone (Sigma–Aldrich) was dissolved in 20 ml of dichloromethane (Merck) and impregnated into the pores of the alumina membrane by applying mild vacuum from the bottom. The membranes were dried at 303 K for 2 h then polished with fine neutral alumina powder to remove the surface layers and ultrasonicated for 20 min to remove the residual alumina powder used for polishing. The membrane was placed in a quartz boat kept in a tubular furnace and carbonized at 1173 K under argon gas flow. After 3 h of carbonization, the quartz tube was naturally cooled to room temperature. The resulting carbon–nitrogen composite was immersed in 48% HF at room temperature for 24 h to remove the alumina template and the nitrogen containing carbon nanotubes were obtained. The nanotubes were then washed with distilled water to remove the residual HF and then dried at 393 K.

5.2.2. Preparation of NaAlH_4 –NCNT (SAH-NCNT) and LiAlH_4 –NCNT (LAH-NCNT) composites

All material handlings (including weighing and loading) were performed in a glove box with a carefully controlled atmosphere, with low oxygen and water vapor content. Typically 2 g of sodium aluminum hydride (SAH) or lithium aluminum hydride (LAH) powder (Sigma–Aldrich, >99.5%) was admixed with 5 wt. % of Nitrogen

containing carbon nanotubes by grinding manually in mortar in argon filled glove box for 45 min. After that the composites were transferred to the reactor in the glove box.

5.3. RESULTS AND DISCUSSION

Fig. 5.1 shows low and high resolution scanning electron micrograph of the prepared nitrogen containing carbon nanotubes. Bunch of well oriented carbon nanotubes of length 50–60 μm with open tube end were observed from SEM. The tube diameter was found to be 200 nm which is in the order of template pore diameter.

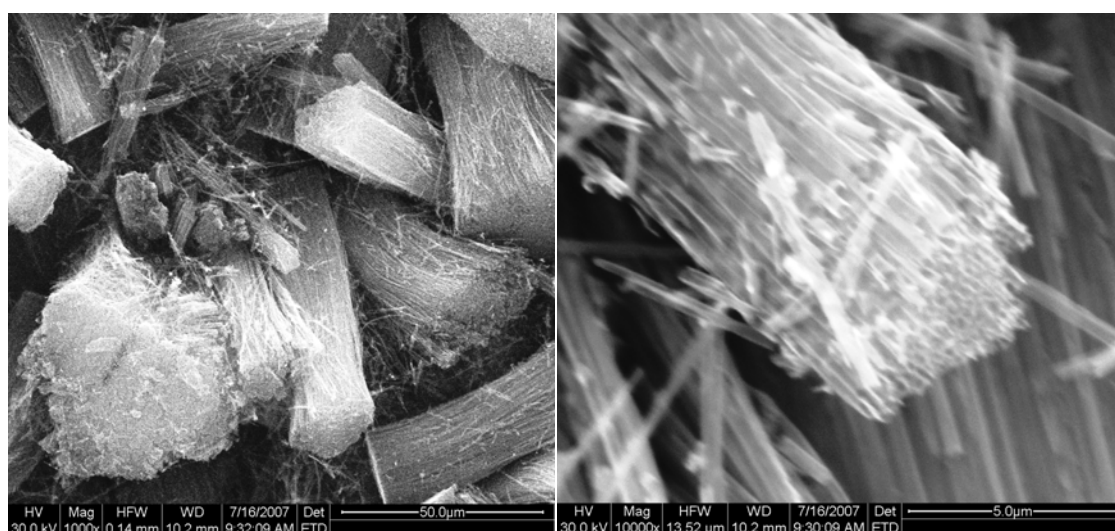


Fig. 5.1 SEM images of Nitrogen containing carbon nanotubes

The XRD pattern of nitrogen containing carbon nanotubes is shown in Fig. 5.2. The peaks at 25.5° and 43.8° correspond to the reflections of (002) and (101) respectively. These peaks are indexed to the reflections of hexagonal graphite. The (002) peak arises due to interlayer stacking of graphene sheets. Broadness of peaks indicates lower crystallinity of prepared nanotubes. The shift of the (002) reflection from $2\theta=26.4^\circ$ for graphite to 25.5° for the carbon nanotubes was observed. This reveals an increase in the interlayer distance from 0.335 nm for graphite to 0.347 nm for the

NCNT (Chen *et al.*, 1999). Nitrogen content in the prepared carbon nanotubes was estimated by using CHN analyzer and it is found to be 6.1%.

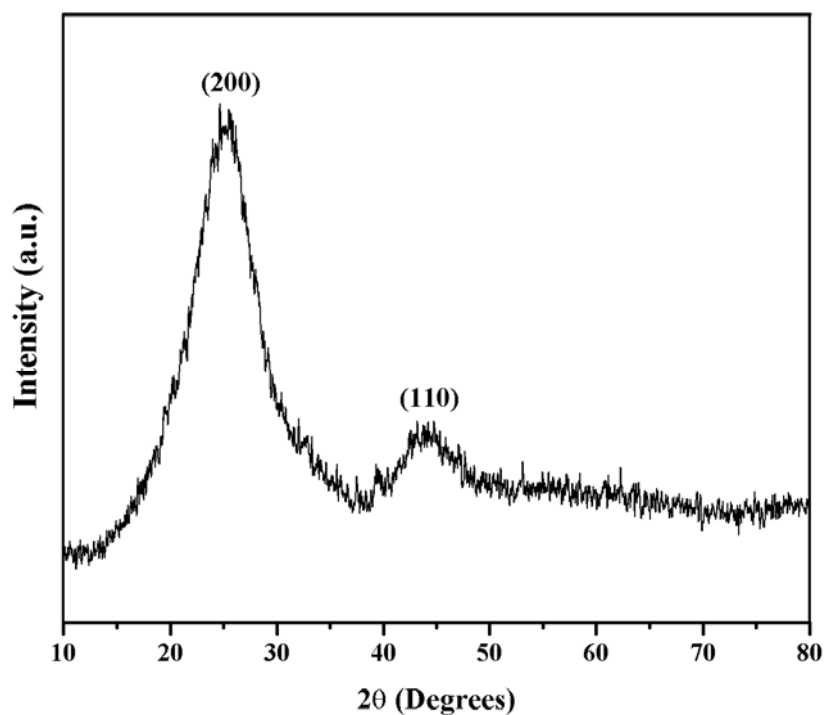


Fig. 5.2 XRD pattern of nitrogen containing carbon nanotubes

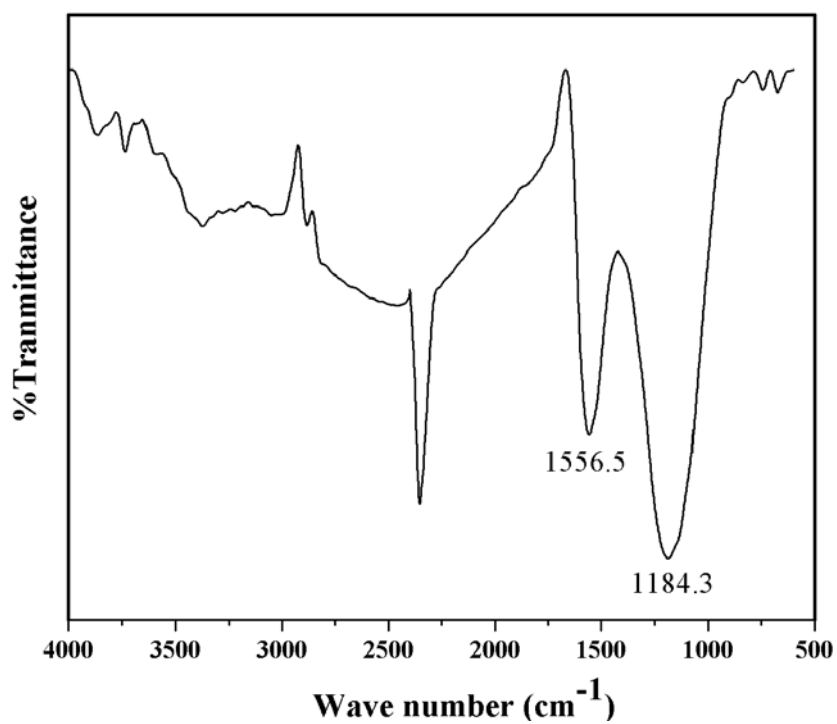


Fig. 5.3 IR spectrum of nitrogen containing carbon nanotubes

IR spectrum of nitrogen containing carbon nanotubes is shown in Fig 5.3. The peak at 1556 cm^{-1} is attributed to the C=N stretching in the aromatic ring and peak at 1184 cm^{-1} corresponds to the characteristic absorbance of single C–N bonds (Liu *et al.*, 1999; Meiyalagan and Viswanathan 2005). This indicates presence of nitrogen atoms in the carbon framework. Sharp peak at 2353 is due to the atmospheric CO_2 .

Fig. 5.4 shows the XRD patterns of as-received SAH and SAH-NCNT composite. In the as-received sample, NaAlH_4 is the only evident phase. Peaks at 29.7, 31.5, 35.7, 48.4, 51.4, 54.5, 60.5 attributed to the reflections of (112) (004), (200) (204) (220) (116) (132) of tetragonal NaAlH_4 (JSPDS -730088) respectively. Upon mixing with NCNT there is no appreciable change in the XRD pattern. The peaks at 2θ values of 15° , 21.7° and 23.8° correspond to the parafilm.

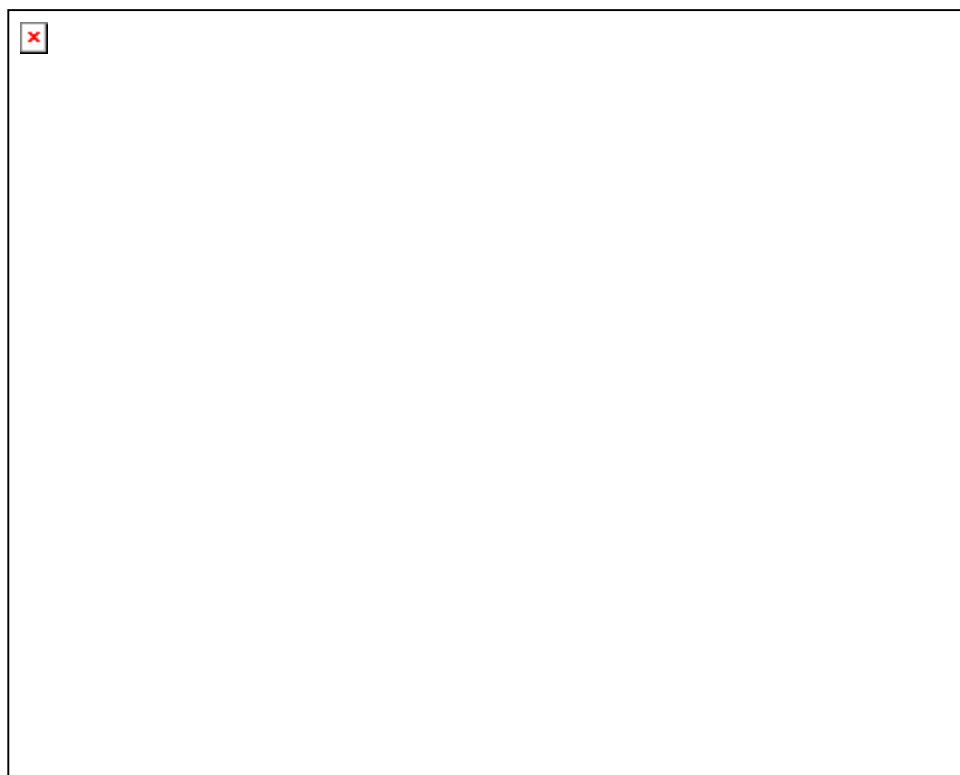


Fig. 5.4 XRD pattern of NAH and NAH-NCNT composites

XRD patterns of the as-received LAH and LAH-NCNT composite materials are shown in Fig. 5.5. In both the materials, peaks corresponding to monoclinic LiAlH_4

(JSPDS-73-0461) were observed. The peaks at 2θ values of 15° , 21.7° and 23.8° are due to the parafilm, which is used to cover the sample to avoid sample exposure to moisture during the XRD measurements. In addition to LiAlH_4 peaks, small traces of Al impurity was found in both as received LAH and LAH-NCNT composites.

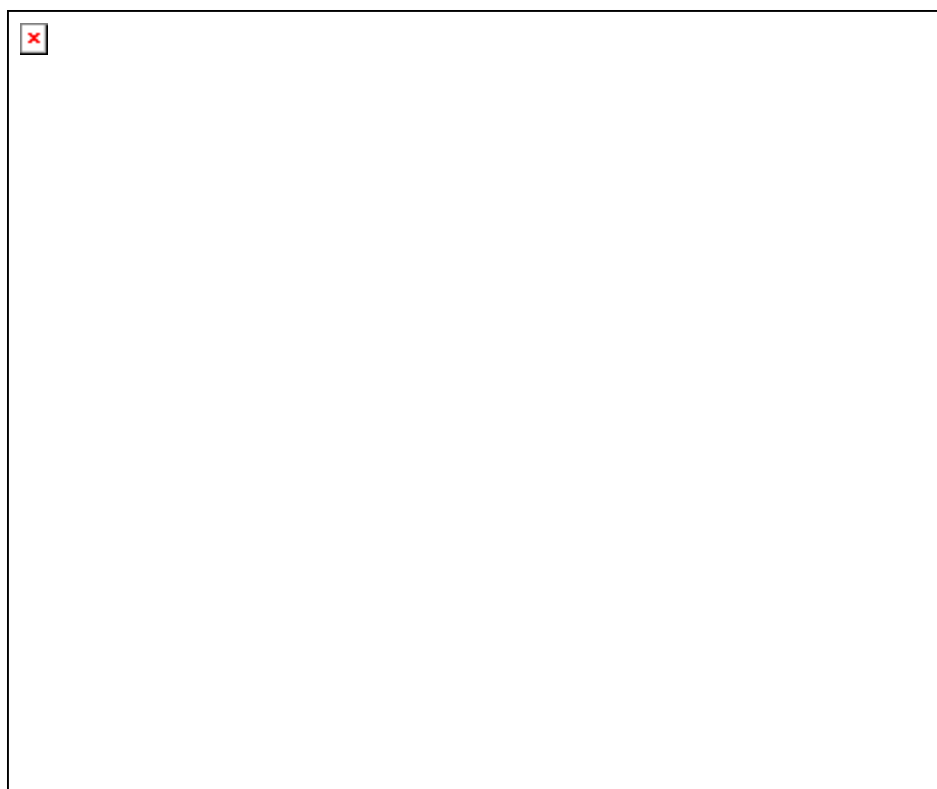


Fig. 5.5 XRD pattern of LAH and LAH-NCNT composites

5.3.1 DSC Studies

The thermal stability of NAH-NCNT composite was studied by differential scanning calorimeter (DSC) measurements. Fig. 5.6 shows the comparison of DSC curves for pure SAH and SAH-NCNT composite with scan rate of 20 K/min. The endothermic peak at 453 K is attributed to the melting of NaAlH_4 . Peak at 551 K corresponds to the first decomposition of NaAlH_4 to give Na_3AlH_6 , Al and H_2 according to reaction 1.9. And the second endothermic peak at 566 K can be attributed to the decomposition of Na_3AlH_6 into NaH, Al and H_2 according to reaction.1.10.

The values of the endothermic peaks of DSC curve are higher than its actual dehydrogenating temperatures reported in literature. It is mainly due to the higher heating rate applied in DSC measurement. As shown in Fig 5.6, peaks for the first and second decomposition reactions were shifted to lower temperatures by 30 K for the SAH-NCNT composite compared to pure SAH (523.2 and 544.7 K for the first and second step dehydrogenation, respectively). This indicates the improvement of dehydrogenation of SAH by the addition of NCNT.

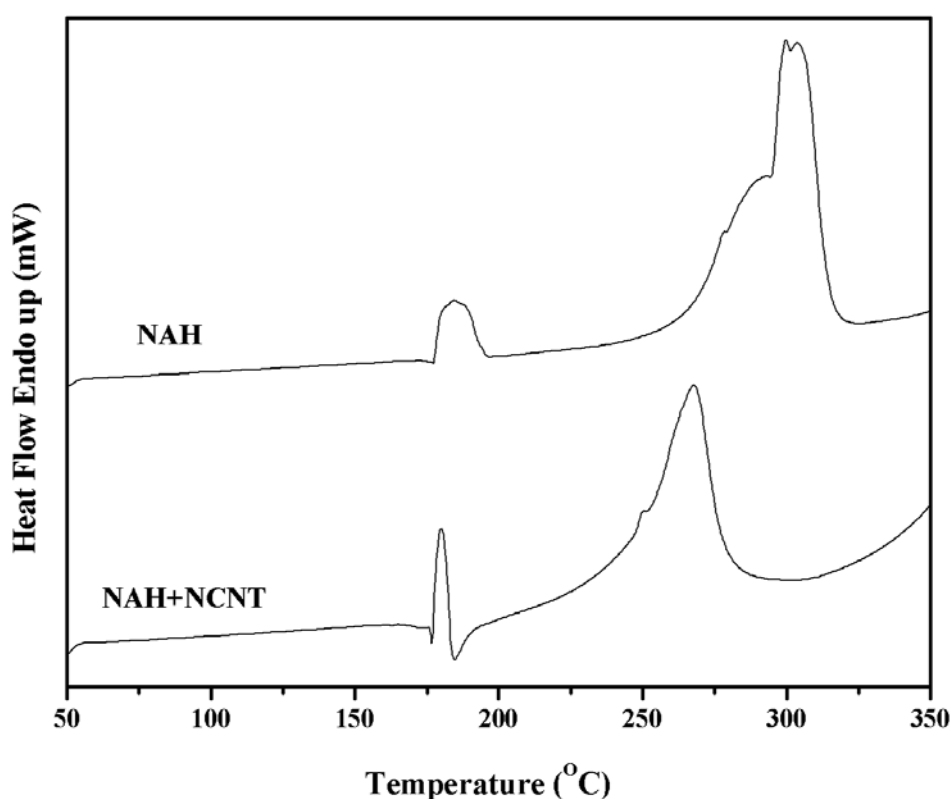


Fig. 5.6 DSC curves of SAH and SAH-NCNT composites

The DSC response curves for the as received LAH and LAH-NCNT composites in the temperature range 323 to 573 K at a heating rate of 20 K/min are shown in Fig. 5.7. DSC curve for the as received LiAlH_4 shows the following features; an exothermic peak at 433K which can be attributed to the interaction of LiAlH_4 with surface hydroxyl impurities, an exothermic peak around 443 K due to first step decomposition

according to reaction 4.1 and an endothermic peak around 493-543 K corresponding to reaction 4.2. Similar features were observed for the LAH-NCNT composite. However, the peak positions of LAH-NCNT are shifted to lower temperatures by 10 K for the first and second decompositions compared to the as received LAH.

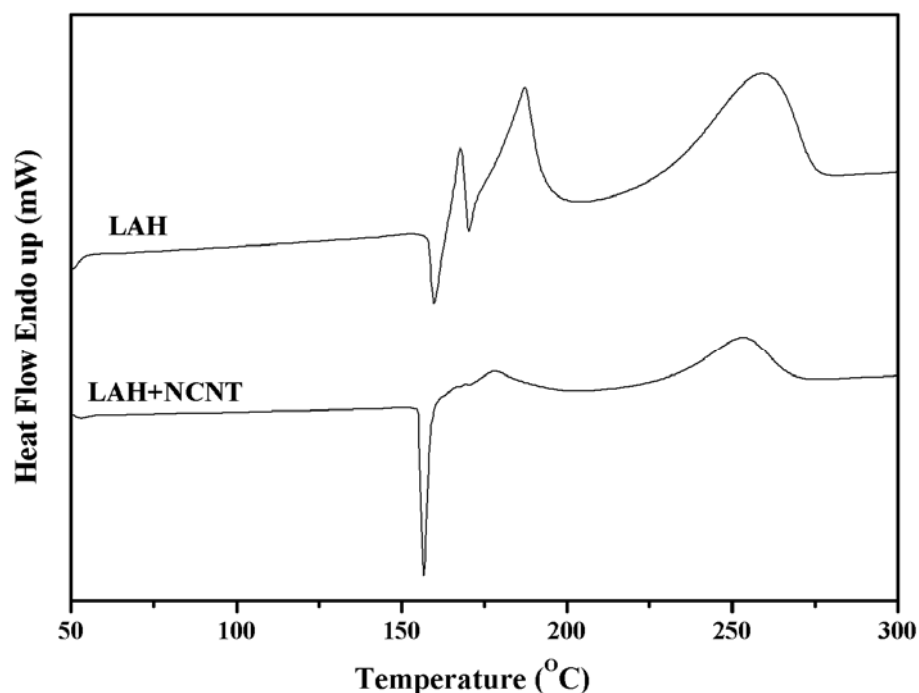


Fig. 5.7 DSC curves of LAH and LAH-NCNT composites

5.3.2 Constant temperature dehydrogenation studies

In order to also investigate the direct solid state decomposition of SAH-NCNT and LAH-NCNT composites, constant temperature dehydrogenation experiments have been carried out. The dehydrogenation profile for LAH-NCNT at 423 K is shown in Fig. 5.8. As can be seen from Fig. 5.8, one cannot distinguish the two stages of dehydrogenation according to equations 4.1 and 4.2. The two dehydrogenation processes appear to be overlapping i.e. apparently they are not separated. Kinetics is fast; at 423 K, it can be dehydrogenated fully in 15 min to release 6.8 wt. % of hydrogen.

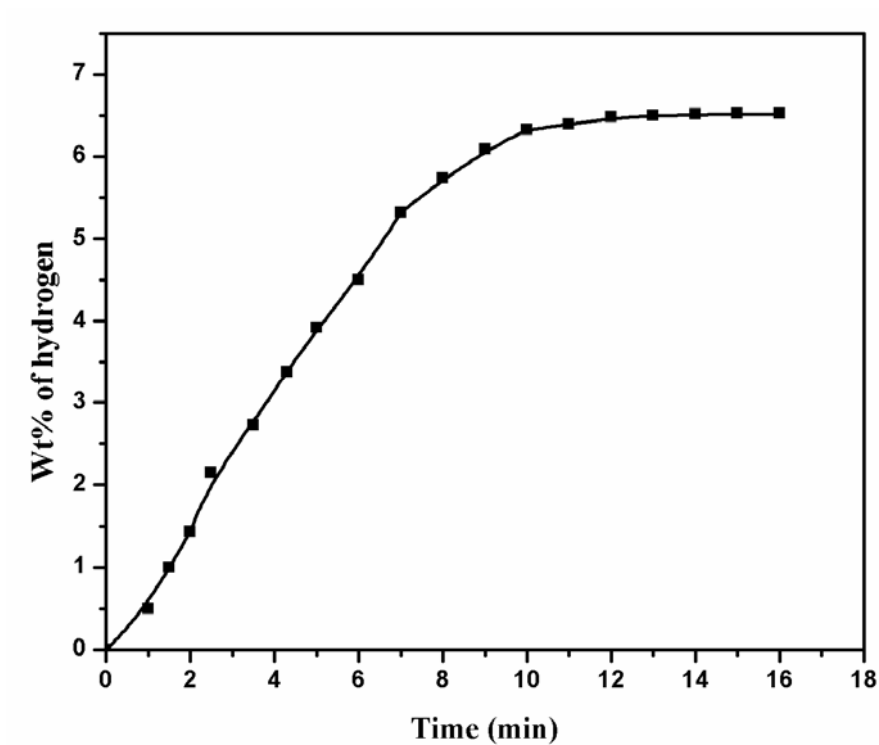


Fig 5.8 Dehydrogenation behavior of LAH-NCNT composite at 423 K

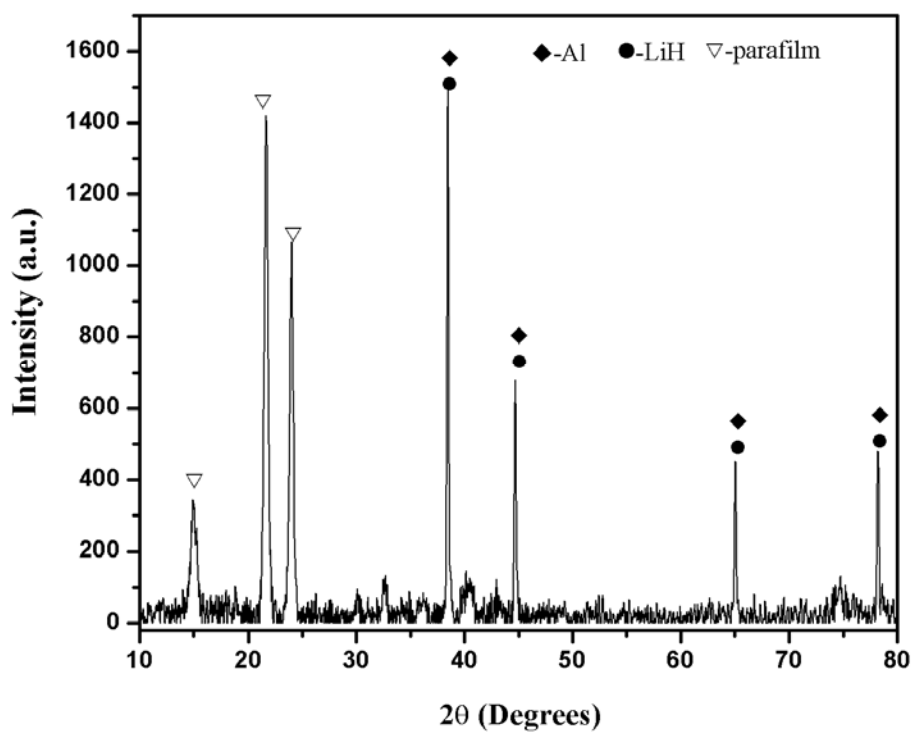


Fig. 5.9 XRD pattern for LAH-NCNT composite after dehydrogenation at 423 K

After complete dehydrogenation LAH-NCNT composite is characterized by XRD. Fig. 5.9 shows XRD pattern of the dehydrogenated LAH-NCNT composite. Only peaks corresponding to Al phase are evident from the XRD pattern. Peaks corresponding to the LiH are not observed, may be because of its amorphous nature and/or masked by the Al peaks, which appear in the same 2θ values.

Fig. 5.10 displays the dehydrogenation profiles for the SAH-NCNT composite at temperatures of 473, 483 and 493 K. The dehydrogenation profiles at all the temperatures clearly demonstrate the two step decomposition of SAH-NCNT composite. With increasing temperatures an increase in the rate of hydrogen release was observed as expected for a thermally activated process. The maximum hydrogen release of 5.3 wt. % is observed.

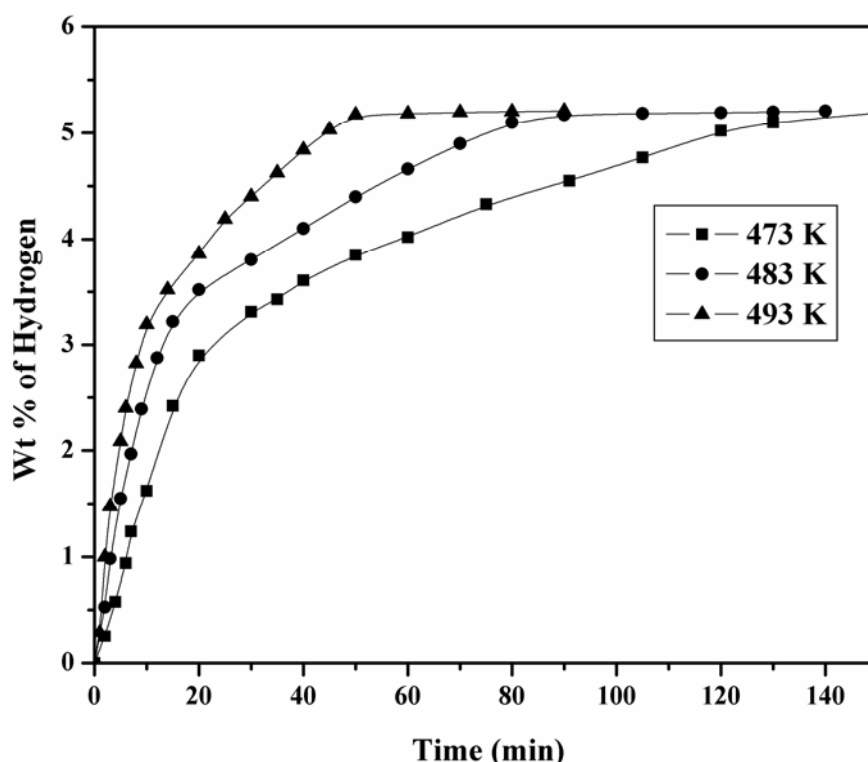


Fig. 5.10 Isothermal dehydrogenation kinetics of SAH-NCNT composite at 473, 483 and 493 K

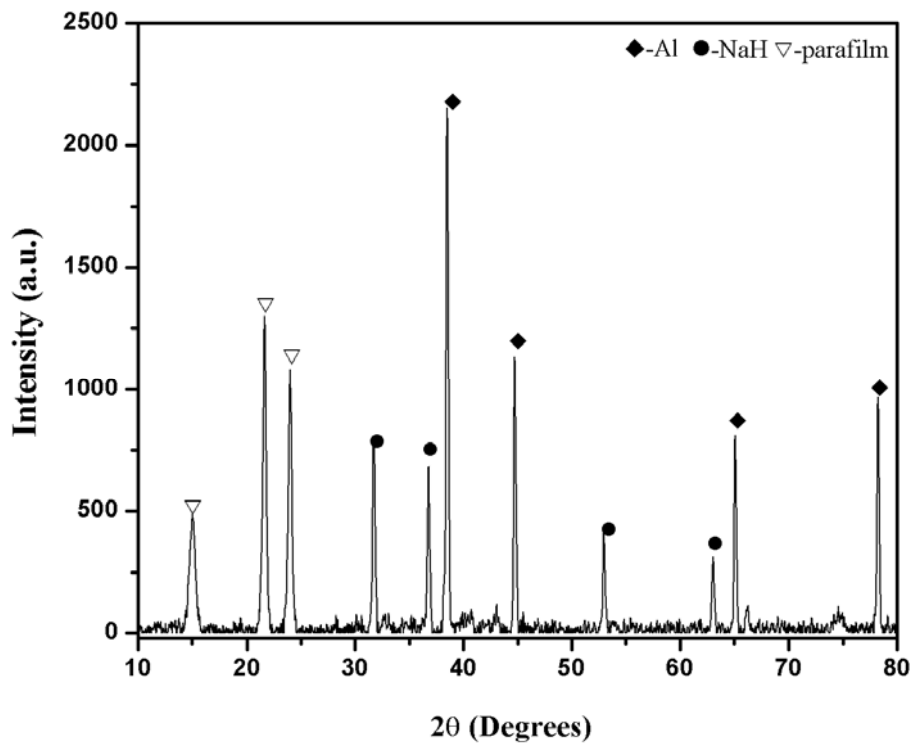


Fig. 5.11 XRD pattern for the dehydrogenated SAH-NCNT composite at 493 K

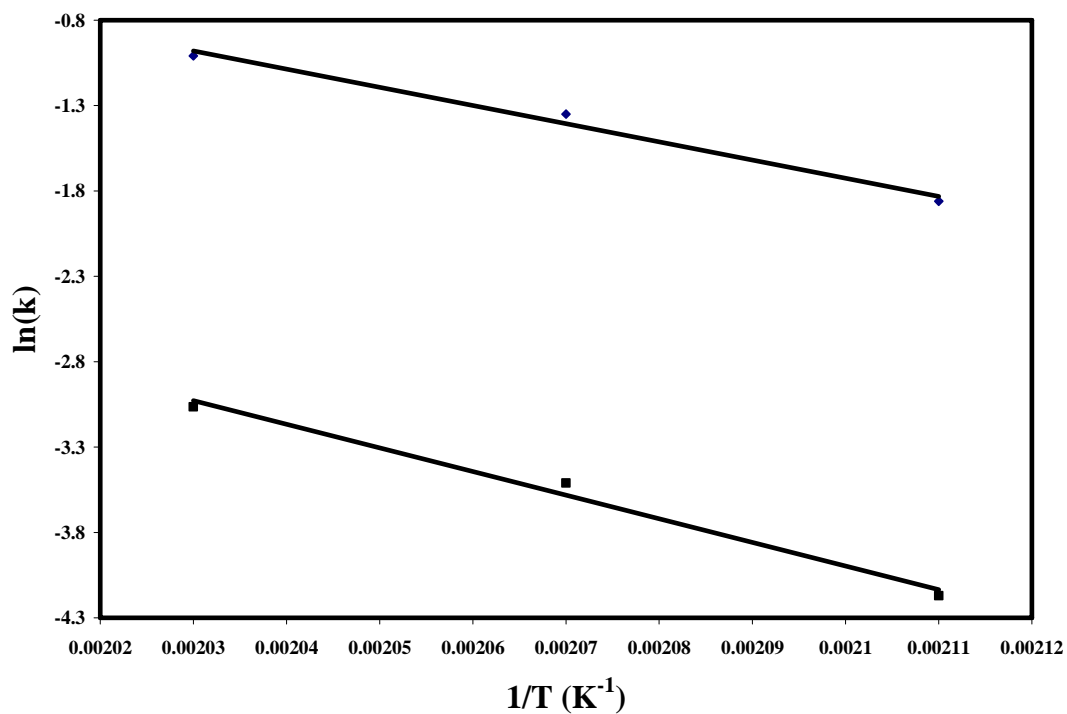


Fig. 5.12 Arrhenius plot of the SAH-NCNT composite for first and second step decomposition reaction.

After dehydrogenation for 150 min at 493 K, XRD pattern for SAH-NCNT composite was recorded and is shown in Fig. 5.11. NaH and Al phases are evident from XRD, indicating the complete dehydrogenation of SAH-NCNT composite. Activation energies for the reaction 1.9 and 1.10 were calculated from the Arrhenius plot for the SAH-NCNT composite and are given in Table 5.1.

Table 5.1 Activation energies for SAH-NCNT

Decomposition process	Activation energy (kJ/mol)
Reaction 1.9	83.4±1.2
Reaction 1.10	114.9±1.5

5.3.3 Kissinger analysis

Among the several thermo-analytical techniques available, thermogravimetry (TG) or DSC, in particular, provides an excellent means for studying the kinetics of single reactions and multiple processes. Although the isothermal technique is favored, non-isothermal TG or DSC offers several advantages. This is very much the case when the complex multiple decomposition reactions involved like in fossil fuel pyrolysis (Elder and Haris, 1984). In such situations, one cannot utilize the isothermal technique with any confidence, since nothing can be said regarding the reactions occurring prior to the system attaining the isothermally set temperature. A number of kinetic analysis schemes, based on relationships between the temperature at which the reaction rate attains a maximum value and the heating rate have been proposed. Perhaps the well known relationship is identified with the name of Kissinger (1957).

By performing an analysis according to Kissinger, i.e. an analysis of the sensitivity of the peak positions to the applied heating rate, the apparent activation energy, E_A , can be obtained from the following equation

$$\frac{\partial \ln \frac{\beta}{T_m^2}}{\partial \frac{1}{T_m}} = -\frac{E_A}{R} \dots\dots\dots (5.1)$$

where T_m is the temperature at peak maximum in the DSC response curve, β , represents the heating rate of the sample in non isothermal experiment conducted in DSC and R is gas constant. Apparent activation energy E_A can be obtained from the slope of the plot of $\ln\left(\frac{\beta}{T_m^2}\right)$ vs. $\frac{1}{T_m}$.

DSC response curves of the SAH and SAH-NCNT composites were obtained with heating rates of 5, 10, 15 and 20 °C/min. Peak positions for the first and second decomposition reactions at these heating rates are obtained from DSC curves and are given in Table 5.2.

Table 5.2 Peak temperatures for SAH and SAH-NCNT composites at different heating rates

Scan rate (K/min)	Peak temperature for reaction 1.9 (K)		Peak temperature for reaction 1.10 (K)	
	SAH	SAH-NCNT	SAH	SAH-NCNT
5	524.5	498.5	545.6	511.8
10	540.8	513.1	554.8	522.7
15	547.0	522.2	561.3	537.2
20	551.3	523.2	566.7	540.7

The plots as per equation 5.1 are given in Fig. 5.13. From the plots the values of apparent activation energies for decomposition NaAlH_4 into Na_3AlH_6 , Al and H_2 and Na_3AlH_6 into NaH, Al and H_2 were calculated and are tabulated in Table 5.3. Activation energies calculated from constant temperature experiments and Kissinger method are found to be nearly equal.

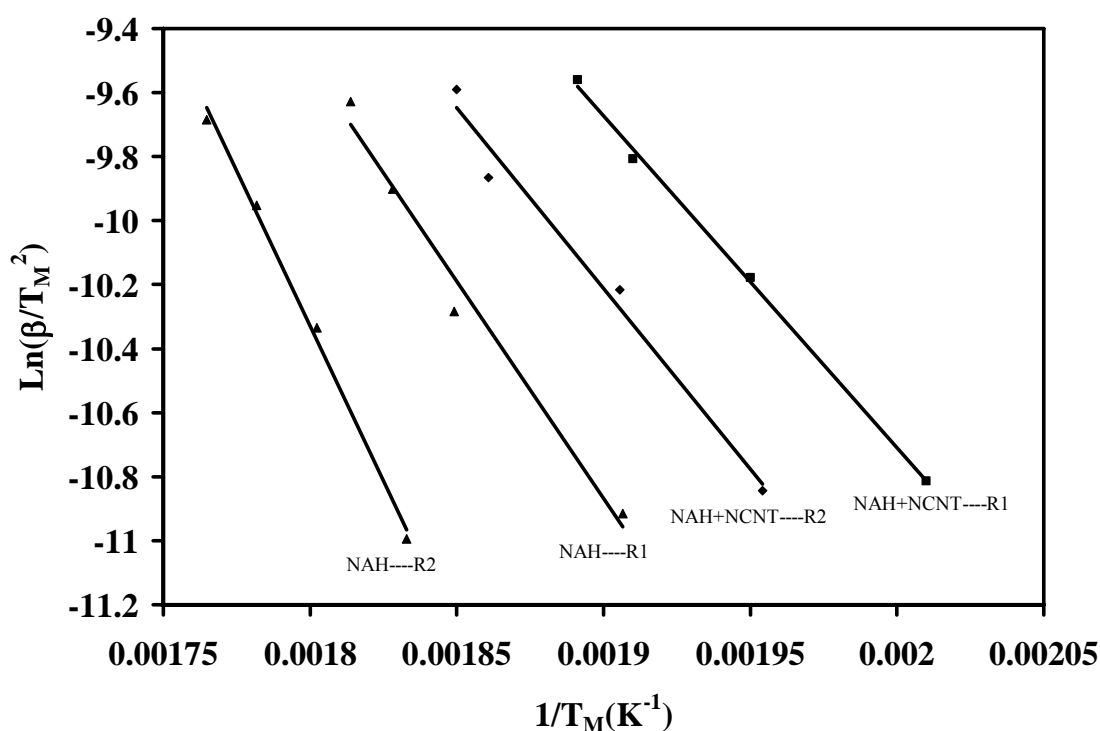


Fig. 5.13 Kissinger plot for dehydrogenation of SAH and SAH-NCNT composites

Table 5.3 Apparent activation energies of two decomposition processes of SAH and SAH-NCNT composites

Decomposition process	Activation energy (kJ/mol)	
	SAH	SAH-NCNT
Reaction 1.9	115.5 ± 1.3	86.3 ± 0.3
Reaction 1.10	160.6 ± 0.9	93.8 ± 1

DSC measurements were performed for the LAH and LAH-NCNT composite at different heating rates (5, 10, 15 and 20 °C/ min). The peaks maximum temperatures (T_m) for the reaction 4.1 and reaction 4.2 were obtained are given in Table 5.4.

Table 5.4 Peak temperatures for LAH and LAH-NCNT composites at different heating rates

Scan rate (K/min)	Peak temperature (T_m) for reaction 4.1 (K)		Peak temperature (T_m)for reaction 4.2 (K)	
	LAH	LAH-NCNT	LAH	LAH-NCNT
5	442.7	433.3	506.8	500.4
10	446.6	443.0	523.5	515.3
15	451.9	449.1	530.0	518.2
20	460.3	451.3	532.0	526.0

The Kissinger method has been used for the calculation of apparent activation energy E_A from the shift in the DSC peak temperature with change of the heating rate (β).

$\ln\left(\frac{\beta}{T_m^2}\right)$ vs. $\frac{1}{T_m}$ plots for the LAH and LAH-NCNT composites were shown in

Fig. 5. 14. From the slope of the straight lines, activation energies were calculated and the values are given in Table 5.5. It can be seen from the Table 5.5 that the activation energies for the as received LAH and LAH-NCNT are more or less the same.

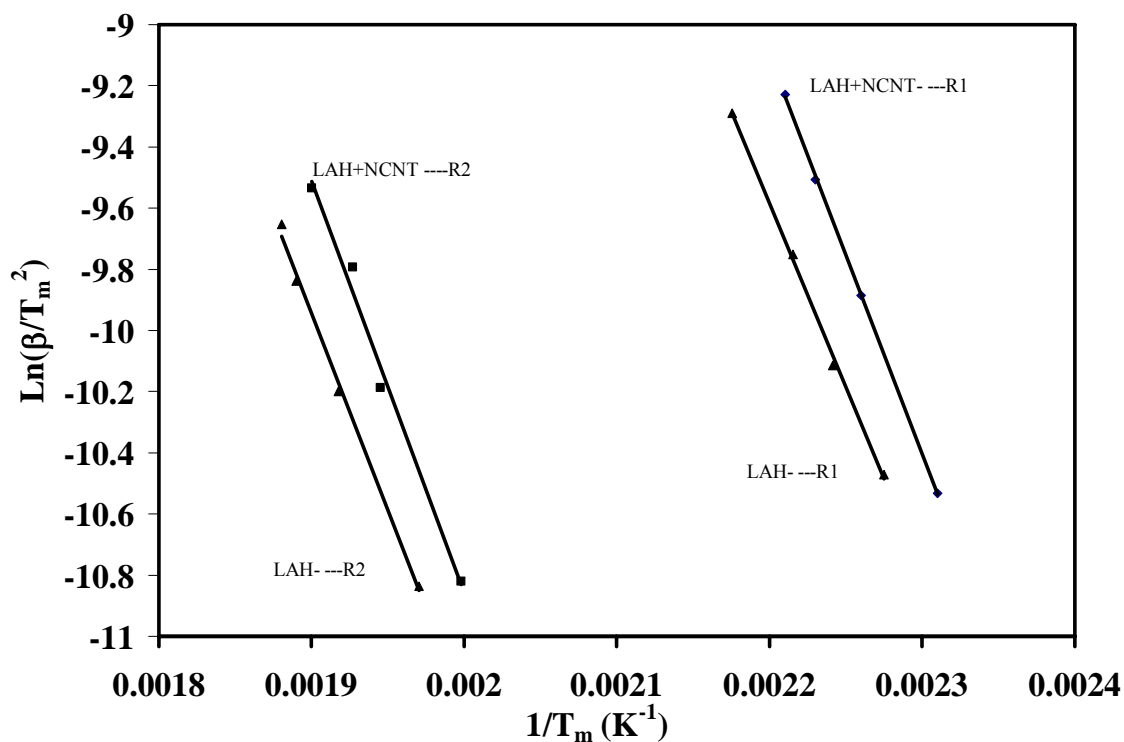


Fig. 5.14 Kissinger plot for dehydrogenation of LAH and LAH-NCNT composites

Table 5.5 Apparent activation energies of two decomposition processes of LAH and LAH-NCNT composites

Decomposition process	Activation energy (kJ/mol)	
	LAH	LAH-NCNT
Reaction 1.9	101.1 ± 0.4	108.03 ± 0.2
Reaction 1.10	108.4 ± 0.6	111.4 ± 1

5.3.4 IR studies

To study the influence of nitrogen containing carbon nanotubes on NaAlH₄ IR spectroscopy was used. IR spectra were recorded with the Fourier transformation infrared (FT-IR) spectrometer in attenuated total reflection mode (ATR) in the spectral range of 500 to 4000 cm⁻¹. Active infrared vibrations of the Al-H bond of NaAlH₄ are found in two regions: Al-H stretching modes (1615 and 1730 cm⁻¹) and H-Al-H, bending modes (895 and 680 cm⁻¹) (Gomes *et al.*, 2005). With regard to

Ni_3AlH_6 (Bureau *et al.*, 1989), it also exhibits two regions of active infrared vibration: Al–H stretching modes (1440 and 1290 cm^{-1}) and H–Al–H bending modes (930 , 842 and 690 cm^{-1}).

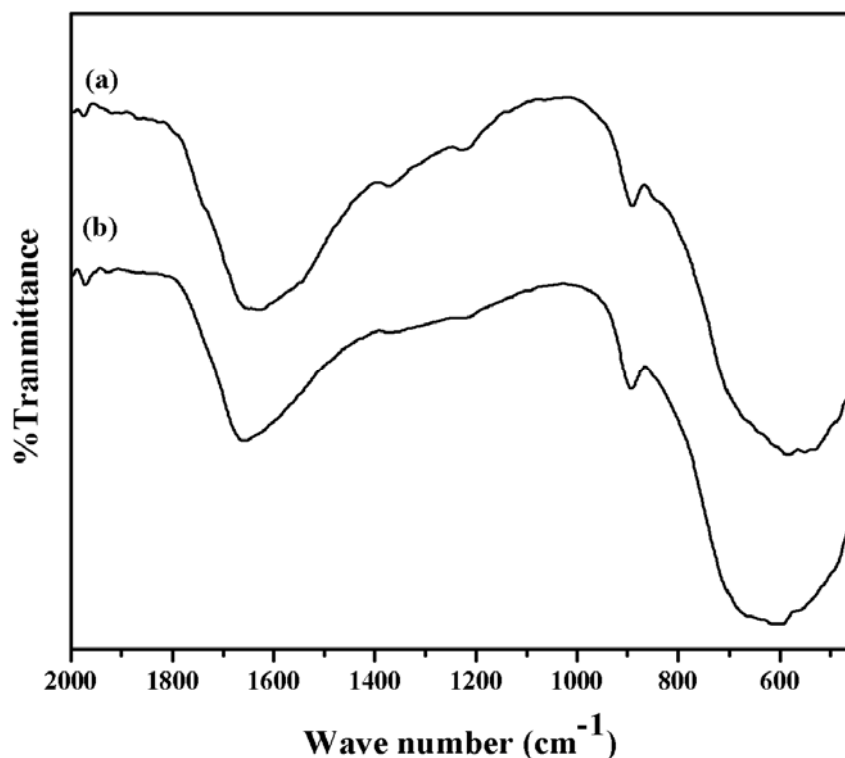


Fig. 5.15 Infrared spectra of (a) SAH and (b) SAH-NCNT composites at room temperature

In-situ DRIFT- IR

Fig. 5.15 shows the IR spectra of SAH and SAH-NCNT composites. The stretching and deformation modes of the two compounds are clearly seen (Table 5.6). For the as received SAH, broad band, centered at 1627 cm^{-1} was observed. This can be attributed to the Al-H stretching frequency of NaAlH_4 . H-Al-H bending frequency is observed at 890 cm^{-1} . These data are in good agreement with data previously reported (Gomes *et al.*, 2005). In addition to these peaks, a broad band centered at 580 cm^{-1} was observed. In SAH-NCNT similar stretching and bending vibration frequencies are observed.

However, the Al–H stretching modes are shifted to higher frequencies (30 cm⁻¹). This shift can be attributed to effect of NCNT on the Al–H bond caused by interaction between NCNT and H atoms in the sodium alanate.

Table 5.6 Infrared frequencies of SAH and SAH-NCNT composites at room temperature

Type of vibration	IR frequency (cm ⁻¹)		
	SAH (ATR) Gomes <i>et al.</i> , 2005	SAH (ATR)	SAH-NCNT (ATR)
H-Al-H bending vibrations	690 895	580 890	595 892
Combination bands	1250 1370	1228 1368	1230 1371
Al-H stretching	1615	1627	1658

In-situ IR spectroscopy measurements have been performed for the SAH-NCNT composite from room temperature to 553 K. The diffuse reflection infrared Fourier transform spectroscopy (DRIFTS) technique is useful, for non-transparent materials and/or for in situ measurements at elevated temperatures and under reactive atmospheres (Armaroli *et al.*, 2004). *In-situ* DRIFT-IR spectra were recorded at 4 cm⁻¹ resolution as an average of 100 scans using DRIFT-IR attachment (Harrick DRP-series) on a Perkin-Elmer FT-IR spectrometer. SAH-NCNT composite was loaded in high temperature reaction chamber in argon filled glove box. Then it was mounted on IR spectrometer and spectra were recorded stepwise at different temperatures under static conditions i.e. sample was heated to required temperature and after reaching the steady state IR spectrum was recorded. This process was continued till temperature of 463 K.

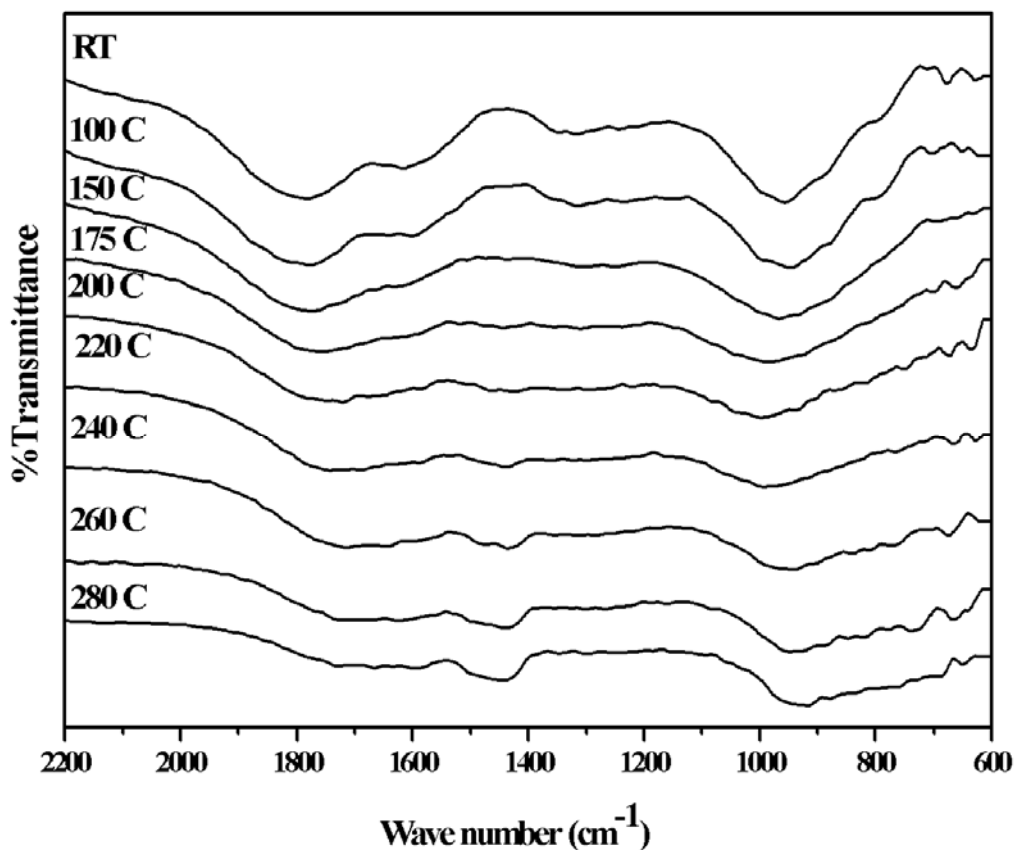


Fig. 5.16 DRIFT-IR spectra of SAH-NCNT composites between the temperatures 300 K and 563 K.

The frequency of the bands at all the temperatures were recorded and given in Table 5.7. Fig. 5.15 shows the DRIFT-IR spectra for the SAH-NCNT composite at different temperatures between 300 K and 563 K. The frequencies of the Al–H stretching and bending vibration modes were observed at 1780 and 950 cm⁻¹, respectively. These are nearly constant from room temperature to 423 K, indicating that the [AlH₄]⁻ anion is a stable unit up to the melting temperature. The phase transition during reaction 1.9 has also been studied by *in-situ* X-ray diffraction measurements (Gross et al., 2000; Balogh et al., 2003) and *in-situ* Raman measurements (Yukawa et al., 2007).

Table 5.7 IR frequencies of SAH-NCNT composite (in cm^{-1}) at different temperatures

Temp. (K)	Al-H stretching in $[\text{AlH}_4]^-$	unknown	Al-H stretching in $[\text{Al}_3\text{H}_6]^{3-}$	Combination bands in $[\text{AlH}_4]^-$	Bending vibrations Al-H-Al in $[\text{AlH}_4]^-$	Bending vibrations Al-H-Al in $[\text{Al}_3\text{H}_6]^{3-}$
300	1786, 1614		-	1317	956.6	-
373	1786, 1618		-	1317	956	-
423	1780, 1612		-	1319	949	-
448	1780		-	1320, 1251	966.2	-
463	1776	1002	1419	1321	-	-
473	1767	995	1440, 1298	-	-	-
483	1755	992	1444, 1301		-	-
493	1720	999	1446, 1299	-	-	
513	1723	995	1440, 1303	-	-	-
523	1722	-	1436, 1305	-		960
533	1718	-	1436, 1301	-	-	943
543	1687	-	1436, 1303			941
553	1687	-	1444	-	-	948

563	1650	-	1440, 1301	-	-	923
-----	------	---	---------------	---	---	-----

Between the temperatures 448 and 513 K, unknown frequency band which is centered around 1000 cm^{-1} was observed. This can be assigned to Al-H stretching frequency of intermediate phase (NaH)(AlH₃) which might be formed after melting at 453 K. Gross *et al.* (2000) reported that an unknown phase, X₁, starts to precipitate just after NaAlH₄ melts at 453 K. Intensity of Al-H stretching frequency of [AlH₄]⁻ decreases with increasing temperature and shifted towards lower frequency region after 448 K. From Fig. 5.6 it is clear that SAH-NCNT starts to melt at 448 K. Moreover, it was reported that the stretching frequency of AlH₃ appears in the range of $1600\text{-}1900\text{ cm}^{-1}$ and bending frequency around 1025 cm^{-1} (Paul, 1988). This band disappeared after 513 K.

Al-H stretching modes for the [Al₃H₆]³⁻ ($1440\text{ and }1300\text{ cm}^{-1}$) observed from the temperature of 448 K and intensity of this band increases with increasing temperature. Bending modes for [Al₃H₆]³⁻ were observed starting from the 523 K. This suggests that after melting NaAlH₄ forms an intermediate which further decomposes to give Na₃AlH₆.

5.3.5. Rehydrogenation studies

After complete dehydrogenation SAH-NCNT composite was subjected to rehydrogenation studies. Rehydrogenation is carried out at 473 K and 8 MPa pressure of hydrogen. Fig. 5.17 shows the rehydrogenation profile for SAH-NCNT. The composite can take 4 wt. % of hydrogen in 2 h. This clearly shows the effect of nitrogen sites in the carbon in facilitating rehydrogenation of NaAlH₄.

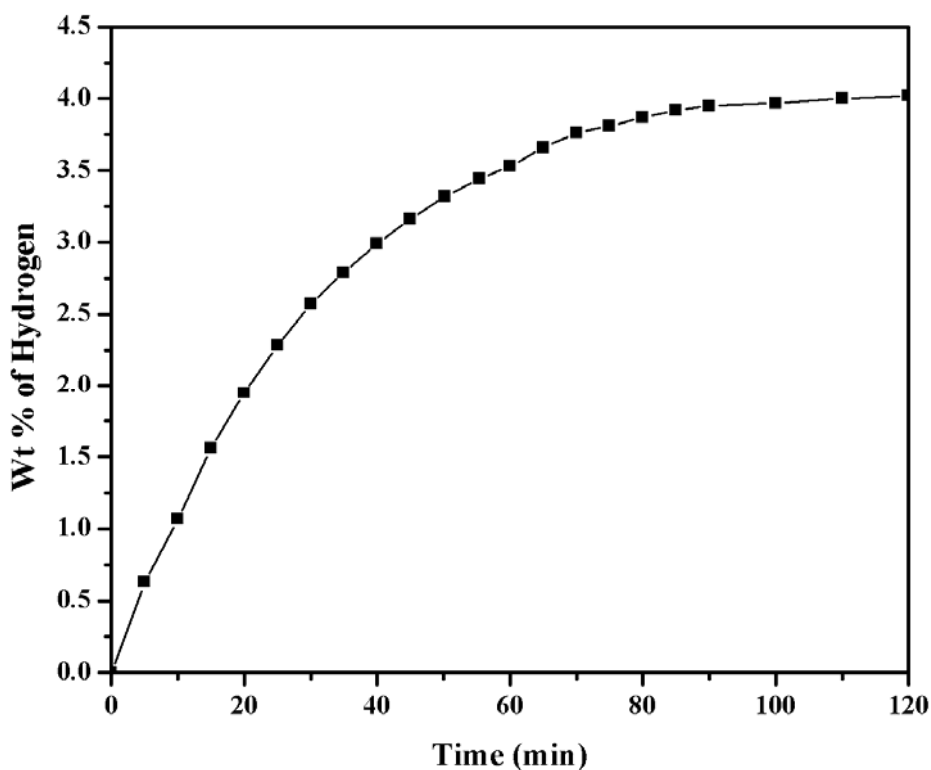
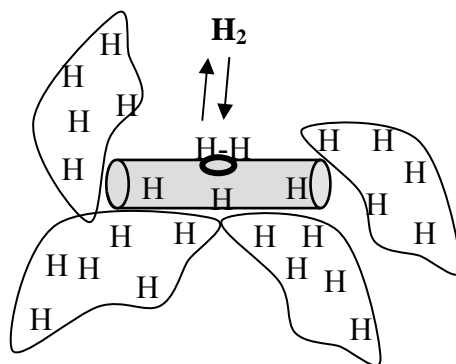


Fig. 5.17 Rehydrogenation profile for the SAH-NCNT composite at 473 K and 8 MPa

5.3.6 Reaction mechanism

Based on these results, the probable mechanism for the dehydrogenation and rehydrogenation has been proposed. A catalyst only functions in the surface transformations. However, to improve the hydrogenation/dehydrogenation kinetics, the diffusion of hydrogen from the bulk to the surface or from surface to the bulk has to be achieved. This is related to some affinity parameters and the kinetics of this transport process is related to the adsorption-desorption that can take place between the hydrogen and the added material like carbon. The role of carbon materials in improving the dehydrogenation process of metal hydrides has been discussed in detail in chapter 4. Addition of carbon materials only facilitates dehydrogenation but not the rehydrogenation. Whereas addition of NCNT favors the rehydrogenation of dehydrogenated NaAlH_4 which demonstrates the effect of active centers in the carbon materials.



Scheme 5.1 Schematic representation of hydrogen spill over from activation centre in carbon nanotubes to metal

Nitrogen sites in nitrogen substituted carbon nanotubes can act as active centers where the adsorption and dissociation of hydrogen molecule can take place. Carbon forms bridge between the source of spill over (activation centers) and receptors (metal particles) and facilitates the hydrogen diffusion from surface to bulk or vice versa. Hence NCNT not only function as catalysts for the hydrogen dissociation but also facilitates the transport of the species. As shown in scheme 5.1, in the rehydrogenation reaction, hydrogen molecule gets adsorbed on the nitrogen sites and then dissociate into the active hydrogen atoms. These hydrogen atoms are spilled over to the NCNT-Metal interface through carbon layer and reacts with the metal to form metal hydride. Smaller the grain size, faster the spill over which avoids the recombination of active hydrogen atoms. The tubular morphology of carbon nanotubes favors transport and diffusion of the hydrogen and thus facilitates dehydrogenation. Typically spill over of hydrogen atoms are observed in metal supported catalysts (Chen and Falconer, 1998). For the dehydrogenation reaction the metal hydrogen bond is activated by the nitrogen atoms and weakens the bond. At these active centers the metal hydrogen bond dissociation takes place and the hydrogen atoms are migrated to surface through the ad-lamination layer of carbon where it combines to form H_2 molecules and desorbs from the surface.

CHAPTER 6

HYDROGEN STORAGE PROPERTIES OF Mg-N OR B CONTAINING CARBON COMPOSITES

6.1 INTRODUCTION

Of the known methods for hydrogen storage (cryogenic liquid, compressed gas, and metal hydrides), metal hydrides offer the best compromise, weighing both safety and cost. The primary importance in the hydrogen storage by metal hydrides is the pressure "plateau" at which the material reversibly absorbs/desorbs quantities of hydrogen. For many applications, the plateau pressure should be close to ambient pressure because this allows the use of lightweight storage containers. The next important consideration is the fast kinetics of absorption/desorption, and this can be achieved by refining the microstructure. Magnesium is excellent hydrogen storage medium since it can store about 7.7 wt. % hydrogen, more than any other metal or alloy. However, MgH_2 has high thermodynamic stability and relatively slow desorption kinetics, which are major barriers for use as a storage material. The high thermodynamic stability of MgH_2 results in a relatively high desorption enthalpy of 75 kJ.mol^{-1} at standard conditions, which corresponds to an equilibrium temperature of 561 K for H_2 - desorption at 0.1 MPa H_2 (Huot *et al.*, 2001; Grochala and Edwards, 2004; Imamura *et al.*, 2005).

A catalyst is needed to accelerate the absorption/desorption of hydrogen in magnesium. Mg-based systems can be modified to improve the sorption characteristics. Alloying Mg with other elements, high energy or reactive ball milling and surface modification of Mg have been reported. Results indicate that the kinetic barriers, and thus the slow hydrogen sorption rates, for this system can be overcome. With ball milling for example, the H_2 sorption rate can be increased by one order of

magnitude because the method is able to impart a strong plastic deformation which can support a fast hydrogen transport on the crystal defects. However, thermodynamics are not affected by such techniques, hence desorption temperature of MgH_2 is not lowered. Some alloying or doping techniques are able to lower the desorption temperature, of MgH_2 by 30-100 K, but this is accompanied by a lower hydrogen storage capacity due to the added weight. In search for improvements, many additives such as transition metals (Ni, Co, Ti, V and Fe), transition metal oxides (Cr_2O_3 , Nb_2O_3 , V_2O_3 , WO_3) and carbon allotropes (graphite and carbon nanotubes) have been tried.

It has been found that better sorption kinetics could be achieved by the mechanical grinding of magnesium with transition metals (Liang, *et al.*, 1999; Bobet *et al.*, 2002), intermetallic phases (Terzieva *et al.*, 1998; Wang *et al.*, 2002), various oxides (Bobet *et al.*, 2003; Oelerich *et al.*, 2001; Barkhordarian *et al.*, 2004; Song *et al.*, 2006) and carbon materials (Imamura *et al.*, 1999; Bobet *et al.*, 2004; Wu *et al.*, 2006; Chen *et al.*, 2004; Imamura *et al.*, 2002; Imamura *et al.*, 2003). The hydrogen storage capacity, recyclability, and the kinetics of hydrogen absorption/desorption are intimately linked to the material microstructure. Powder particles having nanostructured features have some definite advantages. When transition metal nanoparticles used as catalysts, the H_2 molecules adsorb and dissociate into monatomic hydrogen at the transition metal-magnesium interfaces, thus accelerating H-sorption kinetics.

The production of nanocrystalline materials with fresh and highly reactive surfaces can be achieved by the mechanical milling. In most cases, Mg-based composites synthesized by this procedure have shown a facile kinetics/reaction with hydrogen. A proper choice of the processing conditions represents a necessary step since it can affect important parameters like powder particle size and degree of microstructural

refinement imparted by the ball milling. Since Mg is highly ductile it is difficult to prepare in nanosize. This problem could be overcome by adding carbon as anti-sticking agent and for activation purpose (Bouaricha *et al.*, 2001a; Huot *et al.*, 2003).

Among others, the addition of graphite to Mg can assist a relatively fast phase transformation to MgH₂. Imamura *et al.* (2002, 2005) observed that the active composites, as hydrogen absorber, are formed only when Mg is ground with graphite in benzene or THF or cyclohexane. Huang *et al.* (2007) reported that, there is no significant difference in the hydrogen storage capacity of Mg-graphite composite compared to Mg, but the composite displayed remarkable decrease in desorption temperature.

However, the effect of graphite addition to Mg and the role of the organic additives are not completely ascertained and several hypotheses have been formulated, often related to the well-known reducing properties of carbon. The role of these organic additives as envisaged by Imamura *et al.* (1999) is to facilitate the fracture along the graphite layers, thus enhancing the particle size reduction in magnesium with charge transfer. Shang and Guo (2004) investigated the effect of carbon on milled MgH₂ and demonstrated that the carbon addition to MgH₂ leads to fast hydrogen uptake in the rehydrogenated sample. Bouaricha *et al.* (2001b) made the hypothesis that graphite can influence the structure and morphology of the Mg surface oxide. Oxygen on the surface of Mg grains can hinder dissociative chemisorption of hydrogen thus hindering hydriding kinetics.

Despite the improvement on MgH₂ sorption properties after the addition of carbon materials, the problem regarding the stability of magnesium hydride and the role of carbon remain unclear. Addition of carbon materials cannot decrease the thermodynamic stability of magnesium hydride since it cannot activate either

hydrogen molecule or Mg-H bond at moderate conditions. Dissociation of hydrogen molecules can be facilitated by active metals like Pd or Ni that activate and cleave the H-H bond (absorption) and spill over to Mg particles to form MgH₂ (Imamura and Sakasai, 1995). Similar way Mg-H bond is activated and dissociated to release hydrogen during desorption. It was found that the boron and nitrogen sites in boron and nitrogen containing carbon can be the activation centers to facilitate hydrogen absorption (Sankaran and Viswanathan, 2007). In addition, as discussed in previous chapter, addition of nitrogen containing carbon nanotubes result in the decrease of dissociation temperature of NaAlH₄. The aim of the present study is to clarify the effect of carbon materials on the dehydriding properties of MgH₂, paying particular attention to hetero-atom substituted carbon materials particularly boron and nitrogen containing carbon materials, in comparison with conventional graphite. The findings from the present work are of significance for the selection of the suitable carbon materials to enhance the sorption properties of MgH₂.

6.2 EXPERIMENTAL

The magnesium powder (99%, 70 μm) and graphite powder (99%, 60 μm) of 320 mesh were purchased from CERAC, USA and used as-received.

6.2.1 Synthesis of boron containing carbon

Boron containing carbon (BC) material has been synthesized via an esterification reaction of the phenol hydroxyl groups by boric acid and pyrolysed at 1173 K in an inert atmosphere (Xiang *et al.*, 2002). In detail, 35.29 g of phenol and a 62.56 g of formaldehyde solution (>36 wt. %) (Merck) were reacted, through the catalysis of 2.22 g of 20 wt. % NaOH (Merck), at 348 K for 1 h under nitrogen atmosphere. After adding 7.76 g of boric acid, the mixture was heated to reflux temperature and further reacted at the reflux temperature for 0.5 h. The boron-containing phenolic resin was

obtained after removal of water under reduced pressure. It was then heated in an air atmosphere at 383 K for 2 h to get a cured resin. The resin sample was transferred into a quartz boat and carbonized in a flow of argon gas at 1173 K. Then it was washed with distilled water several times in order to remove the impurities and dried in vacuum oven at 343 K for 12 h to obtain boron containing carbon.

6.2.2 Synthesis of Nitrogen containing carbon

Nitrogen containing carbon (NC) materials with high nitrogen content have been prepared by pyrolysis of nitrogen-containing organic precursors. Most of the syntheses have relied on catalytic pyrolysis of C or C and N gas-phase precursors under N-rich atmosphere. The already-reported precursors include pyridine (Sen *et al.*, 1998; and Nath *et al.*, 2000), melamine (Terrones *et al.*, 1999), triazine (Grobert *et al.*, 2000; Terrones *et al.*, 1997), acetonitrile (Che *et al.*, 2003), ethylenediamide, metal phthalocyanines (Suenaga *et al.*, 2000; Wang *et al.*, 2001) and dimethylformamide (Tang *et al.*, 2004). It has been suggested that the presence of C–N bonds in the precursor molecule favors nitrogen incorporation in the carbon structure (Tang *et al.*, 2004). Nitrogen-containing carbon nanomaterials are usually synthesized using the same catalysts as pure carbon nanomaterials, i.e. iron sub-group metals (Fe, Co, Ni) and their alloys.

In the present method, poly(N-vinylpyrrolidone) is used as precursor and Fe as a catalyst. In a typical procedure, ferrous chloride in ethanol solution is added to the poly(N-vinylpyrrolidone) (PVP) dissolved in ethanol (2.5 mmol iron per g of PVP). It is stirred for 30 min and the formed gel is transferred to quartz boat. The quartz boat was placed in a tubular furnace and the sample is heat-treated at 1023 K for 1 h under inert gas atmosphere. Then the resulting material was washed with 20% HCl in order to remove the metal catalyst followed by washing with distilled water and ethanol.

Finally it was dried in vacuum oven at 343 K for 12 h to get the nitrogen containing carbon (NC).

6.2.3 Preparation of Magnesium- N or B containing carbon composites

All material handlings (including weighing and loading) were performed in a glove box with a carefully controlled atmosphere, with low oxygen and water vapor content. Typically 2 g of magnesium powder was admixed with 5 wt. % of carbon by mechanical milling under argon atmosphere for 3 h in toluene. The milling experiments were performed in a Fritsch P5 planetary ball mill at a speed of 300 rpm using WC vial and WC steel balls. Ball-to-powder weight ratio maintained was 15:1. After ball milling the samples were transferred to the reactor in the glove box. The prepared composites are characterized by XRD and DSC and performed the isothermal absorption studies.

6.2.4 Activation

After milling, about 2 g of the composite was introduced in the reactor and connected to a high pressure setup. The whole system is evacuated down to 10^{-3} mbar vacuum then flushed with hydrogen gas for 3 times to remove any other impure gases. Prior to H₂ absorption experiments, the samples were subjected to an activation procedure. Sample is heated to 573 K and hydrogen gas at 2.5 MPa pressure is admitted then sample is allowed to reach steady state. Then the samples were evacuated down to 10^{-3} mbar at the same temperature.

6.3 RESULTS AND DISCUSSION

The boron containing carbon was prepared by pyrolyzing a phenolic resin chemically bonded with boron atoms as reported in the literature (Xiang *et al.*, 2002) and characterized by XRD and SEM analysis. XRD pattern and SEM image of boron containing carbon are shown in Fig. 6.1. Boron containing carbon exhibited the X-ray

powder diffraction patterns which are characteristic of the disordered carbon, as shown in Fig. 6.1a. The broad diffraction peaks observed at 2θ angles of about 24.8° and 44.2° corresponding to the (002) and (100) peaks of carbon respectively. The broadness of the peaks in XRD pattern is due to the amorphous nature of carbon. This is further confirmed by SEM analysis which shows the porous nature of boron containing carbon (Fig. 6.1b).

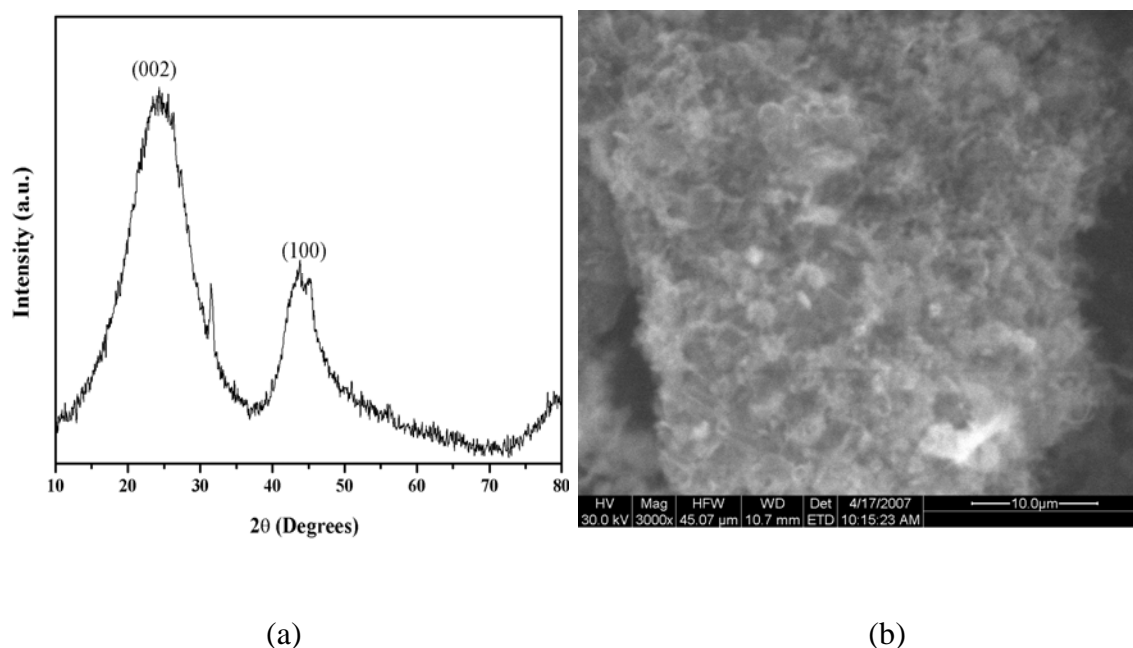


Fig. 6.1 (a) XRD pattern and (b) SEM image of boron containing carbon

The XRD patterns for the nitrogen containing carbon materials before (Fig. 6.2a) and after treatment (Fig. 6.2b) with acid are shown in Fig. 6.2. In the as synthesized material, diffraction peaks are observed at 2θ values of 26° , 43.6° , 44.8° , 50.7° , 65.1° and 74.2° (Fig. 6.2a). The peak at $2\theta = 26.2^\circ$ can be attributed to diffraction from the (002) plane of the hexagonal structure of graphite. Those appearing at 44.8° and 65.1° result from the diffractions of (110) and (200) planes of α -Fe (JCPDS no. 87-0722) and peaks at 43.6° , 50.7° and 74.2° are related to the carbon rich iron carbide $\text{CFe}_{15.1}$ (JCPDS no. 52-0512). Initially Fe ions are reduced by the poly(N-

vinylpyrrolidone) to form iron nanoparticles which act as a catalyst for the growth of graphitic fibers. Fig. 6.3 show the SEM image and corresponding EDX spectrum of carbon obtained by pyrolysis of PVP and FeCl₂ mixture at 1073 K. Fibrous and plate like morphology is observed. SEM image (Fig. 6.3) reveals the formation of graphene layers which are stacked together to form plate like or fibrous morphology. Dimensions of nitrogen containing carbon are in the order of few micro meters. Presence of Fe is evident from the EDX analysis.

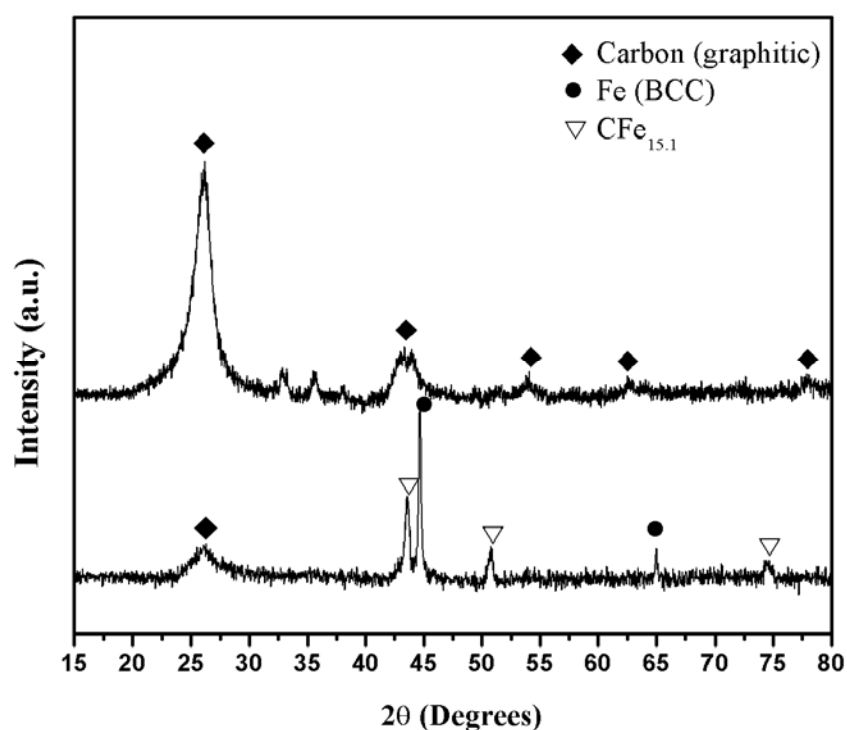


Fig. 6.2 XRD patterns for the boron and nitrogen containing carbon (a) before and (b) after treating with HCl

It is proposed that nanofibers or nanotubes growth processes involve adsorption and decomposition of gases (or gas phase molecular) containing carbon on metal surfaces, dissolution and diffusion of the released carbon atoms in the catalyst, and precipitation of the graphite-like layers (Holstein, 1995). It was reported that during the synthesis of carbon nanotubes from iron phthalocyanines (FePc), Fe particles,

surrounded by carbon was formed on the substrate surface upon thermal decomposition of FePc. These Fe nanoparticles segregate and once an optimum size is formed, it act as nucleation sites on which growth of graphitic carbon nanotubes takes place (Huang *et al.*, 1999). Similarly, Fe nanoparticles, which are formed by decomposition of PVP+FeCl₂ composite, possess a very high catalytic activity for the decomposition of PVP. At high temperature, the decomposed carbon could be dissolved in iron and form an Fe–C phase. As the temperature of the particles was decreased, carbon would precipitate and deposit on the surface of the iron particles. Consequently, graphitic layers are formed.

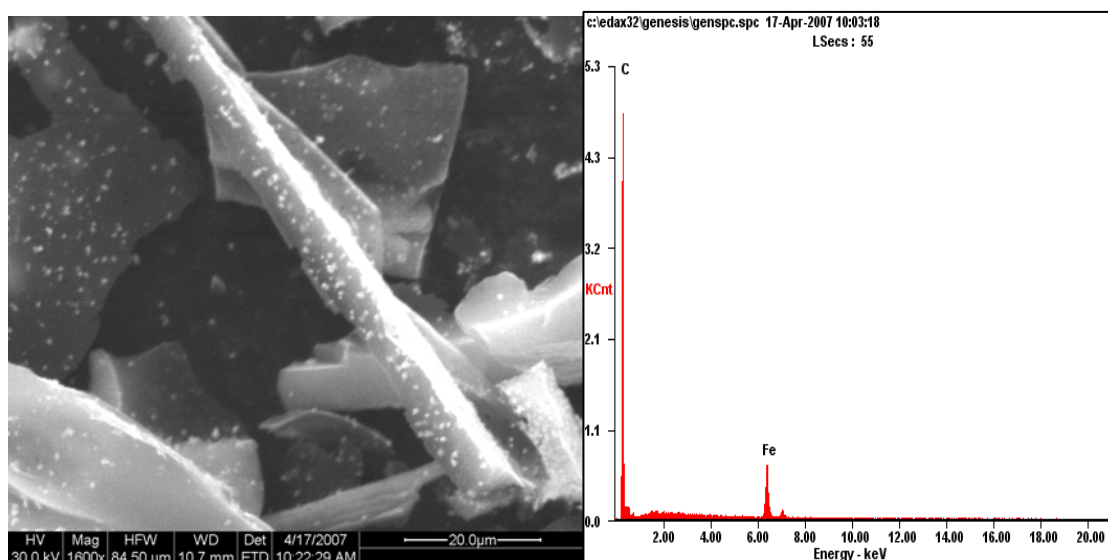


Fig. 6.3 SEM image and EDX spectra of as synthesized carbon fibers

In order to remove the Fe catalyst from carbon, it is treated with 20% HCl for 24 h and then dried in oven at 343 K. After acid purification, the original Fe and CFe_{15.1} phases could no longer be observed, but the carbon remained. XRD pattern of purified carbon is shown in Fig. 6.2b. Sharp intense peaks at 2θ values of 26°, 43.8°, 54° and 77.8° are attributed to the diffraction of (002), (101), (102) and (110) planes of

hexagonal graphite carbon. The small peaks at 2θ values of 33.1° and 35.6° are related to the iron oxide.

Fe catalyst plays two major roles in the synthesis of nitrogen containing carbon: a catalyst that decomposes and precipitates the carbon deposit by acting as template, second graphite layers also formed *in-situ* so that additional steps for graphitization is not required. SEM image of pure nitrogen containing carbon is shown in Fig. 6.4. Different types of morphologies like plates, triangles and fibers are observed from SEM image.

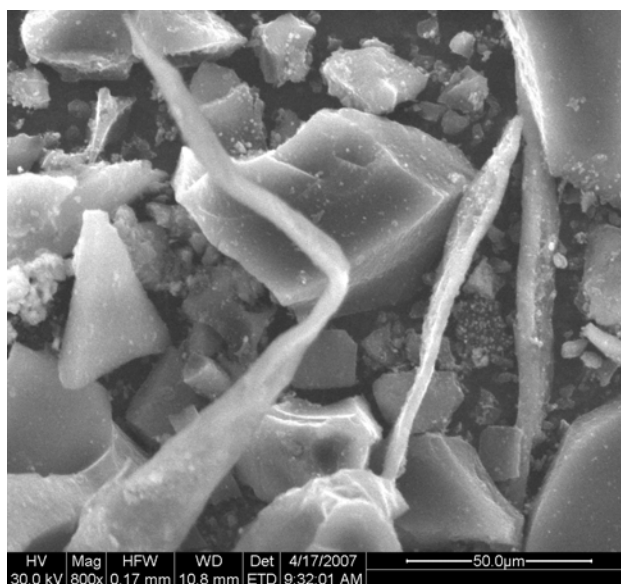
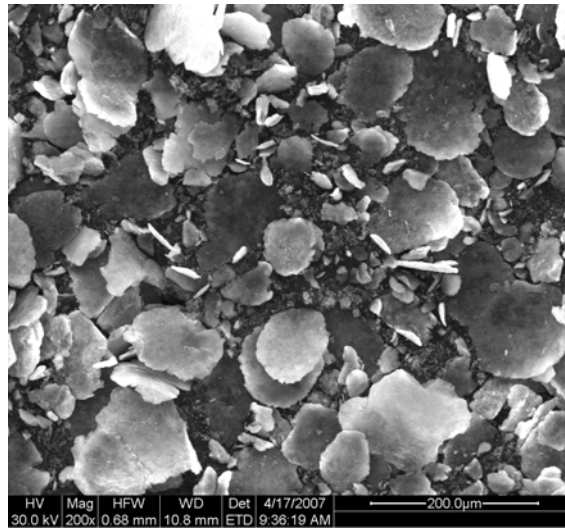


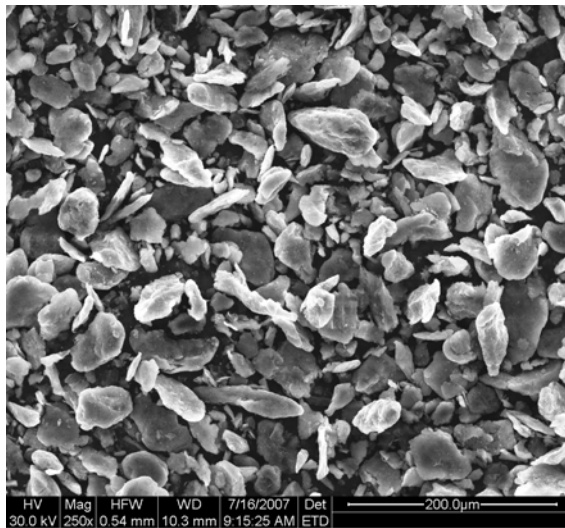
Fig. 6.4 SEM Image of Carbon fibers after HCl treatment

Figs. 6.5(a-c) show the SEM images of Mg-NC, Mg-G and Mg-BC powders, respectively. Particles are irregular in shape and sizes in the range of 5-80 μm for Mg-NC and Mg-BC composites and 5-50 μm for Mg-G composite are observed. No significant reduction in particle size is obtained with the milling conditions used in this work. Even after 3 h milling particle size still is in micrometer range. The particles are flake like structures where one dimension is smaller than the other two.

(a)



(b)



(c)

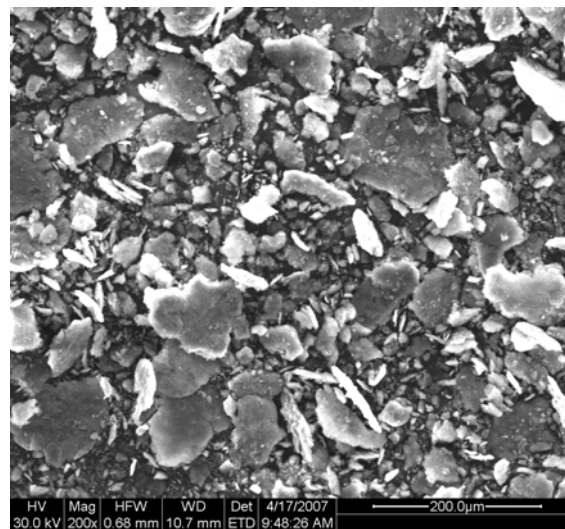


Fig. 6.5 SEM images of Mg-C (a) Mg- NC (b) Mg-G and (c) Mg- BC composites

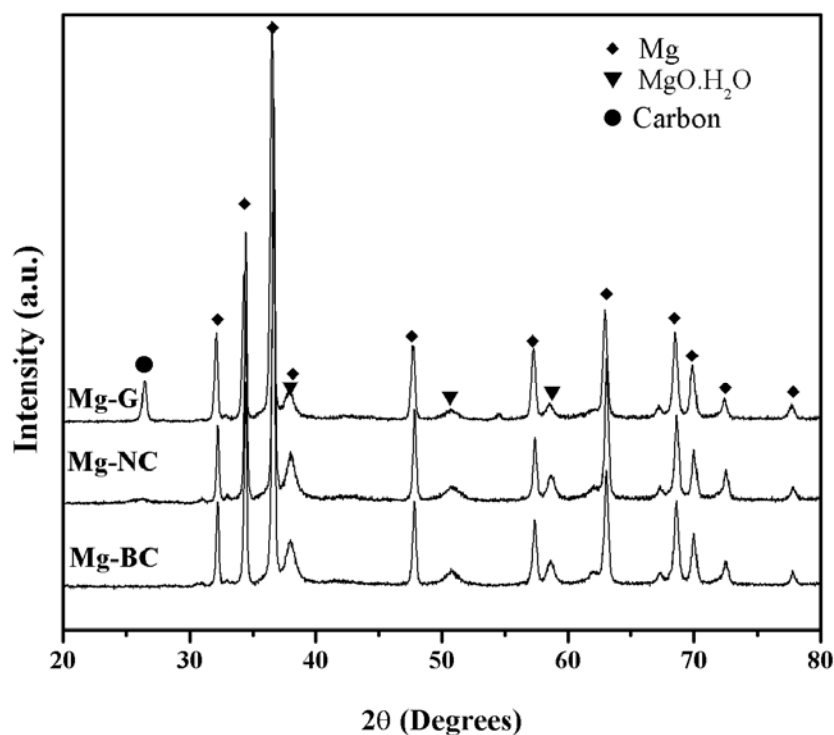


Fig. 6.6 XRD pattern for the Mg-C (G, NC and BC) composites

The XRD patterns obtained from the as-prepared composites (Mg-G, Mg-BC and Mg-NC) are shown in Fig. 6.6. All the composites exhibited similar diffraction peaks at 2θ values of 32.2° , 34.6° , 36.4° , 47.7° , 57.3° , 63° , 68.6° , 69.8° and 72.3° characteristic of hexagonal structured magnesium. In addition, a small amount of $\text{MgO}\cdot\text{H}_2\text{O}$ is observed. It is also evident that the milling of Mg with additives for 3 h does not change the particle size much.

6.3.1 Hydrogen Storage properties

Prior to H_2 absorption experiments, the samples were subject to an activation procedure consisting of one cycle of hydrogen absorption and desorption. Absorption kinetics of Mg-NC, Mg-BC and Mg-G composites at 573 K and 2 MPa pressure of hydrogen are shown in Fig. 6.7. It is observed that both hydrogen capacity and absorption kinetics of Mg could be considerably improved by adding various carbon materials. All composites are able to absorb hydrogen above 4 wt. % within 5 min.

Compared to graphite and boron containing carbon, nitrogen containing carbon shows pronounced effect on the hydrogen absorption rate and hydrogen storage capacity of Mg. The absorption rates are higher than pure Mg with grain size of 30 nm (Zaluska *et al.*, 1999). In particular, for the Mg-NC composite a hydrogen capacity of 5.4 wt. % could be absorbed within about 2 min. The absorption capacities for the all the composites after 15 min are listed Table 6.1.

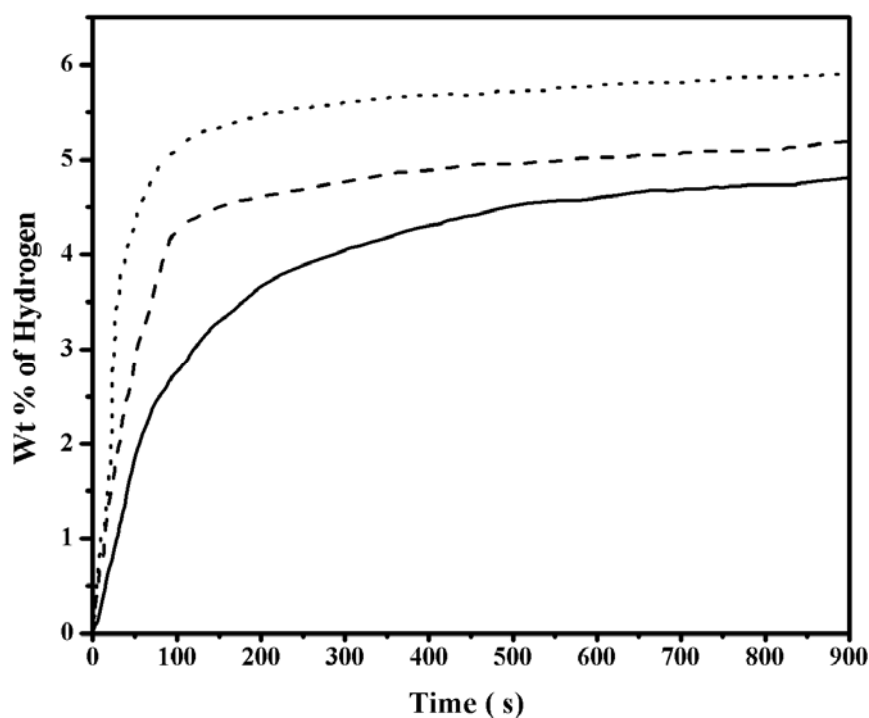


Fig. 6.7 Absorption curves for Mg-C composites at 573 K and 2 MPa pressure.

Table 6.1 Absorption capacities of Mg-C composites for 15 min, at 573 K and 2 MPa

Material	Absorption capacity (wt. %)
Mg-NC	5.92
Mg-BC	5.19
Mg-G	4.8

The absorption capacity is with respect to the total weight of the composite. Maximum theoretical capacity for Mg -10 wt. % C is 6.84 wt. %. Observed capacity is smaller than the actual capacity, this may be due to presence of MgO which is formed during the preparation of composites.

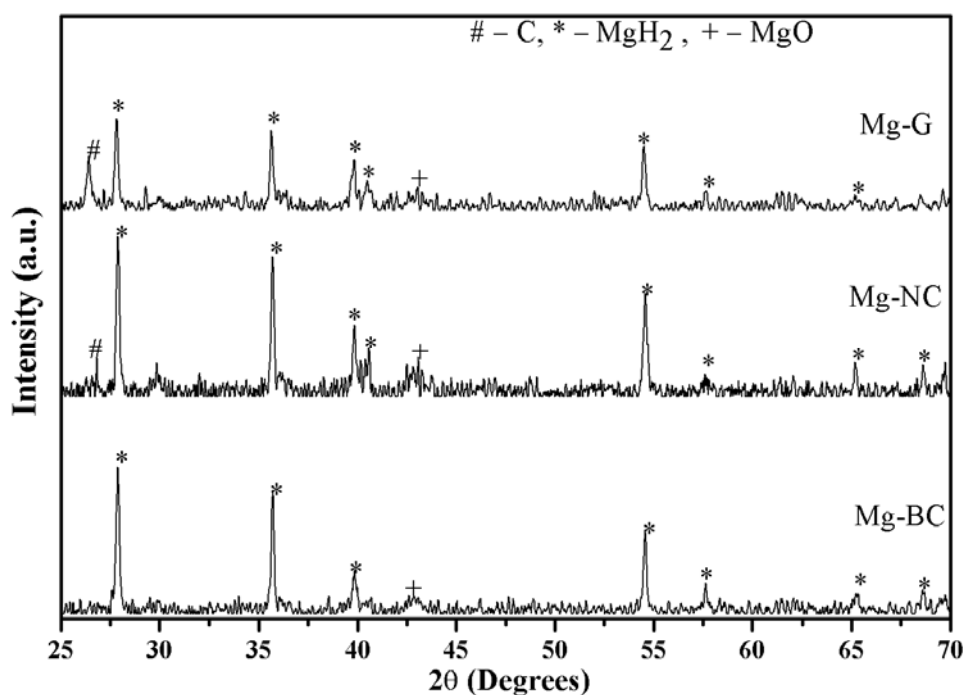


Fig. 6.8 XRD pattern for the hydrided Mg-C composites

After complete hydrogenation at 573 K and 2 MPa pressure of hydrogen, Mg-C composites are subjected to XRD analysis. Fig. 6.8 shows the XRD patterns for all three composites. Only β - MgH_2 is observed for all three composites. In addition, small amount of MgO peaks were also observed from XRD. Carbon peak cannot be seen in Mg-BC composite, this may be due to poor crystallinity. Addition of carbon (graphite), improves the activation of Mg by inhibiting the formation MgO layer (Bouaricha *et al.*, 2001b) which hinders the hydrogen diffusion. Hydrogen molecule adsorption and subsequently dissociation of adsorbed hydrogen will takes place at the grain boundaries. Addition of carbon materials increases the grain boundaries and interfaces which act as catalytic centers for the hydrogen dissociation and nucleation

center for the hydride growth. As theoretical studies (Sankaran and Viswanathan, 2007) suggest hydrogen cannot be activated by carbon at moderate conditions. The role of carbon is to facilitate transport of activated hydrogen atoms to metal through ad-lineation layer (this point is discussed in chapter 4 in detail). As explained in chapter 5 hetero atoms like nitrogen and boron activates the hydrogen molecule and dissociate the hydrogen and spill-over to the Mg via carbon layer to form magnesium hydride.

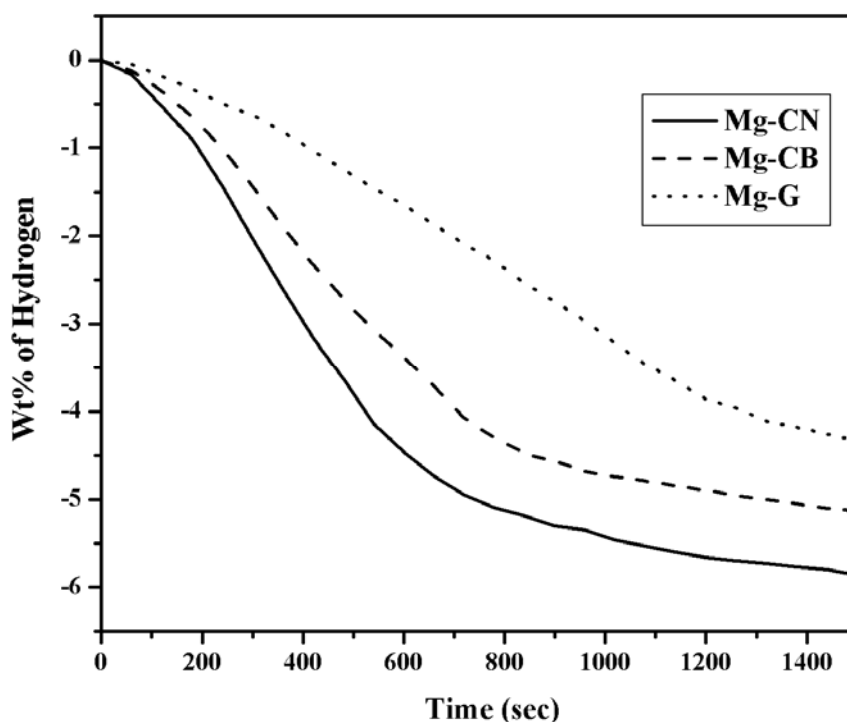


Fig. 6.9 Desorption curves for Mg-C composites at 573 K and 0.1 MPa

Desorption kinetic curves of hydrided Mg-Carbon composites at 573 K are shown in Fig. 6.9. It is found that the carbon additives are effective in catalytic enhancement of hydrogen desorption of Mg. Among the three carbons used, nitrogen containing carbon improved the sorption kinetics of Mg more significantly than boron containing carbon and graphite additives. The hydrogen desorption rates are lower than that of absorption rates. Mg-NC composite desorbed more than 90% of hydrogen in 15 min

at 573 K. This implies that the activating center (N sites) enhances the hydrogen dissociation and spill over of hydrogen atoms into Mg during hydriding. It also facilitates the weakening and breaking of Mg-H bond followed by transportation of hydrogen atoms, towards the Mg surface. Desorption capacities for Mg-C composites after 25 min and at a temperature of 573 K and pressure 10 kPa are shown in Table 6.2.

Table 6.2 Desorption capacities of Mg-C composites for 15 min, at 573 K and 0.1 MPa

Material	Desorption capacity (wt. %)
Mg-NC	5.4
Mg-BC	4.7
Mg-G	4.3

6.3.2 DSC studies

Thermal properties of Mg-C composites are determined by using DSC analysis. For comparison pure MgH₂ is prepared by reacting Mg with hydrogen at 623 K and 3 MPa for 3 h. Thermal decomposition of MgH₂ is evaluated by DSC in nitrogen atmosphere at a heating rate of 5 °C/min. these results used as reference for the decomposition of Mg-C composites. Two endothermic peaks are observed for pure MgH₂ at 725 K and 712 K respectively. This may be due to the presence of impurities like MgO/Mg(OH)₂ in prepared sample (Varin *et al.*, 2004). The appearance of two peaks in the reference magnesium hydride has been previously reported in the literature (Imamura *et al.*, 1999; Huang *et al.*, 2007). Huang *et al.* (2007) attributed the second peak to the thermal decomposition of γ -MgH₂. As seen in XRD patterns from Fig. 6.8 in the hydrided sample the only observed phase is β -MgH₂, no traces of

γ -MgH₂ is found in XRD pattern which confirms that the two endothermic peaks corresponds to the decomposition of β -MgH₂.

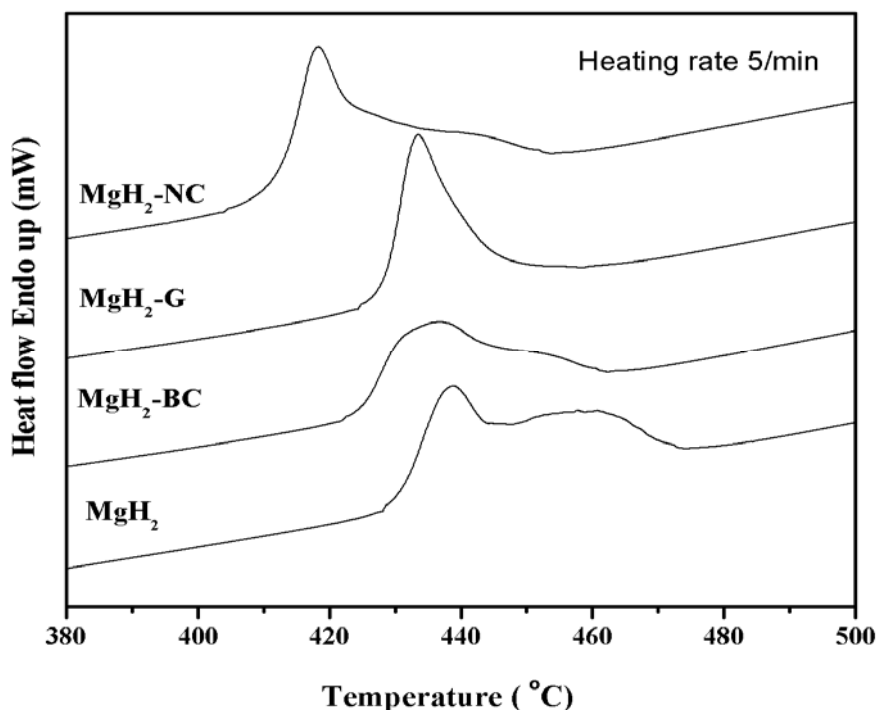


Fig. 6.10 DSC curves for the hydrided Mg-C composites and MgH₂ at the heating rate of 5 °C /min.

Varin *et al.* (2006) studied the particle size effect on the decomposition temperature and found that with decrease in the particle size the decomposition temperature decreases. Moreover, they reported that the appearance of two peaks is due to presence of two different fractions of particles; small and large which could desorb at lower and higher range of DSC temperatures. The same experiments were performed for the Mg-C mixtures. Comparison of DSC curves with that of pure MgH₂ is shown in Fig. 6.10. For both Mg-NC and Mg-BC composite shoulder peaks are observed as in the case of pure magnesium hydride. For Mg-G composite only one endothermic peak is observed. Table 6.3 summarizes the DSC peaks of the three composites. It shows that the decomposition temperature of MgH₂ is slightly reduced with the

graphite and boron containing carbon, varying from 712 K to 707 K and 706 K respectively; where as for the decomposition temperature of MgH₂ is reduced considerably by addition of nitrogen containing carbon from 712 K to 691 K.

Table 6.3 Decomposition temperatures of MgH₂ and Mg-C composites

Material	Peak Temperature (K)
MgH ₂	712, 725
MgH ₂ -NC	691
MgH ₂ -BC	706, 723
MgH ₂ -G	707

Shang and Guo (2004) observed that the graphite has little effect on the decomposition of temperature as found in this study. The reduction in dissociation temperature for Mg-NC composite can be solely attributed to the presence of nitrogen atom in carbon network. Broad endothermic peak reveals the heterogeneity in the surface of hydrided Mg-NC composite. These results suggest that presence of nitrogen atoms in the carbon network can act as activation centers to activate Mg-H bond and hence reduces the decomposition temperature which leads to improve in hydrogen desorption rates. All the composites studied are in micrometer range. Making the Mg and Carbon materials in nanosize may lead to further improvement in the hydrogen storage properties of Mg-C composites.

CHAPTER 7

CATALYTIC EFFECTS IN EVOLUTION OF HYDROGEN FROM NaBH₄

7.1 INTRODUCTION

Group I, II and III elements, namely Li, Na, Mg, B, and Al form a large variety of metal hydrogen complexes. They are of special interest because of their light weight and high hydrogen storage content. The hydrides of boron, (tetra hydroborates M(BH₄)_x) are similar to that of alanates; belongs to complex metal hydrides group.

General formula of metal borohydride is M(BH₄)_x, where x -- valency of metal M; M can be alkali metals, alkaline earth metals or transition metals, Ex: LiBH₄, NaBH₄, etc.

Decomposition of borohydrides is similar to that of alanates but occurs at higher temperatures compared to those of alanates. Another way of generating hydrogen is by the hydrolysis. Chemical hydrides are reactive with water, which results in the release of H₂ (Kong *et al.*, 1999; Aiello *et al.*, 1999; Suda *et al.*, 2001). Among the chemical hydrides, sodium borohydride is safe and practical system suited for storing hydrogen. Hydrolysis of alanates is highly exothermic reaction and is not controllable, while hydrolysis of borohydride is controllable but it is unstable and sensitive to moisture. NaBH₄, extensively studied, has been suggested as a new fuel source for supplying hydrogen under mild conditions. The basic reaction of NaBH₄ is given as follows (Schlesinger *et al.*, 1953):



Based on balanced equation in (7.1) for the hydrolysis of NaBH_4 to form H_2 , the reaction has a theoretical H_2 storage efficiency of $\sim 10.8\%$. In practice NaOH is added to stabilize NaBH_4 during storage.

This reaction is extremely efficient, because the total produced H_2 stems both from NaBH_4 and from H_2O . Moreover, the H_2 thus generated is almost free of impurities, and it may be used in proton exchange membrane (PEM) fuel cells without further purification. To have practical significance in hydrogen production and power evolution, the hydrolysis process of NaBH_4 must occur in such a way to permit a controlled stability in its hydrogen release. Sodium borohydride in alkali medium is stable under ordinary conditions and liberates hydrogen in the presence of catalyst, in a safe and controlled manner. Depending on the solution temperature and salt concentrations, the hydrolysis product, sodium metaborate has relatively high water solubility. It is also environmentally benign and can be recycled back (Schlesinger *et al.*, 1963) to produce NaBH_4 . The NaBH_4 hydrolysis reaction is fast in the presence of a catalyst, and there is no need to supply external heat for the reaction to occur. When used as a fuel, alkaline solution of NaBH_4 fuel can be quickly refueled simply by filling the reservoir with fresh NaBH_4 solution.

The hydrolysis of sodium borohydride was first reported by Schlesinger *et al.* (1953). They extensively and qualitatively studied the accelerating effects of acids and transition metal salts on the rate of NaBH_4 hydrolysis. They observed that in solution hydrolysis reaction proceeded at a very slow rate in the absence of catalysts. Transition metals and their salts were found to be effective and the hydrogen evolution rate can be controlled (Brown and Brown, 1962). Moreover these catalysts can be reusable.

Kaufman and Sen (1985) studied reaction kinetics of NaBH₄ hydrolysis catalyzed by acids, transition metals and their salts. They investigated bulk Co, Ni and Raney Ni as catalysts for controlled evolution of hydrogen from NaBH₄ solutions. The effect of transition metals is characterized by zero-order kinetics.

Korobov *et al.* (1995) examined the effect of inter-metallic LaNi_{4.5}T_{0.5} (T = Mo, Cr, Co, Fe, Cu, Al) compounds on the hydrolysis of NaBH₄ in alkaline solution. However, use of metal hydride as catalysts for the hydrolysis of NaBH₄ was not effective due to their hydrogenation and poor kinetic properties. Catalysts in the form of very fine powders have been mainly used to investigate the catalytic activity towards the hydrogen evolution reaction.

Amendola *et al.* (2000a; b) reported catalytic activity of ruthenium catalysts both unsupported and supported on ion exchange resin beads. Comparatively, anion exchange resins when used as supports for Ru, gave better hydrogen evolution rates than unsupported Ru. They (2000b) observed zero order kinetics for NaBH₄ hydrolysis even at 0.1 wt. % NaBH₄.

The self-hydrolysis rate of NaBH₄ solutions depends on the pH and solution temperature, this rate is empirically represented by

$$\log t_{1/2} = \text{pH} - (0.034 T - 1.92) \dots\dots\dots (2)$$

where $t_{1/2}$ is the time required for one-half of the NaBH₄ solution to decompose (min) and its dependent on the solution pH and temperatures (K) (Amendola *et al.*, 2000a). Hence, the presence of selected catalysts increases the production rate of hydrogen, even in an alkaline solution at normal temperature.

Suda *et al.* (2001) studied the hydrolysis of sodium borohydride with fluorinated metal hydride catalysts. A series of metals, metal alloys and hydrides - Mg, Mg₂Ni, MgH₂, and Mg₂H₄ – were used as catalysts. The authors compared the hydrogen evolution rates by various F-treated metals and untreated Mg₂Ni. They found that comparative to F-treated Mg₂Ni; F-treated Mg₂NiH₄ is more effective catalyst. Catalytic activity of F-treated Mg₂NiH₄ was attributed to the hydride layer formed (NiH₄⁻) during the fluorine treatment.

Pt based catalysts are studied for the hydrolysis reaction of sodium borohydride (Kojima *et al.* (2002, 2004); Krishnan *et al.*, 2005; Bai *et al.*, 2006). Kojima *et al.* (2002) examined the hydrogen evolution from alkaline solution of borohydride by applying mixed metal/metal oxide catalysts such as Pt-TiO₂, Pt-CoO and Pt-LiCoO₂. Layers of Pt-LiCoO₂ were coated on a honeycomb monolith and the structured catalysts employed as catalysts. The hydrogen evolution rate depends on metal crystallite size. As the crystallite size decreases the rate of hydrolysis increases. This route is highly expensive to generate hydrogen from NaBH₄ due to high costs of platinum metal. However, non-noble metal catalysts such as Ni or Co based catalysts have also been investigated for the hydrolysis of NaBH₄ solution.

Hua *et al.* (2003) used heat-treated Ni_xB (x = 4-5) as catalyst for the hydrogen evolution reaction from alkali stabilized sodium borohydride. Ni_xB catalyst was prepared by chemical reaction of nickel salts with borohydride solution. The reaction temperature was controlled below 283 K. The synthesized catalysts are heat treated in a vacuum at 423 K and in air at 353 K. Hydrogen evolution rate for vacuum dried catalyst is compared with that of nickel boride heated in air. The catalyst heated in a vacuum at 423 K showed enhanced catalytic activity and stable under operating conditions.

Kim et al., (2004) carried out the hydrolysis of sodium borohydride with three different catalysts namely spherical nickel powder, filamentary nickel and cobalt powder. They compared the maximum hydrogen evolution rates for these catalysts and found that cobalt is the most effective catalyst. The filamentary nickel showed good performance with fast hydrolysis and short initial induction period. The reason attributed is, it is having the large surface area available is able to provide a large number of reactive sites for the reaction. With these advantageous characteristics, they fabricated a catalyst by mixing cobalt powders and filamentary nickel. It was found that at 30 K, the rate of hydrogen evolution per gram of catalyst varies with the type of nickel used. Rate of hydrogen evolution with filamentary Ni is higher (twice) compared to that evolved with normal Ni. On the other hand, the use of Co catalyst yielded better hydrogen evolution rate than the filamentary Ni catalyst. However, the degradation behavior of the catalyst during long-time operation or usage was not reported. Considering that the catalyst in the hydrolysis of NaBH_4 is exposed to a hot caustic environment, the catalyst durability is crucial for practical application.

Jeong *et al.*, (2005) compared the catalytic activity of various transition metals catalysts like Co, Ni, Mn, Fe, and Cu with Ru catalyst and found that among the non noble metal catalyst Co-B is most effective. Similar type of results is obtained by Wu *et al.* (2005).

Liu et al. (2005) developed catalysts for the hydrolysis of NaBH_4 based on the transition metals, cobalt and nickel. Catalysts in four forms were tested for each metal: fine metal powder, metal salt, metal boride and Raney metal. Fine Ni powder and fine Co powder were examined as the catalysts for borohydride hydrolysis. The catalytic properties of metal salts were measured by using solid hydrated salts - $\text{CoCl}_2 \cdot 6\text{H}_2\text{O}$, $\text{NiCl}_2 \cdot 6\text{H}_2\text{O}$ and $\text{NiF}_2 \cdot 4\text{H}_2\text{O}$. Metal borides were prepared by adding

alkaline borohydride solution (borohydride in 10 wt% NaOH) to the solutions of CoCl_2 and NiCl_2 . Nickel salts and their reduction products showed slower kinetics. Among four chemical forms for Nickel, Raney Ni demonstrated the best performance.

The catalysts based on Ru and Pt has been mostly employed for the hydrolysis of NaBH_4 . Other than Pt and Ru; nickel and cobalt metal catalysts are promising candidates for the catalytic hydrolysis of sodium borohydride. Among the Ni and Co, Co is proven to be effective catalyst (Hua *et al.*, 2003). The aim of present study is to improve the catalytic activity of Co catalyst by the addition of other materials. Cobalt based catalysts (Co, Co-Ni, Co-Cr, Co-Mo, and Co-Sn) are prepared by borohydride reduction in methanol and their effect on the kinetics of hydrolysis reaction of base stabilized sodium borohydride is reported.

7.2 PREPARATION OF COBALT BASED CATALYSTS

Cobalt based catalysts were prepared by the chemical reduction. For the preparation of Co catalyst, cobalt chloride and NaBH_4 are used as cobalt precursor and reducing agent respectively. In the typical procedure, cobalt chloride is dissolved in methanol and the solution was cooled in ice water bath under constant stirring for 30 min, and then slowly an alkaline solution of NaBH_4 was added. Metal to borohydride ratio was taken as 1:4 in order to achieve complete reduction. The reaction temperature was maintained at 283 K. The precipitate was filtered and washed with distilled water several times then dried in vacuum at 343 K and finally annealed in hydrogen atmosphere for 3 h at 623 K. The same procedure was adopted to prepare Co-M catalysts in 1:1 ratio. The metal precursors are NiCl_2 for Ni, CrCl_3 for Cr, SnCl_2 for Sn and Na_2MoO_4 for Mo respectively.

7.3 RESULTS AND DISCUSSION

7.3.1 Characterization

When metal salt is reduced by NaBH_4 in aqueous solution it produces amorphous metal borides (Schlesinger *et al.*, 1953), where as at higher pH and heat treatments it produces metal particles (Lu *et al.*, 1997). In the present study metal salts are reduced in methanol medium and at $\text{pH} > 10$. As synthesized catalysts are annealed at 623 K for 3 h and characterized by X-ray diffractometer. Only peaks corresponding to the Co metal are observed in XRD pattern. Fig. 7.1 shows the main diffraction peaks for the obtained Co powders. Reflections from (111), (200) and (220) planes corresponding to the FCC structure of Co (JSPDS 65-2865) were seen. In order to check the morphology of cobalt catalyst, SEM images are recorded and are shown in Fig. 7.2. SEM image shows that small particles are aggregated to form bigger particles; this may be due to heat treatment at 623 K for 3 h.

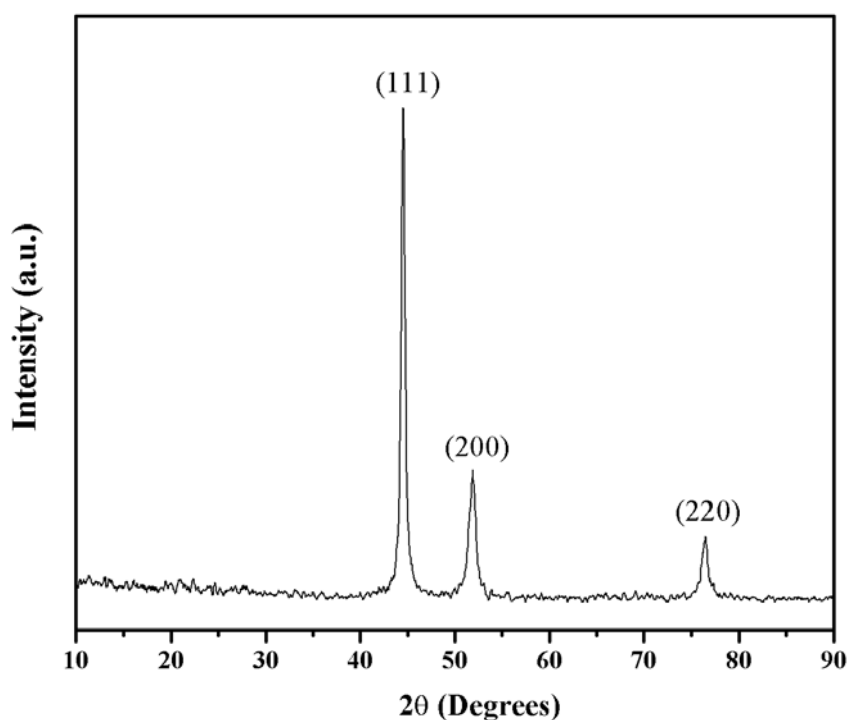


Fig. 7.1 XRD pattern for Co catalyst after annealing in H_2 atm at 623 K

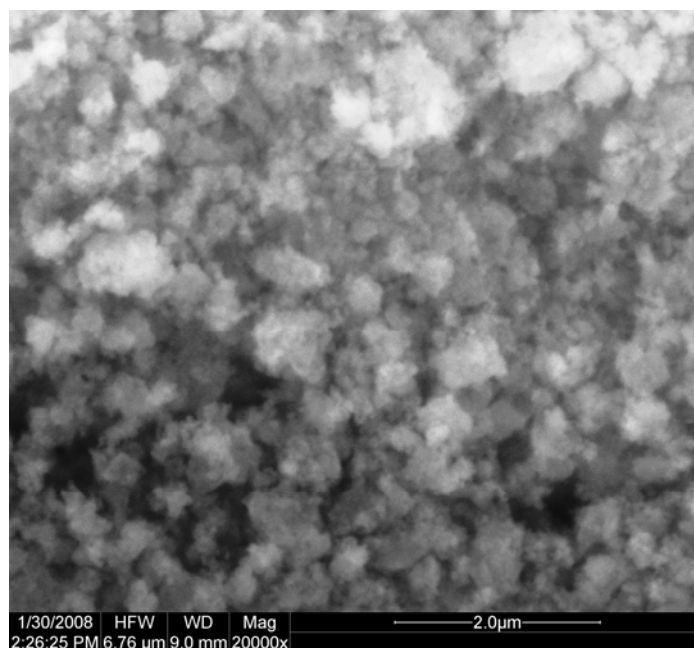


Fig. 7.2 SEM image of Co catalyst after annealing in H₂ atm at 623 K

Fig. 7.3a shows the XRD pattern for the Co-Ni catalyst. It was observed that Co-Ni peaks appear between peaks of the pure metals Co and Ni, indicating an intermediate unit cell size. The preferential growth, favoring (111) direction can be seen from XRD. Since the atomic size difference is less than 1% and similar electronegativity values for Co (1.88) and Ni (1.91); over a wide range of composition Co and Ni form solid solution not the intermetallic compound. The Fig. 7.3b shows the XRD pattern of CoSn alloy. The XRD pattern of a Co:Sn = 1:1 mixture which has been annealed at 623 K under hydrogen atmosphere is mainly constituted by high-intensity reflections of CoSn (XRD file no. 04-0673).

The XRD pattern of the fresh Co-Mo sample with the 1:1 molar ratio as shown in Fig. 7.4a revealed that the sample was present in a typical amorphous structure since no significant reflections were obtained. However, no diffractive peaks indicative of

metallic Mo or the Co were observed even after annealing at 623 K. Since NaBH_4 cannot reduce Na_2MoO_4 to Mo it might present as MoO_x . Similar trend was observed for the Co-Cr catalyst as it shows no significant peaks in diffraction pattern indicative of amorphous nature of catalyst (Fig. 7.4b)

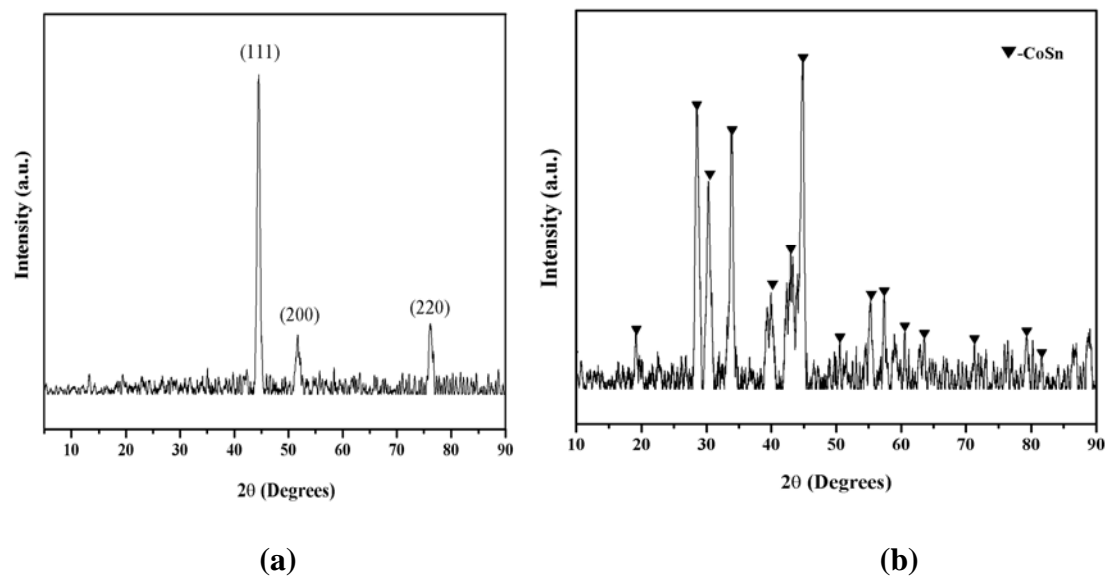


Fig. 7.3 X-ray diffraction pattern of (a) Co-Ni (b) CoSn

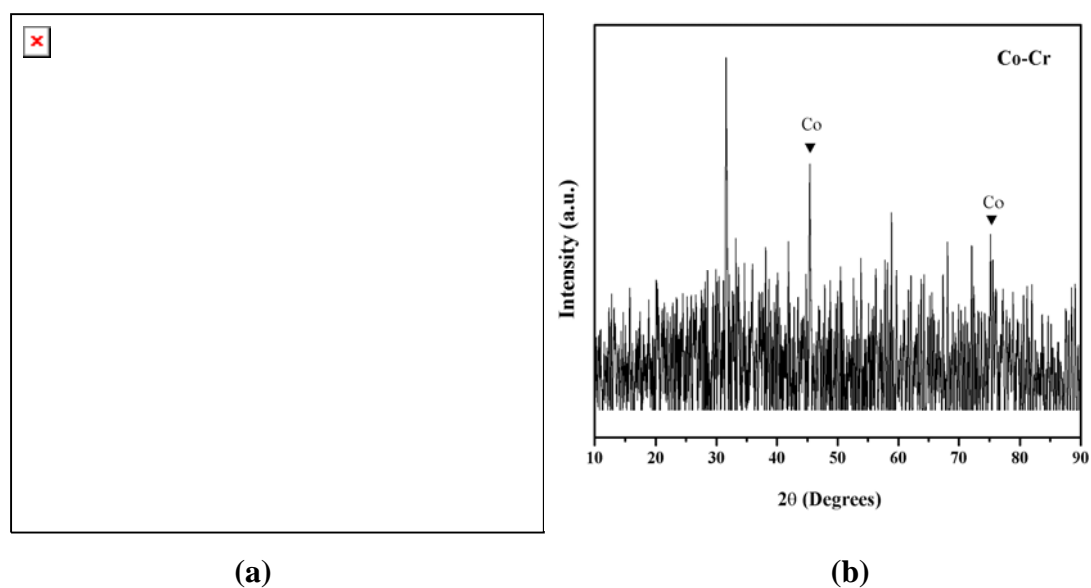
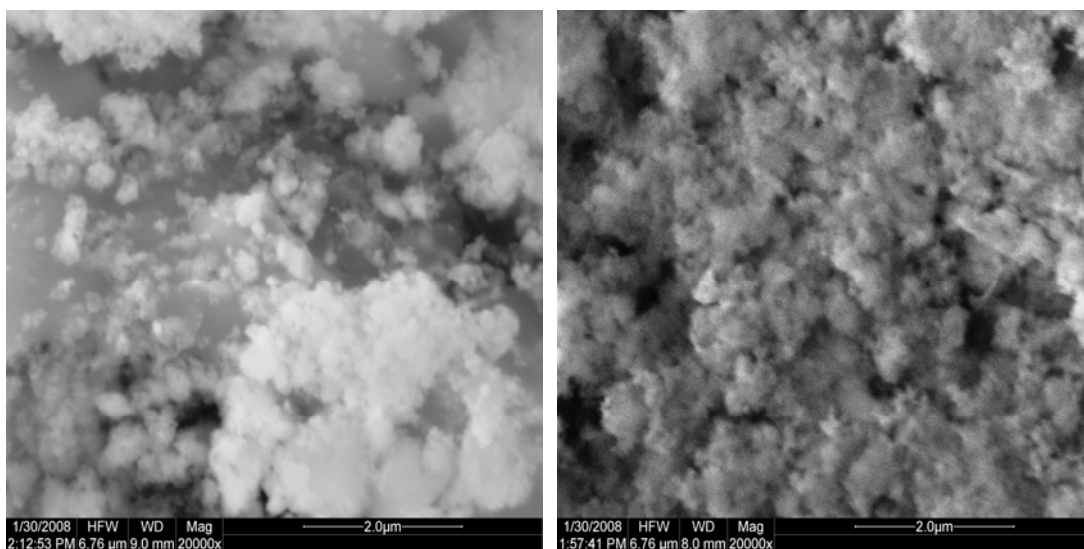
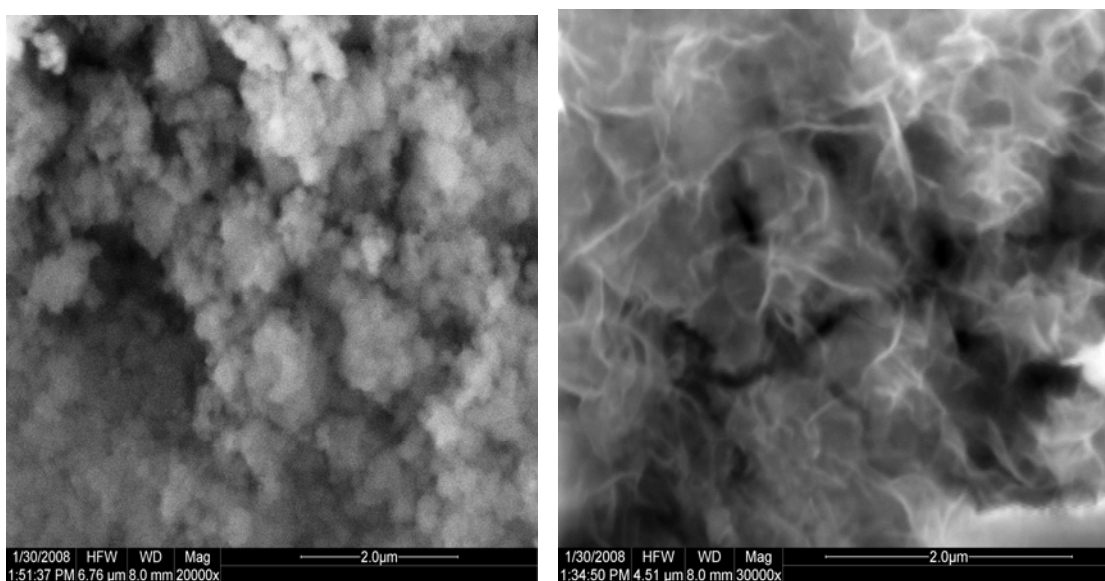


Fig. 7.4 X-ray diffraction pattern of (a) Co-Mo (b) Co-Cr



(a) Co-Sn

(b) Co-Ni



(c) Co-Cr

(d) Co-Mo

Fig. 7.5 SEM images of (a) Co-Sn (b) Co-Cr (c) Co-Ni (d) Co-Mo catalysts.

SEM images of Co-Ni, Co-Sn, Co-Cr and Co-Mo catalysts prepared by borohydride reduction followed by annealing at 623 K are shown in Fig. 7.5 (a), (b), (c) and (d) respectively. As can be seen from the micrograph for Co-Sn catalyst particles are spherical in shape and each particle contain lot of grains which are aggregated to give bigger particles. As it is evident from the images (Fig. 7.5a), the smaller particles are aggregated into a fine powder in the case of both Co-Ni (Fig. 7.5b) and Co-Cr (Fig. 7.5c) catalysts. All particles are in nanometer range. Compared to other catalysts different morphology was observed for the Co-Mo catalyst (Fig. 7.5d). It shows of fibers like particles joining together to form flower like structures.

7.4.2 Calibration of catalytic activity:

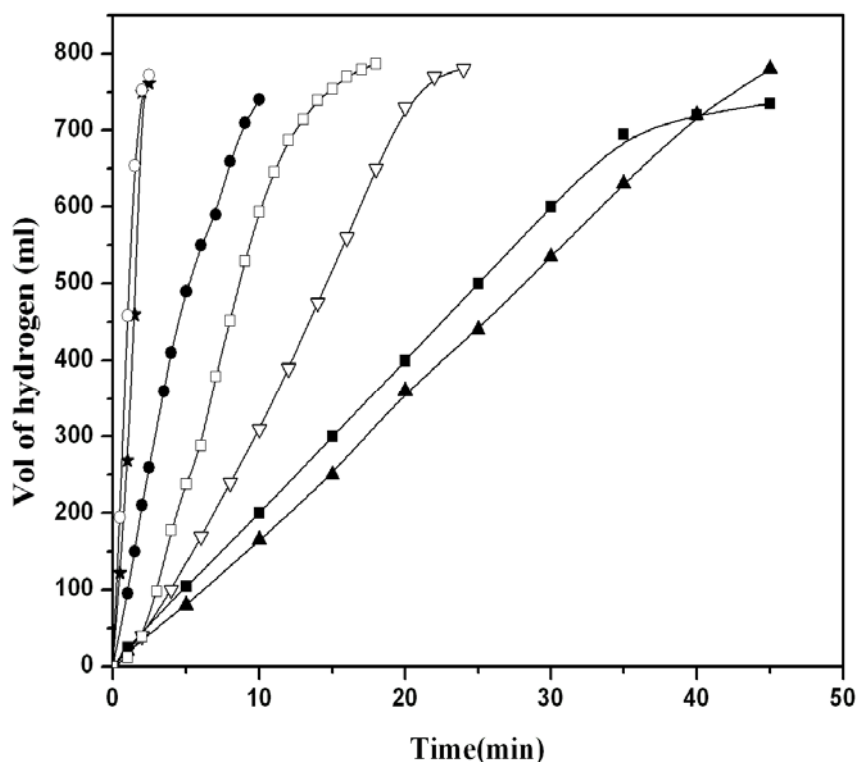


Fig. 7.6 Catalytic performance of cobalt based catalysts (■) Co- commercial (▲) Co-Ni commercial (▽) Co (●) Co-Ni (□) Co-Sn (★) CoCr (○) Co-Mo and (20 ml of 1.5 wt. % NaBH_4 + 4 wt. % NaOH).

In all the measurements, 0.1g of catalyst was taken in the reaction vessel, then the reactor was introduced in the thermostatic bath for about 15 min, after that 20 ml of 1.5 wt. % NaBH_4 + 4 wt. % NaOH solution was rapidly injected with 20 ml syringe. The liberated hydrogen was measured with respect to time from the volume of water displaced in the gas burette. Hydrogen gas was generated from sodium borohydride solution with rapid rate. All the catalysts display good catalytic activity for hydrolysis reaction. Compared to commercial Co and Co-Ni powder samples as synthesized catalysts are more effective. The hydrogen evolution rates for different catalysts obtained from Fig. 7.6 are given in Table 7.1. Among the examined catalysts Co-Mo has shown higher catalytic activity compared to other catalysts. Moreover, Co-M systems (M=Mo, Cr and Ni) are more active than Co alone.

Table 7.1 Hydrogen evolution rates for various catalysts; solution mixture: 1.5 wt. % NaBH_4 + 10 wt. % NaOH

Catalyst	Hydrogen evolution rate (ml/min) At room temperature
Commercial Co	20
Commercial Co-Ni mixture	13
Co	100
Co-Ni	205
Co-Sn	72.6
Co-Cr	370.6
Co-Mo	459.2

The catalysts form three different groups namely metal (Co), solid solution/alloy (Co-Ni, CoSn) and metal-metal oxides (Co-Cr and Co-Mo). The hydrogen evolution rate for of Co-Sn system is lower compared to other catalysts prepared under similar conditions. This may be because of larger particles size of CoSn alloy as observed

from SEM images. Co-Ni shows better catalytic activity when compared to Co catalyst. Similar observation has been reported by Hua *et al.*, (2003). As Co-Cr and Co-Mo forms metal- metal oxides system superior catalytic activity is observed for these systems. The higher activity of Co-Mo system can be attributed to its typical morphology which can have large number of reactive sites.

7.4.3 Effect of NaOH concentration on hydrogen evolution rate:

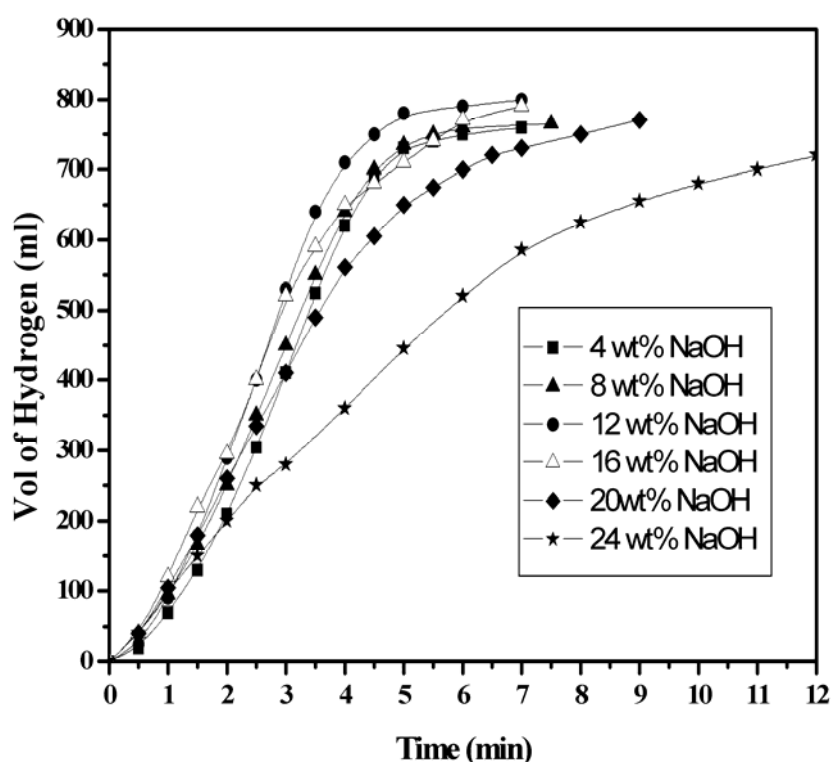


Fig. 7.7 Effects of NaOH concentration on the hydrogen evolution rate measured using 20 ml of x wt. % NaOH + 1.5 wt. % NaBH₄ solutions ($x = 4, 8, 12, 16, 20, 24$) at room temperature using 0.1 g of Co-Ni catalyst.

The results of the study on the dependence of the hydrolysis reaction rate on NaOH concentration is given in Fig. 7.7. In all cases, the amount of hydrogen generated increases linearly with increasing reaction time at the initial stage of hydrolysis reaction. However, as shown in Fig. 7.7, the hydrogen evolution curve gradually deviates from the linear relationship as the hydrolysis reaction proceeds. The gradual

decline in hydrogen evolution rate over time may be due to accumulation of the hydrolysis product (NaBO_2) at the catalyst surface that block the borohydride solution from contact with the catalyst. The reaction rate is enhanced by the increase of NaOH concentration.

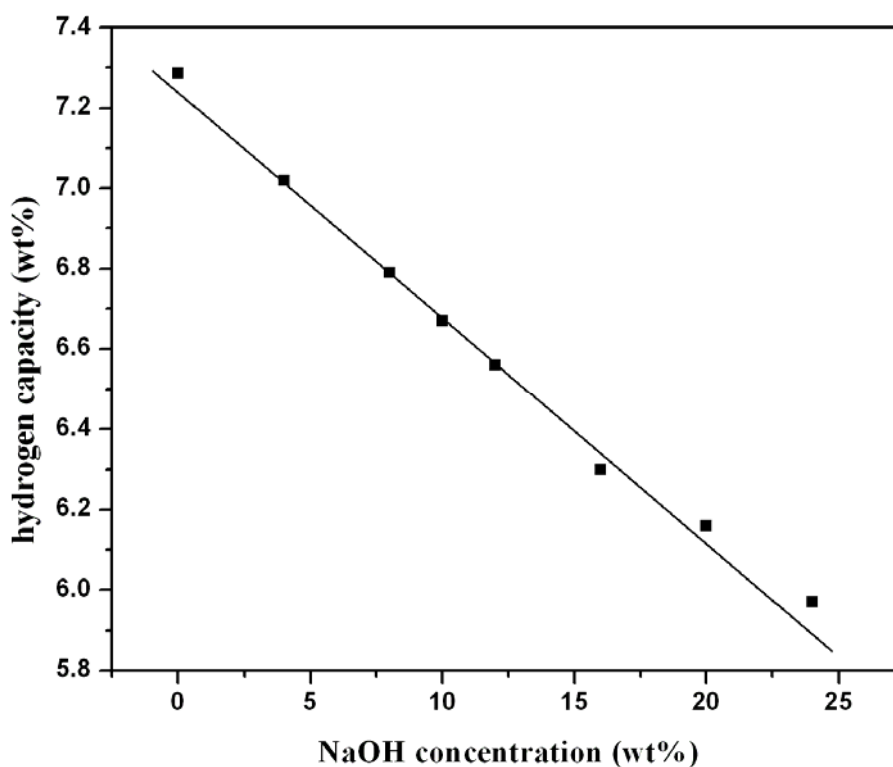


Fig. 7.8 Hydrogen storage capacity of the $\text{NaBH}_4 + \text{NaOH}$ solution system as a function of the NaOH concentration

The reaction rate increases with increasing NaOH concentration up to 12 wt. % and then decreases. This may be because at higher concentration of alkali, the solubility of NaBO_2 is low. Moreover, as shown in Fig. 7.8, as the sodium hydroxide concentration increases total hydrogen released decreases. The optimum value of NaOH is around 8 – 12 wt. % of NaOH. The extent of hydrogen release can be achieved up to 6.8 wt. % in 8 wt. % NaOH solutions and 6.65 wt. % in 10 wt. % NaOH solutions. It is difficult to explain the role of NaOH on the hydrolysis reaction at this stage. To firmly establish effect of NaOH further investigations are required. In the absence of catalyst

it inhibits the reaction and stabilizes the borohydride ions while in the presence of catalyst it accelerates the rate of hydrolysis. As the concentration increases, solution becomes viscous, the water molecules get solvated thus the reaction rate decreases at the higher concentrations of sodium hydroxide.

7.4.4 Effect of temperature hydrogen evolution rate:

The catalysts are active even at low temperature (283 K). Reaction begins immediately after adding the solution to the catalyst. The influence of temperature on the rate of the hydrogen evolution for the all the catalysts was studied. The reaction rate is sensitive to this variable. As expected, the rate increases with increase in temperature. The influence of temperature is clearly shown by the increasing slope values on the linear region of the plots, for increasing values of the reaction temperature.

The plot of volume of hydrogen evolved vs. time at different temperatures for the CoSn catalyst is shown in Fig. 7.9. The solution mixture is 1.5 wt. % NaBH₄ + 10 wt. % NaOH. The reaction rates at different temperatures for other catalysts are given in Table 7.2. The hydrogen evolution rates at various temperatures are used to determine the activation energy. The activation energy was calculated by plotting $\log k$ vs. $1/T$ for the hydrogen evolution process for Co-Sn, Co-Cr and Co-Mo catalysts (refer to Fig. 7.10). The values of activation energies for Co, Co-Ni catalysts for the sodium borohydride hydrolysis were calculated and are given in Table 7.3. The activation energies are comparatively low for Co-Ni and CoSn catalysts than for Co-Cr and Co-Mo and Co but the reaction rates are high for Co-Cr and Co-Mo systems. This indicates that the hydrolysis reaction follows different path in Co-Mo and Co-Cr catalysts.

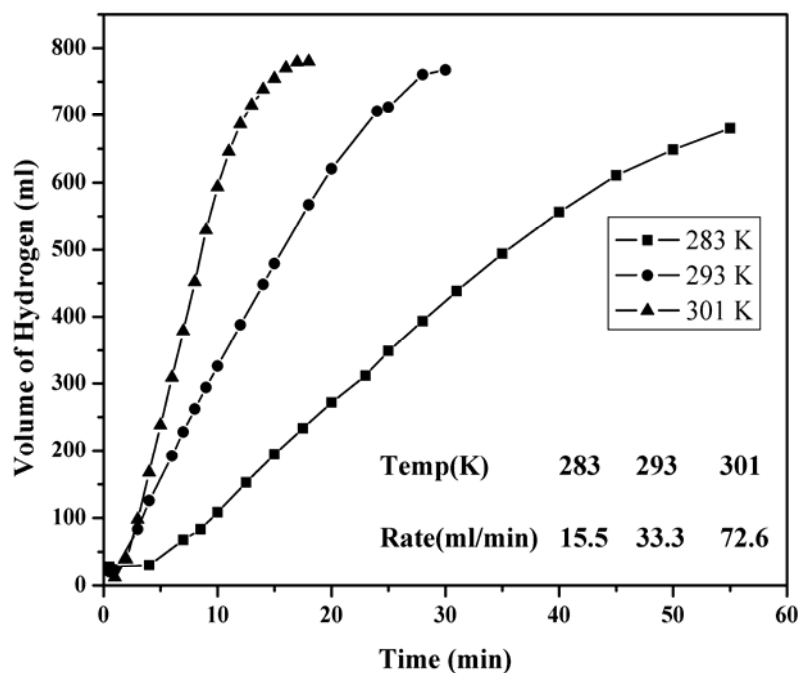


Fig. 7.9 Effect of solution temperature on the hydrogen evolution rate, measured from 1.5 wt. % NaBH_4 + 10 wt. % NaOH solutions using 0.1 g of CoSn catalyst.

Kojima *et al.* (2002) reported the catalytic activity of metal catalyst coated on metal oxide and the catalytic activity was attributed to the functional groups of metal oxide. Mo can be present as MoO_x in Co-Mo catalyst that can act as oxygen source; it induces the surface hydroxyl groups and these hydroxyl groups further reacts with the borohydride anion which is adsorbed on the Cobalt metal surface. The hydroxyl groups are weakly bound to the surface of MoO_x where as strongly adsorbed in the case of metals hence the reaction rate will be faster for Co-Mo compared to Co-Ni or Co-Sn catalysts. In addition the morphology of Co-Mo system can promote the hydrolysis reaction with large number of active sites.

Table 7.2 Hydrogen evolution rates for the Co-Ni, Co-Sn and Co-Mo catalysts at different temperatures from solution mixture of 20 ml of 1.5 wt. % NaBH_4 + 10 wt. % NaOH.

Catalyst: 0.1 g Co-Ni	
Solution temperature (K)	Hydrogen evolution rate (ml/min)
294.5	165
300	205
309.5	290
313	400
320	470
Catalyst: 0.1 g Co-Cr	
283	66.8
293	169.2
301	370.6
Catalyst: 0.1 g Co-Mo	
283	120.2
293	205.6
301	459.2
Catalyst : 0.1 g Co-Sn	
283	15.5
293	33.3
301	72.6

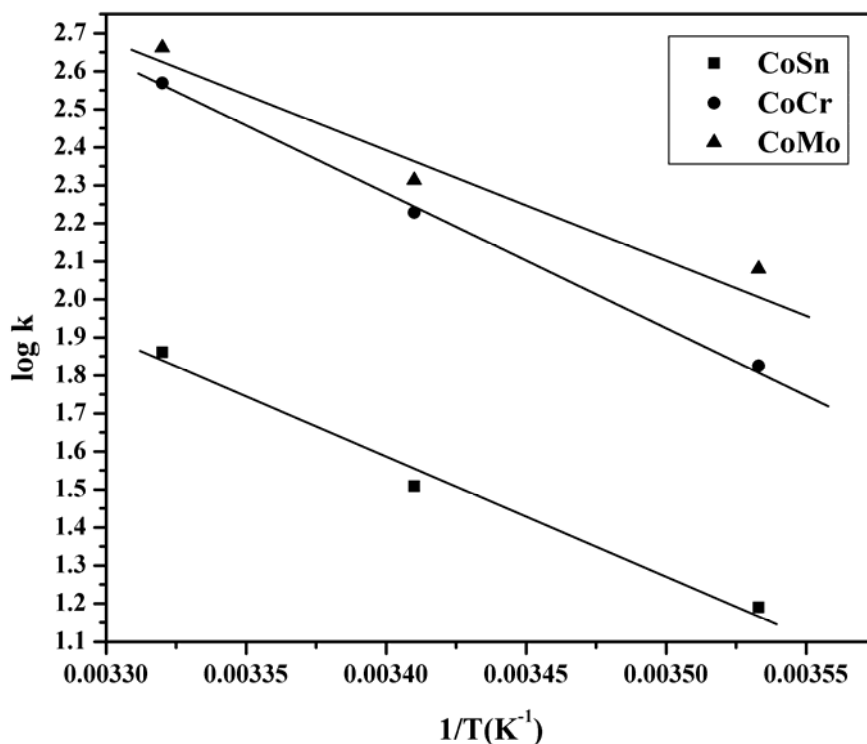


Fig. 7.10 Arrhenius plots of the Co-Sn, Co-Cr Co-Mo catalysts for hydrogen evolution

Table 7.3 Activation energies and borohydride hydrolysis rate for cobalt based catalysts.

Catalyst	Activation energy (kJ/mol)	Reference
Co-B	65	Jeong <i>et al.</i> , 2005
Raney Ni	63	Kaufman and Sen, 1985
Raney Co-Ni	52.5	Liu <i>et al.</i> , 2006
Ru	47	Amendola <i>et al.</i> , 2000b
Co	60	This work
Co-Ni	36.4	This work
Co-Cr	61.2	This work
Co-Mo	74.2	This work
Co-Sn	57.6	This work

To study the reusability of the catalyst, the catalyst used in the particular reaction was removed from the reaction mixture by filtration and then washed and dried. The catalyst was regenerated by heating in hydrogen atmosphere at 573 K for 3 h before its reuse in the reaction. The Co-MoO_x catalyst can be recovered and reused in further reaction without any significant degradation in activity. Although the catalytic activity was gradually diminished, a conversion of over 90% was still achieved after 100 h.

CHAPTER 8

SUMMARY AND CONCLUSIONS

The main objective of the present study is to find suitable material for hydrogen storage. A general overview of the potential storage methods together with their possibilities and limitations is presented. Use of metal hydrides as hydrogen storage materials is emphasized. Among various metal hydrides light weight metal hydrides like MgH_2 , alanates and borohydrides are viable options. However the aforementioned materials require high temperatures for hydrogen desorption. Also the kinetics of hydrogen uptake/release is poor. Therefore the present study focused on improving the hydrogen storage properties of Mg and Mg_2Ni , sodium and lithium alanates and sodium borohydride. This can be achieved by preparing the materials in nanosize and/or addition of a catalyst.

Polyol reduction method is used to synthesize nanosized Mg_2Ni . Addition of transition metal catalysts, because of their high molecular weight will decrease the storage capacity of alanates/Mg. Hence the search is towards low molecular weight catalysts. Carbon materials, especially, nanofibers and nanotubes with heteroatoms like boron and nitrogen is a better option as a catalyst for the decomposition of alanates. Addition of carbon materials enhances grain boundaries and interfaces where hydrogenation and dehydrogenation takes place. More over, carbon materials not only facilitate hydrogen sorption but also enhance transport of the species involved in the reaction, by forming ad-lineation layer between the active center and metal hydrides.

Carbon nanofibers were synthesized by using Ni-Cu (7:3 (at/at %)) alloy supported on H-ZSM-5 as catalyst and using ethylene as carbon source. Nitrogen containing carbon nanotubes were prepared by template method using alumina membrane as template and PVP as carbon source. Nitrogen containing carbon was synthesized by the decomposition of PVP and FeCl₂ composite. Thus a series of carbon materials have chosen logically starting from commercially available carbons (Vulcan XC72, Black Pearls 2000, mesoporous carbon and CDX975) followed by nanocarbons (fibers) and successively the hetero atom (boron and nitrogen) containing carbon to individually evaluate the role and utility of each of the types of carbon materials.

By using different carbon materials, metal hydride and carbon composites were prepared. These materials were characterized by XRD, SEM, TEM, IR and DSC and by absorption measurements (kinetic measurements set-up was fabricated). The role of carbon additives in dehydrogenation and rehydrogenation reactions of alanates was also addressed. Borohydride decomposes at high temperatures compared to alanates; hence, thermal decomposition is not possible route for practical use. The other way of producing hydrogen is hydrolysis. The hydrolysis of NaBH₄ using cobalt based catalysts was studied. The effect of temperature and NaOH concentration on the hydrogen generation rate was studied.

The conclusions drawn from this study are:

- Polyol reduction method is an alternative route to synthesize nanocrystalline / amorphous alloys. Nanosize Mg₂Ni alloy, synthesized by polyol reduction and subsequent annealing at 573 K has shown promising hydrogen absorption as well as electrochemical hydrogen absorption characteristics.

- The maximum hydrogen storage capacity observed is 3.23 wt. % at 603 K. Nano Mg₂Ni alloy absorbed 3.2 wt. % of hydrogen within a 1 min at 573 K and 2.5 MPa pressure of hydrogen. Further, it desorbed 2.8 wt. % of hydrogen in 15 min at 573 K and atmospheric pressure.. The enthalpy and entropy of formation for hydrogen absorption and desorption are -50.03 kJ/mol, -103.60 J/(mol K) for absorption and 56.35 kJ/mol, 105.36 J/(mol K) respectively.
- The maximum discharge capacity is 408 mAh/g at a discharge current density of 20 mA/g. The materials show good stability for degradation. After 15 cycles, reduction in discharge capacity is only 32% of initial discharge capacity.
- Carbon materials like Vulcan XC72R (250 m² g⁻¹), Black Pearls 2000 (1500 m² g⁻¹), CDX 975 (240 m² g⁻¹) and mesoporous carbon (1400 m² g⁻¹) and carbon nanofibers enhanced the dehydrogenation kinetics of LiAlH₄. Dehydrogenation rate increased with increasing carbon content. The optimum carbon content is 10 wt. %.
- Addition of CNFs to Lithium aluminum hydride improved the decomposition kinetics significantly by increasing the grain boundaries and also by providing the transition site for hydrogen transfer. The apparent activation energy of dehydrogenation is considerably lowered by the addition of carbon nanofibers. The apparent activation energy E_a for the dehydrogenation of CNFs admixed LiAlH₄ is 45 ± 0.2 kJ/mol.
- LiAlH₄ doped with 5 wt. % CNFs and 3 mol % VCl₃ exhibited rehydrogenation capacity of 3.9 wt% of hydrogen at 373 K and 20 bar pressure.

- Activation centers (where adsorption and dissociation of hydrogen takes place) are required to facilitate rehydrogenation of dehydrogenated alanates.
- Addition of NCNT to sodium aluminum hydride resulted in lowering of its decomposition temperature by 28 K for first step decomposition and 22 K for the second step decomposition, respectively. Where as for the lithium aluminum hydride, first and second step decomposition temperatures were shifted to lower temperature by 10 K.
- Dehydrogenation kinetics of sodium and lithium aluminum hydrides was improved by the addition of NCNT. NAH-NCNT composite released 5.3 wt. % of hydrogen in 150 min where as LAH-NCNT composite released 6.8 wt. % of hydrogen in 15 min.
- Activation energies for the decomposition reactions of NAH, NAH-NCNT composite, LAH and LAH-NCNT composites were deduced by using Kissinger method. It was found that addition of NCNT lowers the activation energy for the dehydrogenation compared to pure NaAlH_4
- Activation energies obtained from constant temperature experiments and Kissinger method are found to be nearly equal.
- Addition of NCNT to sodium aluminum hydride shifted the Al-H stretching frequency to the higher energy side by 30 cm^{-1}
- NaAlH_4 was rehydrogenated to give 4 wt. % of hydrogen reversibly at 473 K and at a hydrogen pressure of 8 MPa.
- Nitrogen containing carbon materials showed good catalytic activity in improving the sorption properties of magnesium in comparison to either boron containing carbon or graphite. Addition of nitrogen containing carbon resulted in the lowering of dehydriding temperature of MgH_2 by 20 K.

- Metal (Co), metal alloy (Co-Sn and Co-Ni) and metal-metal oxide (Co-Mo and Co-Cr) were evaluated for hydrogen evolution reaction for sodium borohydride. Among afore mentioned catalytic systems, metal-metal oxide systems especially Co-Mo catalyst exhibited good catalytic activity.
- The optimum concentration of NaOH is found to be 8-12 wt. % for better hydrogen evolution rate from sodium borohydride.

SUGGESTIONS FOR THE FUTURE WORK:

- Addition of nitrogen containing carbon nanotubes made the rehydrogenation possible for dehydrogenated NaAlH₄. This knowledge can be extended further to other complex metal hydrides.
- Nitrogen containing carbon materials decreased the decomposition temperature of MgH₂ as well as NaAlH₄ by 20 – 30 K respectively, but still it is has to be lowered. Both magnesium and nitrogen containing carbon materials has to be prepared in nanosize. The physical parameters like morphology and chemical parameters like nitrogen content in the carbon materials have to be optimized.
- Cobalt based catalysts have the potential for practical application for the generation of hydrogen and holds a promise for fuel cell applications.

REFERENCES

1. **Abdellaoui, M., D. Cracco and A.P. Guegan** (1998) Structural characterization and reversible hydrogen absorption properties of Mg₂Ni rich nanocomposite materials synthesized by mechanical alloying, *J. Alloys Compd.*, **268**, 233–240.
2. **Abdellaoui, M., S. Mokbli, F. Cuevas, M. Latroche, A.P. Guegan and H. Zarrouk** (2006) Structural, solid–gas and electrochemical characterization of Mg₂Ni-rich and Mg_xNi_{100-x} amorphous-rich nanomaterials obtained by mechanical alloying. *Int. J. Hydrogen Energy*, **31**, 247–250.
3. **Abe, T., T. Tachikawa, Y. Hatano and K. Watanabe** (2002) Electrochemical behavior of amorphous Mg₂Ni as negative electrodes in rechargeable Ni–MH batteries. *J. Alloys Compd.*, **330–332**, 792–795.
4. **Aiello, R., J.H. Sharp and M.A. Matthews** (1999) Production of hydrogen from chemical hydrides via hydrolysis with steam. *Int. J. Hydrogen Energy*, **24**, 1123–1130.
5. **Akiyama, T., H. Isogai and J. Yagi** (1998) Reaction rate of combustion synthesis of an intermetallic compound. *Powder Technol.*, **95**, 175-181.
6. **Amendola, S.C., S.L. Sharp-Goldman, M.S. Janjua, N.C. Spencer, M.T. Kelly, P.J. Petillo and M. Binder** (2000a) A safe hydrogen generator using aqueous borohydride solutions and Ru catalyst, *Int. J. Hydrogen Energy*, **25**, 969-975.
7. **Amendola, S.C., S.L. Sharp-Goldman, M.S. Janjua, N.C. Spencer, M.T. Kelly, P.J. Petillo and M. Binder** (2000b) An ultrasafe hydrogen generator: aqueous alkaline borohydride solutions and Ru catalyst. *J. Power Sources*, **85**, 186–189.
8. **Andreasen, A., T. Vegge and A.S. Pedersen** (2005) Dehydrogenation kinetics of as-received and ball-milled LiAlH₄. *J. Solid State Chem.*, **178**, 3672-3678.
9. **Anil Kumar, E., M. Prakash Maiya and S. Srinivasa Murthy** (2007) Influence of transient operating conditions on pressure-concentration isotherms and storage characteristics of hydriding alloys, *Int. J. Hydrogen Energy*, **32**, 2382-2389.
10. **Anton, D. L.** (2003) Hydrogen desorption kinetics in transition metal modified NaAlH₄, *J. Alloys Compd.*, **356-357**, 400-404.
11. **Armaroli, T., T. Bécue and S. Gautier** (2004) Diffuse Reflection Infrared Spectroscopy (DRIFTS): Application to the in situ Analysis of Catalysts. *Oil & Gas Science and Technology – Rev. IFP*, **59**, 215-237
12. **Ashby, E. C., G. J. Brendel and H.E. Redman** (1963) Direct Synthesis of Complex Metal Hydrides, *Inorg. Chem.*, **2**, 499-504.

13. **Ashby, E. C. and P. Kobetz** (1966) **The Direct Synthesis of Na₃AlH₆**, *Inorg. Chem.*, **5**, 1615-1617.
14. **Ashby, E. C., R. D. Schewartz and B. D. James** (1970) Preparation of magnesium aluminum hydride. Reactions of lithium and sodium aluminum hydrides with magnesium halides in ether solvents, *Inorg. Chem.*, **9**, 325-332.
15. **Avrami, M.** (1939) Kinetics of phase changes. I: General theory, *J. Chem. Phys.*, **7**, 1103-1112.
16. **Avrami, M.**, (1940) Kinetics of phase change: II. Transformation-time relations for random distribution of nuclei. *J. Chem. Phys.*, **8**, 212-24.
17. **Avrami, M.** (1941) Granulation, phase change and microstructure. Kinetics of phase change. III. *J. Chem. Phys.*, **9**, 177-84.
18. **Aymard, L., M. Ichitsubo, K. Uchida, E. Sekreta and F. Ikazaki** (1997) Preparation of Mg₂Ni alloy by the combination of mechanical alloying and heat treatment at low temperature. *J. Alloys Compd.*, **259**, L5–L8.
19. **Bai, Y., C. Wu, F. Wu and B. Yi** (2006) Carbon-supported platinum catalysts for on-site hydrogen generation from NaBH₄ solution. *Mater. Lett.*, **60**, 2236-2239.
20. **Balde, C.P., P.C.H. Bart, H.B. Johannes and P. de Jong Krijn** (2006) Facilitated hydrogen storage in NaAlH₄ supported on carbon nanofibers. *Angew. Chem. Int. Ed.*, **45**, 3501-3503.
21. **Balema, V. P., J. W. Wiench, K. W. Dennis, M. Pruski and V. K. Pecharsky** (2001) Titanium catalyzed solid-state transformations in LiAlH₄ during high-energy ball-milling, *J. Alloys Compd.*, **329**, 108-114.
22. **Balema, V.P., K.W. Dennis and V.K. Pecharsky** (2000b) Titanium catalyzed solid-state transformations in LiAlH₄ during high-energy ball-milling. *Chem. Comm.*, **17**, 1665-1666.
23. **Balema, V.P., V.K. Pecharsky and K.W. Dennis** (2000a) Solid state phase transformation in LiAlH₄ during high-energy ball milling. *J. Alloys Compd.*, **313**, 69–74.
24. **Balogh, M.P., G.G. Tibbetts, F.E. Pinkerton, G.P. Meisner and C.H. Olk** (2003) Phase changes and hydrogen release during decomposition of sodium alanates. *J. Alloys Compd.* **350**, 136-144.
25. **Barkhordarian, G., T. Klassen and R. Bormann** (2004) Effect of Nb₂O₅ content on hydrogen reaction kinetics of Mg. *J. Alloys Compd.*, **364**, 242-246.
26. **Bassetti, A., E. Bonetti, L. Pasquini, A. Montone, J. Grbović and M.V. Antisari** (2005) Hydrogen desorption from ball milled MgH₂ catalyzed with Fe. *Eur. Phys. J. B* **43**, 19–27.

27. **Best R.J. and W.W. Russell** (1954) Nickel, copper and some of their alloys as catalysts for ethylene hydrogenation. *J. Am. Chem. Soc.*, **76**, 838 -842.
28. **Blanchard, D., H.W. Brinks, B.C. Hauback and P. Norby** (2004) Desorption of LiAlH₄ with Ti- and V-based additives. *Mater. Sci. Eng. B* **108**, 54–59.
29. **Blanchard, D., H.W. Brinks, B.C. Hauback, P. Norby and J. Muller** (2005) Isothermal decomposition of LiAlD₄ with and without additives. *J. Alloys Compd.*, **404–406**, 743–747.
30. **Block, J. and A. P. Gray** (1965) The thermal decomposition of lithium aluminum hydride, *Inorg. Chem.*, **4**, 304-305.
31. **Bobet, J.L., B. Chevalier and B. Darriet** (2002) Effect of reactive mechanical grinding on chemical and hydrogen sorption properties of the Mg +10 wt. % Co mixture. *J. Alloys Compd.*, **330–332**, 738–742.
32. **Bobet, J.-L., E. Grigorova, M. Khrussanova, M. Khristov, P. Stefanov, P. Peshev and D. Radev** (2004) Hydrogen sorption properties of graphite-modified magnesium nanocomposites prepared by ball-milling. *J. Alloys Compd.*, **366**, 298–302.
33. **Bobet, J.-L., S.D. Krawiec, E. Grigorova, F. Cansell and B. Chevalier** (2003) Addition of nanosized Cr₂O₃ to magnesium for improvement of the hydrogen sorption properties. *J. Alloys Compd.*, **351**, 217–221.
34. **Bogdanovic, B. and M. J. Schwickardi** (1997) Ti-doped alkali metal aluminium hydrides as potential novel reversible hydrogen storage materials, *J. Alloys Compd.*, **253**, 1-9.
35. **Bogdanovic, B., M. Felderhoff, M. Germann, M. Härtel, A. Pommerin, F. Schüth, C. Weidenthaler and B. Zibrowius** (2003) Investigation of hydrogen discharging and recharging processes of Ti-doped NaAlH₄ by X-ray diffraction analysis (XRD) and solid-state NMR spectroscopy. *J. Alloys Compd.*, **350**, 246-255.
36. **Bogdanovic, B., R. A. Brand, A. Marjanovic, M. Schwickardi and J. Tölle** (2000) Metal-doped sodium aluminium hydrides as potential new hydrogen storage materials, *J. Alloys Compd.*, **302**, 36-58.
37. **Bouaricha, S., J.-P. Dodelet, D. Guay, J. Huot and R. Schulz** (2001a) Activation characteristics of graphite modified hydrogen absorbing material. *J. Alloys Compd.*, **325**, 245-251.
38. **Bouaricha, S., J.-P. Dodelet, D. Guay, J. Huot and R. Schulz** (2001b) Study of the activation process of Mg-based hydrogen storage materials modified by graphite and other carbonaceous compounds. *J. Mater. Res.*, **16**, 2893–2905
39. **Brinks, H. W. and B. C. Hauback** (2003) The structure of Li₃AlD₆, *J. Alloys Compd.*, **354**, 143-147.

40. **Brown, H.C. and C.A. Brown** (1962) New, highly active metal catalysts for the hydrolysis of borohydride. *J. Am. Chem. Soc.*, **84**, 1493-1494.
41. **Bureau, J.-C., Z. Amri, P. Claudy and J.-M. Letoffe** (1989), Comparative Study of Lithium and Sodium Hexahydrido- and Hexadeuteridoaluminates, I - IR and Raman spectra of Li_3 - and Na_3AlH_6 and Li_3AlD_6 . *Mat. Res. Bull.*, **24**, 23-31.
42. **Bulychev, B. M., V. N. Verbitskii and V. N. Semenko** (1970) *Russ. J. Inorg. Chem.*, **22**, 1611.
43. **Cao, A., H. Zhu, X. Zhang, X. Li, D. Ruan, C. Xu, B. Wei, L. Liang and D. Wu** (2001) Hydrogen storage of dense-aligned carbon nanotubes. *Chem. Phys. Lett.*, **342**, 510-514.
44. **Chambers, A., C. Parks, R. T. K. Baker and N. M. Rodriguez** (1998) Hydrogen storage in graphite nanofibers. *J. Phys. Chem. B* **102**, 4253-4256.
45. **Che, R., L.M. Peng, Q. Chen, X.F. Duan and Z.N. Gu** (2003) Fe_2O_3 particles encapsulated inside aligned CN_x nanotubes. *Appl. Phys. Lett.*, **82** 19, 3319-3321.
46. **Chen, B. and J.L. Falconer** (1998) Spillover rate from Pd to Al_2O_3 . *J. Catal.*, **134**, 737-741.
47. **Chen, C.-M., and J.-M. Jehng**, (2004) Amination application over nano-Mg-Ni hydrogen storage alloy catalysts. *Applied Catal., A* **267**, 103-110.
48. **Chen, D., L. Chen, S. Liu, C.X. Ma, D.M. Chen and L.B. Wang**, (2004) Microstructure and hydrogen storage property of Mg/MWNTs composites. *J. Alloys Compd.*, **372**, 231-237.
49. **Chen, J., N. Kuriyama, Q. Xu, H.T. Takeshita and T. Sakai** (2001) Reversible hydrogen storage via titanium-catalyzed LiAlH_4 and Li_3AlH_6 . *J. Phys. Chem. B* **105**, 11214-11220
50. **Chen, J., S.X. Dou and H.K. Liu** (1996) Crystalline Mg_2Ni obtained by mechanical alloying. *J. Alloys Compd.*, **244**, 184-189.
51. **Chen, P., X. Wu, J. Lin and K.L. Tan** (1999) High H_2 uptake by alkali-doped carbon nanotubes under ambient pressure and moderate temperatures, *Science*, **285**, 91-93.
52. **Chen, P., X. Wu, X. Sun, J. Lin, W. Ji, and K. L. Tan** (1999) Electronic Structure and Optical Limiting Behavior of Carbon Nanotubes. *Physical Review Letters*, **82**, 2548-2551.
53. **Cheng, H.M., C. Liu, Y.Y. Fan, F. Li, G. Su, L.L. He and M. Liu** (2000) Synthesis and hydrogen storage of carbon nanofibers and single-walled carbon nanotubes. *Z. Metallkd.*, **91**, 306-310.

54. **Chidambaram, V. and B. Viswanathan** (2007) Single step catalytic production of diisopropyl ether (DIPE) from acetone feedstock over nickel based catalysts. *Appl. Catal., B* **71**, 32-43.
55. **Chung, S.C. and H. Morioka** (2004) Thermochemistry and crystal structures of lithium, sodium and potassium alanates as determined by ab initio simulations. *J. Alloys Compd.*, **372**, 92-96.
56. **Clasen, H.** (1961) Synthesis of alanates and its significance, *Angew. Chem.*, **73**, 322-331.
57. **Claudy, P., B. Bonnetot, J. P. Bastide and J. M. Letoffe** (1979) Preparation and physical and chemical properties of magnesium alanate of Mg (AlH₄)₂. *J. Therm. Anal.*, **15**, 119-128.
58. **Claudy, P., B. Bonnetot, G. Chahine and J. M. Letoffe** (1980) Study of the thermal behavior of sodium tetrahydroaluminate NaAlH₄ and sodium hexahydroaluminate Na₃AlH₆ at 298-600 K. *Thermochim. Acta*, **38**, 75-88.
59. **Claudy, P., B. Bonnetot, J. P. Bastide and J. M. Letoffe** (1982) Reactions of lithium and sodium aluminium hydride with sodium or lithium hydride. Preparation of a new alumino-hydride of lithium and sodium LiNa₂AlH₆. *Mater. Res. Bull.*, **17**, 1499-1504.
60. **Colomer, J.F., P. Piedigrosso, A. Fonseca and J.B. Nagy** (1999) Different purification methods of carbon nanotubes produced by catalytic synthesis. *Synthetic Met.*, **103**, 2482-2483.
61. **Cui, N., B. Luan and H.K. Liu** (1995) Characteristics of magnesium-based hydrogen-storage alloy electrodes. *J. Power Sources*, **55**, 263-267.
62. **Darok, X., A. Rougier, V. Bhat, L. Aymard, L. Dupont, L. Laffont, and J.-M. Tarascon** (2006) Benefits of carbon addition on the hydrogen absorption properties of Mg-based thin films grown by Pulsed Laser Deposition. *Thin Solid Films*, **515**, 1299-1306
63. **de Castro, J.F.R., S.F. Santos, A.L.M. Costa, A.R. Yavari, W.J.F. Botta and T.T. Ishikawa** (2004) Structural characterization and dehydrogenation behavior of Mg-5 at.%Nb nano-composite processed by reactive milling. *J. Alloys Compd.*, **376**, 251-256.
64. **Dehouche, Z., L. Lafi, N. Grimard, J. Goyette and R. Chahine** (2005) The catalytic effect of single-wall carbon nanotubes on the hydrogen sorption properties of sodium alanates. *Nanotechnology*, **16**, 402-409.
65. **Dillon, A.C., K.M. Jones, T.M. Bekkedahl, C.H. Kaing, C.S. Bethune and M.J. Heben** (1997) Storage of hydrogen in single-walled carbon nanotubes. *Nature*, **386**, 377-379.
66. **Dilts, J.A. and E.C. Ashby** (1972) Thermal decomposition of complex metal hydrides. *Inorg. Chem.*, **11**, 1230-1236.

67. **Dunn, S.** (2002) Hydrogen futures toward a sustainable energy system, *Int. J. Hydrogen Energy*, **27**, 235-264.
68. **Dymova, T.N.** and **S.I. Bakum** (1969) Thermal decomposition of potassium and sodium hydroaluminates. *Russ. J. Inorg. Chem.*, **14**, 3190-3195.
69. **Dymova, T. N., N.G. Eliseeva, S.I. Bakum, Yu.M. Dergachev** (1974) direct synthesis of alkali metal tetrahydroaluminates in melts. *Dokl. Akad. Nauk SSSR*, **215**, 1369-1372.
70. **Dymova, T.N., D.P. Aleksandrov, V.N. Konoplev, T.A. Silina** and **N.T. Kuznetsov** (1993) Solid-phase reaction of crystalline aluminum trihydride. Formation of alkali metal tetra- and hexahydroaluminates. *Russ. J. Coord. Chem.*, **19**, 529-534.
71. **Dymova, T.N., D.P. Aleksandrov, V.N. Konoplev, T.A. Silina** and **A.S. Sizareva** (1994) Spontaneous and thermal decomposition of lithium tetrahydroaluminate LiAlH_4 : Promoting effect of mechanochemical action on the process. *Russ. J. Coord. Chem.*, **20**, 279-285.
72. **Dehouche, Z., L. Lafi, N. Grimard, J. Goyette** and **R. Chahine** (2005) The catalytic effect of single-wall carbon nanotubes on the hydrogen sorption properties of sodium alanates. *Nanotechnology* **16**, 402-409.
73. **Easton, D.S., J.H. Schneibel** and **S.A. Speakman** (2005) Factors affecting hydrogen release from lithium alanate (LiAlH_4). *J. Alloys and Compd.*, **398**, 245-248.
74. **Elder, J.P.** and **M.B. Harris** (1984) Thermogravimetry and differential scanning calorimetry of Kentucky bituminous coals. *Fuel*, **63**, 262-267.
75. **Fan, Y.-Y., B. Liao, Y.-L. Wei, M.-Q. Lu** and **H.M. Cheng** (1999) Hydrogen uptake in vapor-grown carbon nanofibers, *Carbon*, **37**, 1649-1652.
76. **Fievet, F., J. P. Lagier, B. Blin, B. Beaudoin,** and **M. Figlarz** (1989) "Homogeneous and heterogeneous nucleations in the polyol process for the preparation of micron and submicron size metal particles. *Solid State Ionics*, **32-33**, 198-205.
77. **Finholt, A.E. A.C. Bond Jr.** and **H.I. Schlesinger**, Lithium Aluminum Hydride, Aluminum Hydride and Lithium Gallium Hydride, and Some of their Applications in Organic and Inorganic Chemistry. *J. Am. Chem. Soc.*, **69** (1947) 1199-1205.
78. **Gomes, S., G. Renaudin, H. Hagemann, K. Yvon, M.P. Sulic** and **C.M. Jensen** (2005) Effects of milling, doping and cycling of NaAlH_4 studied by vibrational spectroscopy and X-ray diffraction. *J. Alloys and Compd.*, **390**, 305-313.
79. **Goo, N.H., J.H. Woo** and **K.S. Lee** (1999) The electrochemical hydriding properties of Mg-Ni-Zr amorphous alloy. *J. Alloys Compd.*, **288**, 286-293.

80. **Grobert, N., M. Terrones, S. Trasobares, K. Kordatos, H. Terrones, J. Olivares et al.** (2000) A novel route to aligned nanotubes and nanofibres using laser-patterned catalytic substrates. *Appl. Phys. A* **70**, 175–183.
81. **Grochala, W. and P.P. Edwards** (2004) Thermal Decomposition of the Non-Interstitial Hydrides for the Storage and Production of Hydrogen. *Chem. Rev.*, **104**, 1283-1315.
82. **Gross, K. J., E. H. Majzoub and S. W. Spangler** (2003) The effects of titanium precursors on hydriding properties of alanates. *J. Alloys Compd.*, 356-357, 423-428.
83. **Gross, K.J., G.J. Thomas and C.M. Jensen** (2002) Catalyzed alanates for hydrogen storage. *J. Alloys Compd.*, **330-332**, 683-690.
84. **Gross, K.J., S. Guthrie, S. Takara and G. Thomas** (2000) In-situ X-ray diffraction study of the decomposition of NaAlH₄. *J. Alloys Compd.* **297**, 270-281.
85. **Güther, V. and A. Otto** (1999) Recent developments in hydrogen storage applications based on metal hydrides. *J. Alloys Compd.*, **293-295**, 889-892.
86. **Hua, D., Y. Hanxi, A. Xinping and C. Chuansin** (2003) Hydrogen production from catalytic hydrolysis of sodium borohydride solution using nickel boride catalyst. *Int. J. Hydrogen Energy*, **28**, 1095-1100.
87. **Hauback, B. C., H. W. Brinks and H. Fjellvag** (2002) Accurate structure of LiAlD₄ studied by combined powder neutron and X-ray diffraction. *J. Alloys Compd.*, **346**, 184-189.
88. **Hauback, B.C., H.W. Brinks, C.M. Jensen, K. Murphy and A.J. Maeland** (2003) Neutron diffraction structure determination of NaAlD₄. *J. Alloys Compd.*, **358**, 142-145.
89. **Hirscher, M., M. Becher, M. Haluska, U.D. Weglikowska, A. Quintel and P. Bernier** (2001) Hydrogen storage in sonicated carbon materials. *Appl. Phys. A* **722**, 129–132.
90. **Hirscher, M., M. Becher, M. Haluska, A. Quintel, V. Skakalova and Y.M. Choi et al.**, (2002) Hydrogen storage in carbon nanostructures. *J. Alloys Compd.*, **330**, 654–658.
91. **Holstein, W.L.**, (1995) The roles of ordinary and Soret diffusion in the metal-catalyzed formation of filamentous carbon. *J. Catal.*, **152**, 42–45.
92. **Holtz, R.L. and M.A. Imam** (1997) Hydrogen storage capacity of submicron magnesium–nickel alloys. *J. Mater. Sci.*, **32**, 2267–2274.
93. **Hong, T.W. and Y.J. Kim** (2002) Fabrication and evaluation of hydriding/dehydriding behaviors of Mg–10 wt. % Ni alloys by rotation-cylinder method. *J. Alloys Compd.*, **333**, L1-L6.

94. **Huang, S.M., L.M. Dai and A.W.H. Mau** (1999) Patterned growth and contact transfer of well-aligned carbon nanotube films. *J. Phys. Chem. B* **103**, 4223–4227.
95. **Huang, Z.G., Z.P Guo, A. Calka, D. Wexler and H.K. Liu** (2007) Effects of carbon black, graphite and carbon nanotube additives on hydrogen storage properties of magnesium. *J. Alloys Compd.*, **427**, 94-100.
96. **Huot, J., G. Liang and R. Schulz** (2001) Mechanically alloyed metal hydride systems. *Appl. Phys. A: Mater. Sci. Process.*, **72**, 187-195.
97. **Huot, J., M.-L. Tremblay and R. Schulz** (2003) Synthesis of nanocrystalline hydrogen storage materials. *J Alloys Comp.*, **356–357**, 603–607.
98. **Huot, J., S. Boily, V. Guthier and R. Schulz** (1999) Synthesis of Na_3AlH_6 and $\text{Na}_2\text{LiAlH}_6$ by mechanical alloying. *J. Alloys Compd.*, **283**, 304-306.
99. **Ichikawa, T., S. Isobe, No Hanada and H. Fujii** (2004) Lithium nitride for reversible hydrogen storage. *J. Alloys Compd.*, **365**, 271-276.
100. **Ichikawa, T., K. Tokoyoda, H. Leng and H. Fujii** (2005) Hydrogen absorption properties of Li–Mg–N–H system, *J. Alloys Compd.*, **400**, 245-248.
101. **Imamura, H., K. Masanari, M. Kusuhara, H. Katsumoto, T. Sumi and Y. Sakata** (2005) High hydrogen storage capacity of nanosized magnesium synthesized by high energy ball-milling. *J. Alloys Compd.*, **386**, 211–216.
102. **Imamura, H., I. Kitazawa, Y. Tanabe and Y. Sakata** (2007) Hydrogen storage in carbon/Mg nanocomposites synthesized by ball milling. *Int. J. Hydrogen Energy*, **32**, 2408-2411.
103. **Imamura, H., M. Kusuhara, S. Minami, M. Matsumoto, K. Masanari, Y. Sakata, K. Itoh and T. Fukunaga** (2003) Carbon nanocomposites synthesized by high-energy mechanical milling of graphite and magnesium for hydrogen storage. *Acta Mater.* , **51**, 6407-6424.
104. **Imamura H. and N. Sakasai** (1995) Hydriding characteristics of Mg-based composites prepared using a ball mill. *J. Alloys Compd.*, **231**, 810–814.
105. **Imamura, H., N. Sakasai and K. Yi** (1996) Hydrogen absorption of Mg-based composites prepared by mechanical milling: factors affecting its characteristics. *J. Alloys Compd.*, **232**, 218–23.
106. **Imamura, H., S. Tabata, N. Shigetomi, Y. Takesue and Y. Sakata** (2002) Composites for hydrogen storage by mechanical grinding of graphite carbon and magnesium. *J. Alloys Compd.*, **330–332**, 579-583.
107. **Imamura, H., Y. Takesue, S. Tabata, N. Shigetomi, Y. Sakata and S. Tsuchiya** (1999) Hydrogen storage composites obtained by mechanical grinding of magnesium with graphite carbon, *Chem. Comm.*, 2277–2278.

108. **Imamura, H., Y. Takesue, T. Akimoto and S. Tabata** (1999) Hydrogen-absorbing magnesium composites prepared by mechanical grinding with graphite: effects of additives on composite structures and hydriding properties. *J. Alloys Comp.*, **293–295**, 564–568.
109. **Iwakura, C., S. Nohara, H. Inoue and Y. Fukumoto** (1996) Surface modification of MgNi alloy with graphite by ball-milling for use in nickel-metal hydride batteries. *Chem. Comm.*, 1831-1832.
110. **Iwakura, C., Y. Kajiya, H. Yoneyama, T. Saki, K. Oguro and H. Ishikawa** (1989) Self-discharge mechanism of nickel-hydrogen batteries using metal hydride anodes. *J. Electrochem. Soc.*, **136**, 1351.
111. **Jackson, K.A. (2004)** Kinetic processes: Crystal growth, diffusion and phase transformations in materials, Wiley-VCH, Weinheim.
112. **Janot, R., L. Aymard, A. Rougier, G.A. Nazri and J.-M. Tarascon** (2004) Fast Hydrogen Sorption Kinetics for Ball-Milled Mg₂Ni Alloys. *J. Phys. Chem. Solids*, **65**, 529–534.
113. **Jensen, C. M., and K. J. Gross** (2001) Development of catalytically enhanced sodium aluminum hydride as a hydrogen-storage material. *Appl. Phys. A*, **72**, 213-219.
114. **Jensen, C.M., R. Zidan, N. Mariels, A. Hee and C. Hagen** (1999) Advanced titanium doping of sodium aluminum hydride: segue to a practical hydrogen storage material?. *Int. J. Hydrogen Energy*, **24**, 461-465.
115. **Jensen, M., R. A. Zidan, N. Mariels, A.G. Hee and C. Hagen** (1999) Advanced titanium doping of sodium aluminum hydride: segue to a practical hydrogen storage material?. *Int. J. Hydrogen Energy*, **24**, 461-465.
116. **Jeong, S.U., R.K. Kim, E.A. Cho, H.J. Kim, S.W. Nam, I.H. Oh, S.A. Hong and S.H. Kim** (2005) A study on hydrogen generation from NaBH₄ solution using the high-performance Co-B catalyst, *J. Power Sources*, **144**, 129-134.
117. **Kang, J.K., J.Y. Lee, R.P. Muller and W.A. Goddard III** (2004) Hydrogen storage in LiAlH₄: Predictions of the crystal structures and reaction mechanisms of intermediate phases from quantum mechanics. *J. Chem. Phys.*, **121**, 10623-10633.
118. **Kaufman, C.M. and B. Sen** (1985) Hydrogen generation by hydrolysis of sodium tetrahydroborate: effects of acids and transition metals and their salts, *J. Chem. Soc. Dalton Trans.*, 307-313.
119. **Kim, J.H., H. Lee, S.C. Han, H.S. Kim, M.S. Song and J.Y. Lee** (2004) Production of hydrogen from sodium borohydride in alkaline solution: development of catalyst with high performance. *Int. J. Hydrogen Energy*, **29**, 263-267.

120. **Kissinger, H. E** (1957) Reaction kinetics in differential thermal analysis. *Anal. Chem.*, **29**,1702-1706
121. **Kiyobayashi, T., S.S. Srinivasan, D. Sun and C.M. Jensen** (2003) Kinetic study and determination of the enthalpies of activation of the dehydrogenation of titanium- and zirconium-doped Mg_2Ni and Mg_2Co . *J. Phys. Chem. A* **107**, 7671-7674.
122. **Köhler, U., J. Kumpers, and M. Ullrich** (2002) Life duration of Ni–MH cells for high power applications. *J. Power Sources*, **105**, 139-144.
123. **Kohno, T., S. Tsuruta and M. Kanda** (1996) The Hydrogen Storage Properties of New Mg_2Ni Alloy. *J. Electrochem. Soc.*, **143**, L198-L199.
124. **Kohno, T., M. Yamamoto and M. Kanda** (1999) Structural characterization and reversible hydrogen absorption properties of Mg_2Ni rich nanocomposite materials synthesized by mechanical alloying. *J. Alloys Compd.*, **293–295**, 643–647.
125. **Kojima, Y., K. Suzuki, K. Fukumoto, M. Sakaki, T. Yamamoto, Y. Kawai and J. Hayashi** (2002) Hydrogen generation using sodium borohydride solution and metal catalyst coated on metal oxide. *Int. J. Hydrogen Energy*, **27**, 1029.
126. **Kojima, Y., K. Suzuki, K. Fukumoto, Y. Kawai, M. Kimbara, H. Nakanishi and S. Matsumoto** (2004) Development of 10 kW-scale hydrogen generator using chemical hydride. *J. Power Sources*, **125**, 22–26.
127. **Kong, V.C.Y., F.R. Foulkes, D.W. Kirk and J.T. Hinatsu** (1999) Development of hydrogen storage for fuel cell generators. I: Hydrogen generation using hydrolysis hydrides. *Int. J. Hydrogen Energy*, **24**, 665-675.
128. **Korobov, I.I., N.G. Mozgina and L.N. Blinova** (1995) Effect of intermetallic $\text{LaNi}_{4.5}\text{T}_{0.5}$ (T = Mn, Cr, Co, Fe, Cu, Al) compounds on the hydrolysis of sodium borohydride in alkaline solutions. *Kinet. Catal.*, **48**, 380-384.
129. **Krishnan, P., T.H. Yang, W.Y. Lee and C.S. Kim** (2005) PtRu–LiCoO₂—an efficient catalyst for hydrogen generation from sodium borohydride solutions. *J. Power Sources*, **143**, 17-23.
130. **Kuznetsov, V.A., N.D. Gloubeva and K.N. Semenenko** (1974) Thermal behavior of sodium tetra- and hexahydroaluminates. *Russ. J. Inorg. Chem.*, **19**, 1230-1233.
131. **Liang, G., J. Huot, S. Boily, A.V. Neste and R. Schulz** (1999) Catalytic effect of transition metals on hydrogen sorption in nanocrystalline ball milled MgH_2 –Tm (Tm = Ti, V, Mn, Fe and Ni) systems. *J. Alloys Compd.*, **292**, 247–252.
132. **Liang, G., S. Boily, J. Huot, A. Van Neste and R. Schulz** (1998) Mechanical alloying and hydrogen absorption properties of the Mg–Ni system. *J. Alloys Compd.*, **267**, 302-306.

133. **Liu, B.H., Z.P. Li and S. Suda** (2005) Nickel- and cobalt-based catalysts for hydrogen generation by hydrolysis of borohydride. *J. Alloys Compd.*, **415**, 288-293.
134. **Liu, C., Y.Y. Fan, M. Liu, H.T. Chong, H.M. Cheng and M.S. Dresselhaus** (1999) Hydrogen storage in single walled carbon nanotubes at room temperature. *Science*, **286**, 1127-1129.
135. **Liu, W., H. Wu, Y. Lei, Q. Wang and J. Wu** (1997) Amorphization and electrochemical hydrogen storage properties of mechanically alloyed Mg–Ni. *J. Alloys Compd.*, **252**, 234-237.
136. **Liu, Y., C. Jiaa and H. Do** (1999) Correlation of deposition and IR properties of amorphous carbon nitride films. *Surf. Coat. Technol.* **115**, 95-102.
137. **Lovvik, O.M.S., M. Opalka, H.W. Brinks and B.C. Hauback** (2004) Crystal structure and thermodynamic stability of the lithium alanates LiAlH_4 and Li_3AlH_6 . *Phys. Rev. B* **69**, 134117/1- 134117/9
138. **Lu, J., D.B. Dreisinger and W.C. Cooper** (1997) Cobalt precipitation by reduction with sodium borohydride. *Hydrometallurgy*, **45**, 305-322
139. **Majzoub, E.H. and K.J. Gross** (2003) Titanium–halide catalyst-precursors in sodium aluminum hydrides. *J. Alloys Compd.*, **356-357**, 363-367.
140. **G. Marbán and T. Valdés-Solís** (2007) Towards the hydrogen economy?. *Int. J. Hydrogen Energy*, **32**, 1625–1637.
141. **Meiyalagan, T. and B. Viswanathan** (2005) Template synthesis and characterization of nitrogen containing carbon nanotubes, *Mater. Chem. Phys.* **93**, 291-295.
142. **Mestl, G., N.I. Maksimova, N. Keller, V.V. Roddatis and R. Schlögl** (2001) Carbon nanofilaments in heterogeneous catalysis: an industrial application for new carbon materials?. *Angew. Chem. Int. Ed.*, **40**, 2066-2068.
143. **Miesner, G.P., G.G. Tibbetts, F.E. Pinkerton, C.H. Olk and M.P. Balogh** (2002) Enhancing low pressure, hydrogen storage in sodium alanates. *J. Alloys Compd.*, **337**, 254-263.
144. **Mueller, W.M., J.P. Blackledge and G.G. Libowitz** *Metal Hydrides*, Academic Press, New York, 1968.
145. **Narayanan, R. and B. Viswanathan** *Chemical and Electrochemical Energy Systems*, Universities Press (India) Limited, Hyderabad, 1998.
146. **Nath, M., B.C. Satishkumar, A. Govindaraj, C.P. Vinod and C.N.R. Rao**, (2000) Production of bundles of aligned carbon and carbon–nitrogen nanotubes by the pyrolysis of precursors on silica-supported iron and cobalt catalysts. *Chem. Phys. Lett.*, **322**, 333–340.

147. **Oelerich, W., T. Klassen and R. Bormann** (2001) Metal oxides as catalysts for improved hydrogen sorption in nanocrystalline Mg-based materials. *J. Alloys Compd.*, **315**, 237–242.
148. **Oesterricher, H., K. Ensslen, A. Kerlin and E. Bucher** (1980), Hydriding behavior in Ca/1bMg/1bNi/1bB, *Mater. Res. Bull.*, **15**, 275-283.
149. **Orimo, S., G. Meyer, T. Fukunaga, A. Züttel, L. Schlapbach and H. Fujii**, (1999) Hydrogen in mechanically prepared nanostructured graphite. *Appl. Phys. Lett.*, **75**, 3093–3095.
150. **Orimo, S. and H. Fujii** (1997) Effects of nanometer-scale structure on hydriding properties of Mg---Ni alloys: a review. *Intermetallics*, **1998**, 185-192.
151. **Orimo, S. and H. Fujii** (2001) Materials science of Mg–Ni-based new hydrides. *Appl. Phys. A* **72**, 167–186.
152. **Park C. and R.T.K. Baker** (1998) Carbon deposition on iron–nickel during interaction with ethylene–hydrogen mixtures. *J. Catal.* **179**, 361-374.
153. **Park, C., N.M. Rodriguez and R.T.K. Baker** (1997) Carbon deposition on iron– nickel during interaction with carbon monoxide–hydrogen mixtures. *J. Catal.*, **169**, 212-227.
154. **Paul, J.** (1988) Hydrogen absorption on Al (001). *Physical Review B* **37**, 6164-6174
155. **Pinkerton, F.E., B.G. Wicke, C.H. Olk, G.G. Tibbetts, G.P. Meisner and M.S. Meyer et al.**, (2000) Thermogravimetric measurement of hydrogen absorption in alkali-modified carbon materials. *J. Phys. Chem. B* **104**, 9460–9467.
156. **Pukazhselvan, D., B.K. Gupta, A. Srivastava and O.N. Srivastava** (2005) Investigations on hydrogen storage behavior of CNT doped NaAlH₄. *J. Alloys Compd.*, **403**, 312-317.
157. **Resan, M., M.D. Hampton, J.K. Lomness and D.K. Slattery** (2005) Effects of various catalysts on hydrogen release and uptake characteristics of LiAlH₄. *Int. J Hydrogen Energy*, **30**, 1413–1416.
158. **Reilly, J.J. and R.H. Wiswall** (1967) The reaction of hydrogen with alloys of magnesium and copper. *Inorg. Chem.*, **6**, 2220-2230.
159. **Reilly, J.J. and R.H. Wiswall** (1968) The reaction of hydrogen with alloys of magnesium and nickel and the formation of Mg₂NiH₄. *Inorg. Chem.*, **7**, 2254-2256.
160. **Reilly, J.J., and R.H. Wiswall Jr.** (1974) Formation and properties of iron titanium hydride. *Inorg Chem.*, **13**, 218–222.
161. **Rodriguez, N.M.** (1993) A review of catalytically grown carbon nanofibers. *J Mater. Res.*, **8**, 3233-3250.

162. **Rongeat, C., M.-H. Grosjean, S. Ruggeri, M. Dehmas, S. Bourlot, S. Marcotte and L. Roue** (2006) Evaluation of different approaches for improving the cycle life of MgNi-based electrodes for Ni-MH batteries. *J. Power Sources*, **158**, 747-753.
163. **Rosi, N.L., J. Eckert, M. Eddaoudi, D.T. Vodak, J. Kim and M. O’Keeffe et al.** (2003) Hydrogen storage in microporous metal-organic frameworks, *Science*, **300**, 1127–1129.
164. **Sandrock, G.** (1999) A Panoramic Overview of Hydrogen Storage Alloys from a Gas Reaction Point of View. *J. Alloys Compd.*, **293-295**, 877-888.
165. **Sandrock, G. and G. Thomas** (2007) Hydride Information Center, <http://hydpark.ca.sandia.gov>
166. **Sandrock, G., K.J. Gross, G. Thomas, C.M. Jensen, D. Meeker and S. Takara** (2002a) Engineering considerations in the use of catalyzed sodium alanates for hydrogen storage. *J. Alloys Compd.*, **696**, 330-332.
167. **Sandrock, G., K.J. Gross and G. Thomas** (2002b) Effect of Ti-catalyst content on the reversible hydrogen storage properties of the sodium alanates. *J. Alloys Compd.*, **339**, 293-308.
168. **Sanguesa, C.D., R. Herrera-Urbina, and M. Figlarz** (1992) Synthesis and characterization of fine and monodisperse silver particles of uniform shape. *J. Solid State Chem.*, **100**, 272-280.
169. **Sanguesa, C.D., R. Herrera-Urbina, and M. Figlarz** (1993) Fine palladium powders of uniform particle size and shape produced in ethylene glycol. *Solid State Ionics*, **63-65**, 25-30.
170. **Sankaran M., and B. Viswanathan** (2006) The role of heteroatoms in carbon nanotubes for hydrogen storage. *Carbon*, **44**, 2816-2821.
171. **Sastry, M.V.C., B. Viswanathan and S. Srinivasa Murthy** *Metal Hydrides*, Narosa Publishing House, New Delhi, 1998
172. **Schlapbach, L.** (ed.) (1988). *Hydrogen in Intermetallic Compounds I: Electronic, Thermodynamic, and Crystallographic Properties, Preparation*, Topics in Applied Physics Vol. **63**, Springer.
173. **Schlapbach, L. and A. Züttel** (2001) Hydrogen-storage materials for mobile applications. *Nature*, **414**, 353–358.
174. **Schlesinger, H.I. and H.C. Brown** (1940) Metallo borohydrides. III. Lithium borohydride. *J. Am. Chem. Soc.*, **62**, 3429-35.
175. **Schlesinger, H. I., H.C. Brown and A.E. Finholt** (1953) The Preparation of Sodium Borohydride by the High Temperature Reaction of Sodium Hydride with Borate Esters. *J. Am. Chem. Soc.*, **75**, 205-209.

176. **Schlesinger, H.I., H.C. Brown, A.E. Finholt, J.R. Gilbreath, H.R. Hoekstra and E.K. Hyde** (1953) Sodium Borohydride, Its Hydrolysis and its Use as a Reducing Agent and in the Generation of Hydrogen. *J. Am. Chem. Soc.*, **75**, 215–219.
177. **Sen, R., B.C. Satishkumar, A. Govindaraj, K.R. Harikumar, G. Raina, J.P. Zhang et al.** (1998) “B–C–N, C–N and B–N nanotubes produced by the pyrolysis of precursor molecules over Co catalysts. *Chem. Phys. Lett.* **287** 671–676.
178. **Serp, P., M. Corrias and P. Kalck** (2003) Carbon nanotubes and nanofibers in catalysis. *Appl. Catal., A*, **253**, 337-358
179. **Shaltiel, D.** (1978) Hydride properties of AB₂ laves phase compounds, *J. Less-Common Met.*, **62**, 407-416.
180. **Shang C.X., and Z.X. Guo** (2004) Effect of carbon on hydrogen desorption and absorption of mechanically milled MgH₂. *J. Power Sources*, **129**, 73–80.
181. **Shirk, A.E. and D.F. Shriver** (1973) Raman and infrared spectra of tetrahydroaluminate, AlH₄⁻ and tetrahydrogallate, GaH₄⁻, salts. *J. Am. Chem. Soc.*, **95**, 5904-5912.
182. **Silvert, P.Y. and K. Tekaiia-Elhsissen** (1995) Synthesis of monodisperse submicronic gold particles by the polyol process. *Solid State Ionics*, **82**, 53-60.
183. **Sinfelt, J.H. J.L. Carter and D.J.C. Yates** (1972) Catalytic hydrogenolysis and dehydrogenation over copper–nickel alloys, *J. Catal.* **24**, 283-296.
184. **Singh, A.K., A.K. Singh and O.N. Srivastava** (1995) On the synthesis of the Mg₂Ni alloy by mechanical alloying. *J. Alloys Compd.*, **227**, 63-68.
185. **Smith, M.B. and G. E. Bass Jr.** (1963) Heats and free energies of formation of the alkali aluminum hydrides and of cesium hydride. Heat of formation of aluminum chloride in hydrochloric acid. *J. Chem. Eng. Data*, **8**, 342-346.
186. **Song, M.Y.** (1995) Effects of mechanical alloying on the hydrogen storage characteristics of Mg-x wt. % Ni (x = 0, 5, 10, 25 and 55) mixtures. *Int. J. Hydrogen Energy*, **20**, 221-227.
187. **Song, M.Y., I.H. Kwon, S.-N. Kwon, C.G. Park, S.-H. Hong and J.-S. Bae et al.** (2006) Hydrogen-storage properties of Mg–oxide alloys prepared by reactive mechanical grinding. *J. Alloys Compd.*, **415**, 266-270.
188. **Song, M.Y., M. Pezat, B. Darriet and P.A. Hagenmuller** (1984) Kinetics study of the H-(Mg₂Ni-2:7 wt. % Ni) system, *J. Less-Common Met.*, **103**, 145–52.
189. **Spassov, T. and U. Koster** (1999) Hydrogenation of amorphous and nanocrystalline Mg-based alloys. *J. Alloys Compd.*, **287**, 243-250.

190. **Srinivasan, S. S., H.W. Brinks, B.C. Hauback, D. Sun and C.M. Jensen** (2004) Long term cycling behavior of titanium doped NaAlH₄ prepared through solvent mediated milling of NaH and Al with titanium dopant precursors. *J. Alloys Compd.*, **377**, 283–289.
191. **Stasinevich, D.S., and G.A. Egorenko** (1968) Thermographic study of borohydrides of alkali metals and magnesium at pressures up to 10 atm. *Zh. Neorg. Khim.*, **13**, 654-658.
192. **Stioui, M., A. Gayevsky, A. Resnik, D. Shaltiel, and N. Kaplan** (1986) Macroscopic and microscopic kinetics of hydrogen in magnesium-rich compounds. *J. Less-Common Met.*, **123**, 9-24.
193. **Suda, S., Y.-M. Sun, B.-H. Liu, Y. Zhou, S. Morimitsu, K. Arai, N. Tsukamoto, M. Uchida, Y. Candra and Z.-P. Li** (2001) Catalytic generation of hydrogen by applying fluorinated-metal hydrides as catalysts. *Appl. Phys. A* **72**, 209
194. **Suenaga, K., M. Yudasaka, C. Colliex and S. Iijima** (2000) Radially modulated nitrogen distribution in CN_x nanotubular structures prepared by CVD using Ni phthalocyanine. *Chem. Phys. Lett.*, **316**, 365-372.
195. **Sun, D., S.S. Srinivasan, G. Chen and C.M. Jensen** (2004) Rehydrogenation and cycling studies of dehydrogenated NaAlH₄. *J. Alloys Compd.*, **373**, 265-269.
196. **Sun, D., S.S. Srinivasan, T. Kiyobayashi, N. Kuriyama and C.M. Jensen** (2003) Rehydrogenation of Dehydrogenated NaAlH₄ at Low Temperature and Pressure. *J. Phys. Chem. A* **107**, 10176.
197. **Sun, D., T. Kiyobayashi, H.T. Takeshita, N. Kuriyama and C.M. Jensen** (2002) X-ray diffraction studies of titanium and zirconium doped NaAlH₄: elucidation of doping induced structural changes and their relationship to enhanced hydrogen storage properties. *J. Alloys Compd.*, **337**, L8-L11
198. **Sun, D.L., Y.Q. Lei, W.H. Liu, J.J. Jiang, J. Wu and Q.D. Wang** (1995) The relation between the discharge capacity and cycling number of mechanically alloyed Mg_xNi_{100-x} amorphous electrode alloys. *J. Alloys Compd.*, **231**, 621-624.
199. **Suryanarayana, C.** (2001) Mechanical alloying and milling. *Prog. Mater. Sci.*, **46**, 1-184.
200. **Tang, C., Y. Bando, D. Golberg and F. Xu** (2004) Structure and nitrogen incorporation of carbon nanotubes synthesized by catalytic pyrolysis of dimethylformamide. *Carbon*, **42**, 2625–2633.
201. **Temme, F.P. and T.C. Waddington** (1973) Librational motion in sodium and lithium aluminum hydrides, studied by inelastic neutron scattering. *J. Chem. Soc., Faraday Trans. 2*, **69**, 783-790.

202. **Terrones, M., H. Terrones, N. Grobert, W.K. Hsu, Y.Q. Zhu, J.P. Hare et al.** (1999) Efficient route to large arrays of CN_x nanofibers by pyrolysis of ferrocene/melamine mixtures. *Appl. Phys. Lett.*, **75**, 3932–3934.
203. **Terrones, M., N. Grobert, J. Olivares, J.P. Zhang, H. Terrones, K. Kordatos et al.** (1997) Controlled production of aligned-nanotube bundles. *Nature*, **388**, 52–55.
204. **Terzieva, M., M. Khrussanova and P. Peshev** (1998) Hydriding and dehydriding characteristics of Mg-LaNi₅ composite materials prepared by mechanical alloying. *J. Alloys Compd.*, **267**, 235-239.
205. **Toshima, N., and Y. Wang.,** (1994) Preparation and Catalysis of Novel Colloidal Dispersions of Copper/Noble Metal Bimetallic Clusters. *Langmuir*, **10**, 4574-4580.
206. **van Mal, H.H., K. H. J. Buschow and F. A. Kuijpers** (1973) *J. Less-Common Met.*, **32**, 289.
207. **Varin, R.A., S. Li and A. Calka** (2004) Environmental degradation by hydrolysis of nanostructured β-MgH₂ hydride synthesized by controlled reactive mechanical milling (CRMM) of Mg. *J. Alloys Compd.*, **376**, 251-256.
208. **Varin, R.A., T. Czujko, C. Chiu and Z. Wronski** (2006) Particle size effects on the desorption properties of nanostructured magnesium dihydride (MgH₂) synthesized by controlled reactive mechanical milling (CRMM). *J. Alloys Compd.*, **424**, 356-364
209. **Viau, G., F. Fievet-Vincent, and F. Fievet** (1996) Nucleation and growth of bimetallic CoNi and FeNi monodisperse particles prepared in polyols. *Solid State Ionics*, **84**, 259-270.
210. **Vijay, R., R. Sundaresan, M.P. Maiya and S.S. Murthy** (2005) Comparative evaluation of Mg–Ni hydrogen absorbing materials prepared by mechanical alloying. *Int. J. Hydrogen Energy*, **30**, 501–508.
211. **Wang, J. A.D. Ebner, R. Zidan and J.A. Ritter** (2005a). Synergistic effects of co-dopants on the dehydrogenation kinetics of sodium aluminum hydride. *J. Alloys Compd.* **391**, 245-255.
212. **Wang, J., A.D. Ebner, T. Prozorov, R. Zidan and J.A. Ritter** (2005b) Effect of graphite as a co-dopant on the dehydrogenation and hydrogenation kinetics of Ti-doped sodium aluminum hydride. *J. Alloys Compd.*, **395**, 252-262
213. **Wang, P., A.M. Wang, B.Z. Ding and Z.Q. Hu** (2002) Mg–FeTi_{1.2} (amorphous) composite for hydrogen storage. *J. Alloys Compd.*, **334**, 243–248.
214. **Wang, Q.Y. and J.K. Johnson** (1999) High H₂ uptake by alkali-doped carbon nanotubes under ambient pressure and moderate temperatures. *J. Phys. Chem. B*, **103**, 4809-4813.

215. **Wang, X.B., W.P. Hu, Y.Q. Liu, C.F. Long, Y. Xu, S.Q. Zhou, D. Zhu and L. Dai** (2001) Bamboo-like carbon nanotubes produced by pyrolysis of iron (II) phthalocyanine. *Carbon*, **39**, 1533–1536.
216. **Wang, Y., J.W. Ren, K. Deng, L.L. Gui and Y.Q. Tang** (2000) Preparation of tractable platinum, rhodium, and ruthenium nanoclusters with small particle size in organic media. *Chem. Mater.*, **12**, 1622-1627.
217. **Wiberg, E.** (1953) New results of preparative hydride research. *Angew. Chem.*, **65**, 16-33.
218. **Wiberg, E. and E. Amberger**, (1971) *Hydrides of the elements of main groups I-IV*, Elsevier publishing company, Amsterdam.
219. **Wiench, J.W., V.P. Balema, V.K. Pecharsky and M. Pruski** (2004) Solid-state ^{27}Al NMR investigation of thermal decomposition of LiAlH_4 , *J. Solid State Chem.*, **177**, 648-653.
220. **Wu, C., F. Wu, Y. Bai, B. Yi and H. Zhang** (2005) Cobalt boride catalysts for hydrogen generation from alkaline NaBH_4 solution. *Mater. Lett.*, **59**, 1748-1751.
221. **Wu, X.B., P. Chen, J. Lin and K.L. Tan** (1999) Hydrogen uptake by carbon nanotubes, *Int. J. Hydrogen Energy*, **25**, 261-265.
222. **Wu, C.Z., P. Wang, X. Yao, C. Liu, D.M. Chen and G.Q. Lu and H.M. Cheng** (2006) Effect of carbon/noncarbon addition on hydrogen storage behaviors of magnesium hydride. *J. Alloys Compd.*, **414**, 259-264.
223. **Xiang, H.-Q., S.-B. Fang and Y.-Y. Jiang** (2002) Carbons prepared from boron-containing polymers as host materials for lithium insertion. *Solid State Ionics*, **148**, 35–43.
224. **Yang, R.T.**, (2000) Hydrogen storage by alkali-doped carbon nanotubes—revisited, *Carbon*, **38**, 623–626.
225. **Ye, Y., C.C. Ahn, C. Witham, B. Fultz, J. Liu, A.G. Rinzler, D. Colbert, K.A. Smith and R.E. Smalley** (1999) Hydrogen adsorption and cohesive energy of single-walled carbon nanotubes, *Appl. Phys. Lett.*, **74** (16), 2307–2309.
226. **Yin, Y.F., T. Mays and B. McEnaney** (2000) Molecular simulations of hydrogen storage in carbon nanotubes arrays, *Langmuir*, **16**, 10521-10527.
227. **Yuan, H.T., H.B. Yang, Z.X. Zhou, D. Song and Y. Zhang** (1997) Pressure-composition isotherms of the $\text{Mg}_2\text{Ni}_{0.75}\text{Fe}_{0.25}\text{-Mg}$ system synthesized by replacement-diffusion method. *J. Alloys Compd.*, **260**, 256.
228. **Yukawa, H., N. Morisaku, Y. Li, K. Komiya, R. Rong, Y. Shinzato, R. Sekine and M. Morinaga** (2007) Raman scattering and lattice stability of NaAlH_4 and Na_3AlH_6 . *J. Alloys and Compd.*, **446-447**, 242-247

229. **Zakharkin, L.I. and V.V. Gavrilenko** (1961) Preparation of sodium and potassium aluminum hydrides. *Bull. Acad. Sci. SSSR, Div. Chem. Sci.* 2246-2248.
230. **Zaluska, A., L.Zaluski, J.O. Strom-Olsen** (1999) Synergy of hydrogen sorption in ball-milled hydrides of Mg and Mg₂Ni, *J. Alloys Compd.*, **289**, 197-206.
231. **Zaluska, A., L. Zaluski and J.O. Ström-Olsen** (2000) Sodium alanates for reversible hydrogen storage, *J. Alloys Compd.*, **298**, 125-134.
232. **Zaluska, A., L. Zaluski and J.O. Ström-Olsen** (2001) Structure, catalysis and atomic reactions on the nano-scale: a systematic approach to metal hydrides for hydrogen storage. *Appl. Phys. A* **72**, 157–65.
233. **Zaluski, L., A. Zaluska, J.O. Ström-Olsen** (1995) Hydrogen absorption in nanocrystalline Mg₂Ni formed by mechanical alloying, *J. Alloys Compd.*, **217**, 245-249.
234. **Zaluski, L., A. Zaluska, J.O. Ström-Olsen** (1997) Nanocrystalline metal hydrides, *J. Alloys Compd.*, **253–254**, 70–79.
235. **Zaluska, A., L. Zaluski and J.O. Strom-Olsen** (1999a) Nanocrystalline magnesium for hydrogen storage, *J. Alloys Compd.*, **288**, 217-225.
236. **Zaluski, L., A. Zaluska and J.O. Storm-Olsen** (1999b) Hydrogenation properties of complex alkali metal hydrides fabricated by mechano-chemical synthesis, *J. Alloys Compd.*, **290**, 71-78.
237. **Zaluski, L., A. Zaluska, P. Tessier, J.O. Strrm-Olsen, R. Schulz** (1995) Catalytic effect of Pd on hydrogen absorption in mechanically alloyed Mg₂Ni, LaNi₅ and FeTi. *J. Alloys Compd.*, **217**, 295-300.
238. **Zhu, H., X. Li, C. Lijie, C. Xu, D. Wu and Z. Mao** (2003) Hydrogen storage in heat-treated carbon nanofibers prepared by the vertical floating catalyst method. *Mater. Chem. Phys.*, **78**, 670–675.
239. **Zhu, M., H. Wang, L.Z. Ouyang and M.Q. Zeng** (2006) Composite structure and hydrogen storage properties in Mg-based alloy. *Int. J. Hydrogen Energy*, **31(2)**, 251–57.
240. **Zidan, R. A., S. Takara, A. G. Hee and C. M. Jensen** (1999) Hydrogen cycling behavior of zirconium and titanium–zirconium-doped sodium aluminum hydride, *J. Alloys Compd.*, **285**, 119-122.
241. **Zuttel, A.** (2003) Materials for hydrogen storage, *Mater. Today*, **9**, 24-33.,
242. **Zuttel, A., S. Rentsch, P. Fischer, P. Wenger, P. Sudan, P. Mauron and C. Emmenegger**, (2003) Hydrogen storage properties of LiBH₄, *J. Alloys Compd.*, **356-357**, 515-520.

LIST OF PUBLICATIONS BASED ON RESEARCH WORK

I REFEREED JOURNALS

1. **L. Hima Kumar, B. Viswanathan and S. Srinivasa Murthy**, Alanates – Are they the appropriate hydrogen storage material? *Photo/Electro chemistry and photobiology in the environmental Energy and Fuel* **4** (2005) 13-42.
2. **L. Hima Kumar, B. Viswanathan and S. Srinivasa Murthy**, On the role of carbon additive in the hydrogenation and dehydrogenation of LiAlH_4 , *Bulletin of the Catalysis Society of India* **5** (2006) 45-54.
3. **M. Helen, B. Viswanathan, L. Hima Kumar and S. Srinivasa Murthy**, Strategies for the design of membranes for fuel cells, *Photo/Electro chemistry and photobiology in the environmental Energy and Fuel* **5** (2006) 1-42.
4. **L. Hima Kumar, B. Viswanathan and S. Srinivasa Murthy**, Catalytic effects in the generation of hydrogen from NaBH_4 , *Bulletin of the Catalysis Society of India* **5** (2006) 94-100.
5. **L. Hima Kumar, B. Viswanathan and S. Srinivasa Murthy**, Hydrogen absorption by Mg_2Ni prepared by polyol reduction, *Journal of alloys and compounds* (2007), doi:10.1016/j.jallcom.2007.07.028
6. **L. Hima Kumar, B. Viswanathan and S. Srinivasa Murthy**, Dehydrating behaviour of LiAlH_4 —the catalytic role of carbon nanofibers, *International Journal of Hydrogen Energy* **33** (2007) 366-373.

II NATIONAL/INTERNATIONAL CONFERENCE

1. Alanates as hydrogen storage materials, **B. Viswanathan, L. Hima Kumar and S. Srinivasa Murthy**, Indo-Belarus workshop on ‘Advances in sorption based thermal devices’ held at Minsk, Belarus, Nov 2nd - 3rd, 2004.
2. Hydrogen generation from alkaline solution of sodium borohydride using cobalt based catalysts, **L. Hima Kumar, B. Viswanathan and S. Srinivasa Murthy**, National workshop on ‘Catalysis for Energy’ held at Banaras Hindu University, Varanasi, India, Feb 23rd - 25th, 2006.
3. Dehydrating behaviour of LiAlH_4 – The catalytic role of carbon nanofibers, **L. Hima Kumar, B. Viswanathan and S. Srinivasa Murthy**, International Workshop on ‘Hydrogen Energy (Production, Storage and Application)’ held at Jaipur, India, Nov 5th - 9th, 2006.